The Pennsylvania State University

The Graduate School

Department of Mechanical Engineering

DYNAMICS AND DIMENSIONAL SIMILITUDE OF VEHICLE IMPACTS UPON SOIL-FIXED BOULDERS IN COHESIONLESS SOIL

A Thesis in

Mechanical Engineering

by

Mark Palmer Keske

Submitted in Partial Fulfillment
of the Requirements
for the Degree of

Master of Science

August 2012

The thesis of Mark Palmer Keske was reviewed and approved* by the following:

Sean Brennan
Associate Professor, Department of Mechanical Engineering
Thesis Advisor

Eric Marsh
Professor, Department of Mechanical Engineering
Thesis Reader

Karen A. Thole
Professor, Department of Mechanical Engineering
Head of the Department of Mechanical Engineering

*Signatures are on file in the Graduate School

ABSTRACT

This thesis describes development and application of a 2-D low-order model, scaling laws, and dimensionless equations of motion (DEOM) for a vehicle impact upon a soil-fixed boulder in cohesionless soil. The vehicle is represented as a lumped-parameter Maxwell model, the boulder is treated as a rigid body with non-negligible mass, and the soil is represented as a system of lumped-parameter Kelvin models. The low-order model has three degrees-of-freedom (DOFs), which are the linear translation of the vehicle and boulder and the angle of rotation of the boulder.

The low-order model is used to simulate a vehicle impact on a soil-fixed boulder using numerical integration techniques. The simulation is then compared and validated against past full scale crash tests. All full scale crashes were performed according to ASTM F2656-07 at an M30 rating using a 6,800 kg (15,000 lb.) medium-duty sized truck. The results of the full scale simulation agree to within $\pm$ 3° of the measured boulder angle of rotation from full scale tests.

Dimensional analysis is performed on the low-order model to develop the DEOM and scaling laws. The DEOM and scaling laws are then used to simulate small scale vehicle impacts and are first validated against full-scale simulations and full-scale crashes. Next, small scale crash tests are then designed, preformed, and validated against full scale crash tests using the scaling laws. The small scale crash tests are performed using a small equivalent vehicle mass of 8 kg. The small-scale simulations are in full similitude with the full-scale simulations, which implies 100% matching between scaled simulations. The experimentally-measured angles of rotation of the boulder for the small scale tests were found agree to within $\pm$ 3° of the full-scale past crash tests.

The results from the low-order model simulations are then used to create pass/fail boundaries for various sized boulders. The pass/fail boundaries are chosen such that failures

include boulder rotation beyond 20°; predicted boulder fracture; and excessive boulder masses. The pass/fail boundaries are then used to design a boulder of potential minimum mass that will rotate no more than 20°. At this time, simulations and small scale testing has been performed which show and an agreement of $\pm$ 3° of boulder rotation between the simulations and the small scale testing. The full scale test has not taken place at this time.

TABLE OF CONTENTS

LIST OF FIGURES

LIST OF TABLES

NOMENCLATURE

The following variables used throughout Chapter 3 and Chapter 9 are defined as the follows:

Variable	Definition
a	constant used in curve fitting for Maxwell model parameterization
$A_{\mathbb{D}}$	upper right hand matrix found within the $\mathbb{D}$ matrix
α_n	depth of soil element n with respect to the soil surface
α^*	arbitrary angular acceleration used in creation of π groupings
A_n	cross sectional area of soil element n
a_{peak}	peak acceleration observed in a rigid-wall vehicular impact
A_{rod}	cross sectional area of a long slender rod
a_{sled}	linear acceleration of the impact sled used in fracture testing
a^*	arbitrary linear accelerations used in creation of π groupings
$a_{vehicle}$	equivalent linear acceleration of a 6,800 kg vehicle from medium scale fracture testing
B	width of a pile
b	constant used in curve fitting for Maxwell model parameterization
$B_{\mathbb{D}}$	Upper left hand matrix within the $\mathbb{D}$ matrix
β^*	arbitrary constant of horizontal subgrade reaction used in creation of π groupings
β	constant of horizontal subgrade reaction
b'	slope of the linear curve fit of the modulus of subgrade reaction vs. depth
CBR	California Bearing Ration in percent
c_n	damping constant for soil element n
c_p	distance from the pivot point to the center of mass of the small scale pendulum
c^*	arbitrary damping constant used in creation of π groupings
c_v	damping constant for the impact vehicle
c_x	distance from the local origin to the center of mass of the boulder-soil subsystem in the X direction
c_y	distance from the local origin to the center of mass of the boulder-soil subsystem in the Y direction
d	embedment depth of the boulder
δ	small scale parameter
Δ	full scale parameter
Δx_{bv}	change in linear displacement of the contact point between the vehicle and boulder
Δn	change in linear displacement of soil element n
d_i	depth at increment i of the dynamic cone penetrometer
d_n	depth of soil element n with respect to the center of mass of the boulder-soil subsystem

$\frac{d\vec{P}_n}{dt}$	Change in momentum of soil element n
D_r	relative dry density of the soil
e	eccentricity of the vehicle impact with respect to the soil surface
E	unity matrix
e_{bumper}	distance from the soil surface to the bottom of the vehicle bumper
e'	distance from the soil surface to either the top of the boulder or the top of the vehicle hood
E_{rod}	Young's modulus of a long slender rod
$\vec{F}_n$	arbitrary force vector acting on the boulder from soil element n
F_{c_n}	force from soil representative damper n
$F_{distributed}$	assumed distributed load acting on the boulder from the front of the vehicle
$F_{fracture}$	fracture force acting on the boulder from a vehicle impact
F_{k_n}	force from soil representative spring n
F_n	total force from soil element n
F_{u_n}	ultimate lateral load of soil element n
F_v	force acting on the boulder from the vehicle
$F_v{}'$	force acting on the vehicle from the boulder
g	gravitational constant
γ	unit weight of soil
$\gamma_b{}'$	angle between the center of mass of the boulder and the boulder-soil subsystem
γ_n	angle between vertical and soil element n
$\gamma_n{}^*$	dimensionless representation of γ_n
γ_v	angle between the center of mass of the boulder-soil subsystem and impact vehicle
$\gamma_v{}^*$	dimensionless representation of γ_v
H	boulder height with respect to impact direction
h_e	height of one soil element
I	area moment of inertia of the boulder in the XZ plane
J_b	mass moment of inertia of the boulder about the Z axis
J_{eff}	mass moment of inertia of the boulder-soil subsystem about the Z axis
J_p	mass moment of inertia of the small scale pendulum about the pivot point, p
j^*	arbitrary linear jerk used in creation of π groupings
K_ε	strain rate loading constant
K_i	modulus of subgrade reaction at increment i, from dynamic cone penetrometer test
k_n	linear spring constant of soil element n
K_p	passive earth pressure coefficient
k_{rod}	equivalent linear spring constant of a long slender rod
k^*	arbitrary spring constant used in creation of π groupings
k_v	equivalent linear spring constant of the impact vehicle

L	length of the boulder with respect to impact direction
l_n	distance from the center of mass of the boulder-soil subsystem to the soil element n in the X direction
l_p	length of the small scale pendulum arm from the pivot point, p
L_{rod}	length of a long slender rod
L_{soil}	length of the top of the passive soil wedge
L^*	arbitrary length used in creation of π groupings
m_b	mass of the boulder
m_{eff}	mass of the boulder-soil subsystem
$M_{fracture}$	bending moment acting on the from the impact vehicle
m_n	mass of soil element n
M_n	moment from soil element n about the center of mass of the boulder-soil subsystem
$\dot{m}_n$	time rate of change of the mass of soil element n
$m_n{}'$	added soil from translation of soil element n
$\dot{m}_n{}'$	time rate of change of the added soil, $m_n{}'$
m'	inertial mass
M_R	restoring moment from boulder tip
$M_{R_{max}}$	maximum restoring moment of the boulder
m_{sled}	mass of the medium scale impact sled
m_v	mass of the vehicle
M_v	moment from the vehicle impact about the center of mass of the boulder-soil subsystem
$m_{vehicle}$	mass of the ideal M30 vehicle
N	number of soil elements
N_{bd}	number of base dimensions
$n_{fracture}$	factor of safety with respect to fracture
N_π	number of independent π groupings
N_v	number of governing variable in the low-order model
ω^*	arbitrary angular velocity used in creation of π groupings
$\bar{}$	notation for desired parameter in either small or full scale testing
$\vec{P}_n$	momentum of soil element n
φ'	effective angle of internal friction of the soil
PI	penetration index from DCPT
π_{α_n}	dimensionless π grouping for the depth of soil element n with respect to the soil surface, α_n
π_{α^*}	dimensionless π grouping for the arbitrary angular acceleration used in creation of π groupings, α^*
π_{a^*}	dimensionless π grouping for the arbitrary linear accelerations used in creation of π groupings, a^*
π_β	dimensionless π grouping for the constant of horizontal subgrade reaction, β

π_{β^*}	dimensionless π grouping for the arbitrary constant of horizontal subgrade reaction used in creation of π groupings, β^*
π_{c^*}	dimensionless π grouping for the arbitrary damping constant used in creation of π groupings, c^*
π_{c_v}	dimensionless π grouping for the damping constant for the impact vehicle, c_v
π_{c_x}	dimensionless π grouping for the distance from the local origin to the center of mass of the boulder-soil subsystem in the X direction, c_x
π_{c_y}	dimensionless π grouping for the distance from the local origin to the center of mass of the boulder-soil subsystem in the Y direction, c_y
π_d	dimensionless π grouping for the embedment depth of the boulder, d
π_{d_n}	dimensionless π grouping for the depth of soil element n with respect to the center of mass of the boulder-soil subsystem, d_n
π_e	dimensionless π grouping for the eccentricity of the vehicle impact with respect to the soil surface, e
$\pi_{F_{c_n}}$	dimensionless π grouping for the force from soil representative damper n, F_{c_n}
$\pi_{F_{k_n}}$	dimensionless π grouping for the force from soil representative spring n, F_{k_n}
π_{F_n}	dimensionless π grouping for the total force from soil element n, F_n
$\pi_{F_{u_n}}$	dimensionless π grouping for the ultimate lateral load of soil element n, F_{u_n}
π_H	dimensionless π grouping for the boulder height with respect to impact direction, H
π_{h_e}	dimensionless π grouping for the height of one soil element, h_e
π_{J_b}	dimensionless π grouping for the mass moment of inertia of the boulder about the Z axis, J_b
$\pi_{J_{eff}}$	dimensionless π grouping for the mass moment of inertia of the boulder-soil subsystem about the Z axis, J_{eff}
π_{j^*}	dimensionless π grouping for the arbitrary linear jerk used in creation of π groupings, j^*
π_{k^*}	dimensionless π grouping for the arbitrary spring constant used in creation of π groupings, k^*
π_{k_v}	dimensionless π grouping for the equivalent linear spring constant of the impact vehicle, k_v
π_L	dimensionless π grouping for the length of the boulder with respect to impact direction, L
π_{l_n}	dimensionless π grouping for the distance from the center of mass of the boulder-soil subsystem to the soil element n in the X direction, l_n
π_{L^*}	dimensionless π grouping for the arbitrary length used in creation of π groupings, L^*
π_{m_b}	dimensionless π grouping for the mass of the boulder, m_b
$\pi_{m_{eff}}$	dimensionless π grouping for the mass of the boulder-soil subsystem, m_{eff}
π_{m_n}	dimensionless π grouping for the mass of soil element n, m_n
π_{M_n}	dimensionless π grouping for the moment from soil element n about the center of mass of the boulder-soil subsystem, M_n
π_{M_R}	dimensionless π grouping for the restoring moment from boulder tip, M_R
$\pi_{M_{Rmax}}$	dimensionless π grouping for the maximum restoring moment of the boulder,

	M_{Rmax}
π_{M_v}	dimensionless π grouping for the moment from the vehicle impact about the center of mass of the boulder-soil subsystem, M_v
π_{ω^*}	dimensionless π grouping for the arbitrary angular velocity used in creation of π groupings, ω^*
π_{ρ_b}	dimensionless π grouping for the mass density of the boulder, ρ_b
$\pi_{\rho_{soil}}$	dimensionless π grouping for the mass density of the soil, ρ_{soil}
π_{ρ^*}	dimensionless π grouping for the arbitrary mass density used in creation of π groupings, ρ^*
π_{R_n}	dimensionless π grouping for the radial distance from the center of mass of the boulder-soil subsystem to soil element n, R_n
π_{R_v}	dimensionless π grouping for the radial distance from the center of mass of the boulder-soil subsystem to the impact vehicle contact point, R_v
π_t	dimensionless π grouping for the time, t
$\pi_{\ddot{\theta}_b}$	dimensionless π grouping for the angular acceleration of the boulder-soil subsystem about the Z axis, $\ddot{\theta}_b$
$\pi_{\dot{\theta}_b}$	dimensionless π grouping for the angular velocity of the boulder-soil subsystem about the Z axis, $\dot{\theta}_b$
π_{t^*}	dimensionless π grouping for the arbitrary time used in creation of the π groupings, t^*
π_{v^*}	dimensionless π grouping for the arbitrary velocity used in the creation of π groupings, v^*
π_W	dimensionless π grouping for the width of the boulder with respect to the impact direction, W
π_{x_b}	dimensionless π grouping for the linear displacement of the center of mass of the boulder-soil subsystem, x_b
$\pi_{\dot{x}_b}$	dimensionless π grouping for the linear velocity of the center of mass of the boulder-soil subsystem , $\dot{x}_b$
$\pi_{\ddot{x}_b}$	dimensionless π grouping for the linear acceleration of the center of mass of the boulder-soil subsystem , $\ddot{x}_b$
π_{x_v}	dimensionless π grouping for the linear displacement of the impact vehicle, x_v
$\pi_{\dot{x}_v}$	dimensionless π grouping for the linear velocity of the vehicle, $\dot{x}_v$
$\pi_{\ddot{x}_v}$	dimensionless π grouping for the linear acceleration of the vehicle, $\ddot{x}_v$
$\pi_{\dddot{x}_v}$	dimensionless π grouping for the linear jerk of the impact vehicle, $\dddot{x}_v$
p_u	ultimate lateral pressure of soil element n
q	dimensional change of basis vector
$R_b{}'$	radial distance from the center of mass of the boulder to the center of mass of the boulder-soil subsystem
ρ_b	mass density of the boulder
ρ_{soil}	mass density of the soil
$\rho_{soil_{max}}$	maximum mass density of the soil
ρ^*	arbitrary mass density used in creation of π groupings
R_n	radial distance from the center of mass of the boulder-soil subsystem to soil element n

R_v	radial distance from the center of mass of the boulder-soil subsystem to the impact vehicle contact point
$\sigma_{1,2}$	principle stresses on the XZ and YZ planes
σ_n	normal stress acting on the YZ face of soil element n
σ_y	bending stress on the cross section of the boulder about the Y axis
S_{uc}	ultimate compressive strength of granite
S_{ut}	ultimate tensile strength of granite
t	time
τ_{yx}	shear stress acting on the boulder cross section
θ_b	angular rotation of the boulder-soil subsystem about the Z axis
$\ddot{\theta}_b$	angular acceleration of the boulder-soil subsystem about the Z axis
$\dot{\theta}_b$	angular velocity of the boulder-soil subsystem about the Z axis
$\ddot{\theta}_p$	angular acceleration of the small pendulum about the Z axis
$\dot{\theta}_p$	angular velocity of the small pendulum about the Z axis
θ_p	angular rotation of the small pendulum about the Z axis
θ_w	defining angle of the passive soil wedge measured from vertical
t^*	arbitrary time used in creation of the π groupings
v_o	initial velocity of the impact vehicle
v^*	arbitrary velocity used in the creation of π groupings
W	width of the boulder with respect to the impact direction
X	global X axis, right
x	distance from the centroid of the cross section to the impact face which corresponds to maximum bending stress
x_b	linear displacement of the center of mass of the boulder-soil subsystem
$\ddot{x}_b$	linear acceleration of the center of mass of the boulder-soil subsystem
$\dot{x}_b$	linear velocity of the center of mass of the boulder-soil subsystem
$x_b{}'$	linear displacement of the center of mass of the boulder
x_n	linear displacement of soil element n
$\dot{x}_n$	linear velocity of soil element n
x_p	linear displacement of the impact point on the small pendulum
$\ddot{x}_p$	linear acceleration of the impact point on the small pendulum
$\dot{x}_p$	linear velocity of the impact point on the small pendulum
x'	linear displacement of the inertial mass
$\dot{x}'$	linear velocity of the inertial mass
$\ddot{x}'$	linear acceleration of the inertial mass
$\dddot{x}'$	linear jerk of the inertial mass
x_v	linear displacement of the impact vehicle
$\dddot{x}_v$	linear jerk of the impact vehicle
$\ddot{x}_v$	linear acceleration of the vehicle
$\dot{x}_v$	linear velocity of the vehicle

Y	global Y axis, down
Z	global Z axis, into the page
z	depth along a pile from the soil surface

ACKNOWLEDGEMENTS

First and foremost, I would like to thank God. There is none greater; without Him, His loving and saving grace, or His Son, Jesus Christ, who died for me on the cross, I am nothing. Through Him, however, I can do all things. To God be the glory, forever and ever.

I would also like to thank all of those people with whom I came into contact while at Penn State and those that supported me from afar.

Alex Brown, your mind truly is a beautiful thing, and without you I would not be here today. Thank you for your insight and your devotion to higher education. I would also like to thank Sam Hoskins, who fought the good fight with me on those cold mornings in the winter and the scorching afternoons in the summer out at the test track. Your work ethic is far greater than any I've ever come across, and I hope someday that I too will have people telling me to stop running everywhere. Jesse Pentzer, I would like to thank you for your help, knowledge, and being my officemate. Thank you for suffering through the Markisms which I'm sure only got worse as I tumbled farther and farther down the rabbit hole. Dr. Brennan, don't think I forgot about you. Thank you for being my advisor and leader during my time here at Penn State. Your patience, dedication, and profound knowledge of seemingly all things have never once failed to amaze me. I personally don't know how you do it all.

Thank you to all of the Larson Transportation Institute, Crash Safety Research Facility, and Civil Infrastructure Testing and Evaluation Laboratory personnel. Thank you for your support and willingness to help. Thank you to all of my friends both here at Penn State and back at home. I am so grateful that I have gotten the opportunity to meet and spend time with all of you. From playing basketball with the Saturday Morning Ballers and flag football and running with my fellow Geeks in Sneaks to riding motorcycles during the balmy Thanksgiving weather, I've had the time of my life. I would especially like to thank the students in Dr. Brennan's

research group. You are one of my favorite groups of people with whom I have had the opportunity to work and play. Big potato moths!

Last but certainly not least, I would like to thank my family for their love, support, and understanding over the past two years. I realize that my actions may have seemed erratic or that I must have fallen off the side of the earth, but thank you keeping me tied to the ground and not letting me lose contact. I love you all.

WAR EAGLE!

CHAPTER 1

INTRODUCTION

This thesis presents a low-order model for a vehicle impact upon a soil-fixed boulder and the use of dimensional analysis to perform dimensionally similar small scale versions of past crash tests. The model is limited to cohesionless soils which are typically sands and gravels, which allow water to permeate even when firmly compacted [1]. In addition, methodology is presented which demonstrates how to use the results from dimensional analysis and the low-order model as a design tool for developing full scale boulders. The low-order model presented in Chapter 3 can be idealized as a lumped-parameter vehicle model impacting a soil-embedded object. A brief introduction into the modeling techniques for vehicle impacts and laterally loaded soil-fixed objects is first presented. Then, the applications of dimensional analysis will be briefly discussed.

1.1 Vehicle models

Modeling vehicles crashes is a well-studied subject in which several models have been created. The two simplest and most taught are the lumped-parameter Kelvin model and the lumped-parameter Maxwell model. The lumped-parameter Kelvin model is oft used in crash tests which exhibit little to no permanent damage to the vehicle during impact [2]. The Kelvin model will always return to the same equilibrium position after deflections occur since the spring is in parallel with the damper. Such cases involve low speed collisions. The lumped-parameter Maxwell model, however, is oft used in cases which involve the crushing of the front end of the vehicle [2]. Unlike the Kelvin model, the Maxwell model allows for permanent deflections since

the spring is placed in series with the damper. Such cases involve high-speed crashes. The scope of this thesis pertains to M30 rated vehicle impacts as defined by ASTM F2656-07 in which a 15,000 lb. (6800 kg) impact vehicle is accelerated to 30 mph (13.4 m/s). As shown in Figure 1-1, a 30 mph car crash, even for smaller vehicles, would induce a vast amount of permanent damage and front end deformation. The use of a lumped-parameter Maxwell model for vehicle impacts is further reviewed in Chapter 2.

Figure 1-1. 31 mph crash test of a 2009 Volvo C30 into a rigid wall [3]

1.2 Laterally loaded pile models

Similarly, numerous models and analytical methods have been proposed in an attempt to predict displacements, stresses, and reaction forces of a loaded structure embedded in soil.

Models of particular interest as related to the scope of this thesis include laterally loaded soil models. More specifically, the idea of a vehicular impact upon a soil embedded boulder may be conceptually idealized as an embedded object that is laterally loaded at some arbitrary point at or above the soil surface. In civil engineering, the research that most closely resembles this line of reasoning involves laterally loaded piles, where a pile is typically a long, slender elastic beam that is most often embedded vertically in the soil. Figure 1-2 shows the configuration of a typical laterally loaded pile embedded in soil. The variables in Figure 1-2 are the applied moment, M_g, applied lateral load, Q_g, depth of pile at location z, and total length of the pile, L.

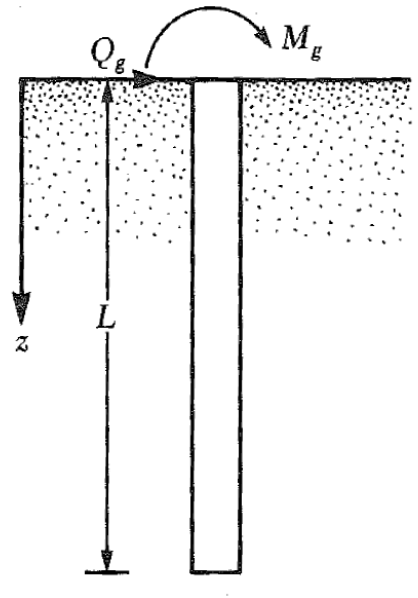

Figure 1-2. Typical configuration of laterally loaded piles [4].

1.3 Dimensional analysis

Dimensional analysis is applied to the low-order model as a means of developing dimensionless equations of motion and scaling laws. The scaling laws would allow for the

creation of small scale crash test from which the results can be scaled up to the full scale size. The major selling point in small scale testing is that an expensive full scale crash test can be duplicated on a much smaller and cheaper scale. Industry has already verified this concept with the simple advent of wind tunnels.

1.4 Thesis organization

The organization of this thesis is presented as follows:

The salient literature pertaining to the development of a low-order model and application of dimensional analysis is briefly reviewed in Chapter 2. Salient soil property measurement techniques and boulder properties are also reviewed in Chapter 2. Following the review of salient literature, the development of the low-order model and boulder fracture prediction methodology is presented in Chapter 3. Next, Chapter 4 presents the verification of the low-order model and fracture prediction methodology by comparing them to past full scale crash tests which include two soil-fixed tests and two rigidly embedded tests. After the low-order model has been verified against past crash data, the development of the dimensionless equations of motion and associated scaling laws for the low-order model are presented in Chapter 5. Similarly, the validation of the dimensionless equations of motion and scaling laws through the creation of dimensionally similar small scale crash tests is presented in Chapter 6. Chapter 7 presents the development of a tool which can be used in the selection of boulder geometries based on desired boulder motion, and the application of the design tool is presented in Chapter 8 by proactively designing and verifying a boulder to meet dynamic constraints. Lastly, the summarization of results presented and proposed future work as related to this thesis topic are discussed in Chapter 9.

CHAPTER 2

LITERATURE REVIEW

The concept of a low-order dynamic model for vehicular impacts on soil-fixed boulders is a relatively unaddressed topic in common literature; however, individual aspects of such a model have been widely researched and are commonly used. This work combines aspects of prior art to derive the models presented later. An in-depth look at prior work will be presented here with the goal of developing a low-order model of a vehicle during front end collision with a soil embedded boulder, including consideration of both static and dynamic loads. Previous works of particular interest include low-order vehicle models for front end collisions, a model for laterally loaded piles in cohesionless soils, boulder fracture mechanics, and scaling laws associated with both vehicle impacts and laterally loaded piles.

2.1 Low-order vehicle modeling

Several low-order vehicle models have been developed regarding the representation of a vehicle during a front end collision. The Maxwell model is a commonly used model in representing vehicles during a front end collision. The Maxwell models will be briefly reviewed in an attempt to create a low-order vehicle representation.

It is common practice in literature to represent a front end vehicle collision as a 1-D Maxwell model [2]. Figure 2-1 shows a typical Maxwell model for vehicular impacts. The variables in Figure 2-1 are the effective spring constant, k, damping constant, c, lumped vehicular mass, m, vehicle displacement, d, and inertial mass, m', and inertial mass displacement, d'.

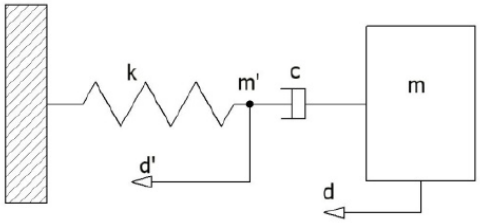

Figure 2-1. Maxwell model for front end vehicle collision [2]

Pawlus [2] performed a series of pole impact tests for various types of vehicles and compared the predicted displacements to measured displacements when using a Maxwell model. Pawlus [2] fit the spring and damper coefficients for the Maxwell model from full scale crash tests and plotted the estimated displacement, speed, and acceleration compared to the actual measurements from of the vehicle. The results presented in [2] can be seen in Figure 2-2.

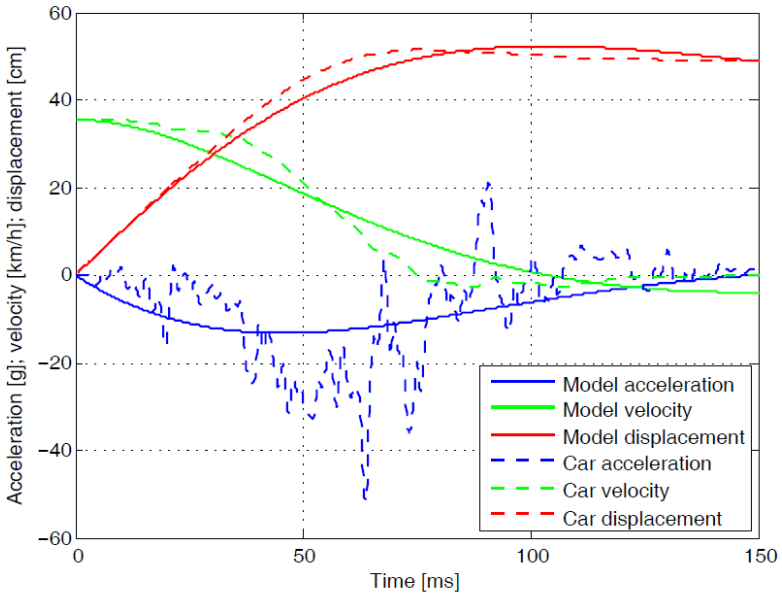

Figure 2-2. Maxwell model and full scale test responses of a rigid pole impact test [2]

As seen in Figure 2-2, the values obtained for the spring and damper coefficients using the method proposed in [2] show good agreement between predicted and measured responses of

the vehicle. The Maxwell will also be used model a vehicle impacting a soil fixed boulder in this work and will be compared against the Kelvin model as well as full scale crash tests.

2.2 Dimensional analysis of vehicle collisions

The effects of various vehicle parameters have significant influences on the forces and displacements during impact. These effects can be experimentally determined through full scale tests, but full scale testing is often expensive, time consuming, and experimentally cumbersome. Rather than performing several full scale tests, it is common practice to develop small scale experiments in order to study the effects of various vehicle parameters during impact.

The effectiveness of small scale crash tests were confirmed by Homes and Sliter [5], who conducted full and small scale vehicle crash tests under matching scaling parameters. They compared the results seen in full- and small-scale experiments. A comparison between the full scale and ¼ scale model is shown in Figure 2-3.

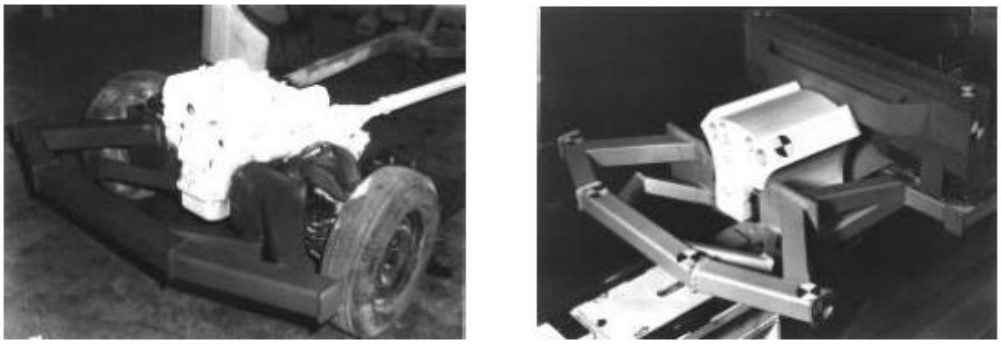

Figure 2-3. Full scale vehicle test apparatus (left), ¼ scale vehicle test apparatus (right) [6]

The small scale crash test parameters, such as material properties, were derived using scaling laws obtained from the dimensional analysis of vehicular impacts. Both the full and small scale vehicles impacted a rigid pole during which the accelerations, velocities and positions of

both full and small scale were measured using the appropriate sensors and high-speed video. Both the full scale and small scale crash tests demonstrated similar deformations and material failure as shown in Figure 2-4 and Figure 2-5.

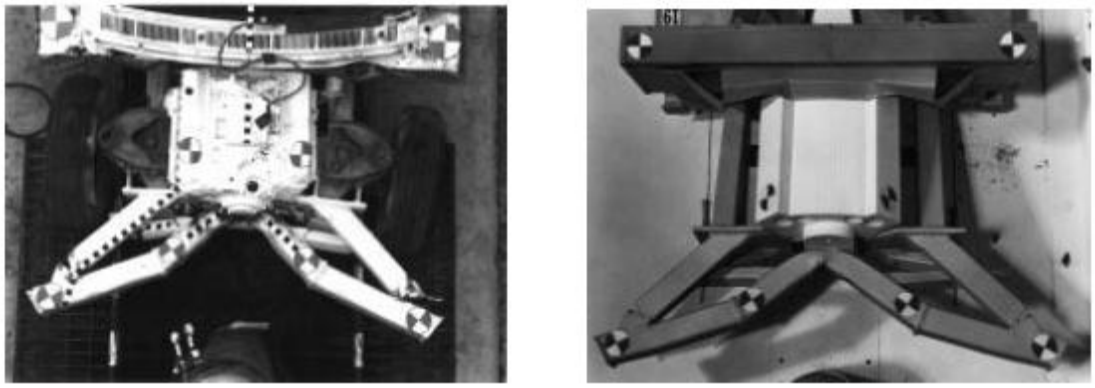

Figure 2-4. Full scale vehicle deformations (left), ¼ scale vehicle deformations (right) [6]

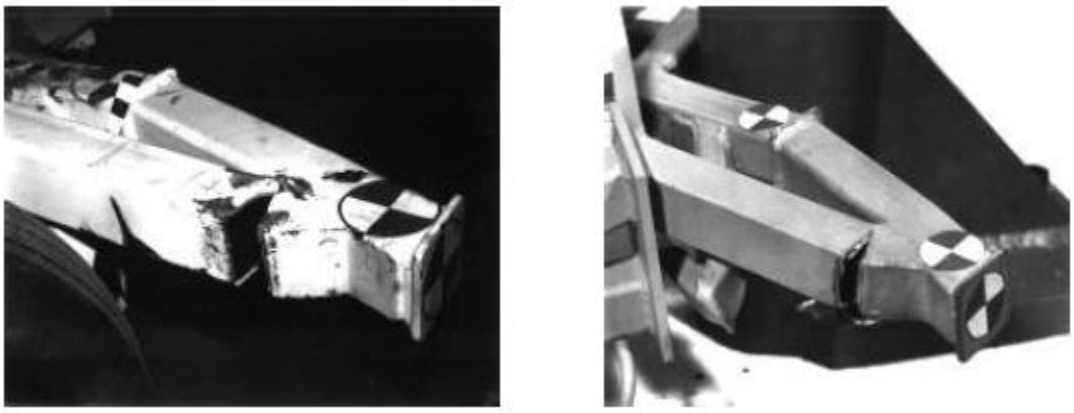

Figure 2-5. Full scale material failure (left), ¼ scale material failure (right) [6]

The velocities and accelerations measured during impact are shown in Figure 2-6. Table 2–1 shows the measured distances during the impacts and comparison of observed deformations.

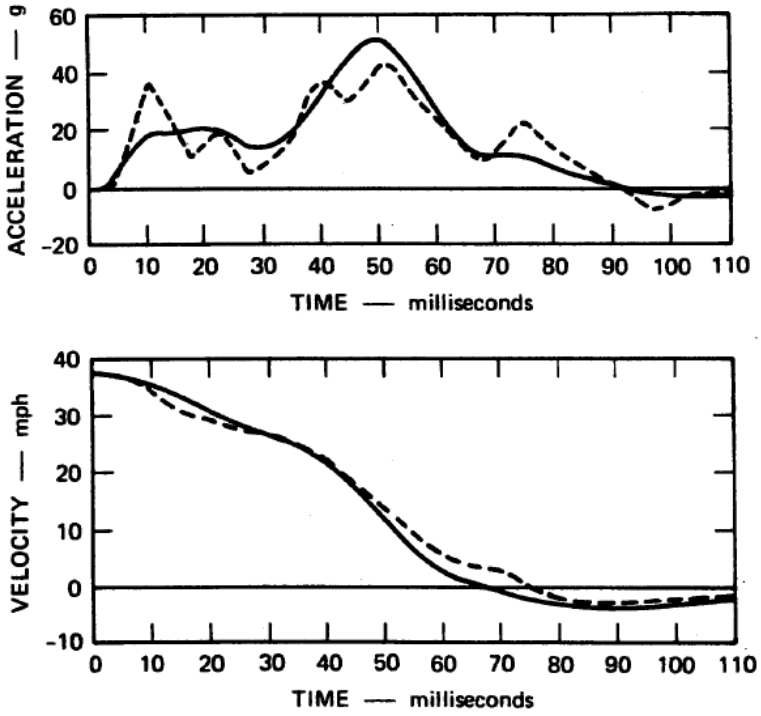

Figure 2-6. Comparison of full (dashed line) and small (solid line) scale velocities and accelerations for vehicular front end collisions [5] (units are in full scale dimensions).

Table 2–1. Measured distance and deformation comparison between full and small scale front end vehicular collisions

	Full Scale	Scale Model*
1.	Total collapse of front end was 22 inches	20 inches
2.	Vehicle rebounded from pole - 18 inches	20 inches**
3.	The two outer hinges fractured near front bumper	Same response
4.	The two inner hinges fractured near their connection points	Same response, but fractures less extensive
5.	Outside frame members failed downward just aft of reinforcing plates	Some deflection but much less than in full-scale
6.	The firewall was displaced approximately 3 inches	1 inch
7.	Box support behind engine crushed 3 inches	3 inches
8.	Steering post moved aft 1 inch	Not applicable
9.	Peak deceleration 44 g	51 g
10.	Compartment forward motion ceased 79 ms after impact.	70 ms

* Measurements are scaled to the prototype size for direct comparison.

** This rebound is often affected by gravity and may not scale.

As seen in Figure 2-4, Figure 2-5, and Table 2–1, the results from the scaled model tests closely agree with those measured during full scale testing. This scaling methodology is used to model a small scale vehicle during impact.

2.3 Low-order Soil Modeling

Several models and analytical methods have been developed in the literature to predict soil pile interaction during lateral loading. Such analytical models include methodologies proposed by Zhang [7] and Naggar and Bentley [8]. An in-depth look will be taken into these commonly used laterally loaded pile models.

2.3.1 Nonlinear analysis of laterally loaded rigid piles

Zhang [7] developed a computational method for predicting the displacement of a laterally loaded, short rigid pile in cohesionless soil due to static loading. Zhang [7] proposed that, for small displacements, short rigid piles rotate about a single point as shown in Figure 2-7. The variables in Figure 2-7 are the applied lateral load, H, load eccentricity, e, depth of pile at location z, total length of the pile, L, lateral displacement, y, lateral displacement of the pile head, y_o, and angular rotation of the pile, ω.

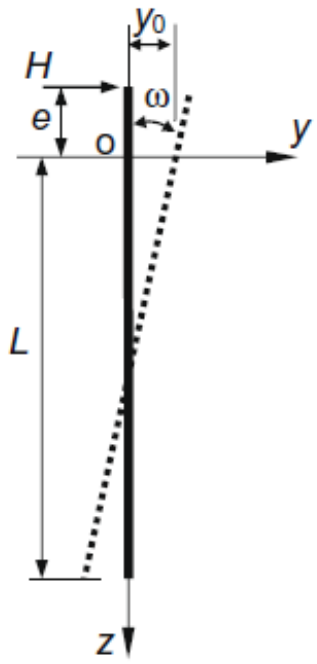

Figure 2-7. Short rigid pile model as defined in [7]

Rather than representing the soil as a system of non-linear springs and using explicitly measured pressure-displacement curves in the prediction of pile motion, Zhang [7] calculated the soil reaction pressure as a function of embedment depth and static forces within the soil. The lateral soil pressure is limited to the ultimate lateral load which the soil can support at a given depth based on soil properties such as the horizontal modulus of subgrade reaction. The

horizontal modulus of subgrade reaction for cohesionless soils is assumed to vary linearly with depth [7]. Zhang [7] classifies three cases of lateral loading based on soil yielding and respective soil reaction pressures. Figure 2-8 shows the three cases of lateral loading with respect to soil yielding as the lateral load and applied moment, M, is increased. The variables in Figure 2-8 are the distance from the pile head to the fixed point of rotation moment, a, the depth from the pile head to the ending point of nonlinear soil-pile interaction above the fixed point of rotation, b, and the depth from the pile head to the point at which nonlinear soil-pile interaction begins below the fixed point of rotation, c.

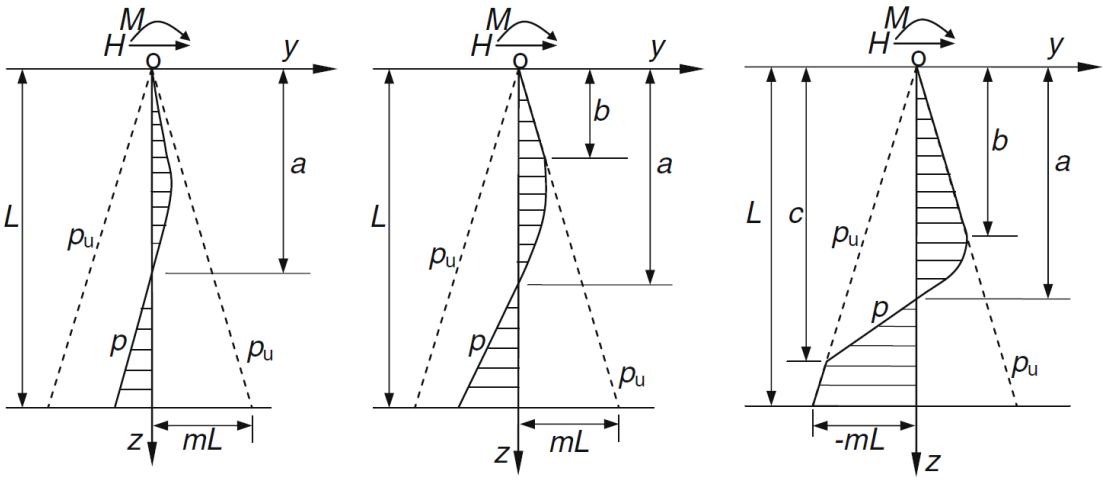

Figure 2-8.Soil reactions for laterally loaded, short rigid piles in which there is no soil yielding (left), soil yielding in the region above the point of rotation (middle), and soil yielding in the regions both above and below the fixed point of rotation [7]

Zhang [7] compared predicted results for statically, laterally loaded, short rigid piles against full scale tests which can be seen in Figure 2-9, where D_r is the relative density of the soil. The full scale tests were conducted by Prasad and Chari [9].

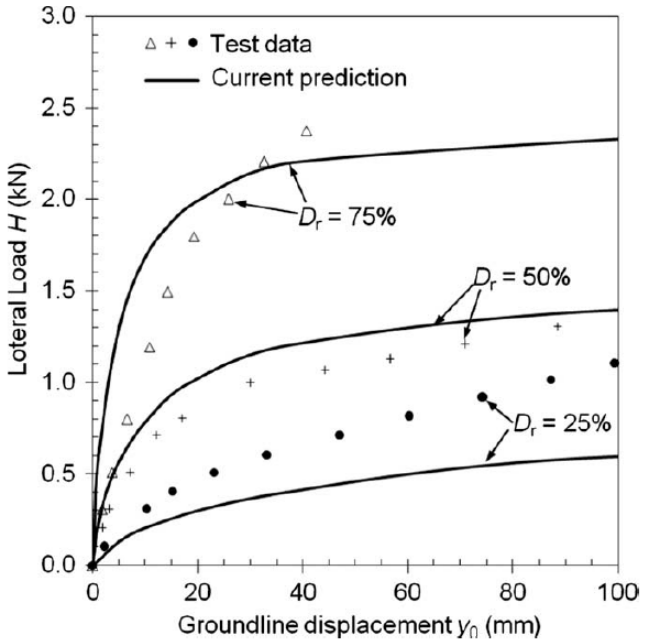

Figure 2-9. Predicted pile head displacement compared to measured values [7]

As seen in Figure 2-9, the predicted pile displacements agree to within reason with the measured pile displacements resulting from static loading for short rigid piles. The methodology presented in [7] does not, however, account for explicit pile translation or the effect of pile inertial properties such as mass moment of inertia. Furthermore, the methodology in [7] assumes a static load. The determination of ultimate lateral loads for cohesionless soils and the corresponding relationship between the embedment depth and the ultimate soil lateral load are used in this work in the modeling of the soil-boulder interaction.

2.3.2 Dynamic analysis for laterally loaded piles

Naggar and Bentley [8] developed a method for predicting the displacements of a laterally loaded, long elastic pile under dynamic loading. The methodology proposed by Naggar and Bentley [8] incorporates the p-y method applied to a Winkler model as well as wave

propagation and energy dissipation to develop static p-y curves. The static p-y curves are transformed into dynamic p-y curves through the addition of dampers as shown in Figure 2-10. The variables in Figure 2-10 are the applied force as a function of time, $F(t)$, linear spring and damper constants for the far field soil, k_L and c_L, nonlinear spring and damper constants for the near field soil, k_{NL} and c_{NL}, mass of the soil associated with the near field soil, m_1, and the mass of the soil associated with the far field, m_2.

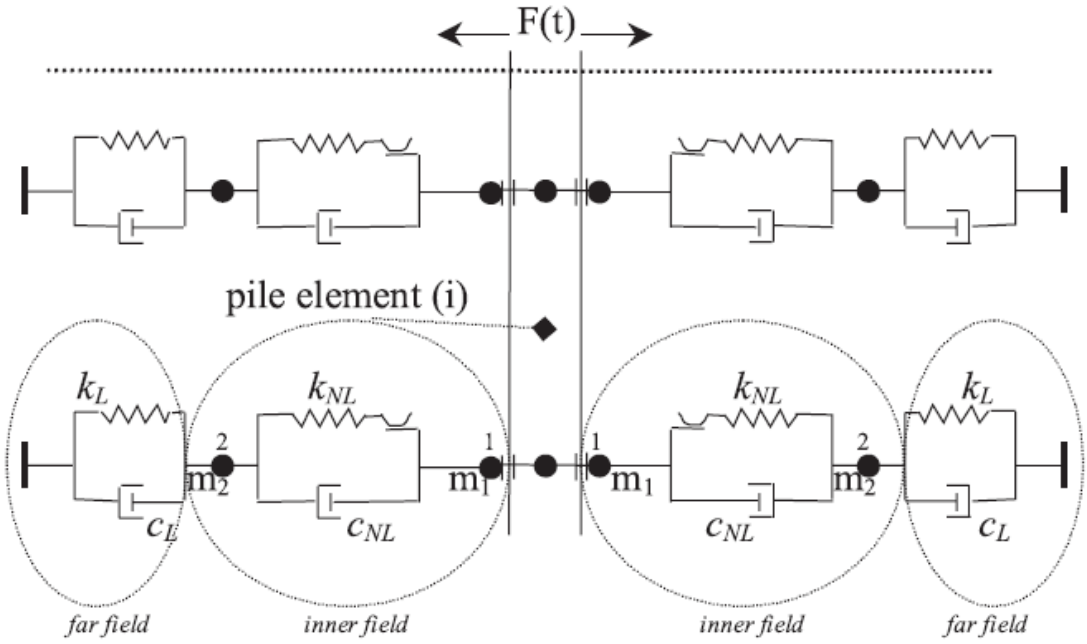

Figure 2-10. Dynamic soil-pile model as proposed by Naggar and Bentley Dynamic [8]

The mass of the soil within the inner field is lumped against the pile due to the assumed massless area as demonstrated by Novak and Sheta [10]. Naggar and Bentley [8] calculate the spring and dashpot constants for the soil element based on empirical data from cyclic pile head loading tests for specific soils. The empirically derived spring and dashpot constants are then used in predicting the displacement of a dynamically laterally loaded pile. Naggar and Bentley [8] compared the predicted pile head displacements against measured pile head deflections for

two cases of dynamically, laterally loaded, long elastic piles using a statnamic device, which incorporates both static and dynamic loading. The two cases involved a lateral dynamic load of 350 kN and 470 kN respectively. Further soil and pile conditions of the tests can be found in [11]. The results of the methodology used in [8] compared to measured data from full scale experiments are shown in Figure 2-11.

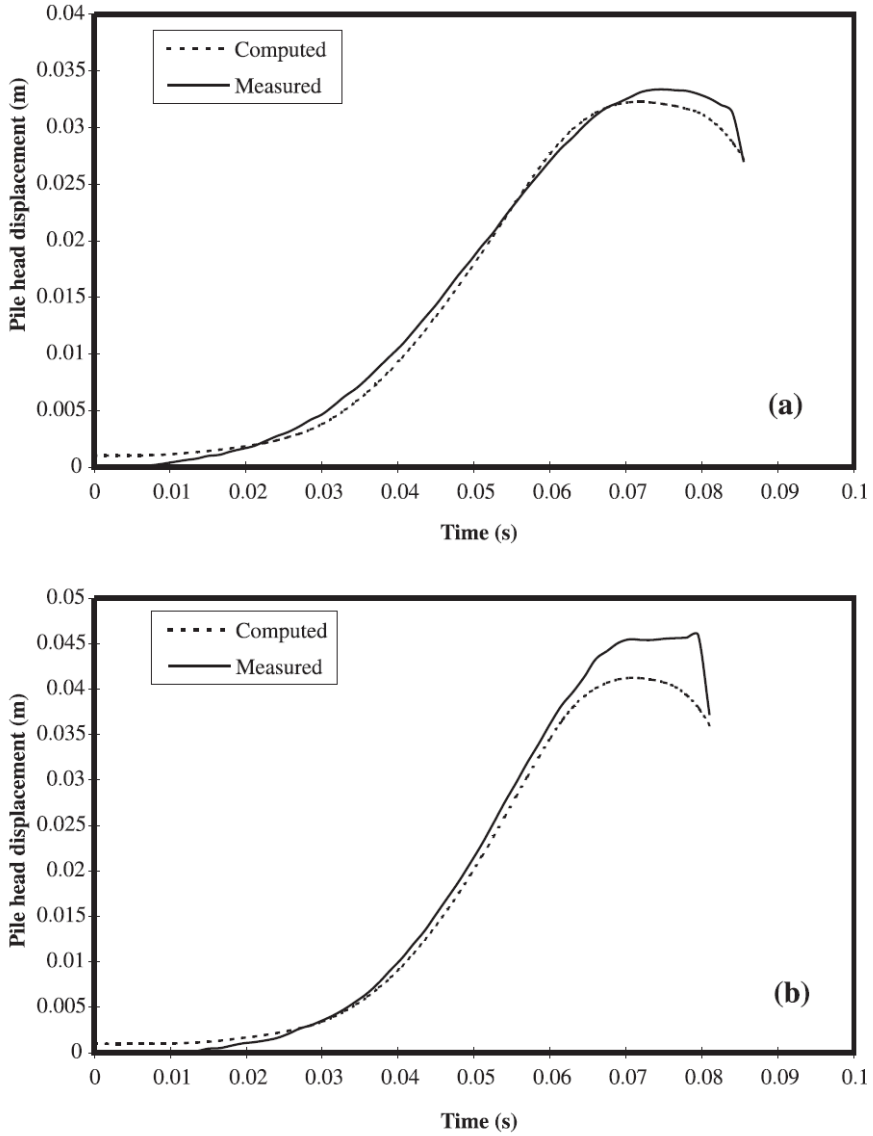

Figure 2-11. Comparison of predicted and measured results from a lateral load of 350 kN (a) and 470 kN (b) [8]

As seen in Figure 2-11, the predicted pile displacements agree with the measured pile displacements quite well. The methodology proposed in [8], however, determines the soil damping explicitly through experiments and curve fitting. It is the goal of this work, rather, to develop a theoretical model using a minimal number of empirical relations. Additionally, the methodology in [8] was developed for long elastic piles whereas this work is limited to short rigid boulders. The inclusion of soil damping to create a set of dynamic p-y curves as well as the lumped soil mass against the pile will be used in this work in the modeling of boulder motion in soil.

2.4 Dimensional analysis of laterally loaded piles

As seen in the above literature review, the effects of various soil and pile parameters have significant influence on the on pile displacement during lateral loading. These effects can be experimentally determined through full scale tests, but similar to full scale vehicular testing, full scale testing of piles is often expensive, time consuming, and cumbersome. Rather than performing several full scale tests, it is common practice to develop small scale models in order to study the effects of soil and pile parameters on the displacement of laterally loaded piles. There are numerous applications of scaled testing for laterally loaded piles in literature. Those of particular interest include scaled centrifuge testing and scaled testing of short rigid piles.

2.4.1 Dimensional analysis for centrifuge testing on small scale piles

According to Ting et al. [12], the ambient stresses in the soil observed during a $1/\alpha$ small scale test do not match those observed during full scale testing, where α is a constant related to the scaled size. The ambient stresses found in soils during lateral loading are functions of

experimental constants such as gravity and soil mass density [12]. As demonstrated in [12], either the mass density of the soil must be increased by a factor of α or the gravity must be increased by a factor of α in order to obtain matching ambient stresses in a small scale experiment. The first option of increasing soil mass density is rarely used since it is beneficial to use the same soil in model test as that found in the full scale case. A feasible alternative to increasing the soil mass density is to increase the gravitational acceleration by a factor of α using a centrifuge [12].

Ting et al. [12] performed a series of centrifugal tests of laterally loaded small scale piles to confirm the applicability of scaling the ambient soil stresses due to gravity. Table 2–2shows the resulting scaling laws when dimensional analysis is applied to a laterally loaded soil-fixed pile.

Table 2–2. Scaling laws associated with centrifugal tests [12]

Quantity	Full-scale (prototype) at 1 *g*	Centrifuge model at α g
Stress	1	1
Strain	1	1
Mass density	1	1
Length	1	$1/\alpha$
Acceleration	1	α
Area	1	$1/\alpha^2$
Volume	1	$1/\alpha^3$
Force	1	$1/\alpha^2$
Moment	1	$1/\alpha^3$
Mass	1	$1/\alpha^3$
Energy	1	$1/\alpha^3$
Velocity	1	1
Time, dynamics	1	$1/\alpha$
Time, diffusion	1	$1/\alpha^2$
Frequency, dynamics	1	α

The results of the small scale tests were compared to full tests and are shown in Figure 2-12. The solid lines in Figure 2-12 represent the fit of small scale lateral displacements as a function of applied lateral load in a centrifuge test and the dashed lines represent the full scale deflections as a function of applied load for various relative density sands.

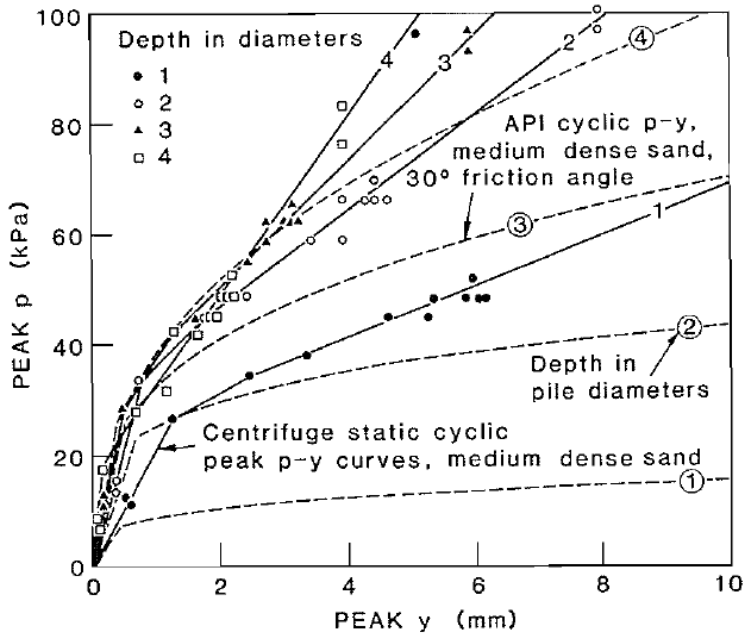

Figure 2-12. Full scale and small scale test results, where dashed lines are full scale and solid lines are small scale [12]

As seen in Figure 2-12, the small scale and full scale results agree to within moderate reason. The use of a centrifuge for model scale results, however, is not ideal for the scope of this work. Various input parameters used in scaling in [12] are used in this work to develop small scale soil and boulder parameters.

2.4.2 Dimensional analysis for cyclically loaded rigid piles

Leblanc et al. [13] developed a set of dimensionless equations of motion used in developing design guidelines for monopoles used in wind farms and parameterizing the displacements of the pile as a result of varying relative densities of sand. Even though the intent of Leblanc et al. [13] was determining the effect on soil stiffness due to cyclic loading, the methods used in reaching the conclusions are applicable and noteworthy to this work. The model used in [13] is shown in Figure 2-13 and assumes that the pile undergoes an angular rotation about a fixed point below the soil surface similar to that seen in [7]. The variables in Figure 2-13 are the applied moment, M, applied horizontal load, H, applied vertical load, V, friction angle factor as defined by [14], K, pile diameter, D, effective unit weight of the soil, γ', depth of pile below grade, z, depth to fixed point of rotation, d, length from fixed point of rotation to the bottom of the pile, L, a dimensionless constant, c_3, and the soil critical state friction angle, ϕ_{cr}.

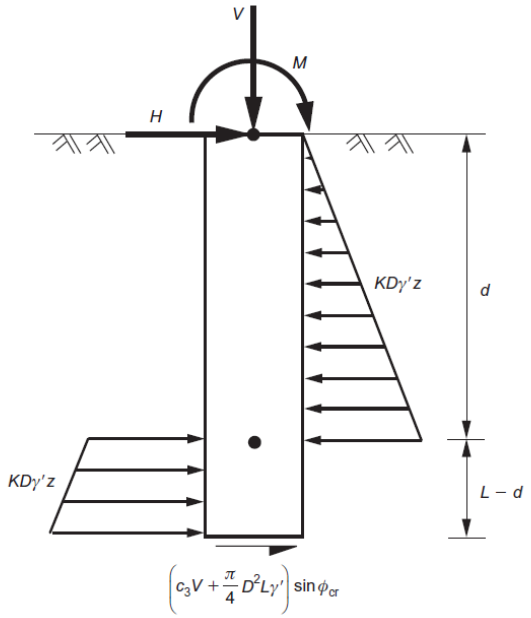

Figure 2-13. Leblanc et at. model for dynamically, laterally loaded, short rigid piles [13]

Table 2–3 shows the dimensionless input parameters for a laterally loaded short rigid pile in sand as calculated by [13].

Table 2–3. Non-dimensional parameters for the soil-pile model presented in [13]

Moment loading	$\tilde{M} = \frac{M}{L^3 D\gamma'}$
Vertical force	$\tilde{V} = \frac{V}{L^2 D\gamma'}$
Horizontal force	$\tilde{H} = \frac{H}{L^2 D\gamma'}$
Rotation: degrees	$\tilde{\theta} = \theta\sqrt{\frac{p_a}{L\gamma'}}$
Load eccentricity	$\tilde{e} = \frac{M}{HL}$
Aspect ratio	$\eta = \frac{L}{D}$

The non-dimensional parameters found in Table 2–3 are used to predict the static rotation of piles by creating and solving dimensionless equations of motion. The dimensionless results of the dimensionless equations of motion are transformed into dimensioned results using the non-dimensional parameters found in Table 2–3. Leblanc et al. [13] measured the lateral bearing capacity of several model scale tests and compared the results to predicted lateral bearing capacities using the dimensionless equations of motion. Figure 2-14 shows the results of the small scale test results as compared to the theoretical results. The salient features in Figure 2-14 are the dashed line representing the theoretical bearing capacity and the circles representing the measured bearing capacity. $\widetilde{M}$ and $\widetilde{H}$ are the dimensionless applied moment and dimensionless applied horizontal lateral load. The other variables are outside the scope of this work.

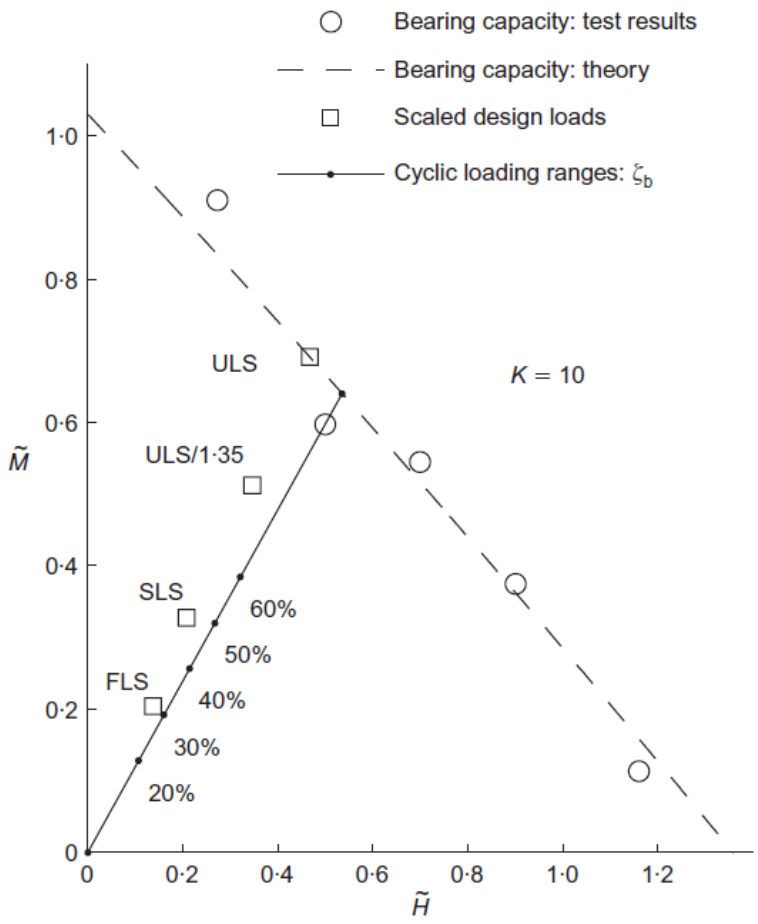

Figure 2-14. Theoretical bearing capacity as determined by the model presented in [13] compared to measured bearing capacity [13]

As seen in Figure 2-14, the theoretical bearing capacity agrees with the measured bearing capacity of the scaled tests. The loads used in [13], however, were static loads whereas the loading as related to this work are dynamic loads which are generally not considered to rotate about a stationary point below the soil surface. The usage of dimensionless equations of motion, similar to LeBlanc's study, is employed in this work to predict the boulder displacement during scaled vehicle impacts.

2.5 In-situ soil property measurement

Soil parameters can be obtained either via laboratory tests which generally involve undisturbed soil samples or via in situ tests which often take advantage of disturbed soil conditions. The testing methods within the scope of this work will be limited to in-situ methods which can be used as quick guidelines. The three most prominent in-situ soil testing methods are the pressuremeter test, flat plate bearing test, and the dynamic cone penetration test (DCPT). The greatest advantage observed in the DCPT is handheld nature of the test equipment and the low cost associated with purchasing the test apparatus [15]. The DCPT is a method often used by state departments of transportation as a quick means of measuring soil properties [16]. For these reasons, an in-depth look will be taken into the DCPT method for preforming in-situ soil measurements with the goal of developing rapid field soil measurements which can be used in modeling of the soil.

The dynamic cone penetration test is a testing method which incorporates methodology from both the Standard Penetration Test (SPT) and the Cone Penetration Test (CPT) in order to estimate soil properties [17]. Dynamic cone penetration tests are performed by hammering a weighted cone into soil and measuring the associated penetration depth per blow [17]. The penetration depth per blow can then be correlated to soil parameters such as relative density or the constant of horizontal subgrade reaction [17].

Although the DCPT is not as well used as the SPT or CPT, the results obtained from the DCPT can be correlated to SPT results as demonstrated in [18] and California Bearing Ratio (CBR) test results as demonstrated in [19] which have been correlated to strength of soil properties. The correlated SPT results and CBR results are used in this work to determine the constant of horizontal subgrade reaction for cohesionless soils.

2.6 Boulder properties

Unlike a vast majority of the soil-pile models seen in literature, a boulder acting as a soil-fixed boulder is subject to not only translation and rotation, but also to mechanical failure in the form of fracture. The deformation of the soil surrounding a boulder during vehicle impact absorbs and dissipates energy from a vehicle impact. If the soil were not to deform, as if the boulder were embedded in concrete, then the boulder itself would have to withstand the entirety of the vehicle impact. If the boulder is not "strong enough" then it is plausible that the boulder will fracture during impact. Theories involving the prediction of fracturing of rocks will be investigated with the goal of developing minimum boulder dimensions and material properties with respect to fracture prediction.

A widely used method for predicting the force which will cause a rock specimen to fracture is the application of the Brittle Mohr Coulomb failure criteria when calculating internal stresses as a result of an applied load [20]. The results from Mohr Coulomb failure criteria often produce conservative estimates for a load which will cause fracture [20]. The manner the load is applied also plays in important role in the ultimate resistive load a rock specimen can supply before it fractures. Cho et al. [21] performed a series of experiments in which the tensile strength of rock was compared against the loading strain rate. The loading strain rate was increased from static values, $\dot{\varepsilon} \leq 0.1$, into dynamic ranges of $1 \leq \dot{\varepsilon} \leq 10$. The results from [21] are shown in Figure 2-16 and Figure 2-16.

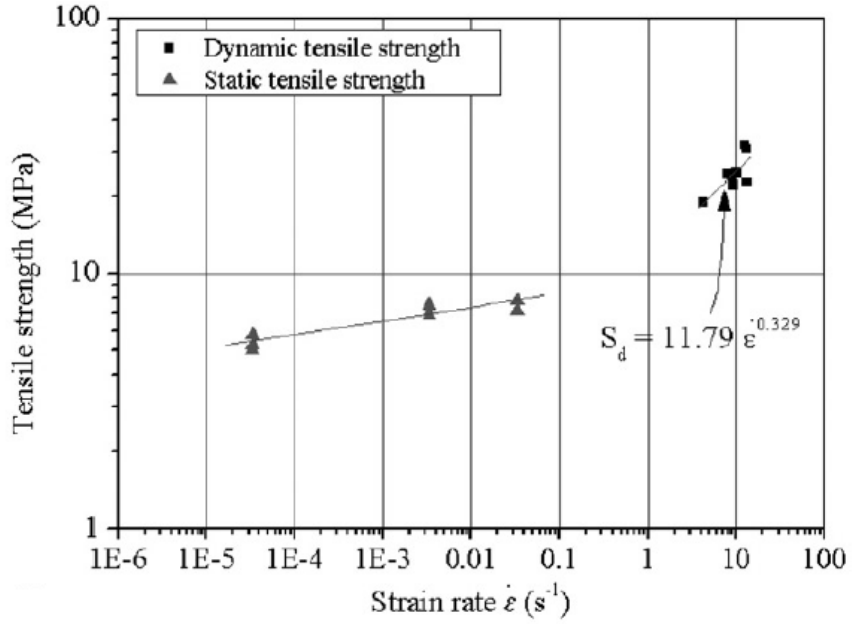

Figure 2-15. Tensile strength vs. loading rate for Inada granite [21]

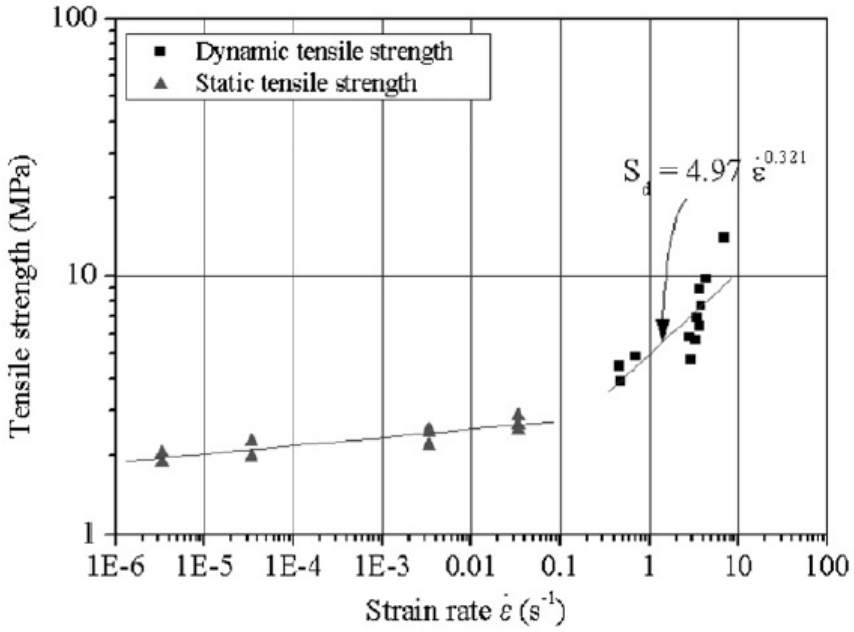

Figure 2-16. Tensile strength vs. loading rate for Tage tuff [21]

As expected, the dynamic strength of rock was shown to increase with increasing loading rate. The use of a dynamic strength in the prediction of boulder fracture, however, may err towards fracture if the actual applied loading rate is smaller than the predicted loading rate for the same loading magnitude. The use of Mohr Coulomb failure criteria from a static loading standpoint predicts lower fracture loads than those associated with dynamic strength calculation which may act as conservative guidelines for minimum boulder dimensions. For conservatism, the static loading criteria will be used in this work to predict the minimum dimensions needed for a boulder assuming rigid soil conditions.

CHAPTER 3

LOW-ORDER MODEL THEORY AND METHODS

The intent of this chapter is to present the development of a low-order model for a vehicle impact upon a soil-fixed boulder in cohesionless soil such as sand or gravel. From the low-order model, it will be possible to not only predict vehicle and boulder motion but also boulder failure criteria. Potential failure criteria during vehicular impact include excessive boulder motion and/or material failure of the boulder in the form of facture.

The low-order model used throughout this thesis will be presented as a combination of commonly used vehicle and pile models. The low-order model will capture both motion of the vehicle as well as material failure of the boulder. A method for simulating the results of various model parameters will be presented as well as preferred methods for in-situ and laboratory measurement of the various model parameters.

This chapter is organized as follows:

The coordinate system pertaining to the low-order model is described in Section 3.1. The development of the low-order model and governing equations is presented in Section 3.2, and the derivation of the forces seen in the governing equations is presented in Section 3.2.1 through Section 3.2.3. The prediction of boulder failure criteria in the form of fracture will be discussed in Section 3.3. Methods for determining in-situ soil properties will be presented in Section 3.4, and finally the preferred method of model simulation will be presented in Section 3.5.

3.1 Coordinate systems and nomenclature

The global coordinate used throughout this thesis is oriented such that the X direction is to the right, the Y direction is down, and the Z direction is into the page. All displacements and

corresponding time derivatives along the X axis will be noted as x, $\dot{x}$,… etc., and all rotational displacements about the Z axis will be noted as θ, $\dot{\theta}$,… etc. The motion of the vehicle is assumed to be one dimensional in the positive X direction. The variable x_v is the X direction displacement of the vehicle with respect to the global reference frame.

Similar to the motion of the vehicle, the motion of the boulder is assumed to translate solely in the positive X direction and independently rotate about the Z axis as illustrated in Figure 3-1. The variables in Figure 3-1 are the X direction displacement of the center of mass of the boulder-soil subsystem, x_b, and the angle of rotation of the boulder-soil subsystem about the Z axis, θ_b. It should be noted that the center of mass of the boulder and soil system is not the same as the center of mass for the boulder alone. The location of the center of mass for the boulder is shown in Figure 3-1.

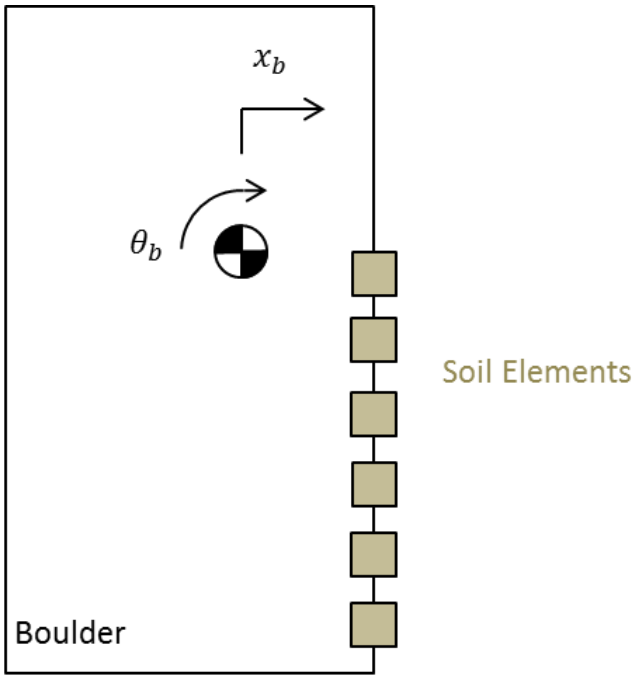

Figure 3-1. Coordinates associated with boulder-soil subsystem (not to scale)

It will be assumed throughout this thesis that the length, L, width, W, and height, H, of the boulder will be such that the length is always parallel to the direction of impact in the XY

plane, the width is perpendicular to the direction of impact in the XY plane, and the height is in the YZ plane. Figure 3-2 illustrates a typical scenario for a vehicle impact upon a soil-fixed barrier. The variable d in Figure 3-2 is the embedment depth of the boulder.

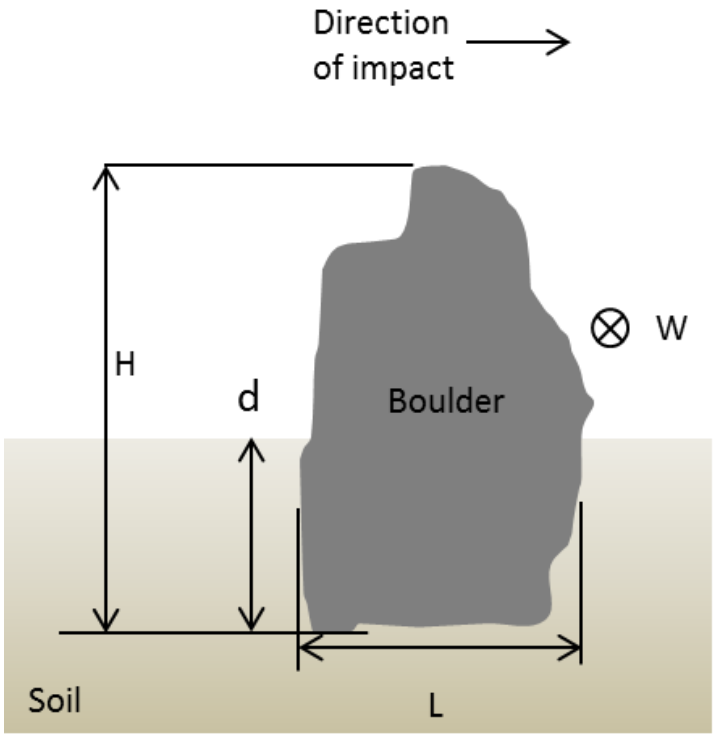

Figure 3-2. Layout for a typical vehicle impact

3.2 Low-order modeling of vehicle-boulder motion

The low-order model presented in this thesis is a combination of a lumped-parameter vehicle model, a rigid body representing the boulder, and a lumped-parameter soil model consisting of individual masses and nonlinear springs and dampers representing the affected soil during vehicular impact. As presented in [2], the use of a lumped-parameter Maxwell model is most aptly used for collisions in which a relatively large amount of crush is observed. Figure 3-3

shows the low-order model as presented using a lumped-parameter Maxwell model for the vehicle.

The variables in Figure 3-3 are the mass of the vehicle, m_v, the equivalent vehicle spring and damper constants, k_v and c_v, respectively, the mass of the boulder, m_b, the mass moment of inertia of the boulder about the center of mass of the boulder-soil subsystem, J_b, and the equivalent mass, spring constants and damper constants for the discretized soil elements, m_n, k_n, and c_n, respectively. Additionally a inertial mass, m', is inserted into the Maxwell model which will be used in deriving the governing equations of motion and then set to zero, x' is the displacement of the inertial mass in the X direction.

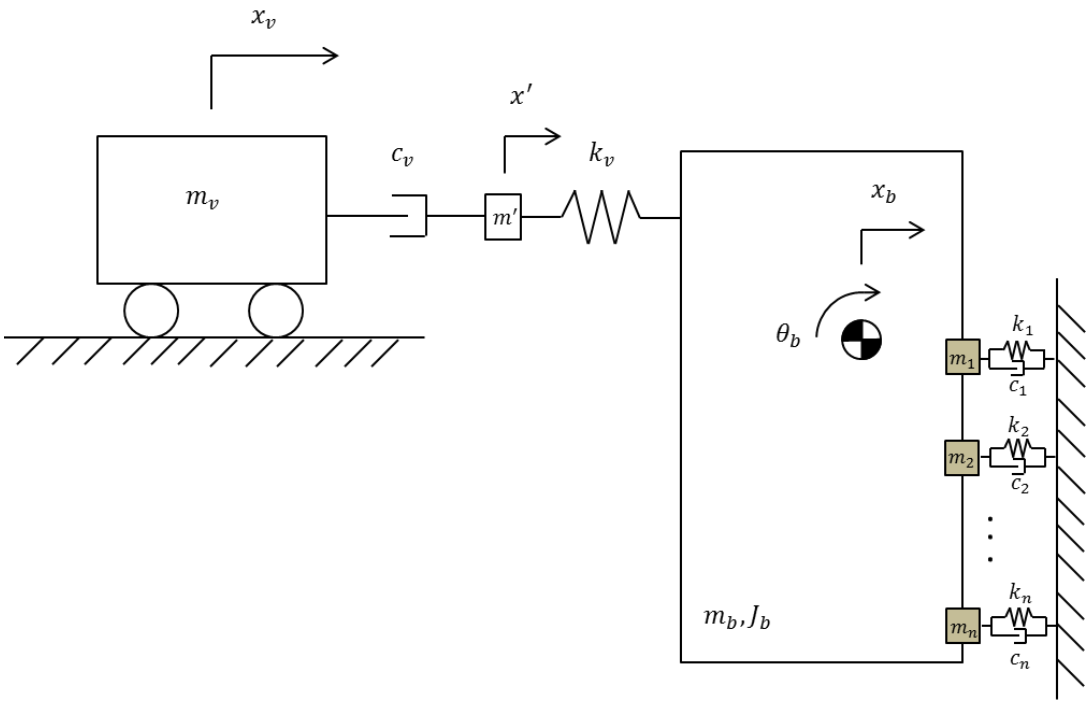

Figure 3-3. Low-order model for vehicle impacts upon soil-fixed boulders

There are three degrees-of-freedom for the low-order model: the displacement of the vehicle, x_v, displacement of the boulder, x_b, and the rotation of the boulder-soil subsystem, θ_b. As seen in literature, the soil surrounding a laterally loaded pile can be represented as a system of

nonlinear springs and dampers [11]. The underlying principle for the boulder-soil subsystem of the low-order model is that a one dimensional pile within infinite-dimensional deformable soil is replaced with a two dimensional rigid object with non-negligible mass. As presented in [22], the general shape of affected soil surrounding the boulder during lateral loading can be found using the effective angle of internal friction of the soil and the embedded pile or boulder geometries. According to Kim et al. [22], the affected soil surrounding a pile during loading can take several possible shapes depending on the associated shear plane of the soil, illustrated in Figure 3-4.

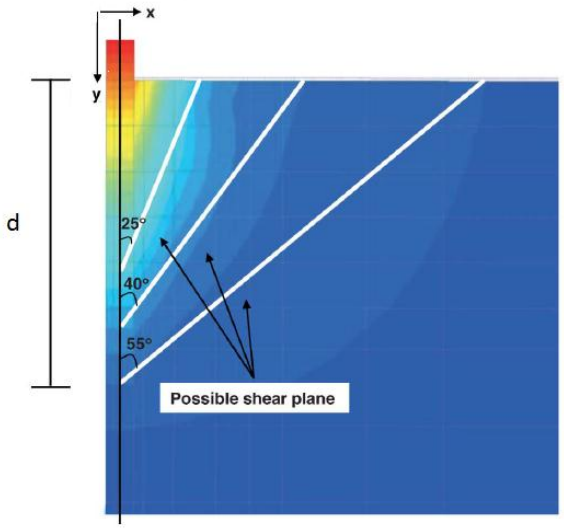

Figure 3-4. Definition of soil wedge during lateral loading [22]

Similar to Kim et al. [22], the overall shape of the soil wedge is found from the shear plane of the soil as defined by θ_w in Figure 3-5. The defining soil wedge angle, θ_w, is found using

$$\theta_w = \frac{\pi}{4} + \frac{\varphi'}{2}, \tag{3.1}$$

where φ' is the effective angle of internal friction for the soil [22].

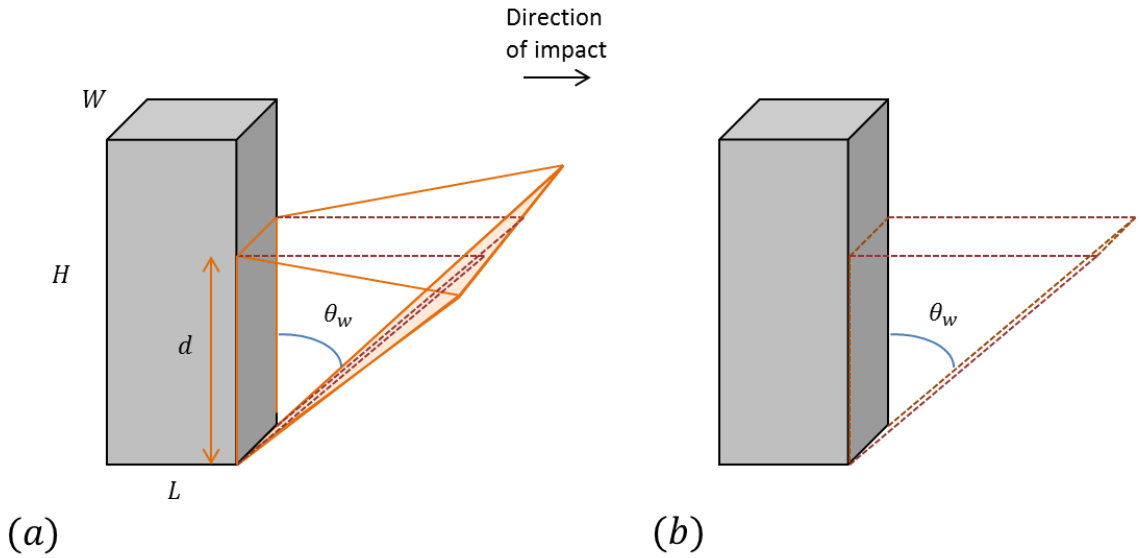

Figure 3-5. 3-D representation of soil wedge which develops during lateral loading

The three-dimensional boulder-soil subsystem in Figure 3-5 (a) is reduced by considering only the soil directly behind the boulder, marked as the dotted lines in Figure 3-5. The reduced soil wedge is then transformed into a two-dimensional soil wedge and a two-dimensional boulder as shown in Figure 3-6.

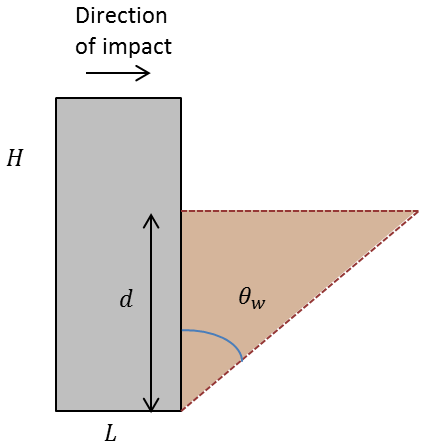

Figure 3-6. Idealized 2-D wedge shape based on the 3-D soil wedge geometries

The soil in Figure 3-6 is discretized into N evenly distributed elements, illustrated in Figure 3-7 (a), and replaced by a system of springs and dampers, illustrated in Figure 3-7 (b). Similar to Naggar and Bentley [8], the mass of the soil elements are lumped against the boulder and attached to the springs and dampers such that the springs and dampers are in parallel. The variable L_{soil} in Figure 3-7 is the original length of the soil wedge, and the variable h_e is the height of a single soil element.

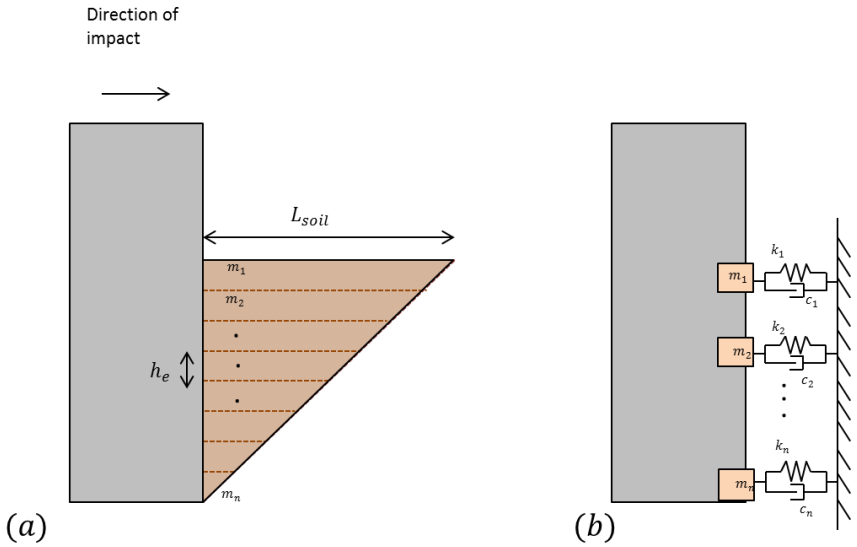

Figure 3-7. Transformation from discretized soil subsystem to a system of soil representative Kelvin models

The soil elements are assumed to be trapezoidal where the mass of the n^{th} soil element, m_n, is found using

$$m_n = \rho_{soil} W h_e [d \tan(\theta_w) - n h_e \tan(\theta_w)] + \frac{1}{2} \rho_{soil} W {h_e}^2 \tan(\theta_w), \tag{3.2}$$

where ρ_{soil} is the mass density of the soil. It is assumed that the springs and dampers representing the soil do not undergo rotation and act solely in the X direction.

A free body diagram of the boulder-soil subsystem is presented in Figure 3-8 and Figure 3-9, where the force exerted on the boulder from the vehicle, noted as F_v, is applied at an eccentricity, e, above the soil line. Additionally, a restoring moment due to gravity, M_R, is added to the boulder since the mass of the boulder is non-negligible. The friction acting on the boulder from the surrounding soil is neglected, as seen in Zhang [7]. The variables in Figure 3-8 are the center of mass in the X direction as measured from the lower left corner of the boulder, c_x, the center of mass in the $-Y$ direction as measured from the lower left corner of the boulder, c_y, the depths of each soil layer with respect to the center of mass of boulder-soil subsystem, d_1, d_2, $\ldots d_N$, the mass of the boulder, m_b, and the mass moment of inertia of the boulder about the center of mass for the boulder-soil subsystem, J_b.

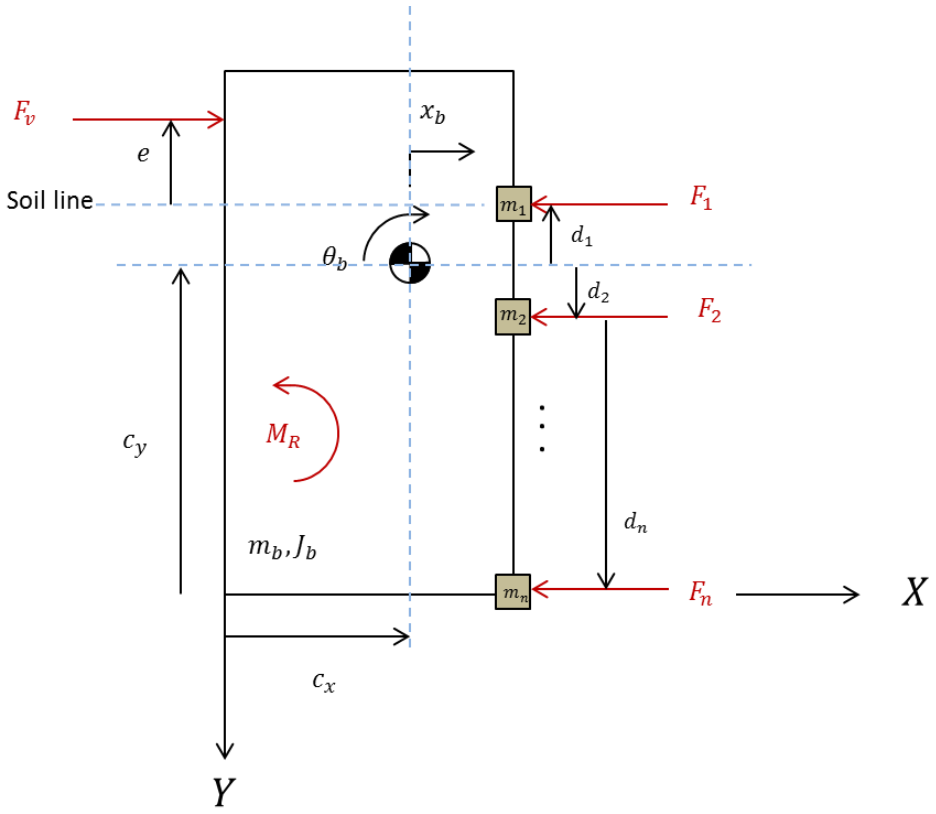

Figure 3-8. Free body diagram of the boulder-soil subsystem

The center of mass for the boulder-soil system, as measured with respect to the local origin in the X direction, is found using

$$c_x = \frac{1}{(\sum_{n=1}^{N} m_n) + m_b} \left[\left(\sum_{n=1}^{N} m_n \right) L + m_b \, \frac{L}{2} \right], \tag{3.3}$$

and the center of mass for the boulder-soil system, as measured with respect to the local origin in the Y direction, is found using

$$c_y = -\frac{1}{(\sum_{n=1}^{N} m_n) + m_b} \left[\left(\sum_{n=1}^{N} m_n d \frac{-(n-N-1)}{N} \right) + m_b \, \frac{H}{2} \right]. \tag{3.4}$$

The depth of each soil layer with respect to the boulder-soil subsystem, d_n, is the n^{th} element in the range $\left((c_y - d),\ c_y,\ N \right)$.

As a means of rapidly calculating moments, additional coordinates are employed as illustrated in Figure 3-9. The variables in Figure 3-9 are the radial distance from the center of mass of the boulder-soil system to the impact point of the vehicle, R_v, the radial distances from the center of mass of the boulder-soil subsystem to the soil elements, R_n, the angle measured from vertical to the vehicle impact point, γ_v, and the angles measured from vertical to the soil elements, γ_n.

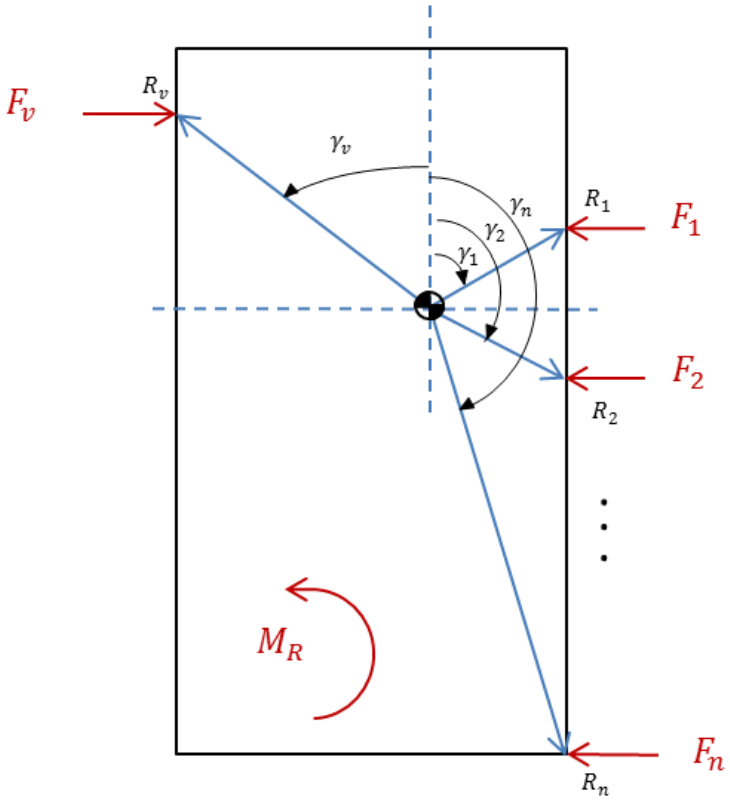

Figure 3-9. Secondary free body diagram of the boulder-soil subsystem used to calculate the moment about the center of mass

The radial distance from the center of mass of the boulder-soil system to the impact point of the vehicle, R_v, the radial distances from the center of mass of the boulder-soil subsystem to the soil elements, R_n, the angle measured from vertical to the vehicle impact point, γ_v, and the angles measured from vertical to the soil elements, γ_n, are found using

$$\gamma_v = \tan^{-1}\frac{c_x}{(e + d_1)} \tag{3.5}$$

$$R_v = \sqrt{(e + d_1)^2 + {c_x}^2} \tag{3.6}$$

$$\gamma_n = \tan^{-1}\left(\frac{d_n}{(L - c_x)}\right) + \frac{\pi}{2} \tag{3.7}$$

$$R_n = \sqrt{{d_n}^2 + (L - c_x)^2}. \tag{3.8}$$

The eccentricity of the vehicle impact is found by first treating the force from the vehicle as an evenly distributed load across the impact area on the face of the boulder, as shown in Figure 3-10 (a). In terms of the boulder's reaction, the distributed load is consolidated into an equivalent point load, as shown in Figure 3-10 (b). The variables in Figure 3-10 are the distance from the ground to the bottom of the vehicle bumper, e_{bumper}, and the distance from the ground to either the top of the boulder or to the top of the vehicle hood, e'.

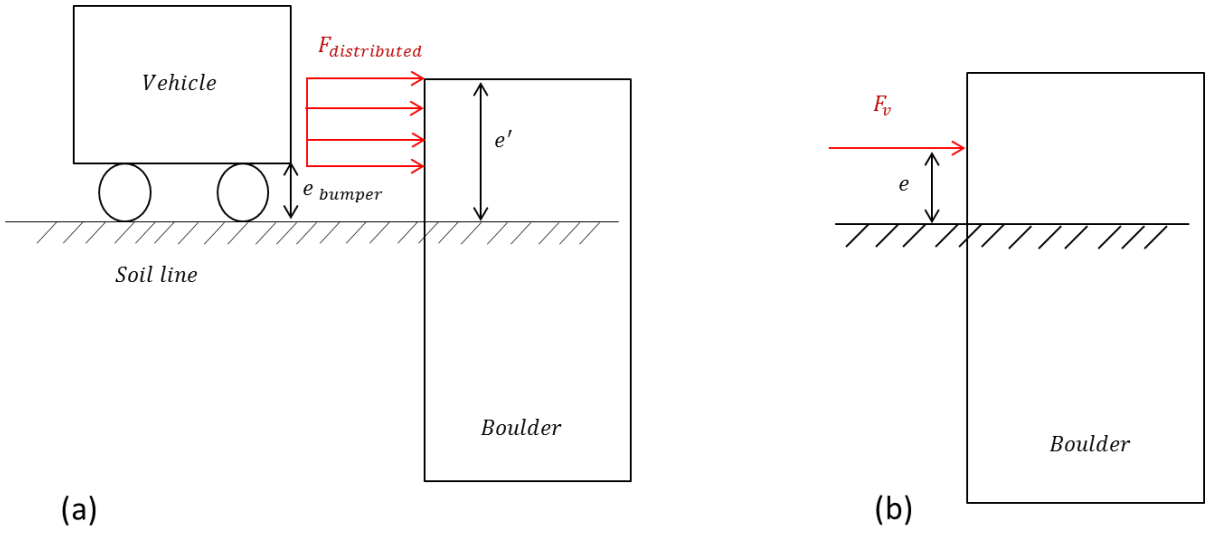

Figure 3-10. Consolidation of distributed load on the boulder

The eccentricity of the vehicle load is then calculated using

$$e = \frac{e' - e}{2} + e. \tag{3.9}$$

3.2.0.1 Boulder-soil subsystem governing equations of motion

Applying Newton's second law to the free body diagram in Figure 3-9 yields

$$m_{eff}\ddot{x}_b = \sum_{n=1}^{N}\{F_n\} + F_v \tag{3.10}$$

$$J_{eff}\ddot{\theta}_b = \sum_{n=1}^{N}\{M_n\} + M_v + M_R \tag{3.11}$$

where m_{eff} and J_{eff} are the effective mass of the boulder-soil subsystem and the mass moment of inertia of the boulder-soil subsystem about the center of mass for the boulder-soil subsystem. The effective mass of the boulder-soil subsystem and the mass moment of inertia of the boulder-soil subsystem about the center of mass for the boulder-soil subsystem, m_{eff} and J_{eff}, are found using

$$m_{eff} = \left(m_b + \sum_{n=1}^{N}\{m_n\}\right) \tag{3.12}$$

$$J_{eff} = \left(J_b + \sum_{n=1}^{N}\{m_n\,({d_n}^2 + {l_n}^2)\}\right), \tag{3.13}$$

where l_n is the distance in the X direction from the center of mass of the boulder-soil subsystem to the soil elements. The mass of the boulder, m_b, is found using

$$m_b = \rho_{boulder} \cdot L \cdot W \cdot H, \tag{3.14}$$

where $\rho_{boulder}$ is the mass density of the boulder. The distance from the center of mass of the boulder-soil subsystem to the soil elements is found using

$$l_n = L - c_x, \tag{3.15}$$

And the mass moment of inertia of the boulder about the center of mass is found using

$$J_b = \frac{1}{12} m_b \left(\left(\frac{H}{2} \right)^2 + \left(\frac{L}{2} \right)^2 \right) + m_b \left(\left(c_y - \frac{H}{2} \right)^2 + \left(c_x - \frac{L}{2} \right)^2 \right). \tag{3.16}$$

3.2.0.2 Vehicle subsystem governing equations of motion

Similar to the boulder-soil subsystem, a free body diagram can be created for the lumped-parameter Maxwell vehicle model. It is assumed that there is no slip at the point which makes contact between the vehicle and the boulder. Applying Newton's second law to the lumped-parameter Maxwell vehicle model in Figure 3-3 yields

$$m_v \ddot{x}_v = -F_v{}' \tag{3.17}$$

$$m' \ddot{x}' = F_v{}' - F_v. \tag{3.18}$$

Sections 3.2.1 through 3.2.3 will present the methods for solving the unknown forces and moments, F_n, F_v, M_n, M_v, M_v, M_R in (3.10) and (3.11) as well as the unknown inertial force, $F_v{}'$, in (3.17) and (3.18).

3.2.1 Derivation of soil forces and resulting moments

As presented in [8], the springs and dampers representing the soil in Figure 3-7 are placed in parallel; thus, the *N* soil forces are found using

$$F_n = -\left(F_{k_n} + F_{c_n}\right), \tag{3.19}$$

where F_{k_n} is the force from the n^{th} soil representative spring and F_{c_n} is the force from the n^{th} soil representative damper. The *N* moments resulting from the soil forces are found using

$$M_n = -F_n R_n \cos(\gamma_n + \theta_b - \pi). \tag{3.20}$$

The soil representative spring forces, F_{k_n}, in (3.19) are found using

$$F_{k_n} = k_n \Delta x_n, \tag{3.21}$$

where Δx_n is the linear displacement in the *X* direction of the n^{th} soil mass element, and k_n is the effective spring constant of the n^{th} soil element. Since the boulder is assumed to undergo rigid body motion, all x_n can be related geometrically to the lateral position of the boulder, x_b, and the angle of rotation of the boulder, θ_b, using

$$\Delta x_n = x_b + R_n \sin(\gamma_n + \theta_b) - R_n \sin(\gamma_n). \tag{3.22}$$

The spring constants for the soil elements are found by idealizing the soil elements as long, slender rods. The equivalent spring constant of a long slender rod can be estimated using

$$k_{rod} = \frac{E_{rod} A_{rod}}{L_{rod}}, \tag{3.23}$$

where E_{rod} is the Young's modulus of the rod material, A_{rod} is the cross sectional area of the rod, and L_{rod} is the original length of the rod. Similarly, the equivalent spring constant of the soil elements can be calculated using

$$k_n = \frac{1 \cdot 10^6 \, \beta \, d \, W}{L_{soil} \, N} \alpha_n, \tag{3.24}$$

where β is the constant of horizontal subgrade reaction of the soil in $(\mathrm{MN/m^3})$, L_{soil} is an estimation of the original soil wedge length, and α_n is the depth of the soil elements from the soil line to the bottom of the boulder in the range $\left(0, \frac{d}{N}, d\right)$. As defined in Figure 3-7, The length of the soil wedge, L_{soil}, would be found using

$$L_{soil} = d \, \tan\theta_w \tag{3.25}$$

which would increase as the effective angle of internal friction of the soil increases. As noted in [23], the stiffness of soil increases as the effective angle of internal friction for soil increases. Therefore instead of using (3.25), the original length of the soil wedge, L_{soil}, is estimated from Figure 3-11.

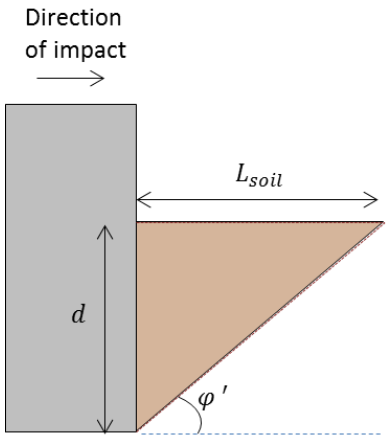

Figure 3-11. Definition of soil wedge length as used to calculated a representative spring constant for each soil element

The length of the soil wedge, L_{soil}, is then found using

$$L_{soil} = \frac{d}{\tan \varphi'}. \tag{3.26}$$

Having derived the equivalent spring constant for laterally loaded soil, the resulting spring force is calculated by multiplying the spring constant with the displacement of each soil element, x_n. Thus, the force exerted on the boulder from the equivalent soil spring is found by substituting (3.22) into (3.21), resulting in

$$F_{k_n} = \frac{1 \cdot 10^6 \, \beta \, W \, \tan \varphi'}{N} \alpha_n \, [x_b + R_n \sin(\gamma_n + \theta_b) - R_n \sin(\gamma_n)]. \tag{3.27}$$

An ultimate lateral resistance, however, exists for soil at a given depth [7]. The spring force for each soil element, therefore, is limited such that the absolute value does not exceed the ultimate lateral resistance of the soil at the given depth, α_n. As presented in [7], the ultimate lateral pressure per unit length of a laterally loaded pile can be estimated using

$$p_u = {K_p}^2 \, \gamma \, B \, z, \tag{3.28}$$

where K_p is the passive earth pressure coefficient, γ is the effective unit weight of soil, B is the width of the pile, and z is the depth from the ground surface. The passive earth pressure coefficient is found using [7]

$$K_p = \tan^2 \theta_w. \tag{3.29}$$

Modifying (3.28) to match the nomenclature used in this thesis, the ultimate lateral pressure for each soil element, σ_n, is found using

$$\sigma_n = \frac{{K_p}^2 \, \rho_{soil} \, g \, W \, \alpha_n \, K_\varepsilon}{d}, \tag{3.30}$$

where g is the gravitation constant and K_ε is a constant based on strain rate loading of the soil and the undrained shear strength. As presented in [24], shear stress within a soil increases as the strain rate of loading is increased. As pertaining to the research in this thesis, it is assumed that a maximum strain rate for the soil is achieved during vehicle impact. Under such assumptions, the value for K_ε for a particular soil is found using

$$K_\varepsilon = \frac{\tan \theta_w}{\cos \varphi'}. \tag{3.31}$$

The ultimate lateral force of each soil element is then found using

$$F_{u_n} = \sigma_n \, A_n, \tag{3.32}$$

where A_n is the cross sectional area of each soil element, found using

$$A_n = \frac{W\ d}{N}. \tag{3.33}$$

Substituting (3.30) and (3.33) into (3.32) yields

$$F_{u_n} = \frac{{K_p}^2\ \rho_{soil}\ g\ W^2\ \alpha_n\ K_\varepsilon}{N}. \tag{3.34}$$

This expression for the ultimate force on each element is used in the simulation models that follow.

Although the low-order model lumps the discretized soil elements against the boulder, the damping constant for the representative soil dampers is derived analytically by applying the conservation of momentum to the boulder-soil subsystem as the boulder plows through the soil during a full scale crash. Since the low-order model assumes that all translations of the soil elements are purely in the X direction, the sum of the forces acting on the boulder from the soil elements is found using the momentum transfer formulation of Newton's law:

$$\frac{d\vec{P}_n}{dt} = \sum \vec{F}_n = (m_n + {m_n}')\ddot{x}_n + (\dot{m}_n + {\dot{m}_n}')\dot{x}_n, \tag{3.35}$$

where $\vec{P}_n$ is the momentum of the n^{th} soil element, ${m_n}'$ is the accumulated mass of the n^{th} soil element as the boulder plows through the soil, $\dot{m}_n$ is the time derivative of the lumped soil masses defined in Figure 3-3, and ${\dot{m}_n}'$ is the time derivative of the accumulated mass of the n^{th} soil element. Since it is assumed the soil masses lumped against the boulder do not change with respect to time, the time derivative of the lumped soil masses, $\dot{m}_n$, is set to zero. The accumulated mass can be calculated using

$${m_n}' = \rho_{soil}\ A_n\ x_n, \tag{3.36}$$

and the time derivative of the accumulated mass is

$$\dot{m}_n{}' = \rho_{soil}\, A_n\, \dot{x}_n. \tag{3.37}$$

Substituting (3.37) into (3.35) and setting $\dot{m}_n$ to zero yields

$$\frac{d\vec{P}_n}{dt} = \sum \vec{F}_n = (m_n + m_n{}')\ddot{x}_n + \rho_{soil}\, A_n\, \dot{x}_n{}^2. \tag{3.38}$$

Recognizing that (3.38) is of similar form to fluid drag flow, (3.38) may be rewritten as

$$\frac{d\vec{P}_i}{dt} = \sum \vec{F} = (m_n + m_n{}')\ddot{x}_n + c_n \dot{x}_n{}^2, \tag{3.39}$$

where

$$c_n = \rho_{soil}\, A_n. \tag{3.40}$$

Thus the analysis performed for a boulder undergoing rotation uses damper elements for soil that provide a resistive force proportional to velocity squared, and their proportionality constants, c_n, are each equal to a discrete elemental swept area times soil density. This velocity-squared damping represents the physics of momentum transfer between the boulder and accumulating soil mound in front of each moving mass element.

The soil damping forces, F_{c_n}, in (3.19) are found using

$$F_{c_n} = c_n\, \dot{x}_n{}^2\, sign(\dot{x}_n), \tag{3.41}$$

where $\dot{x}_n$ is the linear displacement in the X direction of the n^{th} soil mass element, and c_n is the effective damping constant as defined by (3.40). Similar to the linear displacement of each soil

element, the lateral velocity of each soil element can be related to the lateral angular velocity of the boulder using

$$\dot{x}_n = \dot{x}_b + \dot{\theta}_b R_n \cos(\gamma_n + \theta_b). \tag{3.42}$$

Substituting (3.42) and (3.33) into (3.41) results in the final expression for the damping force on each soil element used in the simulations that follow:

$$F_{c_n} = \frac{\rho_{soil} W d}{N} \left(\dot{x}_b + \dot{\theta}_b R_n \cos(\gamma_n + \theta_b)\right)^2 \cdot sign\left(\left[\dot{x}_b + \dot{\theta}_b R_n \cos(\gamma_n + \theta_b)\right]\right). \tag{3.43}$$

3.2.2 Derivation of restoring moment

Since the pile geometries in [7] were slender, Zhang [7] neglected the restoring moment which would resist tipping of a rigid object seated flatly on the ground. The restoring moment acting on the boulder during vehicle impact is calculated such that it is equal and opposite in direction to the sum of all of the other moments acting on the boulder until the maximum restoring moment due to gravity is achieved. Calculating the restoring moment in the aforementioned manner allows for zero boulder rotation in the event that the vehicle does not enact a large enough moment to cause the boulder to tip. Since it is also assumed that the boulder-soil subsystem center of mass does not translate in the Y direction, the maximum restoring moment due to gravity acting on the boulder is first estimated under the following conditions

$$for\ \dot{\theta}_b > 0 \qquad M_{R\,max} = -sign(\sin(\gamma_N + \theta_b)) \cdot m_b g R_N \cos(\gamma_N + \theta_b) \tag{3.44}$$

$$for\ \dot{\theta}_b \leq 0 \qquad M_{R\,max} = 0. \tag{3.45}$$

The estimated restoring moment is compared to the sum of the moments on the boulder such that

$$M_R = -sign(\sin(\gamma_N + \theta_b)) \left[\sum_{n=1}^{N} \{M_n\} + M_v \right], \tag{3.46}$$

$$for \left(M_v + \sum_{n=1}^{N} \{M_n\} \right) \neq 0$$

The absolute value of the restoring moment is then limited such that it cannot exceed the absolute value of the estimated maximum restoring moment calculated in (3.44). If the value exceeds the maximum, it is simply set as the maximum theoretical restoring moment.

3.2.3 Derivation of vehicle force based on lumped-parameter Maxwell model

The governing equations for the lumped-parameter Maxwell model as defined by Figure 3-3 are

$$m_v \ddot{x}_v = -F_v{}' = -c_v(\dot{x}_v - \dot{x}') \tag{3.47}$$

$$m' \ddot{x}' = F_v{}' - F_v = c_v(\dot{x}_v - \dot{x}') - k_v(x' - \Delta x_{bv}), \tag{3.48}$$

where $\dot{x}'$ is the linear velocity of the inertial mass, m', and Δx_{bv} is the change in linear displacement between the vehicle and the contact point of the vehicle on the boulder. Differentiating (3.47) and (3.48) with respect to time yields

$$m_v \ddot{x}_v = -c_v(\ddot{x}_v - \ddot{x}') \tag{3.49}$$

$$m'\ddot{x}' = c_v(\ddot{x}_v - \ddot{x}') - k_v(\dot{x}' - \dot{x}_{bv}), \tag{3.50}$$

and setting the inertial mass, m', to zero results in

$$0 = c_v(\ddot{x}_v - \ddot{x}') - k_v(\dot{x}' - \dot{x}_{bv}). \tag{3.51}$$

Equations (3.49) and (3.51) are then summed yielding

$$m_v \ddot{x}_v = -k_v(\dot{x}' - \dot{x}_{bv}). \tag{3.52}$$

Solving (3.52) in terms of the inertial velocity, $\dot{x}'$, yields

$$\dot{x}' = -\frac{m_v \ddot{x}_v}{k_v} + \dot{x}_{bv}, \tag{3.53}$$

and substituting (3.53) into (3.47) yields the governing equation of motion for the lumped-parameter Maxwell vehicle model,

$$\dddot{x}_v + \frac{k_v}{c_v}\ddot{x}_v + \frac{k_v}{m_v}\dot{x}_v = \frac{k_v}{m_v}\left[\dot{x}_b + \dot{\theta}_b\, R_v\, \cos(\gamma_v + \theta_b)\right]. \tag{3.54}$$

The force acting on the boulder during an impact under a lumped-parameter Maxwell model can be found by setting the inertial mass, m', in (3.48) to zero. Doing so yields

$$F_v = F_v{}'. \tag{3.55}$$

Using (3.47) and (3.55), the force acting on the boulder from the vehicle can then be calculated using

$$F_v = -m_v\, \ddot{x}_v. \tag{3.56}$$

In the event of vehicular rebound and separation, the vehicle would simply separate from the boulder rather than pulling the boulder. This discontinuity of the contact point between the boulder and the vehicle is modeled such that the force exerted on the boulder from the vehicle is set to zero in the case of a negative, or pulling, force.

The resulting moment from the vehicle impact is calculated using

$$M_v = F_v\, R_v\, \cos(\gamma_v + \theta_b). \tag{3.57}$$

As reported in [2], the spring and damper coefficients for a Maxwell model in which vehicle rebound is observed can be estimated by fitting an expected response to crash test data. The expected response for a crash in which vehicle rebound is observed takes the form of

$$x_v = -\frac{2av_o}{a^2+b^2} + exp\left[\left(\frac{v_o - \frac{2a^2v_o}{a^2+b^2}}{b}\right)\sin(bt) + \frac{2av_o}{a^2+b^2}\cos bt\right], \tag{3.58}$$

where a and b are constants, v_o is the initial impact velocity of the vehicle, and t is time [2]. The constants a and b can then be correlated to the effective vehicle spring and damper coefficients using [2]

$$c_v = \frac{m_v(a^2 + b^2)}{-2a} \tag{3.59}$$

$$k_v = -2ac_v. \tag{3.60}$$

3.2.4 Governing equations of motion for the low-order model

The governing equation of motion for the boulder subsystem in the X direction is formed by substituting (3.28) and (3.56) into (3.3). The governing equation of motion for rotation of the boulder subsystem about the Z direction is formed by substituting (3.20), (3.46) and (3.57) into (3.6). The governing equations of motion for the boulder-soil subsystem will be left in the form seen in (3.3) and (3.6) due to the underlying force limitation factors such as ultimate lateral resistance.

3.3 Predicting boulder fracture

Due to the simplistic nature of the low-order model, unrealistic geometries for boulders which will survive a vehicle impact may be obtained from simulations when considering the boulder as completely rigid. Namely, the model may predict that a thin but relatively wide boulder would effectively act as a soil-fixed barrier, when in actuality it would be expected to fracture. Additionally, circumstances may appear in which the soil is extremely rigid or a boulder may be embedded in an engineered foundation such as reinforced concrete. Such boundary conditions increase internal stresses within the boulder as energy is no longer able to be dissipated through the deformation of the surrounding soil. Methods for predicting boulder

fracture will be presented for scenarios in which the boulder is rigidly fixed at the point of embedment as this is expected to be a worst-case scenario. These boulder geometries will then be used as a set of minimum dimensions to be used with a boulder acting as a soil-fixed barrier.

The approach for determining boulder fracture as a result of a vehicular impact is based on calculations of the principle stresses in the boulder. The boulder is modeled as a cantilever, with fracture initiation based on Brittle Coulomb Mohr failure criteria, similar to [20]. The peak forces on the boulder are assumed to arise from the peak decelerations observed in vehicle crash tests.

The analysis may be generous because it does not include rock fracture planes and other possible faults. Additionally, the analysis ignores moments due to the inertia of the boulder which may cause fracture to occur below the soil line. In some respects, the approach might also be conservative as it ignores soil motion which will greatly mitigate some of the stresses on the boulder.

Due to the combination of assumptions, the analysis is expected to provide only approximations of fracture behavior that can guide recommendations for suitable boulders. But the results will not be exact predictions of pass/fail events for all boulders under all situations. The soil damping and soil spring rate are both assumed to be infinite, resulting in a rigid cantilever soil boundary condition. Additionally, the vehicle and corresponding crush zone is replaced by a single maximum force as measured during previous full scale crashes. The representation of the infinite soil damping and spring rate can be seen in Figure 3-12.

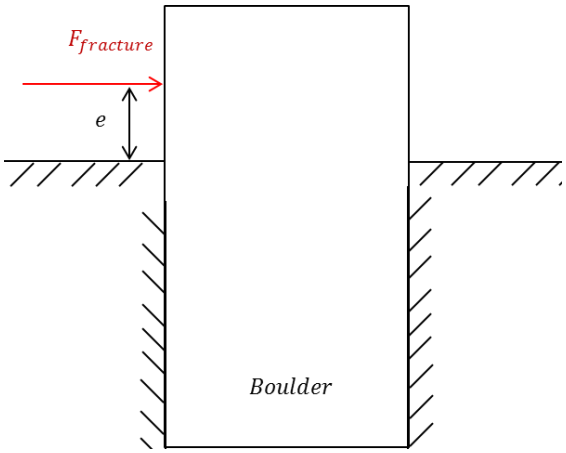

Figure 3-12: Cantilevered beam model for infinite soil damping and stiffness

The peak force $F_{fracture}$ can be estimated from the peak deceleration of the vehicle using

$$F_{fracture} = m_v \, a_{peak}, \tag{3.61}$$

where a_{peak} is the estimated peak acceleration during impact.

Failure in the form of fracture is determined by analyzing the internal principles stresses resulting from an equivalent vehicle impact. The principle stresses are functions of both bending and shear stress. Since the boulder is composed of a brittle material and failure is due primarily to tension along the impact face of the boulder, the shear stress induced by bending may be neglected. The bending stress, σ_y, is found using,

$$\sigma_y = \frac{M_{fracture} x}{I}, \tag{3.62}$$

and the transverse shear stress, τ_{yx}, is found using,

$$\tau_{yx} = \frac{F_{fracture}}{WL}, \tag{3.63}$$

where M is the bending moment about the base of the boulder, x is the distance from the centroid of the cross section to the impact face which corresponds to maximum bending stress, and I is the area moment of inertia about the centroid. The values of $M_{fracture}$, x, and I are found using

$$M_{fracture} = F_{fracture}\, e \tag{3.64}$$

$$x = \frac{L}{2} \tag{3.65}$$

$$I = \frac{1}{12} W\, L^3. \tag{3.66}$$

Noting that the normal stress acting on the impact face of the boulder, σ_x, is zero, the principle stresses are found using

$$\sigma_{1,2} = \frac{\sigma_y}{2} \pm \sqrt{\left(\frac{\sigma_y}{2}\right)^2 + {\tau_{yx}}^2}. \tag{3.67}$$

The factor of safety, $n_{fracture}$, is then found using the Brittle Coulomb Mohr failure criteria by using

$for\ \sigma_1 \geq \sigma_2 > 0$

$$\sigma_1 = \frac{S_{ut}}{n_{fracture}} \tag{3.68}$$

$for\ \sigma_1 > 0 > \sigma_2$

$$\frac{\sigma_1}{S_{ut}} - \frac{\sigma_2}{S_{uc}} = \frac{1}{n_{fracture}} \tag{3.69}$$

$$for\ 0 > \sigma_1 \geq \sigma_2 \qquad \sigma_2 = -\frac{S_{uc}}{n_{fracture}}, \tag{3.70}$$

where S_{ut} is the ultimate tensile strength and S_{uc} is the ultimate compressive strength of the boulder material. A factor of safety less than 1 implies a boulder geometry for which fracture is anticipated for the given material properties.

3.4 In-situ measurement of soil parameters

One of the goals of this thesis is to develop an in-situ method for rapidly determining the soil properties found in the low-order model, namely the constant of horizontal subgrade reaction, β, the effective angle of internal friction, φ', and the bulk soil density, ρ_{soil}. After reviewing literature pertaining to in-situ soil property measurement, it was determined that a majority of soil properties pertaining to the low-order model can be determined through the use of a dynamic cone penetrometer and various correlations. The methodology for performing a DCPT is covered in ASTM D6951, and the results from a DCPT are given as a penetration index, PI, in $\mathrm{mm/blow}$. The goal of this section is to present a correlation between the penetration index to the constant of horizontal subgrade reaction, effective angle of internal friction, and density of soil. Figure 3-13 outlines the procedure for correlating the penetration index from a DCPT to the constant of horizontal subgrade reaction.

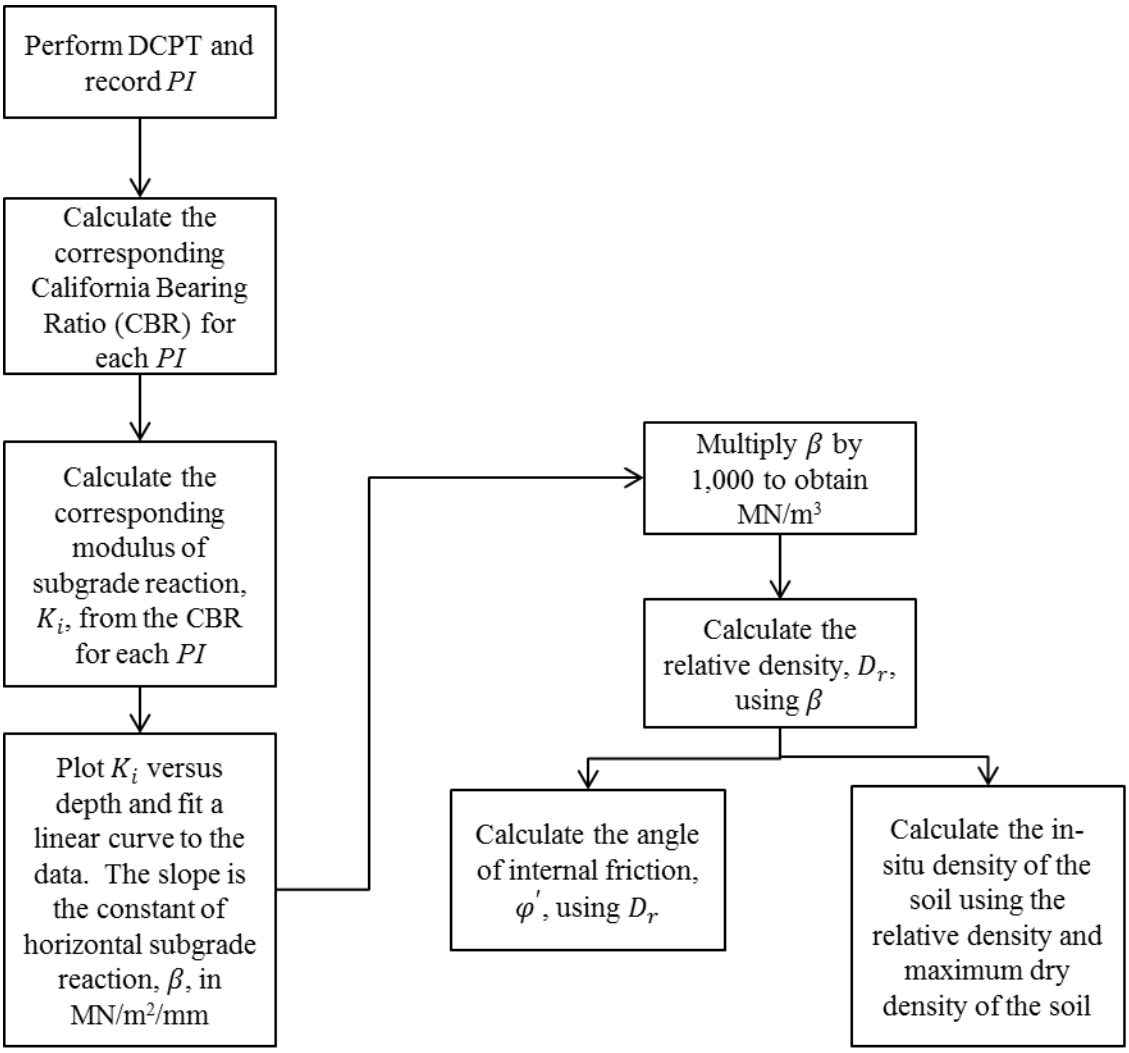

Figure 3-13. Flow chart for determining in-situ soil properties

The results from the penetration index at each blow increment, i, is first correlated to the California Bearing Ratio using [16]

$$CBR_i = 10^{2.628} \cdot PI_i^{-1.27}, \tag{3.71}$$

where CBR_i is in percent. The penetration index, PI_i, at a given increment is found using

$$PI_i = d_i - d_{i-1}, \tag{3.72}$$

where d_i is the total penetrated depth in mm at blow increment i. The California Bearing Ratio at each increment is then correlated to the modulus of subgrade reaction, K_i, in $\mathrm{MN/m^2}$ using [25]

$$K_i = 10^{\left(\frac{\log(CBR_i)\cdot 14.304}{1.71512}\right)}. \tag{3.73}$$

The modulus of subgrade reaction at each blow increment is then plotted against the total depth at each increment, d_i , and a linear curve is fit to the data since the modulus of subgrade reaction is assumed to increase linearly with depth. Since the plot of the modulus of subgrade reaction against depth is in mm, the constant of horizontal subgrade reaction, β, in $\mathrm{MN/m^3}$ is found using

$$\beta = b' \cdot 1000, \tag{3.74}$$

where b' is the slope of the linear fit curve.

Knowing the constant of horizontal subgrade reaction, it is then possible to estimate the relative density of the soil using Figure 3-14.

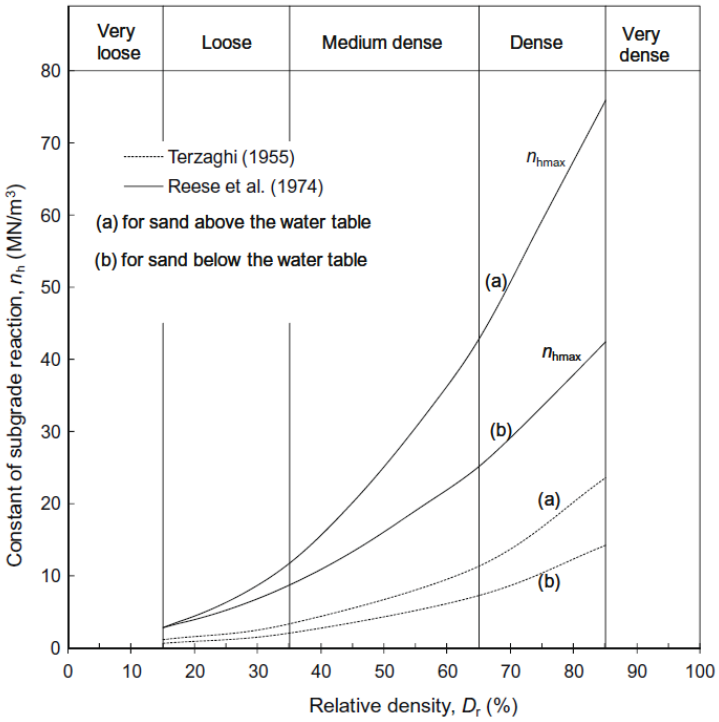

Figure 3-14. Constant of [horizontal] subgrade reaction vs. relative density [7]

Since it is expected that the soil used in testing will be compacted beyond 90% relative density and remain above the water table, curve (a) in Figure 3-14 is fit to a quadratic polynomial of the form

$$\beta = 0.01221 \cdot {D_r}^2 - 0.1748 \cdot D_r + 2.86, \tag{3.75}$$

where D_r is the relative density of soil in percent and β is measured in $\mathrm{MN/m^2}$. The maximum theoretical constant of horizontal subgrade reaction using (3.75) is found by setting D_r to 100 which results in $\beta_{max} = 107.48 \ \ (\mathrm{MN/m^3})$. Solving (3.75) for the relative density yields

$$D_{r_{1,2}} = \frac{0.1748 \pm \sqrt{0.17484^2 - 4 \cdot (0.01221) \cdot (2.86 - \beta)}}{2 \cdot (0.01221)}. \tag{3.76}$$

The lesser of the two values obtained form (3.76) can be neglected since it would correspond to a negative constant of horizontal subgrade reaction. Similar to Zhang [7], (3.76) can be graphically represented for quicker interpretation, as illustrated in Figure 3-15.

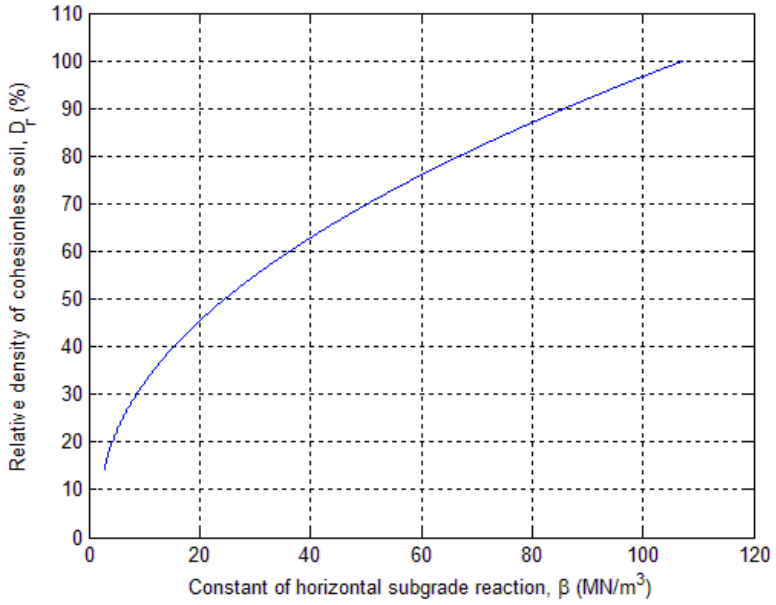

Figure 3-15. Relative density vs. constant of horizontal subgrade reaction for cohesionless soils

Knowing the relative density from Figure 3-15, the bulk density of the soil is found using

$$\rho_{soil} = \rho_{soil_{max}} D_r, \tag{3.77}$$

where $\rho_{soil_{max}}$ is the maximum bulk density of the soil. The maximum density can be found using the modified proctor test as performed according to ASTM D698. The effective angle of internal friction can also be estimated from the relative density using Figure 3-16.

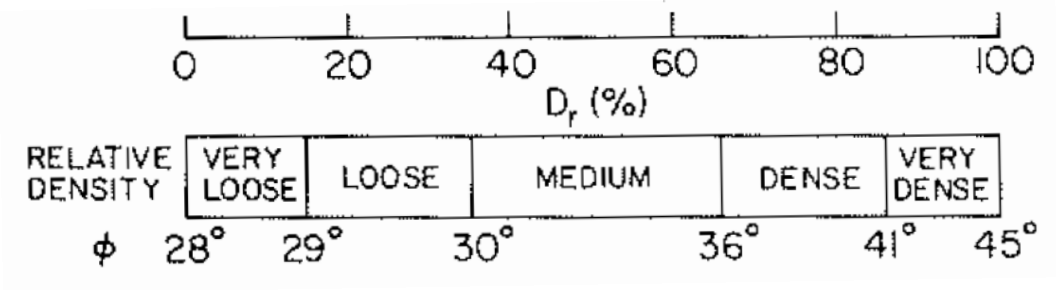

Figure 3-16. Effective angle of internal friction as correlated to relative density [23]

Similar to Figure 3-14, Figure 3-16 can be represented by a quadratic equation which takes the form

$$\varphi' = 0.0015 \cdot {D_r}^2 + 0.02 \cdot D_r + 28. \tag{3.78}$$

Equation (3.84) can also be graphically represented for quicker and more accurate interpretation, as illustrated in Figure 3-17.

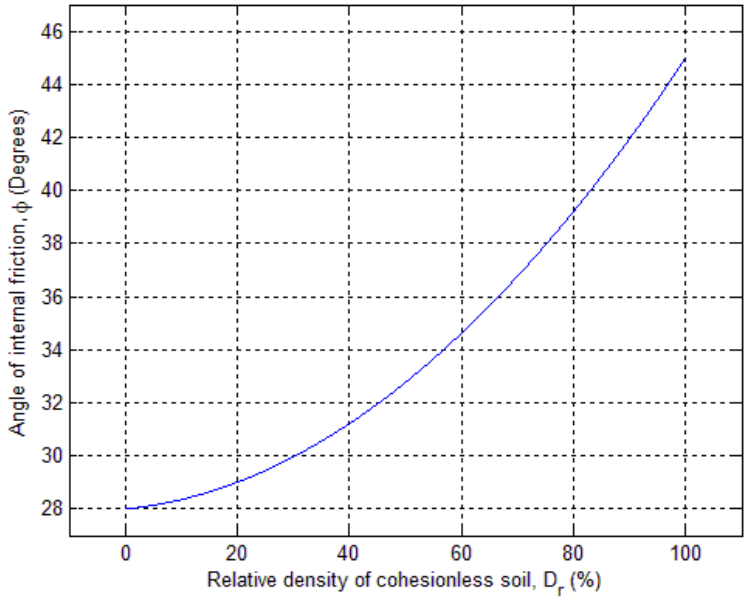

Figure 3-17. Effective angle of internal friction vs. relative density

3.5 Simulation of Model

The governing equations of motion for the low-order model, (3.3), (3.6), and (3.54), can be arranged into a state-space form and solved via numerical integration. The states and corresponding time derivatives are listed in Table 3–1. It should be noted that all forces in the governing equations of motion can be written explicitly as functions of the states. The change in linear displacement and linear velocity of the contact point between the boulder and the vehicle, Δx_{bv} and $\dot{x}_{bv}$, are not transformed into the state space representation as a matter of general housekeeping, but they can also be expressed explicitly as functions of the states.

Table 3–1. States for governing equations of motion of the low-order model

$x_1 = x_b$	(3.79)	$\dot{x}_1 = x_2$	(3.80)
$x_2 = \dot{x}_b$	(3.81)	$\dot{x}_2 = \frac{1}{m_{eff}}\left[\sum_{n=1}^{N}\{F_n\} + F_v\right]$	(3.82)
$x_3 = \theta_b$	(3.83)	$\dot{x}_3 = x_4$	(3.84)
$x_4 = \dot{\theta}_b$	(3.85)	$\dot{x}_4 = \frac{1}{J_{eff}}\left[\sum_{n=1}^{N}\{M_n\} + M_v + M_R\right]$	(3.86)
$x_5 = x_v$	(3.87)	$\dot{x}_5 = x_6$	(3.88)
$x_6 = \dot{x}_v$	(3.89)	$\dot{x}_6 = x_7$	(3.90)
$x_7 = \ddot{x}_v$	(3.91)	$\dot{x}_7 = -\frac{k_v}{c_v}x_7 - \frac{k_v}{m_v}x_6 + \frac{k_v}{m_v}[x_2 + x_4\, R_v\, \cos(\gamma_v + x_3)]$.	(3.92)

The set of equations (3.79) – (3.92) are coupled first-order, nonlinear, non-stiff ordinary differential equations which can be readily solved via numerical integration. The MATLAB® ODE45 solver is used to solve the state-space equations. The use of ODE45 allows for quick and easy comparison of simulated and full scale results. The ODE45 simulation is driven by the initial

velocity of the vehicle, v_o, as an initial condition. No external forcing or forcing function is necessary.

3.6 Contributions of this chapter

The contributions of this chapter are as follows:

(1) Introduce coordinate system and model nomenclature

(2) Develop the low-order model for a vehicle impact upon a soil-fixed boulder

(3) Derive the governing equations of motion for the low-order model

(4) Present fracture prediction methodology for boulders impacted by a vehicle based on peak deceleration force

(5) Present the methodology for in-situ soil property measurement

(6) Represent the governing equations of motion in state-space form

CHAPTER 4

VALIDATION OF LOW-ORDER MODEL AND STATIC FRACTURE PREDICITION METHODOLOGY

The intent of this chapter is present the validation of the low-order model and static fracture prediction methodology presented in Chapter 3. The simulated low-order model is compared to past full scale crash test results of vehicles impacting soil-fixed boulders. The static fracture prediction methodology is compared to full scale vehicle impacts on rigidly-fixed boulders. Additional small scale fracture tests were performed to verify the static fracture prediction methodology and are presented in Chapter 6. All full scale crash tests were performed at a M30 rating as specified in ASTM F2656-07. The methodology for in-situ measurement of the soil properties as presented in Chapter 3 had not been developed prior to the full scale crash tests presented in this chapter.

This chapter is organized as follows:

The test equipment and apparatus used in performing a full scale crash test are presented in Section 4.1, and the test equipment for medium scale fracture tests is presented in Section 4.2. A summary of past full scale crash tests is presented in Section 4.3, and a summary of medium scale fracture tests is presented in Section 4.4. The comparison and validation of the simulated low-order model to full scale crash tests of vehicles impacting soil-fixed boulders is presented in Section 4.4. The validation of the fracture prediction in the full scale vehicle crash tests and medium scale fracture tests on rigidly-fixed boulders is presented in Section 4.6 and Section 4.7, respectively.

4.1 Full scale crash test equipment and test procedure

All full scale crash tests took place at the Penn State Crash Safety Research Facility under the supervision of Larson Transportation Institute personnel. Larson Institute personnel followed the procedures described in ASTM Standard Test Method F2656-07 to perform M30 designated vehicle impacts on boulders embedded in a compacted soil foundation. The Crash Safety Research Facility uses a guiderail system for steering the impact vehicle, a reverse towing system for accelerating the impact vehicle up to the desired speed, and a cable release device for separating the tow cable from the impact vehicle just prior to the crash. An aerial view of the Crash Safety Research Facility is shown in Figure 4-1.

Figure 4-1. Aerial view of the Larson Institute Crash Safety Research Facility at Penn State

The guiderail is approximately 320 m long, and was manufactured such that additional rail pieces may be added to or removed from the impact end to account for various crash geometries. A bogey catch is attached to the end of the guiderail which serves as the tow cable release device. The bogey is attached to a medium-duty truck on the steering arms directly underneath the front center of the vehicle. Figure 4-2 shows a general layout of the guiderail with impact and tow vehicle, bogey catch, and impact area. Figure 4-3 shows photographs of the bogey as installed on a typical medium-duty sized truck and the bogey catch device.

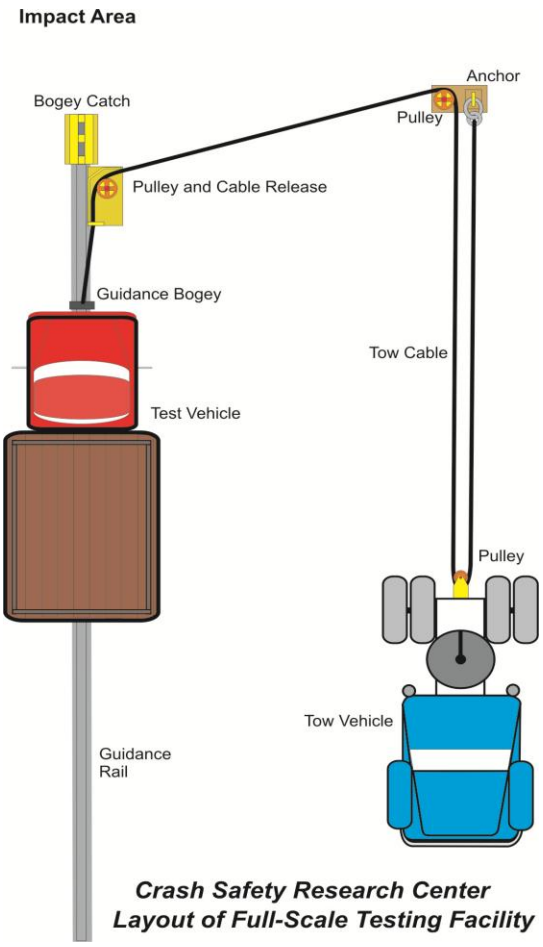

Figure 4-2. CRSF impact setup

Figure 4-3. Full scale guidance system: bogey assembly (left) and bogey catch (right)

The towing system consists of a tow vehicle, tow cable, redirection pulleys, and a speed multiplier pulley attached to the tow vehicle. The speed multiplier allows the tow vehicle to travel at half the speed of the impact vehicle. Figure 4-4 shows the towing system configuration and tow vehicle.

Figure 4-4. Full scale towing system: first re-directional pulley (left), speed multiplier (center), and second re-directional pulley (right)

The soil for all full scale crash tests was 2A modified limestone gravel. The soil was obtained from Hanson Aggregates in Boalsburg, Pennsylvania. The gravel was compacted by Ameron Construction using a hydraulic tamper attached to the arm of a backhoe according to ASTM F2656-07. Figure 4-5 shows the gravel in a loose state, and Figure 4-6 shows the soil in a compacted state. When installing the boulder, they are aligned with the guiderail such that the critical impact point on the boulder is approximately 90° to the centerline of the impact vehicle. The critical impact point for boulders was determined to be the centerline of the boulder.

Figure 4-5. Modified 2A limestone gravel in loose state

Figure 4-6. Modified 2A limestone gravel in compacted state

The primary data acquisition system used for full scale crash tests as related to this research was a Photron Ultima 1024 high-speed imaging system. The Ultima 1024 was located at a 90° angle from the side of the impact vehicle, capturing the crush of the vehicle and translation

and rotation of the boulder. For soil-fixed boulder tests, the camera was set to record 500 frames per second for 2 seconds after receiving a trigger signal. The trigger system consists of two reflective laser beams used to determine when the impact vehicle passes through the trigger point. When both laser beams are broken, a TTL signal is sent to the high-speed camera which initiates recording.

The high-speed imaging analysis software, Photron Motion Tools, was used throughout this work to perform the image processing of the full and small scale crash tests. Photron Motion Tools is analysis software which allows for feature recognition and feature tracking through a series of images. The user can also enter a desired scaling factor which automatically converts pixels to the desired units of displacement. The output from Photron Motion Tools is a Microsoft Excel spreadsheet of the global x and y displacements of each tracked feature, where the x direction is to the right and the y direction is up.

A Stalker Speed Sensor (S3) radar system is used to determine the impact vehicle speed during the towing process. This unit is a stationary Doppler radar speed sensor operating at a frequency of 34.7 GHz and communicating through an RS-232 port. The speed range is 1 mph to 200 mph (1.6 to 321 km/h) and provides an accuracy of ±0.3% with speeds being rounded down to the nearest tenth of a unit. The stationary radar unit is located at the beginning of the guiderail and is aimed at the impact vehicle as it travels to the impact zone. One speed sensor display is located with the stationary unit, and a second speed sensor display is located in the tow vehicle. A FreeWave Spread Spectrum Wireless Data Transceiver system is used to communicate between the stationary unit and the speed display in the tow vehicle. The impact vehicle speed is displayed in the tow vehicle so that the driver can attain the proper test speed.

Some full scale tests included the use of pressure cells embedded in the soil surrounding the boulder in order to measure the pressures within the soil during vehicle impact. The data

from the pressure cells are not used in this work. The pressure cells should simply be noted as part of the installation procedure and test setup.

4.2 Medium scale fracture test equipment and procedure

The medium scale fracture tests were performed using a 2,227 kg impact pendulum. The aerial view of the medium scale test setup is shown in Figure 4-7.

Figure 4-7. Crash Safety Research Institute medium scale impact pendulum

The Crash Safety Research Institute (CSRI) impact pendulum has an approximate height of 15 meters which allows for a maximum arc radius of 13.7 meters for the impact sled. This configuration of the impact pendulum allows for a maximum vertical elevation change of 9.1

meters for the impact sled thus resulting in a maximum horizontal speed of approximately 13.4 m/s upon impact when released from maximum height.

The impact sled is supported by four ¾" steel cables attached at the top of the CRSI pendulum frame. The ¾" support cables are attached to the impact sled via cable thimbles and cable clips. The thimbles and clips can be adjusted for rough initial height change of the impact sled. Turnbuckles are then used for fine adjustment of the impact sled starting height. Two pulleys are located at the top of the north end of the pendulum frame, over which the impact sled cable and quick release cable are fed. Photographs of the pendulum are provided in Figure 4-8.

Figure 4-8. CRSI pendulum frame and components

The impact pendulum is mounted on concrete slabs at the north and south ends of the frame. The concrete slab at the north end of the pendulum has 9 protruding studs to which

mounting hardware for raising the impact sled can be attached. The concrete slab at the south end of the pendulum has 15 threaded inserts of 3-1/4" x 4 TPI into which the mounting bolts for the boulder clamping mechanisms, skewbacks, can be inserted and secured.

Skewbacks are large structural supports made from W12-136 I-beam which are used to rigidly hold the test specimens above ground. The skewbacks consist of three independent structures that hold the boulder during the impact and are independently bolted to the concrete impact slab. Photographs of the skewbacks are provided in Figure 4-9.

Figure 4-9. Skewbacks used in medium scale fracture testing

The impact sled is the device used to impact the boulders. The impact sled consists of two major components. The first component is the main body which can be loaded with additional weights, and the second component is a detachable ram which bolts to the front of the main body. The weight of the fully loaded impact sled is 2,227 kg. Photographs of the impact sled are provided in Figure 4-10.

Figure 4-10. Detailed photographs of the impact sled used in medium scale crash tests

A medium scale fracture test is performed by raising the impact sled to a desired height and using a quick release mechanism to allow the impact sled to swing into the test article. The pendulum uses a cable, pulley, and winch system to raise the impact sled to a desired height or potential energy.

The winch system consists of 145 feet of 7/16” 6 x 37 steel cable which goes up and over a pulley on the top of the pendulum frame on the north end. A separate steel cable is used to trigger the quick release mechanism, and it also goes up and over a second pulley on the top of the pendulum frame. The impact sled is attached to a quick release mechanism which connects

the winch cable to the impact sled. The DC winch is mounted to the concrete slab via 9 threaded studs, W6-36 I-beam, and a mounting plate. The winch is mounted such that it draws in cable vertically. A deep cycle lead acid battery is used to power the winch. Photographs of the winch system are provided in Figure 4-11, and a photograph of the impact sled with the quick release mechanism is provided in Figure 4-12.

Figure 4-11. Impact sled raising system used in medium scale fracture testing

Figure 4-12. Impact sled with quick release mechanism

The impact sled is raised to the desired height using the winch to pull the cable attached to the quick release mechanism. The DC winch is duty cycled while the impact sled is raised. The impact sled is determined to be at the desired elevation level using reference points of 5 meter elevation change along the pendulum frame. The top of each cross section of the pendulum frame is approximately 5 meters high and the sled is stopped upon reaching estimated desired height. Photographs of initial height and relative elevation change of the impact sled are provided in Figure 4-13. The impact sled is stopped after it reaches the desired height, and the winch locks the impact sled in place. The quick release cable is then pulled, and the impact sled is released. The impact sled swings down and impacts the test article. A high-speed camera is used to capture the impact at a rate of 5000 Hz. The high-speed imaging system is the same as that presented in Section 4.1.

Figure 4-13. Example of the change in elevation of the impact sled; equilibrium position (left) and desired elevation change (right)

4.3 Summary of past full scale crash tests

Two past full scale crash tests of vehicles impacting soil-fixed boulders were performed on two boulders with different embedment depths and boulder geometries. The two soil-fixed crashes are referred to as Boulder-Soil-Test-1 (BST-1) and Boulder-Soil-Test-2 (BST-2)

throughout this thesis. Additionally, two full scale crash tests were performed on boulders which were embedded in a reinforced concrete footing. The two concrete footing crash tests are referred to as Boulder-Footing-Test-1 (BFT-1) and Boulder-Footing-Test-2 (BFT-2).

The constant of horizontal subgrade reaction is estimated for both BST-1 and BST-2 since the presented in-situ soil measurement techniques were not yet in place at the time of testing and there were no soil measurements made. As per ASTM F2656-07, the soil must be compacted to at least 90% maximum density which correlates to a minimum constant of horizontal subgrade reaction of 86 MN/m^3. A modified proctor test, however, was performed on a limestone dust soil sample used in small scale testing which was determined to be similar in makeup and content to the 2A modified limestone gravel used in full scale testing. From the modified proctor test results, the maximum soil density was found to be 2,010 kg/m^3. The results of the modified proctor test are provided in Appendix B. The remaining soil properties were calculated as presented in Chapter 3. The average density of the American Black Granite and Rockville White Granite was measured to be 3,074 kg/m^3 and 2,652 kg/m^3, respectively.

4.3.1 Summary of full scale crash test BST-1

BST-1, in which large boulder displacements were observed, was performed on 15 November, 2010. The boulder had dimensions of 0.762 m-L x 1.016 m-W x 2.2 m-H with respect to the impact direction. The American Black Granite boulder, referenced as ABG-01, was embedded 1.2 meters into the soil. The pre-test condition of the boulder is shown in Figure 4-14.

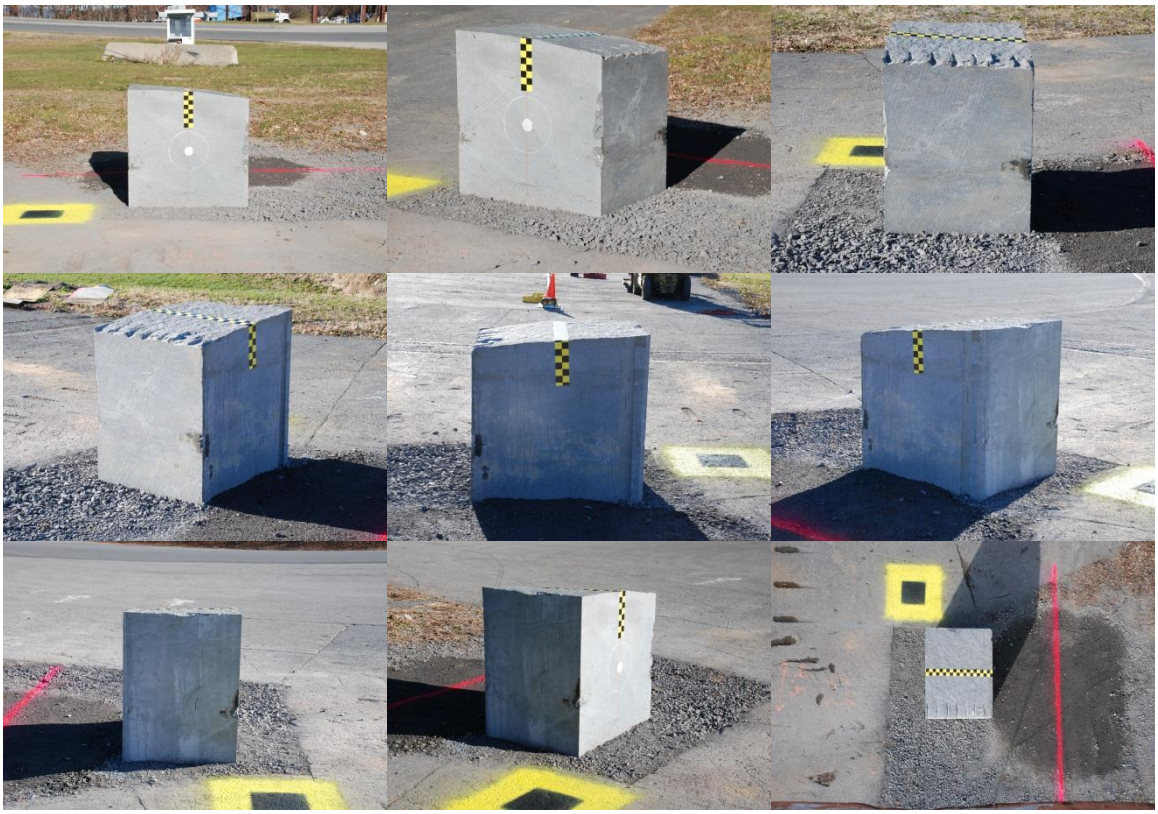

Figure 4-14. Pre-test condition of ABG-01 in BST-1

The impact vehicle for BST-1 was a 2002 Chevrolet C6500 medium-duty sized truck, and was prepared as specified in ASTM F2656-07. Additional ballast was added to the front of the truck bed in order to achieve a total weight of 6,795 kg (14,980 lbs.). Additional vehicle specifications are provided in Appendix A, and photographs of the vehicle are shown in Figure 4-15.

Figure 4-15. Pre-test conditions of the impact vehicle in BST-1

Based on the stationary radar system and confirmed by analysis of the high-speed video, the approach speed at impact was 13.36 m/s (29.9 mph). The centerline of the test vehicle impacted the test article on the critical impact point that was defined as along the centerline of the attack left vertical post, and the angle of approach was 89.1°. Figure 4-16 shows the location of the centerline of the impact vehicle relative to the critical impact point and the impact angle of the vehicle.

The vehicle impacted ABG-01 head-on. The boulder translated and rotated on impact, reaching a peak angle of just under 90° from vertical. The boulder and test vehicle then came to rest in a relatively horizontal orientation. Figure 4-17 shows the side-view still images extracted from the high-speed video in a chronological sequence of the impact.

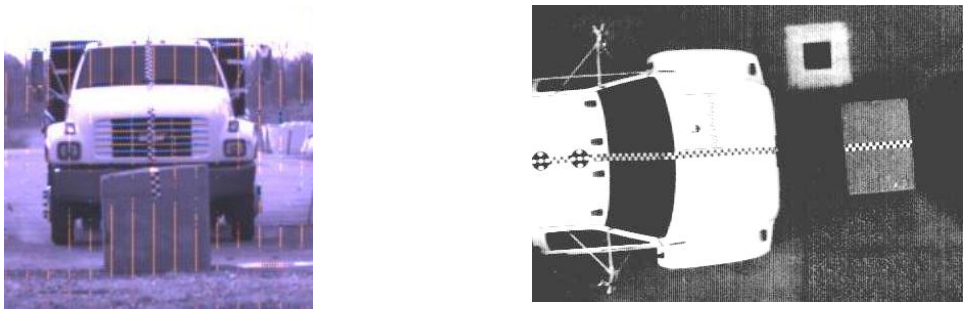

Figure 4-16. Location of impact vehicle centerline (left) and impact angle (right) in BST-1

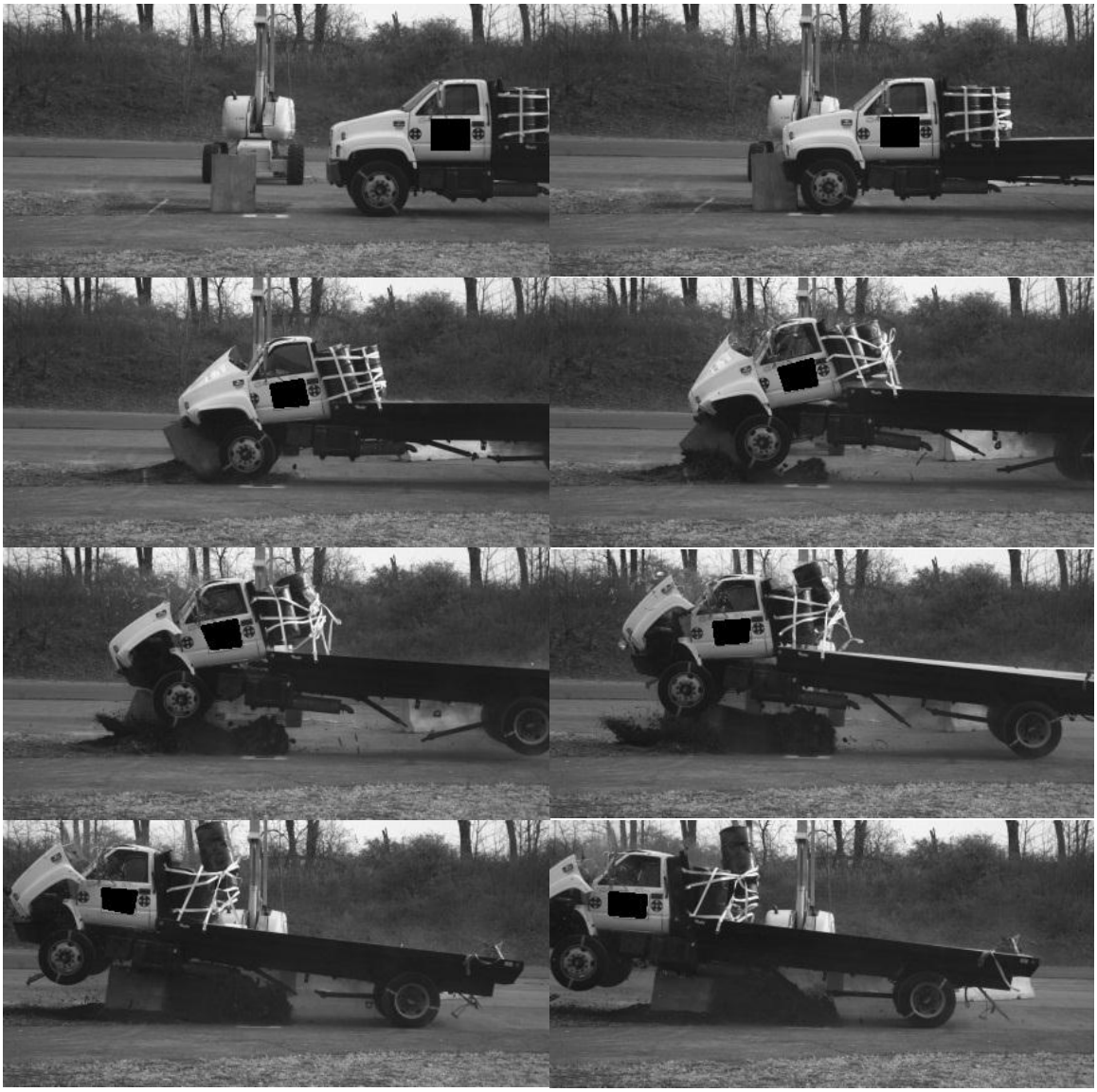

Figure 4-17. High-speed image sequence of BST-1

Figure 4-18 shows the linear displacement of the center of mass of ABG-01 from the point of impact, and Figure 4-19 shows the angle of rotation of ABG-01 from the point of impact. The linear displacement of the vehicle as tracked using the forward fiducial is shown in Figure 4-20. Photographs of the post-test condition and location of the vehicle are shown in Figure 4-21, and Figure 4-22 shows the post-test condition of ABG-01.

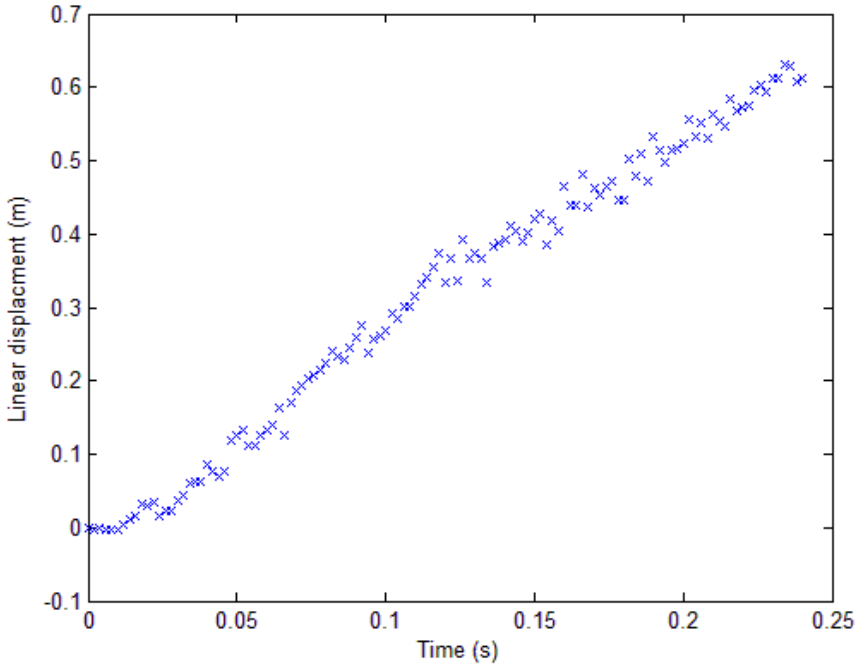

Figure 4-18. Measured linear displacement of the center of mass of ABG-01 in BST-1

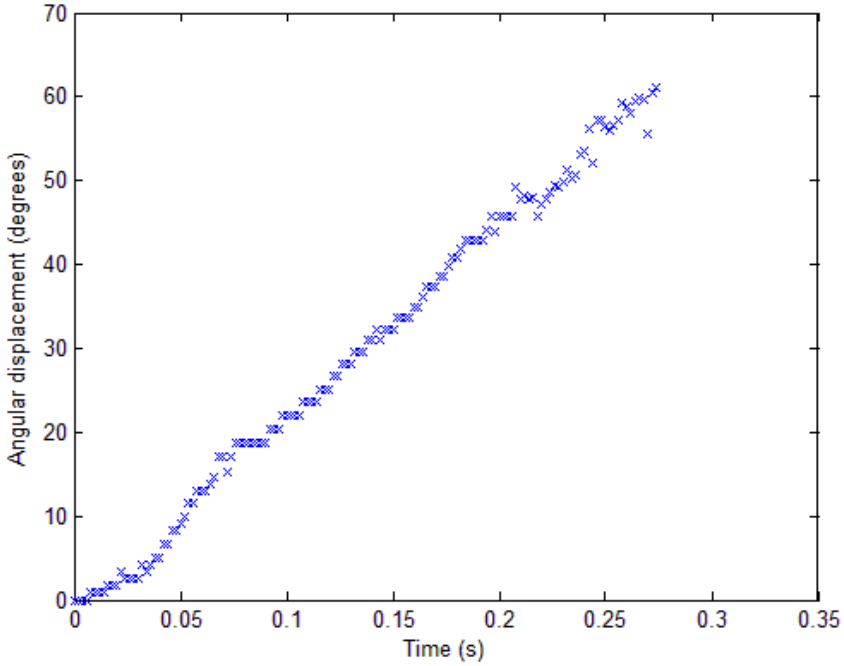

Figure 4-19. Measured angle of rotation of ABG-01 in BST-1

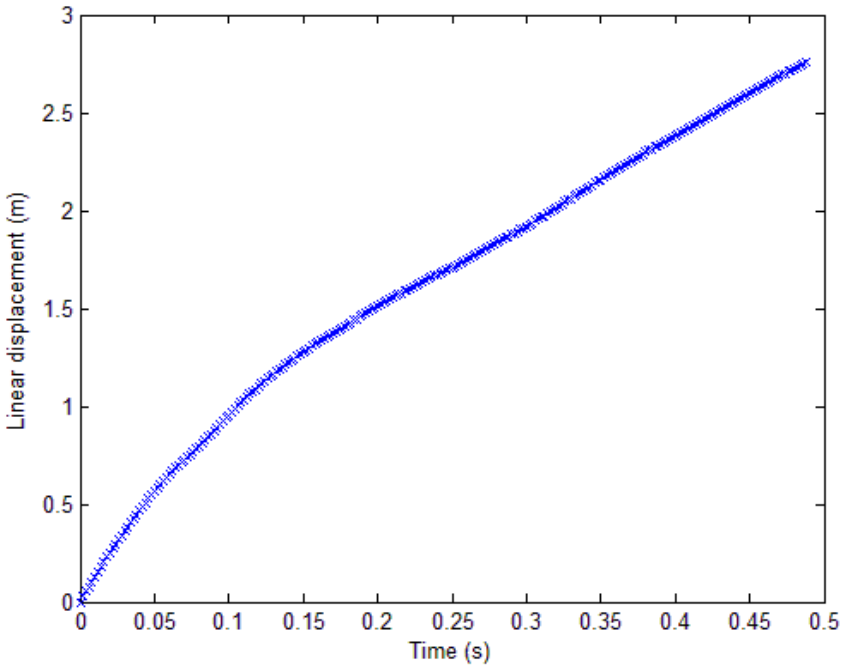

Figure 4-20. Measured linear displacement of the impact vehicle in BST-1

Figure 4-21. Post-test vehicle location in BST-1

Figure 4-22. Post-test condition of ABG-01 in BST-1

Table 4–1 summarizes the measured and estimated governing parameters for BST-1.

Table 4–1. Governing parameters for BST-1

$\rho_{soil} = 1{,}859.9\ \text{kg/m}^3$	$H = 2.2\ \text{m}$	$\beta = 95\ \text{MN/m}^3$
$\rho_b = 3{,}074\ \text{kg/m}^3$	$d = 1.2\ \text{m}$	$e = 0.754\ \text{m}$
$L = 0.762\ \text{m}$	$m_v = 6{,}795\ \text{kg}$	$\varphi' = 43.2°$
$W = 1.016\ \text{m}$	$v_o = 13.36\ \text{m/s}$	

4.3.2 Summary of full scale crash test BST-2

BST-2, in which small boulder displacements were observed, was performed on 11 November, 2011. The boulder had dimensions of 1.65 m-L x 1.68 m-W x 3.43 m-H with respect to the direction of impact. The Rockville White Granite boulder, referenced as RWG-01, was embedded 2.03 meters into the soil. The installation of RWG-01 is shown in Figure 4-23, and the pretest condition of the boulder is shown in Figure 4-24. Pressure cells were installed in the locations marked with white paint and the wooden boards.

Figure 4-23. Installation of RWG-01 in BST-2

Figure 4-24. Pre-test condition of RWG-01 in BST-2

The impact vehicle for BST-2 was a 1999 International 4700 medium-duty sized truck, and was prepared as specified in ASTM F2656-07. Additional ballast was added to the front of the truck bed in order to achieve a total weight of 6,722 kg (14,820 lbs.). Additional vehicle specifications are provided in Appendix A, and photographs of the vehicle are shown in Figure 4-25.

Figure 4-25. Pre-test condition of the impact vehicle in BST-2

Based on the stationary radar system and confirmed by analysis of the high-speed video, the approach speed at impact was 14.5 m/s (32.5 mph). The centerline of the test vehicle impacted the test article 14 cm to the left of the critical impact point that was defined as along the centerline of the attack left vertical post, and the angle of approach was 90°. Figure 4-26 shows the location of the centerline of the impact vehicle relative to the critical impact point and the impact angle of the vehicle.

The boulder translated and rotated slightly on impact, and the front end of the truck rebounded after the impact. Figure 4-27 shows the side-view still images extracted from the high-speed video in a chronological sequence of the impact.

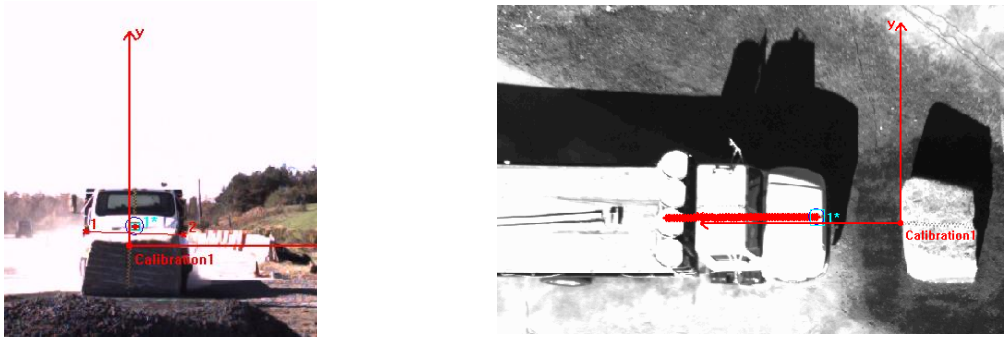

Figure 4-26. Location of impact vehicle centerline (left) and impact angle (right) in BST-2

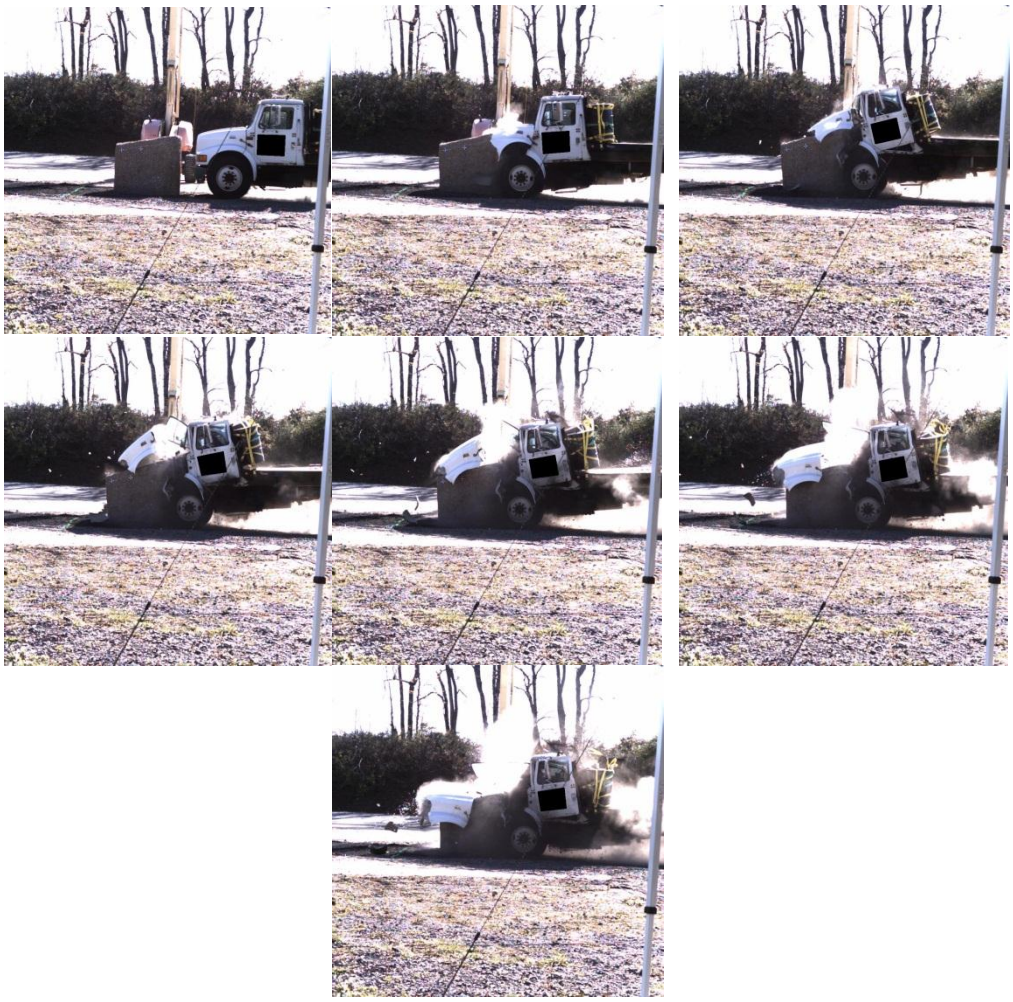

Figure 4-27. High-speed image sequence of BST-2

Figure 4-28 shows the linear displacement of the center of mass of RWG-01 from the point of impact, and Figure 4-29 shows the angle of rotation of RWG-01from the point of impact. The linear displacement of the vehicle as tracked using the forward fiducial is shown in Figure 4-30.

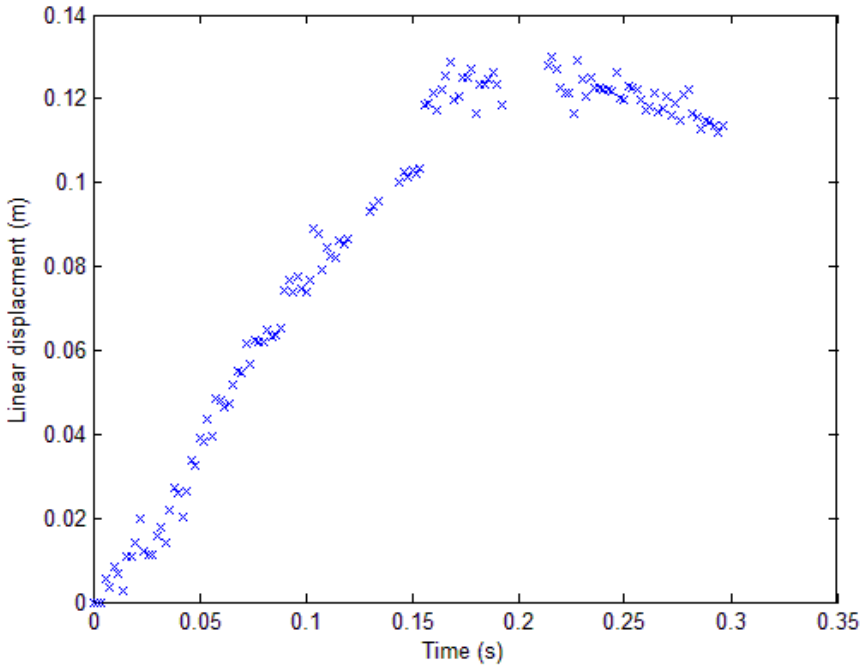

Figure 4-28. Measured linear displacement of the center of mass of RWG-01 in BST-2

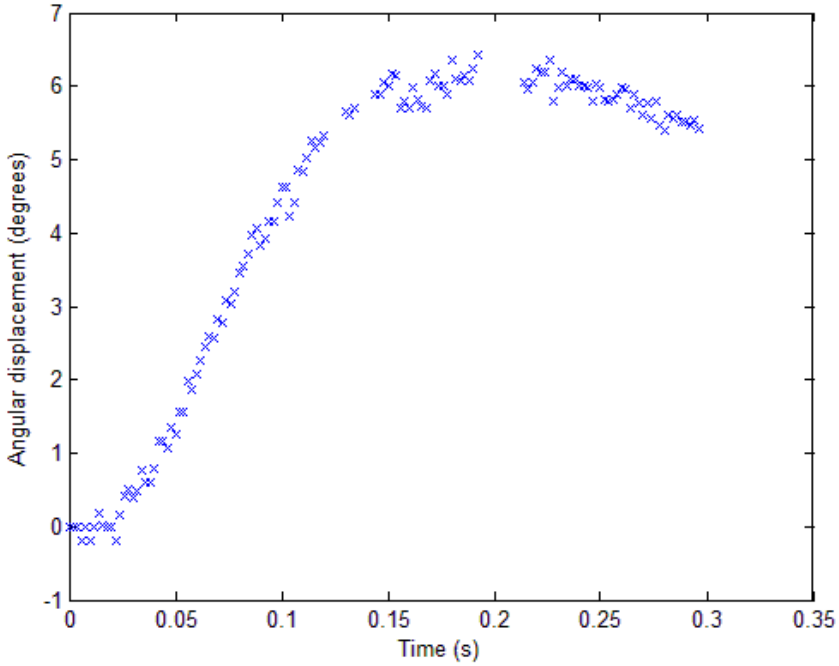

Figure 4-29. Measured angle of rotation of RWG-01 in BST-2

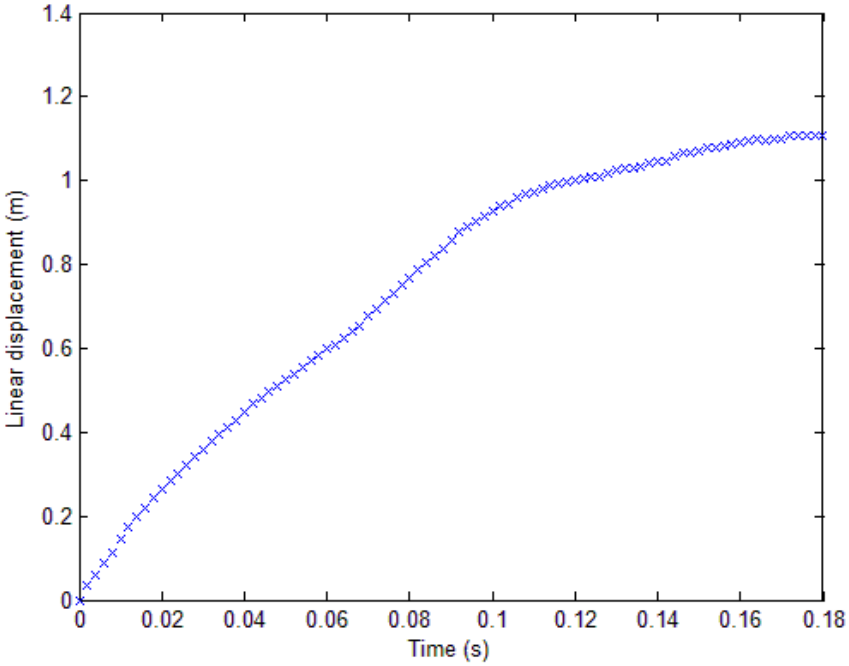

Figure 4-30. Measured linear displacement of the impact vehicle in BST-2

Photographs of the post-test condition and location of the vehicle are shown in Figure 4-31, and Figure 4-32 shows the post-test condition of RWG-01.

Figure 4-31. Post-test condition and location of the impact vehicle in BST-2

Figure 4-32. Post-test condition of RWG-01 in BST-2

Table 4–2 summarizes the measured and estimated governing parameters for BST-2.

Table 4–2. Governing parameters for BST-2

$\rho_{soil} = 1{,}859.9\ \text{kg/m}^3$	$H = 3.44\ \text{m}$	$\beta = 95\ \text{MN/m}^3$
$\rho_b = 2{,}596\ \text{kg/m}^3$	$d = 2.03\ \text{m}$	$e = 0.938\ \text{m}$
$L = 1.65\ \text{m}$	$m_v = 6{,}722\ \text{kg}$	$\varphi' = 43.2°$
$W = 1.68\ \text{m}$	$v_o = 14.5\ \text{m/s}$	

4.3.3 Summary of full scale fracture test BFT-1

BFT-1, in which the boulder was anchored into the reinforced concrete footing using dowel rods, was performed on 03 June, 2011. The boulder had dimensions of 0.99 m-L x 0.74 m-W x 2.03 m-H with respect to the direction of impact. The American Black Granite boulder,

referenced as ABG-02, was embedded 0.914 m into a reinforced foundation. Dowels were used to anchor the boulder into the concrete foundation. The dowels were #6 bars embedded 0.305 m into the boulder on all sides. Once the dowels were placed and the boulder was set into the ground, the concrete foundation (0.914 m) was poured. After the concrete cured, soil was placed on top of the concrete foundation and tamped. The installation of ABG-02 is shown in Figure 4-33, and the pretest condition of ABG-02 is shown in Figure 4-34.

Figure 4-33. Installation of ABG-02 in BFT-1

Figure 4-34. Pre-test condition of ABG-02 in BFT-1

The impact vehicle for BFT-1 was a 2002 Chevy C6500, and was prepared as specified in ASTM F2656-07. Additional ballast was added to the front of the truck bed in order to achieve a total weight of 6,792 kg (14,975 lbs.). Additional vehicle specifications are provided in Appendix A, and photographs of the vehicle are shown in Figure 4-35.

Figure 4-35. Pre-test condition of the impact vehicle in BFT-1

Based on the stationary radar system and confirmed by analysis of the high-speed video, the approach speed at impact was 16.3 m/s (36.5 mph). The centerline of the impact vehicle contacted the test article 0.13 cm to the right of the critical impact point that was defined as along the centerline of the attack left vertical post, and the angle of approach was 89.4°. Figure 4-36 shows the location of the centerline of the impact vehicle relative to the critical impact point and the impact angle of the vehicle. Upon impact, the boulder sheared at the level of the first layer of rebar and rotated under the vehicle. Figure 4-37 shows the side-view still images extracted from the high-speed video in a chronological sequence of the impact. The position of the vehicle from the point of impact is show in Figure 4-38, and the calculated velocity based on the position data is show in Figure 4-39. A 2nd order low-pass Butterworth filter with a cutoff frequency of 25 Hz was used to filter the position.

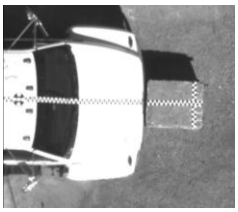

Figure 4-36. Location of the vehicle centerline and impact angle in BFT-1

Figure 4-37. High-speed image sequence of BFT-1

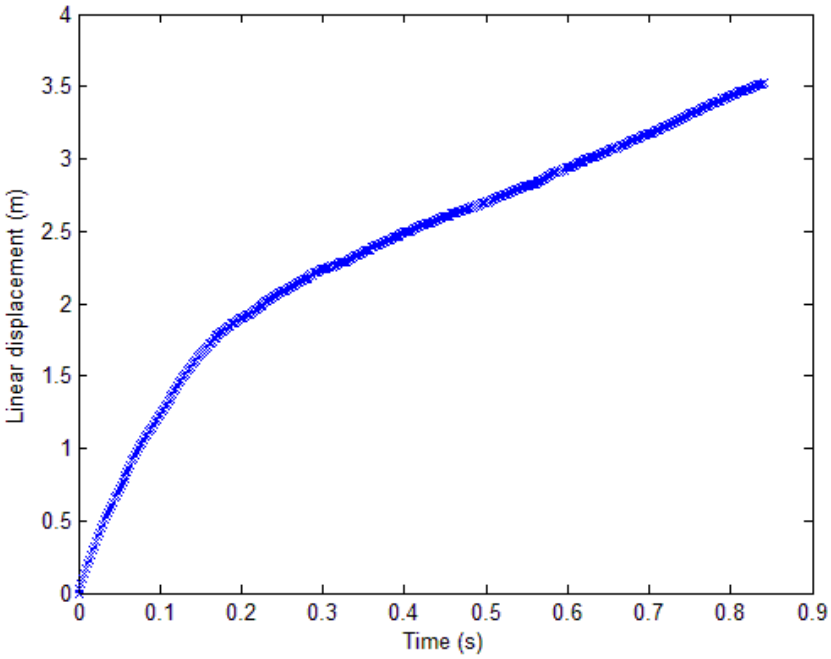

Figure 4-38. Linear displacement of the vehicle in BFT-1 from the time of impact

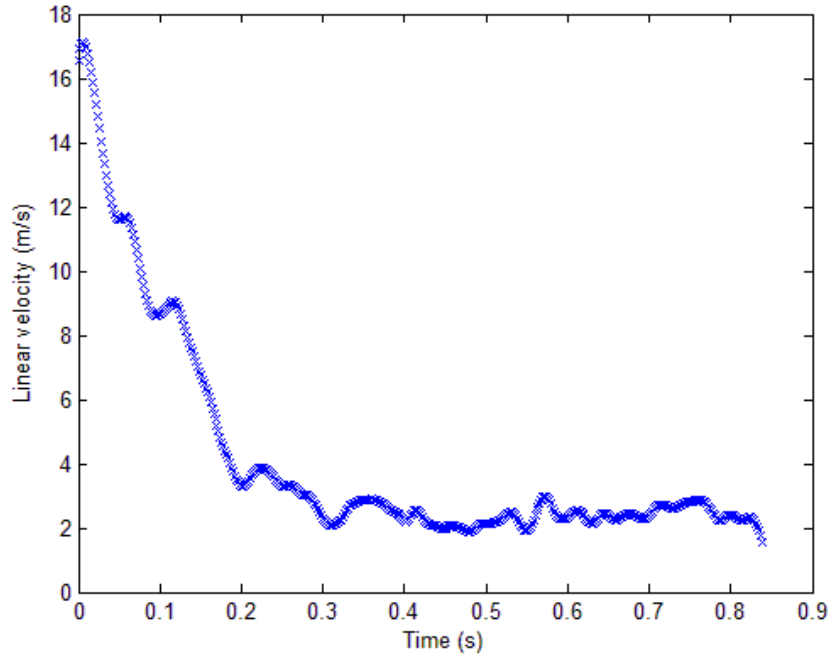

Figure 4-39. Linear velocity of the vehicle in BFT-1 from the time of impact

Photographs of the post-test condition and location of the vehicle are shown in Figure 4-40, and Figure 4-41 shows the post-test condition of the device being tested.

Figure 4-40. Post-test location and condition of the impact vehicle in BFT-1

Figure 4-41. Post-test condition of ABG-02 in BFT-1

4.3.4 Summary of full scale fracture test BFT-2

BFT-2, in which the boulder was embedded in the reinforced concrete footing with no anchoring, was performed on 22 November, 2011. The boulder had dimensions of 1.43 m-L x 0.76 m-W x 2.29 m-H with respect to the direction of impact. The American Black Granite boulder, referenced as ABG-03, was embedded 1.24 meters in a reinforced foundation. The installation of ABG-03 is shown in Figure 4-42, and the pretest condition of the boulder is shown in Figure 4-43.

Figure 4-42. Installation of ABG-03 in BFT-2

Figure 4-43. Pre-test condition of ABG-03 in BFT-2

The impact vehicle for BFT-1 was a 1994 International 4700 medium-duty sized truck, and was prepared as specified in ASTM F2656-07. Additional ballast was added to the front of the truck bed in order to achieve a total weight of 6,786 kg (14,960 lbs.). Additional vehicle specifications are provided in Appendix A, and photographs of the vehicle are shown in Figure 4-44.

Figure 4-44. Pre-test condition of the impact vehicle in BFT-2

Based on the stationary radar system and confirmed by analysis of the high-speed video, the approach speed at impact was 14.75 m/s (33 mph). The centerline of the test vehicle impacted the test article 43 cm to the right of the critical impact point that was defined as along the centerline of the attack left vertical post, and the angle of approach was 91.6°. Figure 4-45 shows the location of the centerline of the impact vehicle relative to the critical impact point and the impact angle of the vehicle.

Figure 4-45. Location of impact vehicle centerline (left) and impact angle (right) in BFT-2

The vehicle impacted the center boulder head-on. The two outer boulders were not impacted. The center boulder fractured and broke completely at the top of the reinforced concrete foundation. Figure 4-46 shows the side-view still images extracted from the high-speed video in a chronological sequence of the impact. The position of the vehicle from the point of impact is shown in Figure 4-47, and the calculated velocity based on the position data is shown in Figure 4-48. A 2nd order low-pass Butterworth filter with a cutoff frequency of 25 Hz was used to filter the position data prior to taking the time derivative.

Figure 4-46. High-speed image sequence of BFT-2

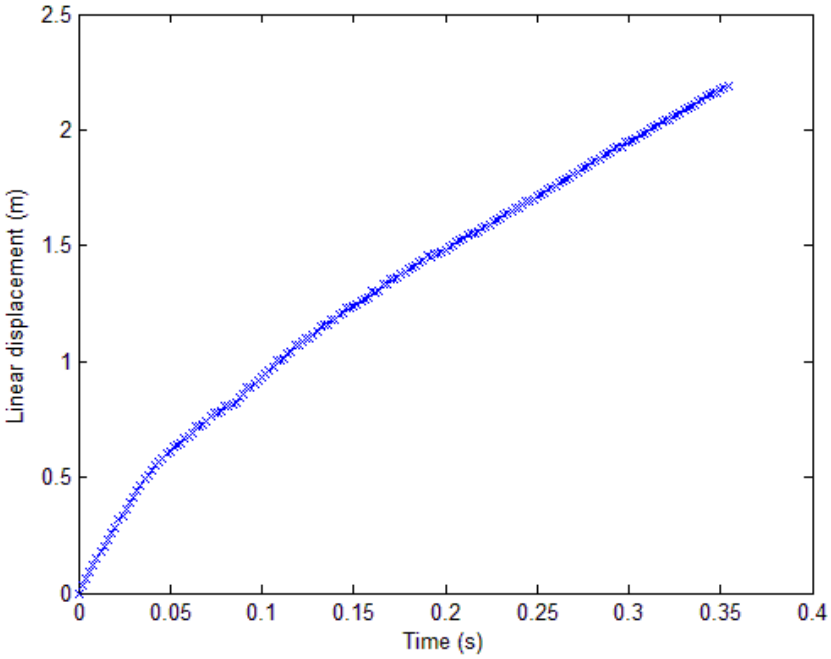

Figure 4-47. Linear displacement of the vehicle in BFT-2 from the time of impact

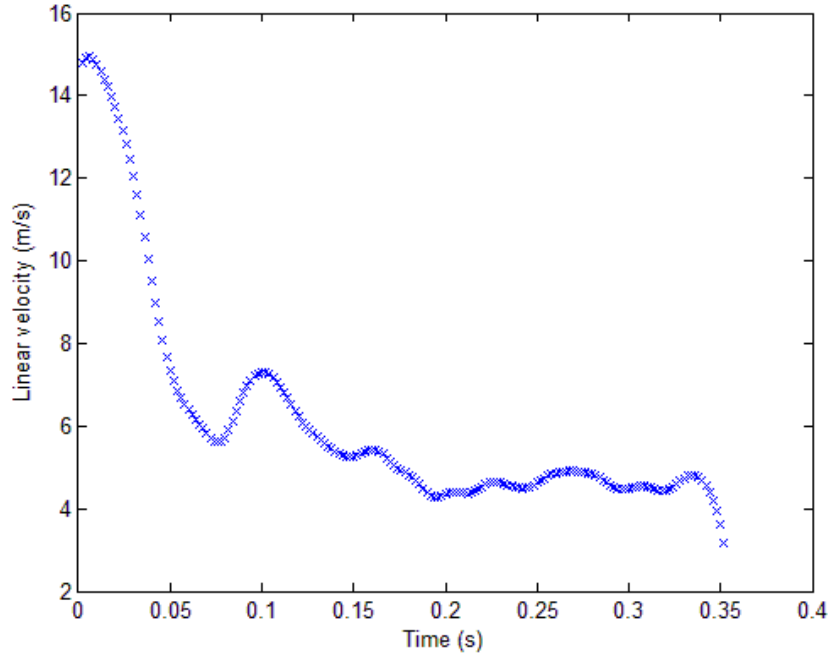

Figure 4-48. Linear velocity of the vehicle in BFT-2 from the time of impact

Photographs of the post-test condition and location of the vehicle are shown in Figure 4-49, and Figure 4-50 shows the post-test condition of the device being tested.

Figure 4-49. Post-test location and condition of the impact vehicle in BFT-2

Figure 4-50. Post-test condition of ABG-03 in BFT-2

4.4 Summary of medium scale fracture tests

Two medium scale fracture tests, MFT-1 and MFT-2, were performed on American Black Granite. The tests were performed on ABG-01, which was the boulder used in BST-1. MFT-1 and MFT-2 were performed on 08 March 2011, and the two tests were performed consecutively since ABG-01 did not fracture during MFT-1.

ABG-01 was rigidly fixed in the skewbacks such that the length of the boulder was 0.762 m and the width was 1.016 m as related to the direction of impact. The installation of the boulder was performed by Ameron Construction, and the impact sled was aligned with the boulder such that the impact face of the ram was approximately 90° to the centerline of the boulder. Figure 4-51 shows ABG-01 as installed prior to MFT-2. The alignment of the boulder and impact sled is shown in Figure 4-52 and Table 4–3.

Figure 4-51. Pre-test condition of ABG-01 in MFT-2

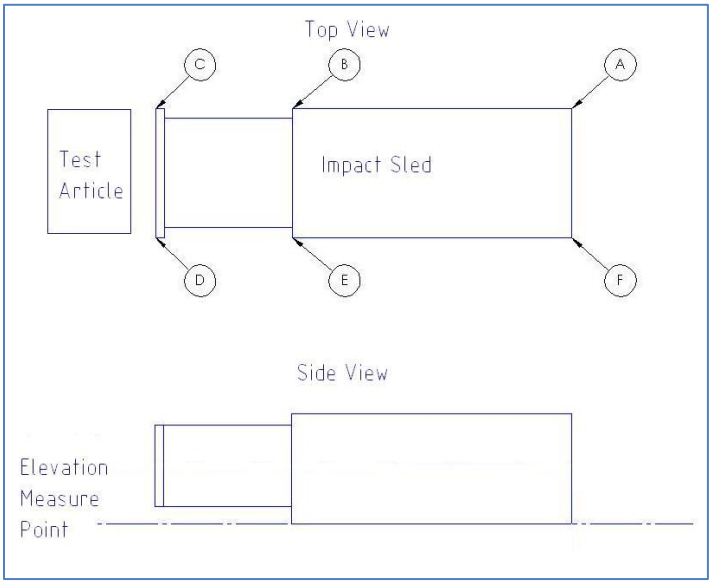

Figure 4-52. Reference for impact sled orientation in MFT-1 and MFT-2

Table 4–3. Impact sled orientation (positive indicates corner extends out past test article)

Corner A Elevation from Ground	1.918 m
Corner B Elevation from Ground	1.981 m
Corner C Distance from Edge of Test Article	-0.216 m
Corner D Distance from Edge of Test Article	+0.127 m
Corner E Elevation from Ground	2.032 m
Corner F Elevation from Ground	2.007 m

Based on the measurements in Table 4–3, the centerline of the impact sled impacted the test article 0.172 m to the left of the center of the front vertical face of ABG-01.

The impact sled fist contacted the test article with the ram face flush against the test article. The impact sled then rebounded from the test article, rotating and translating in the opposite direction of initial impact. The impact sled then contacted the test article again, but at a reduced velocity. The impact sled contacted and rebounded several times until all of the energy from the test had been transferred. Still images extracted from the high-speed video data showing a chronological sequence of the impact are given in Figure 4-53 and Figure 4-54 for the side views of MFT-1 and MFT-2 respectively.

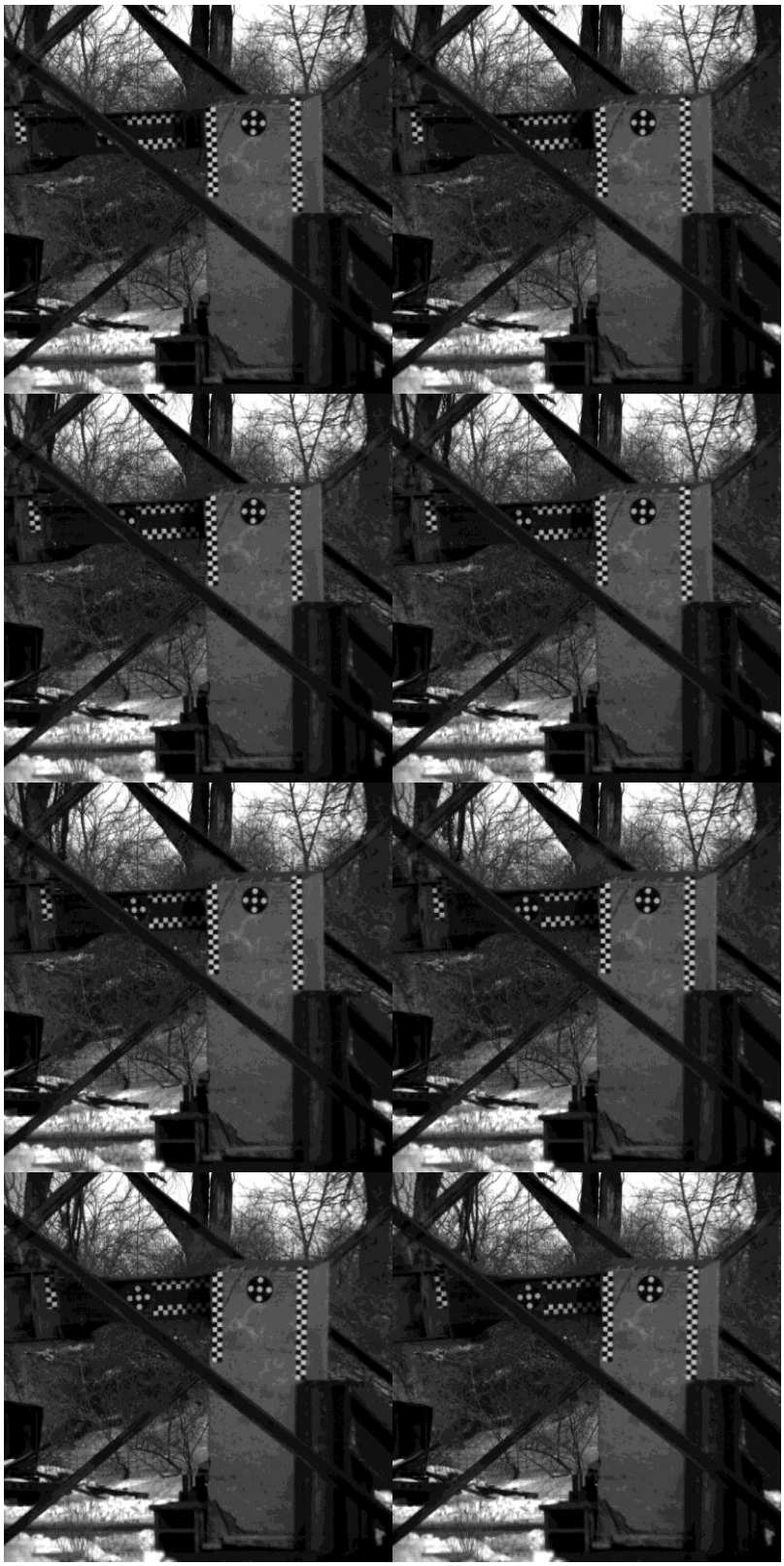

Figure 4-53. Sequence of high-speed images from MFT-1

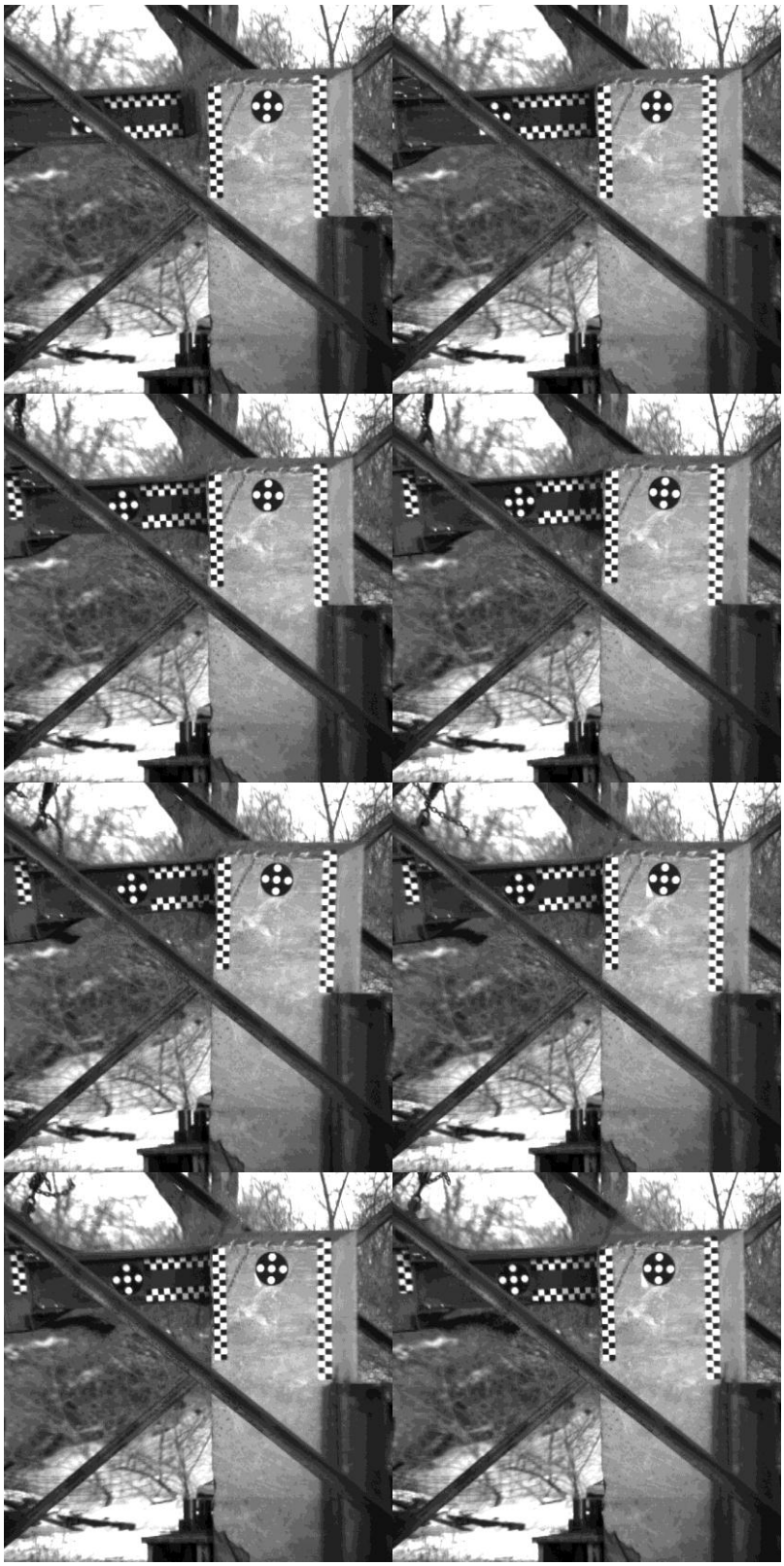

Figure 4-54. Sequence of high-speed images from MFT-2

Photographs of the post-test condition and location of ABG-01 after MFT-1 are shown in Figure 4-55, and Figure 4-56 shows the post-test condition of the impact sled after MFT-1. Photographs of the post-test condition and location of ABG-01 after MFT-2 are shown in Figure 4-57, and Figure 4-58 shows the post-test condition of the impact sled after MFT-2.

Figure 4-55. Post-test condition of ABG-01 after MFT-1

Figure 4-56. Post-test condition of impact sled after MFT-1

Figure 4-57. Post-test condition of ABG-01 after MFT-2

Figure 4-58. Post-test condition of impact sled after MFT-2

4.5 Comparison of low-order model simulation to past full scale crash data

The full scale low-order simulations are performed by first parameterizing a typical medium-duty sized truck in terms of an equivalent spring and damper constant, and then using those results in addition to the remaining crash parameters within the low-order model. The equivalent spring and damper values for the low-order vehicle are found using the methodology presented in [2]. A LS-DYNA™ finite element simulation was performed by Larson Institute

personnel for a medium-duty sized truck traveling at 13.4 m/s impacting a rigid wall. The results of the LS-DNYA truck-wall impact are shown in a chronological sequence in Figure 4-59, and the displacement of the LS-DYNA™ truck is shown in Figure 4-60.

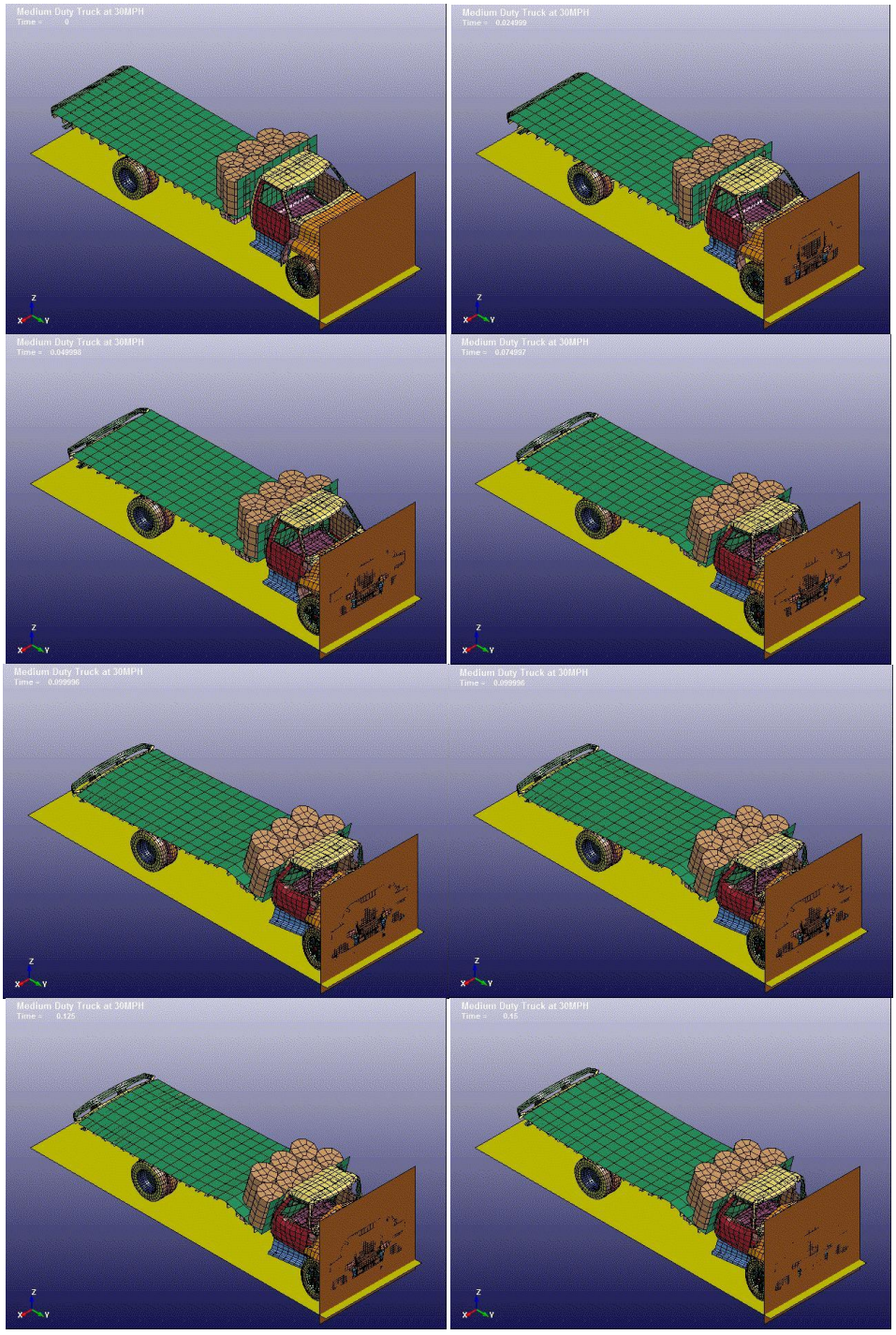

Figure 4-59. Finite Element LS-DYNA™ simulation of an M30 impact with a rigid wall

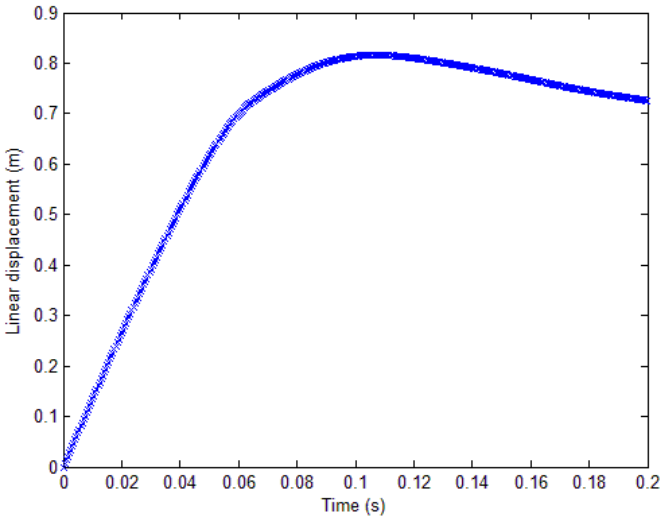

Figure 4-60. Longitudinal displacement of the medium-duty truck in the LS-DYNA™ simulation

The fit of (3.58) to the data in Figure 4-60 results in the equivalent spring and damper values of the low-order vehicle to be 3,103.3 kN/m and 138.91 kN-s/m respectively. The lumped-parameter Maxwell model simulation of an M30 impact on a rigid wall using the aforementioned spring and damper values is shown in Figure 4-61.

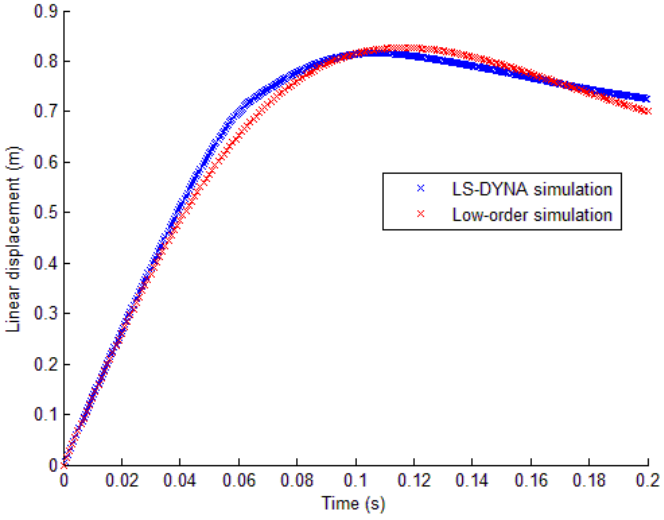

Figure 4-61. Comparison of LS-DYNA™ simulation to lumped-parameter Maxwell model

The measured displacement of the boulder in the full scale crash tests was made with respect to the center of mass of the boulder whereas the simulations are with respect to the center of mass of the boulder-soil subsystem. Since the boulder is treated as a rigid body, the displacement of the center of mass of the boulder, $x_b{}'$, is related to the displacement of the assumed center of mass of the boulder-soil subsystem, x_b, using

$$x_b{}' = x_b + R_b{}' \cos(\gamma_b{}' - \theta_b) \tag{4.1}$$

where $R_b{}'$ is the radial distance from the center of mass of the boulder-soil subsystem to the center of mass of the boulder and $\gamma_b{}'$ is the angle measured from the positive X direction as defined in Section 3.2 to the center of mass of the boulder. The radial distance from the center of mass of the boulder-soil subsystem to the center of mass of the boulder, $R_b{}'$, and the angle measured from the positive X direction as defined in Section 3.2 to the center of mass of the boulder, $\gamma_b{}'$, are found using

$$R_b{}' = \sqrt{\left(c_x - \left(\frac{L}{2}\right)\right)^2 + \left(c_y - \left(\frac{H}{2}\right)\right)^2} \tag{4.2}$$

$$\gamma_b{}' = \tan^{-1}\left(\frac{\left(c_x - \left(\frac{L}{2}\right)\right)}{\left(c_y - \left(\frac{H}{2}\right)\right)}\right) + \frac{\pi}{2}. \tag{4.3}$$

Since the boulder is treated as a rigid body, the measured angle of rotation of the boulder in a full scale crash test is directly comparable to the simulated angle of rotation of the boulder-soil subsystem. The number of soil elements within the low-order model, N, was increased until the model converged between simulations of the same parameters. All full scale crash test

simulations use 5,000 soil elements. Table 4–4 summarizes the remaining low-order model parameters not shown in either Table 4–1 or Table 4–2

Table 4–4. Additional low-order model parameters for BST-1 and BST-2

$k_v = 3{,}103.3\ \mathrm{kN/m}$	$c_v = 138.91\ \mathrm{kN \cdot s/m}$	$N = 5{,}000$

The simulations for BST-1 and BST-2 are performed using a constant of horizontal subgrade reaction of 95 MN/m^3 which correlates to approximately 94% maximum density of the soil. A constant of horizontal subgrade reaction of 95 MN/m^3 is the approximate mean of the minimum constant of horizontal subgrade reaction as per minimum compaction level specified by ASTM F2656-07 and the maximum constant of horizontal subgrade reaction as calculated using (3.75).

4.5.5 Comparison of full scale low-order simulation to BST-1

Figure 4-62, Figure 4-63, and Figure 4-64 show the comparison of the measured crash test results from BST-1 to the simulated low-order results using the parameters listed in Table 4–1 and Table 4–4. Figure 4-62 shows the comparison of the linear displacement of the center of mass of the boulder, Figure 4-63 shows the comparison of the angle of rotation of the boulder, and Figure 4-64 shows the comparison of the linear displacement of the impact vehicle.

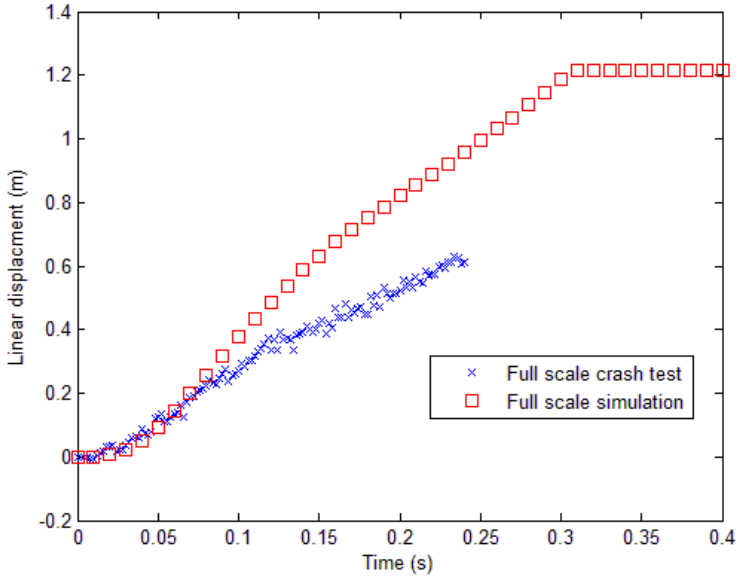

Figure 4-62. Comparison of the measured and simulated displacement of the center of mass of ABG-01 in BST-1

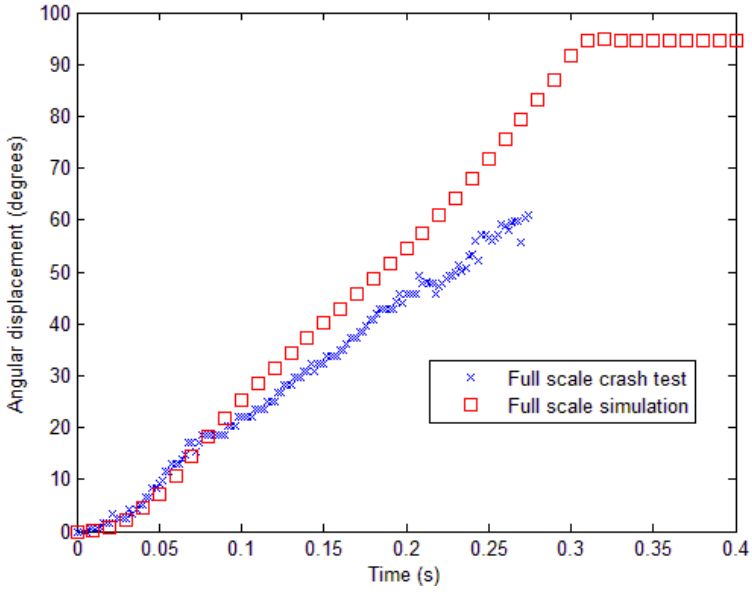

Figure 4-63. Comparison of the measured and simulated angle of rotation of ABG-01 in BST-1

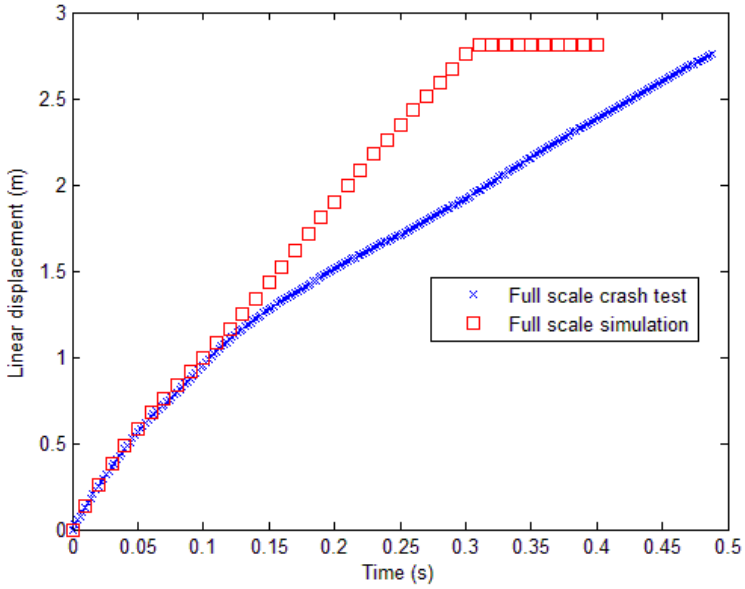

Figure 4-64. Comparison of the measured and simulated displacement of the vehicle in BST-1

As seen in Figure 4-62 – Figure 4-64 the model loses fidelity after approximately 0.1 seconds from impact which corresponds to roughly 20° of rotation of the boulder.

4.5.6 Comparison of full scale low-order simulation to BST-2

Figure 4-65, Figure 4-66, and Figure 4-67 show the comparison of the measured crash test results from BST-2 to the simulated low-order results using the parameters listed in Table 4–2 and Table 4–4. Figure 4-65 shows the comparison of the linear displacement of the center of mass of the boulder, Figure 4-66 shows the comparison of the angle of rotation of the boulder, and Figure 4-67 shows the comparison of the linear displacement of the impact vehicle.

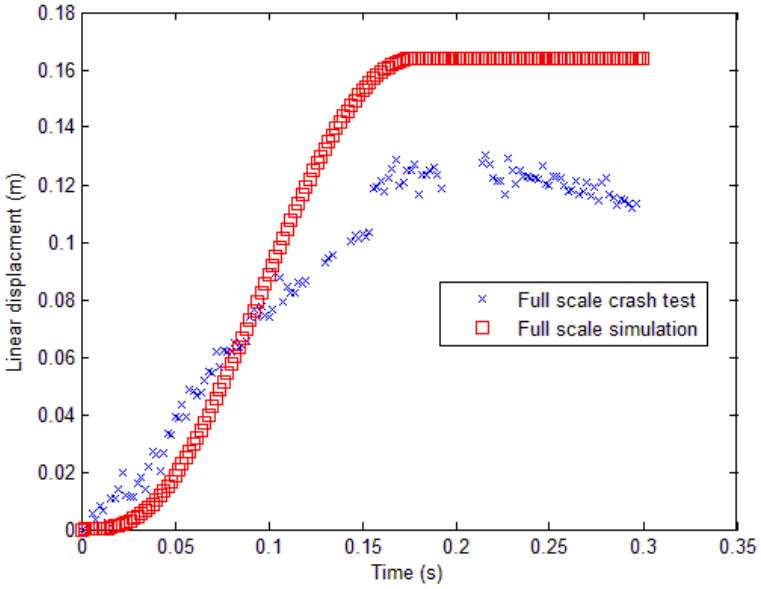

Figure 4-65. Comparison of the measured and simulated displacement of the center of mass of RWG-01 in BST-2

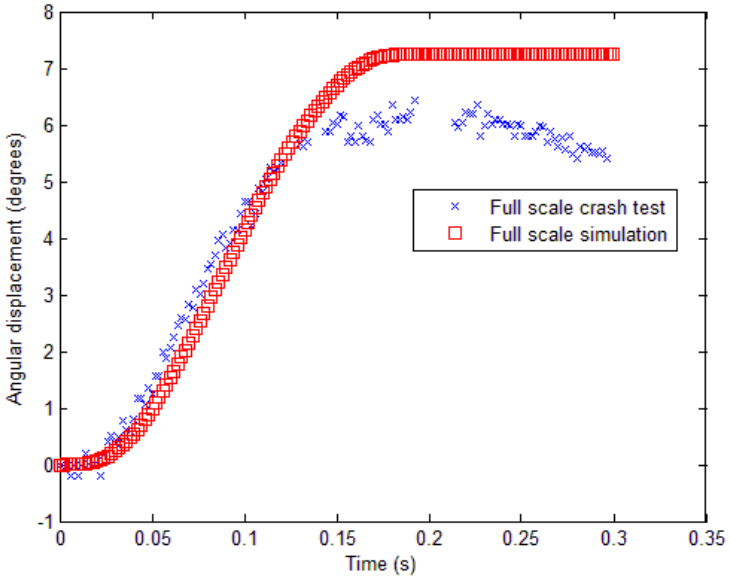

Figure 4-66. Comparison of the measured and simulated angle of rotation of RWG-01 in BST-2

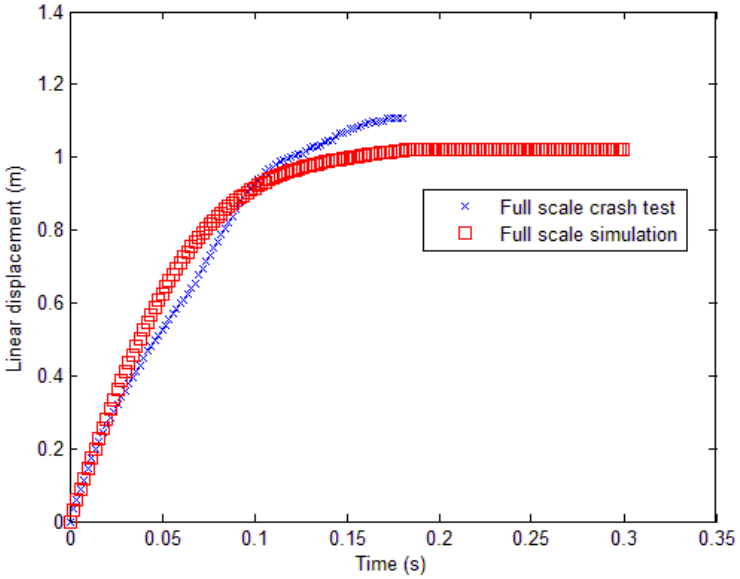

Figure 4-67. Comparison of the measured and simulated displacement of the vehicle in BST-2

Similar to the simulated results from BST-1, the low-order model predicts the motion of the crash test within reason for angular displacement of less than 20° of the bolder. As presented in Chapter 7, the low-order can be used in selecting the dimensions for a boulder based on angular displacement of less than 20°.

4.6 Comparison of static fracture predictions to full scale fracture tests

The full scale fracture predictions are made using the methodology presented in Section 3.3. The peak deceleration used in the fracture prediction was found to be 100 G's from the LS-DYNA™ finite element simulation of the M30 rigid-wall impact presented in Section 4.4. The rock properties used in the fracture prediction are shown in Table 4–5. The material properties for the granite were obtained by LTI personnel following procedures outlined by the International Society of Rock Mechanics [26] [27].

Table 4–5. Material properties for select boulder types

	Compressive Strength	Tensile Strength
American Black granite	182.02 MPa	31.9 MPa

The factors of safety and corresponding pass/fail contour plots for various granite geometries were obtained using MATLAB® iterations through various boulder geometries. The eccentricity of the applied point load was fixed at 0.75 meters of cantilever, as this is the typical value for the equivalent point load as determined in Chapter 3.

The factor of safety is defined in terms of maximum fracture stress in comparison to the stress needed to fracture for the given geometry. Factors of safety less than one indicate fracture. Figure 4-68 estimates minimum pass/fail requirements for boulders based on infinite soil stiffness, boulder geometries, and boulder material properties of American Black granite. The contour plots are interpreted such that areas shaded in black indicate estimated areas of fracture-type failure and gray indicates estimated areas where fracture will not occur. As presented in Chapter 3, it is assumed that the boulder is impacted parallel to the length dimension, or from left to right.

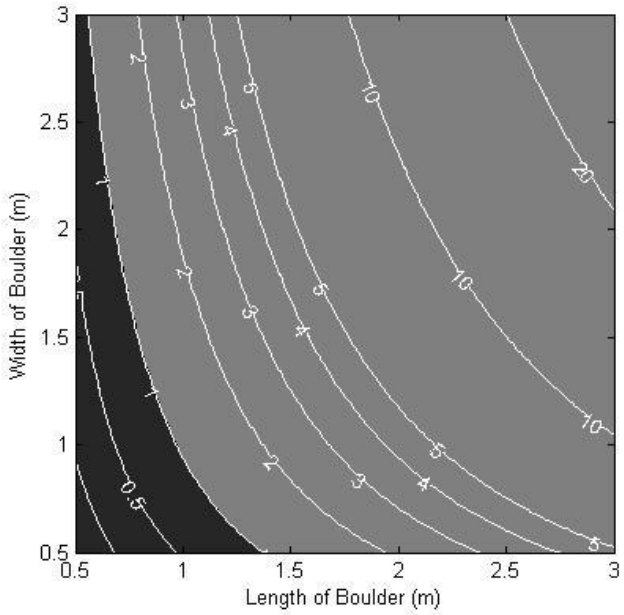

Figure 4-68. Factors of safety for an M30 impact on a rigidly-fixed American Black Granite boulder as determined from static fracture prediction with respect to impact direction

The calculations for estimating fracture failure were compared to past crash tests in which the boulders fractured due to rigid embedment conditions. The full scale fracture results from BFT-1 and BFT-2 are compared to the estimated fracture geometries in Figure 4-69. The contour plot below shows the results of the full scale fracture tests overlaid onto the predicted regions of fracture from Figure 4-68.

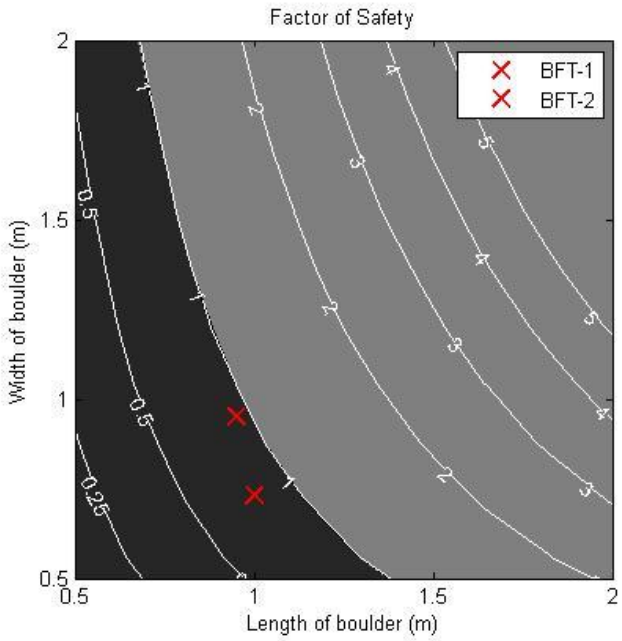

Figure 4-69. Comparison of static fracture prediction to BFT-1 and BFT-2

As shown in Figure 4-69, the static fracture prediction methodology accurately predicts fracture for both BFT-1 and BFT-2. It should be noted that both BFT-1 and BFT-2 lie near the pass/fail line of a factor of safety equal to 1. As shown in Figure 4-39 and Figure 4-48, the post impact speed of the vehicle severely reduced which indicates that a slight increase in boulder dimensions could result in no boulder fracture. It should also be noted that the approach speed in both fracture tests was above the 13.4 m/s from which the static fracture contour plots was derived, which further adds to the plausibility of the static fracture prediction methodology. As presented in Chapter 7, Figure 4-68 and the static fracture prediction methodology can be used in selecting the minimum dimensions for a boulder based on failure in the form of fracture.

4.7 Comparison of static fracture prediction against medium scale fracture tests

This section presents the comparison of past medium scale fracture tests to the predicted fracture mechanics presented in Section 3.3. The medium scale fracture tests consist of a 2227 kg impact pendulum and rigid mounting hardware.

The force acting on the boulder is found by applying acceleration analysis to the global displacements of the impact sled obtained using Photron Motion Tools. The position of the impact sled was filtered using a 2nd order low-pass Butterworth filter with a cutoff frequency of 115 Hz. The pendulum is treated as a point mass that is restricted to 1-D motion since the impact sled is supported by flexible cables and the motion in the Y direction at the time of impact is negligible. The velocity and the acceleration of the impact sled were calculated by taking the time derivatives of the position. The maximum accelerations for MFT-1 and MFT-2 were found to be 163.3 G and 127.5 G, respectively.

Using Newton's 2nd law, the force acting on the impact sled is found by multiplying the acceleration of the impact sled by the mass of the sled. By Newton's 3rd law, the force acting on the sled also represents the force acting on the boulder. The measured force acting on the boulders is then be correlated to the factor of safety using the methodology proposed in Section 3.3 where the eccentricity of the impact was measured to be 0.68 meters. Table 4–6 lists the measured and calculated data with respect to MFT-1 and MFT-2 along with the resulting factors of safety. Additionally, the maximum calculated force form MFT-1 and MFT-2 is correlated to an equivalent maximum acceleration for a 6,800 kg medium-duty sized truck as used in full scale crash tests. Again using Newton's 2nd law, the equivalent accelerations of the 6,800 kg vehicle are found using

$$a_{vehicle} = \frac{m_{sled} a_{sled}}{m_{vehicle}}, \tag{4.4}$$

where $a_{vehicle}$ and a_{sled} are the acceleration of the vehicle and sled and $m_{vehicle}$ and m_{sled} are the mass of the vehicle and sled.

Table 4–6. Medium scale fracture test results for MFT-1 and MFT-2

	MFT-1	MFT-2
Maximum impact sled acceleration	163.3 G	127.5 G
Equivalent vehicle maximum acceleration	53.5 G	41.8 G
Factor of safety calculated using the vehicle maximum acceleration	1.17	1.5

The factors of safety confirm that the boulders should not have fractured upon impact of the sled as predicted using the maximum static fracture force methodology presented in Section 3.3.

4.8 Contributions of this chapter

The contributions of this chapter are as follows:

(1) Present the test equipment and procedure associated with full scale crash and fracture tests

(2) Present the test equipment and procedure associated with medium scale fracture tests

(3) Present a summary of past full scale crash tests, medium scale fracture tests, and results

(4) Compare the simulated low-order model to the full scale crash test results

(5) Compare the fracture predictions to full and medium scale fracture test results

CHAPTER 5

DIMENSIONAL ANALYSIS THEORY AND METHODS

The intent of this chapter is to present the application of dimensional analysis to the low-order model presented in Chapter 3 in order to develop dimensionless equations of motion and scaling laws. Similar to [13], the DEOM allow for direct comparison of boulder and vehicle motion in small scale experiments and simulations to the boulder and vehicle motion in full scale experiments and simulations. The Buckingham Π Theorem states that each of the small scale dimensionless parameters, often represented as the Greek letter π, must be equal to the respective full scale dimensionless π parameters in order to achieve full similitude. The dimensionless π parameters are used to create scaling relationships between small scale and full scale experiments as well as dimensionless equations of motion.

This chapter is organized as follows:

The relevant variables from the low-order model are listed in Section 5.1, and the repeating parameters are then selected from the relevant model variables in accordance with the Buckingham Π Theorem in Section 5.2. Dimensionless π groupings are presented using the repeating parameters and remaining non-repeating parameters in Section 5.3. The dimensionless π groupings are then used to create dimensionless equations of motion for the low-order model which can be used to simulate all variations of input parameters in Section 5.4. The procedure for simulating the dimensionless equations of motion is presented in Section 5.5. Finally, scaling laws between full scale and small scale testing will be presented based on the dimensionless π groupings in Section 5.6.

5.1 Governing low-order model variables

Buckingham's Π Theorem does not require knowledge of the governing equations for a system creating small scale tests, rather, only that the significant parameters need to be known. It is advantageous, however, to know the governing equations, as this will simplify the identification of significant parameters.

Using the low-order model as a guideline, Table 5–1 shows the significant parameters as pertaining to a vehicle impact upon a soil-fixed boulder. For the purposes of analysis, terms that are already dimensionless – angles, friction coefficients, etc. – can be ignored as the terms will appear in identical form between experiments in full similitude. Inherently dimensionless parameters must match between small and full scale experiments as there is no scaling parameter associated with inherently dimensionless parameters. The base dimensions associated with the low-order model in Chapter 3 are mass (m), length (l), and time (s).

Table 5–1. Significant parameters found in the low-order model

Variable	Symbol	Dimension	Classification
Gravitational acceleration	g	$l \cdot s^{-2}$	Input
Mass density of the soil	ρ_{soil}	$m \cdot l^{-3}$	Input
Constant of horizontal subgrade reaction of the soil	β	$m \cdot l^{-2} \cdot s^{-2}$	Input
Mass density of the boulder	ρ_b	$m \cdot l^{-3}$	Input
Length of the boulder	L	l	Input
Width of the boulder	W	l	Input
Height of the boulder	H	l	Input
Embedment depth of the boulder	d	l	Input
Linear displacement of the boulder	x_b	l	Output
Linear velocity of the boulder	$\dot{x}_b$	$l \cdot s^{-1}$	Output
Linear acceleration of the boulder	$\ddot{x}_b$	$l \cdot s^{-2}$	Output
Angular velocity of the boulder	$\dot{\theta}_b$	s^{-1}	Output
Angular acceleration of the boulder	$\ddot{\theta}_b$	s^{-2}	Output
Mass of the vehicle	m_v	m	Input
Linear displacement of the vehicle	x_v	l	Output
Initial linear velocity of the vehicle	v_o	$l \cdot s^{-1}$	Input
Linear velocity of the vehicle	$\dot{x}_v$	$l \cdot s^{-1}$	Output
Linear acceleration of the vehicle	$\ddot{x}_v$	$l \cdot s^{-2}$	Output
Linear jerk of the vehicle	$\dddot{x}_v$	$l \cdot s^{-3}$	Output
Damping constant of the vehicle	c_v	$m \cdot s^{-1}$	Input
Spring constant of the vehicle	k_v	$m \cdot s^{-2}$	Input
Eccentricity of vehicle applied load	e	l	Input
Time	t	s	Output
Height of soil element	$h_{element}$	l	Input

5.2 Selection of repeating parameters

As seen in Table 5–1, there are 26 total variables and three basic unit dimensions: mass (m), length (l), and time (s). According to the Buckingham Π Theorem, the number of independent dimensionless variable grouping is found using

$$N_\pi = N_v - N_{bd} \tag{5.1}$$

where N_π is the number of independent dimensionless groupings, N_v is the total number of variables found in Table 5–1, and N_{bd} is the number of base dimensions found in Table 5–1. Applying (5.1) to the parameters listed in Table 5–1 yields 23 independent dimensionless variable groupings and 3 repeating parameters.

One criterion for repeating parameter selection arises from the inherent nature of the repeating parameters needing to span the dimensions of all the variables. As seen in Table 5–1, however, there are a limited number of variables that include the time dimension and fewer which are considered inputs into the low-order model. The time dependent input parameters in Table 5–1 are the initial velocity of the vehicle, v_o, the gravitational constant, g, the constant of horizontal subgrade reaction of the soil, β, and the equivalent damping and spring constants, c_v and k_v.

A somewhat intuitive approach in satisfying the aforementioned time dimension criterion is to select the gravitational constant as the first repeating parameter since it is expected to remain constant between full scale and small scale testing. The remaining two repeating parameters are then selected such that the rank of the dimensional matrix, shown in Table 5–2, is equal to the number of base dimensions, N_{bd}.

Table 5–2. Example of a dimensional matrix for determining span of variables

	m_v	v_o	g
$length$	0	1	1
$mass$	1	0	0
$time$	0	-1	-2

Following the aforementioned selection criteria, the mass of the vehicle and initial velocity of the vehicle are chosen as the remaining two parameters since the combination of m_v, v_o, and g span the base dimensions found in the low-order model, and both m_v and v_o are driving factors in the model simulation.

5.3 Grouping of dimensionless π parameters

A manual approach is typically used in calculating the π parameters in dimensional analysis, but the manual approach is often very tedious and time consuming. A more methodical approach is offered through the use of matrix mathematics which can be used to rapidly determine the π parameters [28]. Following the methodology presented in [28], the repeating parameters, m_v, v_o, and g, are placed in the $A_{\mathbb{D}}$ submatrix of the dimensional matrix $\mathbb{D}$, shown in Figure 5-1. The remaining non-repeating parameters are then placed in the $B_{\mathbb{D}}$ submatrix, and the E^T submatrix is set as unity. The dimensional set is then formed using

$$\left(-{A_{\mathbb{D}}}^{-1} \cdot B_{\mathbb{D}} \cdot E + {A_{\mathbb{D}}}^{-1} \cdot q\right)^T, \tag{5.2}$$

where q is set to a zero vector. The variable q is set to a zero vector because there is no change in dimensional basis [28].

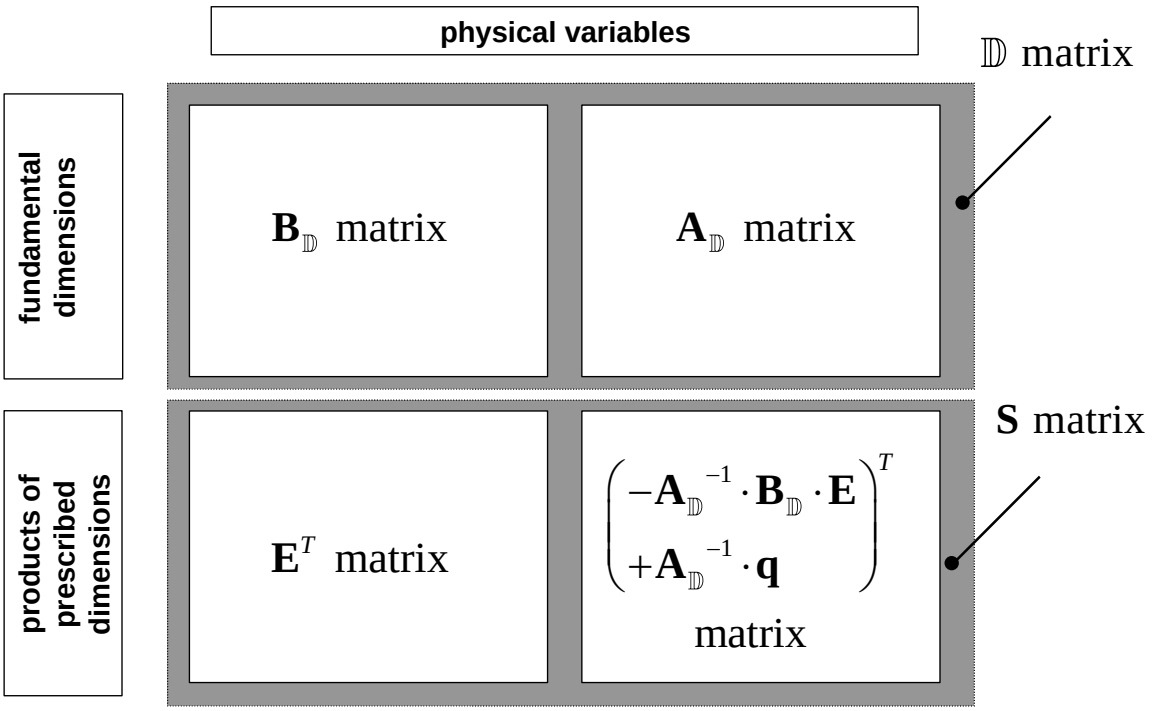

Figure 5-1. Dimensional Matrix [28]

A dimensional set is presented in which the types of variables, such as linear position or acceleration, are used in (5.2) instead of the variables found in Table 5–1. For example, linear velocity will be presented instead of listing both the linear velocity of the boulder and the linear velocity of the vehicle. Both the linear velocity of the boulder and vehicle will have the same scaling factor since they both have the same dimensions. Table 5–3 shows the variations of variables found in the low-order model. The results from applying (5.2) to the parameters listed in Table 5–3 are shown in Table 5–4.

Table 5–3. Types of variables found in the low-order model

Variable	Symbol	Dimension
Mass density	ρ^*	$m \cdot l^{-3}$
Constant of horizontal subgrade reaction	β^*	$m \cdot l^{-2} \cdot s^{-2}$
Length	L^*	l
Linear velocity	v^*	$l \cdot s^{-1}$
Linear acceleration	a^*	$l \cdot s^{-2}$
Linear jerk	j^*	$l \cdot s^{-3}$
Angular velocity	ω^*	s^{-1}
Angular acceleration	α^*	s^{-2}
Damping constant	c^*	$m \cdot s^{-1}$
Spring constant	k^*	$m \cdot s^{-2}$
Time	t^*	s

Table 5–4. Dimensionless groupings associated with (5.2) and Table 5–3

	ρ^*	β^*	L^*	v^*	a^*	j^*	ω^*	α^*	c^*	k^*	t^*	m_v	v_o	g	
$length$	-3	-2	1	1	1	1	0	0	0	0	0	0	1	1	
$mass$	1	1	0	0	0	0	0	0	1	1	0	1	0	0	
$time$	0	-2	0	-1	-2	-3	-1	-2	-1	-2	1	0	-1	-2	
π_{ρ^*}	1	0	0	0	0	0	0	0	0	0	0	-1	6	-3	π_{ρ^*}
π_{β^*}	0	1	0	0	0	0	0	0	0	0	0	-1	6	-4	π_{β^*}
π_{L^*}	0	0	1	0	0	0	0	0	0	0	0	0	-2	1	π_{L^*}
π_{v^*}	0	0	0	1	0	0	0	0	0	0	0	0	-1	0	π_{v^*}
π_{a^*}	0	0	0	0	1	0	0	0	0	0	0	0	0	-1	π_{a^*}
π_{j^*}	0	0	0	0	0	1	0	0	0	0	0	0	1	-2	π_{j^*}
π_{ω^*}	0	0	0	0	0	0	1	0	0	0	0	0	1	-1	π_{ω^*}
π_{α^*}	0	0	0	0	0	0	0	1	0	0	0	0	2	-2	π_{α^*}
π_{c^*}	0	0	0	0	0	0	0	0	1	0	0	-1	1	-1	π_{c^*}
π_{k^*}	0	0	0	0	0	0	0	0	0	1	0	-1	2	-2	π_{k^*}
π_{t^*}	0	0	0	0	0	0	0	0	0	0	1	0	-1	1	π_{t^*}

The resulting dimensionless groupings for each variable type shown in Table 5–4 are given in Table 5–5.

Table 5–5. Dimensionless parameters for variable types

$$\pi_{\rho^*} = \frac{\rho^* \cdot {v_o}^6}{m_v\, g^3} \quad (5.3) \qquad \pi_{j^*} = \frac{j^* \cdot v_o}{g^2} \quad (5.4)$$

$$\pi_{\beta^*} = \frac{\beta^* \cdot {v_o}^6}{m_v\, g^4} \quad (5.5) \qquad \pi_{\omega^*} = \frac{\omega^* \cdot v_o}{g} \quad (5.6)$$

$$\pi_{L^*} = \frac{L^* \cdot g}{{v_o}^2} \quad (5.7) \qquad \pi_{\alpha^*} = \frac{\alpha^* \cdot {v_o}^2}{g^2} \quad (5.8)$$

$$\pi_{v^*} = \frac{v^*}{v_o} \quad (5.9) \qquad \pi_{c^*} = \frac{c^* \cdot v_o}{m_v\, g} \quad (5.10)$$

$$\pi_{a^*} = \frac{a^*}{g} \quad (5.11) \qquad \pi_{k^*} = \frac{k^* \cdot {v_o}^2}{m_v\, g^2} \quad (5.13)$$

$$\pi_{t^*} = \frac{t^* \cdot g}{v_o} \quad (5.12)$$

The dimensionless parameters associated with the variables in Table 5–1 are simply found by replacing the starred variables in Table 5–5 with the corresponding variable from Table 5–1. Returning to the velocity example described earlier in this section, the dimensionless parameter associated with linear velocity of the boulder is found by simply replacing v^* with $\dot{x}_b$ in (5.9). Similarly the dimensionless parameter associated with the linear velocity of the vehicle is formed by replacing v^* with $\dot{x}_v$ in (5.9). Thus, the dimensionless π groupings associated with the salient parameters in the low-order model are found by performing the aforementioned substitution method for the remaining variables in Table 5–1. The results of the substitutions are shown in Table 5–6.

Table 5–6 Dimensionless π groupings for the low-order model

$\pi_{\rho_{soil}} = \frac{\rho_{soil} \cdot {v_o}^6}{m_v \, g^3}$ (5.14)	$\pi_{x_b} = \frac{x_b \cdot g}{{v_o}^2}$ (5.15)	$\pi_{\ddot{x}_v} = \frac{\ddot{x}_v}{g}$ (5.16)
$\pi_{\beta} = \frac{\beta \cdot {v_o}^6}{m_v \, g^4}$ (5.17)	$\pi_{\dot{x}_b} = \frac{\dot{x}_b}{v_o}$ (5.18)	$\pi_{\ddot{x}_v} = \frac{\ddot{x}_v \cdot v_o}{g^2}$ (5.19)
$\pi_{\rho_b} = \frac{\rho_b \cdot {v_o}^6}{m_v \, g^3}$ (5.20)	$\pi_{\ddot{x}_b} = \frac{\ddot{x}_b}{g}$ (5.21)	$\pi_{c_v} = \frac{c_v \cdot v_o}{m_v \, g}$ (5.22)
$\pi_L = \frac{L \cdot g}{{v_o}^2}$ (5.23)	$\pi_{\dot{\theta}_b} = \frac{\dot{\theta}_b \cdot v_o}{g}$ (5.24)	$\pi_{k_v} = \frac{k_v \cdot {v_o}^2}{m_v \, g^2}$ (5.25)
$\pi_W = \frac{W \cdot g}{{v_o}^2}$ (5.26)	$\pi_{\ddot{\theta}_b} = \frac{\ddot{\theta}_b \cdot {v_o}^2}{g^2}$ (5.27)	$\pi_e = \frac{e \cdot g}{{v_o}^2}$ (5.28)
$\pi_H = \frac{H \cdot g}{{v_o}^2}$ (5.29)	$\pi_{x_v} = \frac{x_v \cdot g}{{v_o}^2}$ (5.30)	$\pi_t = \frac{t \cdot g}{v_o}$ (5.31)
$\pi_d = \frac{d \cdot g}{{v_o}^2}$ (5.32)	$\pi_{\dot{x}_v} = \frac{\dot{x}_v}{v_o}$ (5.33)	$\pi_{h_e} = \frac{h_e \cdot g}{{v_o}^2}$ (5.34)

Solving (5.14) - (5.40) for the parameters listed in Table 5–1 results in Table 5–7.

Table 5–7. Low-order model parameters as a function of the π groupings in Table 5–6

$\rho_{soil} = \frac{\pi_{\rho_{soil}} m_v\, g^3}{{v_o}^6}$ (5.35)	$x_b = \frac{\pi_{x_b} {v_o}^2}{g}$ (5.36)	$\ddot{x}_v = \pi_{\ddot{x}_v} g$ (5.37)
$\beta = \frac{\pi_\beta m_v\, g^4}{{v_o}^6}$ (5.38)	$\dot{x}_b = \pi_{\dot{x}_b} v_o$ (5.39)	$\ddot{\bar{x}}_v = \frac{\pi_{\ddot{\bar{x}}_v} g^2}{v_o}$ (5.40)
$\rho_b = \frac{\pi_{\rho_b} m_v\, g^3}{{v_o}^6}$ (5.41)	$\ddot{x}_b = \pi_{\ddot{x}_b} g$ (5.42)	$c_v = \frac{\pi_{c_v} m_v\, g}{v_o}$ (5.43)
$L = \frac{\pi_L {v_o}^2}{g}$ (5.44)	$\dot{\theta}_b = \frac{\pi_{\dot{\theta}_b} g}{v_o}$ (5.45)	$k_v = \frac{\pi_{k_v} m_v\, g^2}{{v_o}^2}$ (5.46)
$W = \frac{\pi_W {v_o}^2}{g}$ (5.47)	$\ddot{\theta}_b = \frac{\pi_{\ddot{\theta}_b} g^2}{{v_o}^2}$ (5.48)	$e = \frac{\pi_e {v_o}^2}{g}$ (5.49)
$H = \frac{\pi_H {v_o}^2}{g}$ (5.50)	$x_v = \frac{\pi_{x_v} {v_o}^2}{g}$ (5.51)	$t = \frac{\pi_t v_o}{g}$ (5.52)
$d = \frac{\pi_d {v_o}^2}{g}$ (5.53)	$\dot{x}_v = \pi_{\dot{x}_v} v_o$ (5.54)	$h_e = \frac{\pi_{h_e} {v_o}^2}{g}$ (5.55)

5.4 Creation of dimensionless equations of motion

The main goal of this thesis is to develop dimensionless equations of motion which can be used to simulate and predict the motion of various parameters associated with vehicle impacts upon a soil-fixed boulder in cohesionless soil. The dimensionless equations of motion are presented following the methodology in [28]. The governing dimensionless equations of motion are formed by representing (3.10), (3.11), and (3.54) in terms of the dimensionless π parameters,

the repeating parameters, and the non-repeating parameters found in Table 5–1 and then simplifying.

It is beneficial at this point to dissect the governing equations of motion into individual components which will be reassembled into the dimensionless equations of motion. The dimensionless equation of motion for the vehicle is presented in Section 5.4.1. The dimensionless equation of motion for the boulder-soil subsystem in the X direction is presented in Section 5.4.2. Lastly, the dimensionless equation of motion for the rotation of the boulder-soil subsystem about the Z axis is presented Section 5.4.3.

5.4.1 Dimensionless equation of motion for the vehicle

The governing dimensionless equation of motion for the vehicle is formed by expressing (3.54) in terms of dimensionless π groupings and repeating parameters found in Table 5–7. It is advantageous to represent the various variables found in (3.54) through the use of intermediate dimensionless π groupings as a means of general housekeeping. The mass of the boulder is expressed in terms of the dimensionless π groupings and repeating parameters by substituting (5.41), (5.44), (5.47), and (5.50) into (3.14), which results in

$$m_b = \frac{\pi_{\rho_b} m_v \, g^3}{{v_o}^6} \cdot \frac{\pi_L {v_o}^2}{g} \cdot \frac{\pi_W {v_o}^2}{g} \cdot \frac{\pi_H {v_o}^2}{g}. \tag{5.56}$$

Combining like terms in (5.56) and simplifying yields

$$m_b = m_v \pi_{m_b} = m_v \pi_{\rho_b} \pi_L \pi_W \pi_H, \tag{5.57}$$

where π_{m_b} is the resulting intermediate dimensionless π grouping as pertaining to the mass of the boulder. Similarly, the mass of the lumped soil against the boulder is formed by substituting (5.35), (5.47), (5.53), and (5.55) directly into (3.2) and simplifying, which results in

$$m_n = m_v \pi_{m_n} = m_v \pi_{\rho_{soil}} \pi_W \pi_{h_e} \tan(\theta_w) \left(\left[\pi_d - n\pi_{h_e} \right] + \frac{1}{2} \pi_{h_e} \right), \tag{5.58}$$

where π_{m_n} is the resulting intermediate dimensionless π grouping as pertaining to the lumped soil masses against the boulder. The center of mass for the boulder-soil system, as measured with respect to the local origin in the X direction, is expressed in terms of the dimensionless π groupings and repeating parameters by substituting (5.44), (5.57), and (5.58) into (3.3) and simplifying, which yields

$$c_x = \frac{\pi_{c_x} {v_o}^2}{g} = \frac{\pi_L {v_o}^2}{g} \frac{\left[\sum_{n=1}^{N} \{\pi_{m_n}\} + \pi_{m_b} \frac{1}{2} \right]}{\sum_{n=1}^{N} \{\pi_{m_n}\} + \pi_{m_b}}, \tag{5.59}$$

where π_{c_x} is the intermediate dimensionless π grouping for the center of mass for the boulder-soil subsystem. Substituting (5.59) and (5.53) into the definition of d_n results in

$$d_n = \frac{\pi_{d_n} {v_o}^2}{g} = range \left(\left[\frac{\pi_{c_x} {v_o}^2}{g} - \frac{\pi_L {v_o}^2}{g} \right], \quad \frac{\pi_{c_x} {v_o}^2}{g}, \ N \right), \tag{5.60}$$

where π_{d_n} is an intermediate dimensionless π grouping associated with the depth of each soil element relative to the center of mass for the soil-boulder subsystem.

In order to rewrite the displacement of the contact point between the vehicle and the boulder, R_v and γ_v are expressed in terms of the dimensionless π groupings and repeating parameters by substituting (5.49), (5.59), and (5.60) with $n = 1$ into (3.5) and (3.6) and simplifying, which yields

$$\gamma_v = \gamma_v{}^* = \tan^{-1}\frac{\pi_{c_x}}{\left(\pi_L + \pi_{d_1}\right)} \tag{5.61}$$

$$R_v = \frac{\pi_{R_v} {v_o}^2}{g} = \frac{{v_o}^2}{g}\sqrt{(\pi_e + \pi_e)^2 + \left(\pi_{d_1}\right)^2}, \tag{5.62}$$

where $\gamma_v{}^*$ is the dimensionless π grouping for γ_v, and π_{R_v} is the dimensionless π grouping for the radial distance from the center of mass of the boulder-soil subsystem to the vehicle impact point. It should be noted that $\gamma_v{}^*$ requires no scaling parameters since it is already dimensionless and a function of dimensionless variables.

Finally, (3.54) is expressed in dimensionless π groupings, repeating parameters, and the non-repeating variables in Table 5–1 by substituting (5.61) and (5.62) into (3.54), which yields

$$\dddot{x}_v + \frac{k_v}{c_v}\ddot{x}_v + \frac{k_v}{m_v}\dot{x}_v = \frac{k_v}{m_v}\left[\dot{x}_b + \dot{\theta}_b\left\{\frac{\pi_{R_v} {v_o}^2}{g}\right\}\cos(\gamma_v{}^* + \theta_b)\right]. \tag{5.63}$$

The dimensionless equation of motion for the vehicle is created by substituting (5.37), (5.39), (5.40), (5.43), (5.45), (5.46), and (5.54) into (5.63) for all of the remaining non-repeating parameters forming

$$\frac{\pi_{\ddot{x}_v} g^2}{v_o} + \frac{\dfrac{\pi_{k_v} m_v\, g^2}{{v_o}^2}}{\dfrac{\pi_{c_v} m_v\, g}{v_o}}\pi_{\dot{x}_v} g + \frac{\dfrac{\pi_{k_v} m_v\, g^2}{{v_o}^2}}{m_v}\pi_{\dot{x}_v} v_o \tag{5.64}$$

$$= \frac{\dfrac{\pi_{k_v} m_v\, g^2}{{v_o}^2}}{m_v}\left[\pi_{\dot{x}_b} v_o + \frac{\pi_{\dot{\theta}_b} g}{v_o}\left\{\frac{\pi_{R_v} {v_o}^2}{g}\right\}\cos(\gamma_v{}^* + \theta_b)\right].$$

Combining like terms in (5.64) and simplifying yields

$$\frac{g^2}{v_o}\pi_{\ddot{x}_v} + \frac{g^2}{v_o}\frac{\pi_{k_v}}{\pi_{c_v}}\pi_{\dot{x}_v} + \frac{g^2}{v_o}\pi_{k_v}\pi_{\dot{x}_v} = \frac{g^2}{v_o}\pi_{k_v}\left[\pi_{\dot{x}_b} + \pi_{\dot{\theta}_b}\,\pi_{R_v}\,\cos(\gamma_v{}^* + \theta_b)\right]. \tag{5.65}$$

Dividing both sides of (5.65) by $\frac{g^2}{v_o}$ yields

$$\pi_{\ddot{x}_v} + \frac{\pi_{k_v}}{\pi_{c_v}}\pi_{\dot{x}_v} + \pi_{k_v}\pi_{\dot{x}_v} = \pi_{k_v}\left[\pi_{\dot{x}_b} + \pi_{\dot{\theta}_b}\pi_{R_v}\cos(\gamma_v{}^* + \theta_b)\right]. \tag{5.66}$$

Thus, the governing equation of motion for the vehicle is now expressed solely in dimensionless π groupings. Equation (5.66) is the governing dimensionless equation of motion for the vehicle.

5.4.2 Dimensionless equation of motion for the boulder-soil subsystem in the *X* direction

The governing dimensionless equation of motion for the boulder-soil subsystem in the *X* direction is presented in manner similar as the dimensionless equation of motion for the vehicle. The left hand side of (3.10) is expressed in dimensionless π groupings and repeating parameters through the use of an intermediate dimensionless π grouping for the effective mass of the boulder-soil subsystem. The π grouping is created for the effective mass of the boulder-soil subsystem by substituting (5.57) and (5.58) into (3.12) and simplifying, which yields

$$m_{eff} = m_v \cdot \pi_{m_{eff}} = m_v\left(\pi_{m_b} + \sum_{n=1}^{N}\{\pi_{m_n}\}\right), \tag{5.67}$$

where $\pi_{m_{eff}}$ is the resulting intermediate dimensionless π grouping as pertaining to the effective mass for the boulder-soil subsystem.

Similarly, the right hand side of (3.10) must be expressed in dimensionless π groupings and repeating parameters. The vehicle force, F_v, acting on the boulder during impact is expressed in dimensionless π groupings and repeating parameters by substituting (5.37) into (3.56), which results in

$$F_v = -m_v\, g\, \pi_{\ddot{x}_v} \tag{5.68}$$

The soil forces are expressed in the dimensionless π groupings and repeating parameters in a similar manner to the derivation of the soil forces presented in Chapter 3. First the soil representative spring forces are expressed in the repeating parameters and dimensionless π groupings, and then the soil representative dampers are expressed in the repeating parameters and dimensionless π groupings.

The three variables in the lateral soil force from the springs which are not dimensionless π groupings or repeating parameters are the locations of the soil masses with respect to center of mass of the boulder-soil, R_n, the angles for each soil element as measured from vertical, γ_n, and the depth of the soil elements from the soil line to the bottom of the boulder, α_n. The locations of the soil masses with respect to center of mass of the boulder-soil, R_n, the angles for each soil element as measured from vertical, γ_n, are expressed in terms of the repeating parameters and dimensionless π groupings by substituting (5.44), (5.59), and (5.60) into (3.7) and (3.8), respectively, and simplifying, which yields

$$\gamma_n = {\gamma_n}^* = \tan^{-1}\left(\frac{\pi_{d_n}}{\left(\pi_L - \pi_{c_x}\right)}\right) + \frac{\pi}{2} \tag{5.69}$$

$$R_n = \frac{\pi_{R_n} {v_o}^2}{g} = \frac{{v_o}^2}{g}\sqrt{{\pi_{d_n}}^2 + \left({\pi_L}^2 - {\pi_{c_x}}^2\right)^2}, \tag{5.70}$$

where $\gamma_n{}^*$ are the dimensionless π groupings for the angles of each soil element as measured from vertical, and π_{R_n} are the dimensionless π groupings for the radial distances from the center of mass of the boulder-soil subsystem to the soil elements. Similar to $\gamma_v{}^*$, it should be noted that $\gamma_n{}^*$ requires no scaling parameters since it is already dimensionless. the depth of the soil elements from the soil line to the bottom of the boulder, α_n, is expressed in terms of the repeating parameters and dimensionless π groupings by substituting (5.53) into the range $\left(0, \frac{d}{N}, d\right)$ and simplifying, which yields

$$\alpha_n = \frac{\pi_{\alpha_n} {v_o}^2}{g} = \text{range}\left(0, \frac{\frac{\pi_d {v_o}^2}{g}}{N}, \frac{\pi_d {v_o}^2}{g}\right) \tag{5.71}$$

where π_{α_n} are the dimensionless π groupings for the depth of the soil elements from the soil line to the bottom of the boulder.

The force acting on the boulder-soil subsystem from the soil representative springs is expressed in terms of dimensionless π groupings and repeating parameters by substituting (5.69), (5.70), and (5.71) into (3.27) and simplifying, which yields

$$\begin{aligned} F_{k_n} &= m_v g\, \pi_{F_{k_n}} \\ &= m_v g \frac{10^6\, \pi_\beta\, \pi_W\, \tan\varphi'}{N} \pi_{\alpha_n} \left[\pi_{x_b} + \pi_{R_n} \sin(\gamma_n{}^* + \theta_b)\right. \\ &\quad \left. - \pi_{R_n} \sin(\gamma_n{}^*)\right], \end{aligned} \tag{5.72}$$

where $\pi_{F_{k_n}}$ is the intermediate dimensionless π grouping for the soil representative spring force.

The ultimate lateral resistance is expressed in terms of the repeating parameters and dimensionless π groupings by substituting (5.35), (5.47), and (5.71) into (3.32) and simplifying, which results in

$$F_{u_n} = m_v g \pi_{F_{u_n}} = m_v g \frac{{K_p}^2 \pi_{\rho_b} {\pi_W}^2 \pi_{\alpha_n} K_\varepsilon}{N}, \tag{5.73}$$

where $\pi_{F_{u_n}}$ is the intermediate dimensionless π grouping for the ultimate lateral resistance of the soil. It should also be noted that K_p and K_ε are not scaled since they are inherently dimensionless and based solely on dimensionless parameters.

The lateral soil force from the soil representative dampers are expressed in terms of the repeating parameters and dimensionless π groupings by substituting (5.35), (5.39), (5.45), (5.69), and (5.70) into (3.43) and simplifying, which yields

$$F_{c_n} = m_v g \pi_{F_{c_n}} = m_v g \frac{\pi_{\rho_{soil}} \pi_W \pi_d}{N} \left(\pi_{\dot{x}_b} + \pi_{\dot{\theta}_b} \pi_{R_n} \cos({\gamma_n}^* + \theta_b)\right)^2 \cdot sign\left(\left[\pi_{\dot{x}_b} + \pi_{\dot{\theta}_b} \pi_{R_n} \cos({\gamma_n}^* + \theta_b)\right]\right), \tag{5.74}$$

where $\pi_{F_{c_n}}$ is the intermediate dimensionless π grouping for the lateral soil force from the soil representative dampers. The total force from the soil representative springs and dampers is represented in terms of the repeating parameters and dimensionless π groupings by substituting (5.72) and (5.74) into (3.19) and simplifying, which yields

$$F_n = -m_v g \pi_{F_n} = -m_v g \left(\pi_{F_{k_n}} + \pi_{F_{c_n}}\right), \tag{5.75}$$

where π_{F_n} is the intermediate dimensionless π grouping for the total soil force from the soil representative springs and dampers.

Having expressed all of the forces on the right hand side of (3.10) in terms of dimensionless π groupings and repeating parameters, the governing dimensionless equation of motion for the boulder-soil subsystem in the X direction is found by substituting (5.67), (5.68), and (5.75) into (3.10) and simplifying, which yields

$$\pi_{m_{eff}}\pi_{\ddot{x}_b} = \sum_{n=1}^{N}\{\pi_{F_n}\} + \pi_{F_v}. \tag{5.76}$$

5.4.3 Dimensionless equation of motion for rotation of the boulder-soil subsystem about the Z axis

The governing dimensionless equation of motion for the rotation of boulder-soil subsystem about the Z axis is presented in the similar manner as the dimensionless equation of motion for the vehicle. Equation (3.11) must be expressed in terms of dimensionless π groupings and repeating parameters. As demonstrated with the dimensionless equations of motion for the vehicle and translational displacement of the boulder-soil subsystem, it is advantageous to develop intermediate dimensionless π groupings as a means of general housekeeping when expressing (3.11) in the dimensionless π groupings and repeating parameters.

The distance from the center of mass of the boulder-soil subsystem to the soil elements is expressed in terms of the dimensionless π groupings and repeating parameters by substituting (5.44) and (5.59) into (3.15) and simplifying, which yields

$$l_n = \frac{\pi_{l_n} {v_o}^2}{g} = \frac{{v_o}^2}{g}\left(\pi_L - \pi_{c_x}\right), \tag{5.77}$$

where π_{l_n} is the intermediate dimensionless π grouping for the distance from the center of mass of the boulder-soil subsystem to the soil elements. The center of mass for the boulder-soil

system, as measured with respect to the local origin in the Y direction, is expressed in terms of the dimensionless π groupings and repeating parameters by substituting (5.50), (5.53), (5.57), and (5.58), into (3.4) and simplifying, which yields

$$c_y = -\frac{\pi_{c_y} {v_o}^2}{g} = -\frac{{v_o}^2}{g} \frac{\left[\sum_{n=1}^{N} \left\{ \pi_{m_n} \pi_d \frac{-(n-N-1)}{N} \right\} + \pi_{m_b} \frac{\pi_H}{2} \right]}{\sum_{n=1}^{N} \{\pi_{m_n}\} + \pi_{m_b}}, \tag{5.78}$$

where π_{c_y} is the intermediate dimensionless π grouping for the distance from the center of mass for the boulder-soil system, as measured with respect to the local origin in the Y direction.

The mass moment of inertia of the boulder about the center of mass of the boulder-soil subsystem is expressed in terms of dimensionless π groupings and repeating parameters by substituting (5.44), (5.50), (5.53), (5.57), (5.59), and (5.78) into (3.16) and simplifying, which yields

$$J_b = \frac{m_v {v_o}^4}{g^2} \pi_{J_b} = \frac{m_v {v_o}^4}{g^2} \left[\frac{1}{12} \pi_{m_b} \left(\left(\frac{\pi_H}{2} \right)^2 + \left(\frac{\pi_L}{2} \right)^2 \right) + \pi_{m_b} \left(\left(\pi_{c_y} - \frac{\pi_H}{2} \right)^2 + \left(\pi_{c_x} - \frac{\pi_L}{2} \right)^2 \right) \right], \tag{5.79}$$

where π_{J_b} is the intermediate dimensionless π grouping for the mass moment of inertia of the boulder about the center of mass of the boulder-soil subsystem. The effective mass moment of inertia of the boulder-soil subsystem about the center of mass of the boulder-soil subsystem is expressed in terms of dimensionless π groupings and repeating parameters by substituting (5.58), (5.60), (5.77), and (5.79) into (3.13) and simplifying, which yields

$$J_{eff} = \frac{m_v {v_o}^4}{g^2}\pi_{J_{eff}} = \frac{m_v {v_o}^4}{g^2}\left(\pi_{J_b} + \sum_{n=1}^{N}\{\pi_{m_n}({\pi_{d_n}}^2 + {\pi_{l_n}}^2)\}\right). \tag{5.80}$$

where $\pi_{J_{eff}}$ is the intermediate dimensionless π grouping for the effective mass moment of inertia of the boulder-soil subsystem about the center of mass of the boulder-soil subsystem.

The left hand side of (3.11) can now be expressed in terms of the dimensionless π groupings and repeating parameters by substituting (5.48) and (5.80) into (3.11) and simplifying, which yields

$$J_{eff}\ddot{\theta}_b = m_v {v_o}^2 \pi_{J_{eff}} \pi_{\ddot{\theta}_b} = \sum_{n=1}^{N}\{M_n\} + M_v + M_R. \tag{5.81}$$

Similarly, the right hand side of (3.11) must be expressed in terms of dimensionless π groupings and repeating parameters. The resulting moments from the lateral soil forces, M_n, are expressed in terms of the dimensionless π groupings and repeating parameters by substituting (5.69), (5.70), and (5.75) into (3.20) and simplifying, which yields

$$M_n = -m_v {v_o}^2 \pi_{M_n} = -m_v {v_o}^2 \left[\pi_{F_n}\pi_{R_n}\cos({\gamma_n}^* + \theta_b - \pi)\right], \tag{5.82}$$

where π_{M_n} is the intermediate dimensionless π grouping for the resulting moments from the lateral soil forces. The resulting moment from the force of the vehicle acting on the boulder is expressed in terms of dimensionless π groupings and repeating parameters by substituting (5.61), (5.62), and (5.68) into (3.57) and simplifying, which yields

$$M_v = m_v {v_o}^2 \pi_{M_v} = \pi_{F_v}\pi_{R_v}\cos({\gamma_v}^* + \theta_b), \tag{5.83}$$

where π_{M_v} is the intermediate dimensionless π grouping for the resulting moment from the force of the vehicle acting on the boulder.

Lastly, the maximum restoring moment due to gravity is expressed in terms of dimensionless π groupings and repeating parameters by substituting (5.57), (5.69), and (5.70) with $n = N$ into (3.44) and simplifying, which yields

$$M_{R\,max} = -sign(\sin({\gamma_N}^* + \theta_b)) m_v {v_o}^2 \pi_{M_{R\,max}} \tag{5.84}$$
$$= -sign(\sin({\gamma_N}^* + \theta_b)) m_v {v_o}^2 \pi_{m_b} \pi_{R_N} \cos({\gamma_N}^* + \theta_b),$$

where $\pi_{M_{R\,max}}$ is the intermediate dimensionless π grouping for the maximum restoring moment acting on the boulder due to gravity. As previously stated in Section 3.2.2, the restoring moment is then calculated by comparing it to the sum of the remaining moments and the maximum restoring moment. The restoring moment, as aforementioned calculated, is expressed in terms of dimensionless π groupings and repeating parameters by substituting (5.82), (5.83), and (5.84) into (3.46) and simplifying, which yields

$$M_R = -sign(\sin({\gamma_N}^* + \theta_b)) m_v {v_o}^2 \pi_{M_R} \tag{5.85}$$
$$= -sign(\sin({\gamma_N}^* + \theta_b)) m_v {v_o}^2 \left[\sum_{n=1}^{N} \{\pi_{M_n}\} + \pi_{M_v}\right]$$

$$for\ \pi_{M_{R\,max}} + \pi_{M_v} + \sum_{n=1}^{N} \{\pi_{M_n}\} \neq 0,$$

where π_{M_R} is the intermediate dimensionless π grouping for the maximum restoring moment acting on the boulder due to gravity.

Having expressed all of the moments on the right hand side of (3.11) in terms of dimensionless π groupings and repeating parameters, the governing dimensionless equation of motion for the rotation of the boulder-soil subsystem about the Z axis found by substituting (5.82), (5.83), (5.84), and (5.85) into (5.81) and simplifying, which yields

$$\pi_{J_{eff}}\pi_{\ddot{\theta}_b} = \sum_{n=1}^{N}\{\pi_{M_n}\} + \pi_{M_v} + \pi_{M_R}. \tag{5.86}$$

5.5 Simulating of dimensionless equations of motion

The dimensionless governing equations of motion can be arranged into state-space form and solved via numerical integration, similar to the dimensioned governing equations of motion for the low-order model. The states and corresponding time derivatives for the dimensionless equations of motion are listed in Table 5–8.

Table 5–8. States for dimensionless governing equations of motion

$x_1 = \pi_{x_b}$	(5.87)	$\dot{x}_1 = x_2$	(5.88)
$x_2 = \pi_{\dot{x}_b}$	(5.89)	$\dot{x}_2 = \frac{1}{\pi_{m_{eff}}}\left[\sum_{n=1}^{N}\{\pi_{F_n}\} + \pi_{F_v}\right]$	(5.90)
$x_3 = \theta_b$	(5.91)	$\dot{x}_3 = x_4$	(5.92)
$x_4 = \pi_{\dot{\theta}_b}$	(5.93)	$\dot{x}_4 = \frac{1}{\pi_{J_{eff}}}\sum_{n=1}^{N}\{\pi_{M_n}\} + \pi_{M_v} + \pi_{M_R}$	(5.94)
$x_5 = \pi_{x_v}$	(5.95)	$\dot{x}_5 = x_6$	(5.96)
$x_6 = \pi_{\dot{x}_v}$	(5.97)	$\dot{x}_6 = x_7$	(5.98)
$x_7 = \pi_{\ddot{x}_v}$	(5.99)	$\dot{x}_7 = \pi_{k_v}\left[\pi_{\dot{x}_b} + \pi_{\dot{\theta}_b}\pi_{R_v}\cos(\gamma_v{}^* + \theta_b) - \frac{\pi_{\ddot{x}_v}}{\pi_{c_v}} - \pi_{\dot{x}_v}\right]$	(5.100)

It should be noted that all forces in the dimensionless governing equations of motion can be written explicitly as functions of the states (5.87), (5.89), (5.91), (5.93), (5.95), (5.97), and (5.99). The set of equations (5.87) – (5.100) are also coupled first-order, nonlinear, non-stiff ordinary differential equations which can be readily solved via numerical integration in the same manner as the dimensioned state-space equations.

5.6 Scaling laws for full scale and small scale experiments

As per the Buckingham Π Theorem, each of the small scale dimensionless parameters must be equal to the respective full scale dimensionless π parameters in order to achieve full similitude. The small scale experiment and simulation parameters are most readily determined from the dimensionless groupings which involve the fixed or input π parameters. Referring to Table 5–1, the input dimensionless π groupings for either an experiment or simulation are–

$\pi_{\rho_{soil}}$, π_{β}, π_{ρ_b}, π_L, π_W, π_H, π_d, π_{k_t}, π_{c_t}, and π_e. The small scale parameters, denoted by the subscript δ, are found by equating the small scale π groupings to the full scale π groupings, denoted by the subscript Δ, and solving for the unknown small scale parameters. The equations used in determining the small scale input parameters are listed in Table 5–9. Similarly, the outputs of the simulations and experiments are scaled using the equations listed in Table 5–10.

Table 5–9. Equations used for determining governing small scale parameters

$$\pi_{\rho_{soil}} = \frac{\rho_{soil_\delta} {v_o}_\delta^{\,6}}{m_{v_\delta} {g_\delta}^3} = \frac{\rho_{s_\Delta} {v_o}_\Delta^{\,6}}{m_{v_\Delta} {g_\Delta}^3} \quad (5.101) \qquad \pi_{\beta} = \frac{\beta_\delta {v_o}_\delta^{\,6}}{m_{v_\delta} {g_\delta}^4} = \frac{\beta_\Delta {v_o}_\Delta^{\,6}}{m_{v_\Delta} {g_\Delta}^4} \quad (5.102)$$

$$\pi_{\rho_b} = \frac{\rho_{b_\delta} {v_o}_\delta^{\,6}}{m_{v_\delta} {g_\delta}^3} = \frac{\rho_{b_\Delta} {v_o}_\Delta^{\,6}}{m_{v_\Delta} {g_\Delta}^3} \quad (5.103) \qquad \pi_L = \frac{L_\delta g_\delta}{{v_o}_\delta^{\,2}} = \frac{L_\Delta g_\Delta}{{v_o}_\Delta^{\,2}} \quad (5.104)$$

$$\pi_W = \frac{W_\delta g_\delta}{{v_o}_\delta^{\,2}} = \frac{W_\Delta g_\Delta}{{v_o}_\Delta^{\,2}} \quad (5.105) \qquad \pi_H = \frac{H_\delta g_\delta}{{v_o}_\delta^{\,2}} = \frac{H_\Delta g_\Delta}{{v_o}_\Delta^{\,2}} \quad (5.106)$$

$$\pi_d = \frac{d_\delta g_\delta}{{v_o}_\delta^{\,2}} = \frac{d_\Delta g_\Delta}{{v_o}_\Delta^{\,2}} \quad (5.107) \qquad \pi_{k_v} = \frac{k_{v_\delta} {v_o}_\delta^{\,2}}{m_{v_\delta} {g_\delta}^2} = \frac{k_{v_\Delta} {v_o}_\Delta^{\,2}}{m_{v_\Delta} {g^2}_\Delta} \quad (5.108)$$

$$\pi_{c_v} = \frac{c_{v_\delta} {v_o}_\delta^{\,2}}{m_{v_\delta} g_\delta} = \frac{c_{v_\Delta} {v_o}_\Delta^{\,2}}{m_{v_\Delta} g_\Delta} \quad (5.109) \qquad \pi_e = \frac{e_\delta g_\delta}{{v_o}_\delta^{\,2}} = \frac{e_\Delta g_\Delta}{{v_o}_\Delta^{\,2}} \quad (5.110)$$

$$\pi_{h_e} = \frac{h_{e_\delta} g_\delta}{{v_o}_\delta^{\,2}} = \frac{h_{e_\Delta} g_\Delta}{{v_o}_\Delta^{\,2}} \quad (5.111)$$

Table 5–10. Scaling laws associated with the outputs form the low-order model

$$\pi_{x_b} = \frac{x_{b\delta} g_\delta}{{v_o}_\delta^{\,2}} = \frac{x_{b\Delta} g_\Delta}{{v_o}_\Delta^{\,2}} \quad (5.112)$$

$$\pi_{x_v} = \frac{x_{v\delta} g_\delta}{{v_o}_\delta^{\,2}} = \frac{x_{v\Delta} g_\Delta}{{v_o}_\Delta^{\,2}} \quad (5.113)$$

$$\pi_{\dot{x}_b} = \frac{\dot{x}_{b\delta}}{v_{o\delta}} = \frac{\dot{x}_{b\Delta}}{v_{o\Delta}} \quad (5.114)$$

$$\pi_{\dot{x}_v} = \frac{\dot{x}_{v\delta}}{v_{o\delta}} = \frac{\dot{x}_{v\Delta}}{v_{o\Delta}} \quad (5.115)$$

$$\pi_{\ddot{x}_b} = \frac{\ddot{x}_{b\delta}}{g_\delta} = \frac{\ddot{x}_{b\Delta}}{g_\Delta} \quad (5.116)$$

$$\pi_{\ddot{x}_v} = \frac{\ddot{x}_{v\delta}}{g_\delta} = \frac{\ddot{x}_{v\Delta}}{g_\Delta} \quad (5.117)$$

$$\pi_{\dot{\theta}_b} = \frac{\dot{\theta}_{b\delta} v_{o\delta}}{g_\delta} = \frac{\dot{\theta}_{b\Delta} v_{o\Delta}}{g_\Delta} \quad (5.118)$$

$$\pi_{\dddot{x}_v} = \frac{\dddot{x}_{v\delta} v_{o\delta}}{{g_\delta}^2} = \frac{\dddot{x}_{v\Delta} v_{o\Delta}}{{g_\Delta}^2} \quad (5.119)$$

$$\pi_{\ddot{\theta}_b} = \frac{\ddot{\theta}_{b\delta} {v_{o\delta}}^2}{{g_\delta}^2} = \frac{\ddot{\theta}_{b\Delta} {v_{o\Delta}}^2}{{g_\Delta}^2} \quad (5.120)$$

$$\pi_t = \frac{t_\delta g_\delta}{v_{o\delta}} = \frac{t_\Delta g_\Delta}{v_{o\Delta}} \quad (5.121)$$

Even though certain parameters in Table 5–9 and Table 5–10 are presented as variable, it is desirable to establish a set of constants between small scale and full scale experiments and simulations. The practice most often presented in literature involves using the same soil between small and full scale testing as this will eliminate any variations in soil properties [12]. It is also desirable to perform both the small and full scale experiments in the same gravitational field. As seen in [12], it may not be feasible to obtain full similitude when considering both gravity and soil properties as constant.

The feasibility of full similitude while assuming gravity and soil properties as constants between full and small scale testing is investigated though the use of an arbitrary set of full scale parameters, listed in Table 5–11.

Table 5–11. Test case full scale input parameters

$m_{v_\Delta} = 2000$ kg	$v_{o_\Delta} = 20$ m/s
$g_\Delta = 9.81$ m/s^2	$\beta_\Delta = 50$ MN/m^3
$\rho_{s_\Delta} = 1500$ kg/m^3	$L_\Delta = 1.5$ m
$\rho_{b_\Delta} = 2500$ kg/m^3	$H_\Delta = 4$ m
$W_\Delta = 2$ m	$k_v = 1$ MN/m
$d_\Delta = 2$ m	$e_\Delta = 0.5$ m
$c_{v_\Delta} = 100$ kN · s/m	$h_{e_\Delta} = 0.0004$ m

It should be noted that a height of the full scale soil element, h_{e_Δ}, of 0.0004 m corresponds to 5000 soil elements. It is assumed that both the gravitational constant and constant of horizontal subgrade reaction of the soil are constant between full and small scale tests, which results in

$$g_\delta = g_\Delta \tag{5.122}$$

$$\beta_\delta = \beta_\Delta. \tag{5.123}$$

Substituting (5.122), (5.123), $m_{v_\Delta} = 2000$ kg, and $v_{o_\Delta} = 20$ m/s into (5.102) and simplifying yields

$$\frac{{v_{o_\delta}}^6}{m_{v_\delta}} = 32{,}000. \tag{5.124}$$

Equation (5.124) is a single equation with two unknowns, m_{v_δ} and v_{o_δ}, thus one of the two unknowns must be explicitly specified. Arbitrarily setting $m_{v_\delta} = 200$ kg and solving (5.124) for the initial velocity of the small scale vehicle results in $v_{o_\delta} = 13.626$ m/s. The

remaining governing small scale parameters are then determined by substituting $m_{v_\delta} = 200\ \text{kg}$ and $v_{o_\delta} = 13.626\ \text{m/s}$ into the scaling laws listed in Table 5–9. Doing so leads to the small scale parameters listed in Table 5–12.

Table 5–12. Test case small scale input parameters

$m_{v_\delta} = 200\ \text{kg}$	$v_{o_\delta} = 13.626\ \text{m/s}$
$g_\delta = 9.81\ \text{m/s}^2$	$\beta_\delta = 50\ \text{MN/m}^3$
$\rho_{s_\delta} = 1500\ \text{kg/m}^3$	$L_\delta = 0.696\ \text{m}$
$\rho_{b_\delta} = 2500\ \text{kg/m}^3$	$H_\delta = 1.856\ \text{m}$
$W_\delta = 0.9283\ \text{m}$	$k_{v_\delta} = 215\ \text{kN/m}$
$d_\delta = 0.9283\ \text{m}$	$e_\delta = 0.232\ \text{m}$
$c_{v_\delta} = 14.7\ \text{kN} \cdot \text{s/m}$	$h_{e_\delta} = 0.000185\ \text{m}$

Similar to [5], certain parameters changed in value, such as the equivalent vehicle spring and damper constants and boulder dimensions. Unlike [12], however, it should be noted that the small scale mass densities of the boulder and the soil are the exact same as that seen in the full scale scenario. Therefore, it is possible to achieve full similitude between full and small scale experiments and simulations not only under constant gravity and constant soil properties, but also constant boulder material properties. It should be further noted that the number of elements did not change between small and full scale.

5.7 Contributions of this chapter

The contributions of this chapter are as follows:

(1) Present the governing parameters in the low-order model

(2) Select the repeating parameters for dimensionless π groupings

(3) Create the dimensionless π groupings

(4) Develop the governing dimensionless equations of motion

(5) Represent the governing dimensionless equations of motion in state-space form

CHAPTER 6

VALIDATION OF DIMENSIONAL ANALYSIS AND STATIC FRACTURE PREDICTION

The intent of this chapter is to show the comparison of simulated and experimental results in dimensionless form across many different scales. This will be conducted in stages. First, the dimensionless equations of motion are simulated and compared to the equivalent forms of full scale and small scale simulation results. Then the small scale simulations are compared to equivalent forms of small scale crash results. Next, dimensionally scaled versions of the small scale crash results are compared to the full scale crash results recorded to date.

This chapter is organized as follows:

The equipment and methods for conducting a small scale crash test is outlined in Sections 6.2 and 6.3. A summary of the small scale crash tests is presented in Section 6.4, and the small scale crash test results are compared to the equivalent small scale simulations in Section 6.5. The small scale crash test results are then compared to the full scale crash test results through the use of scaling laws in Section 6.6.

6.1 Validation of dimensional analysis through simulation of dimensionless equations of motion

The state-space, dimensionless equations of motion are simulated by substituting the values for the dimensionless parameters into (5.87) – (5.100) and solving via numerical integration techniques. The governing dimensionless π groupings for BST-1 and BST-2 are shown in Table 6–1 and Table 6–2, respectively.

Table 6–1. Dimensionless governing parameters for BST-1

$\pi_{\rho_{soil}} = 1{,}680.5$	$\pi_H = 0.1209$	$\pi_\beta = 8.5841 \cdot 10^6$
$\pi_{\rho_b} = 2{,}724.9$	$\pi_d = 0.066$	$\pi_e = 0.0414$
$\pi_L = 0.0419$	$\pi_{k_v} = 847.05$	$\varphi' = 43.2°$
$\pi_W = 0.0558$	$\pi_{c_v} = 27.84$	$\pi_{h_e} = 1.3191 \cdot 10^{-5}$

Table 6–2. Dimensionless governing parameters for BST-2

$\pi_{\rho_{soil}} = 2{,}776.6$	$\pi_H = 0.16$	$\pi_\beta = 1.4183 \cdot 10^7$
$\pi_{\rho_b} = 3{,}802$	$\pi_d = 0.0947$	$\pi_e = 0.0438$
$\pi_L = 0.077$	$\pi_{k_v} = 1{,}008.6$	$\varphi' = 43.5°$
$\pi_W = 0.0784$	$\pi_{c_v} = 30.54$	$\pi_{h_e} = 1.8943 \cdot 10^{-5}$

It should be noted that the number of soil elements for the simulations, N, is found from π_{h_e} using

$$N = \frac{\pi_d}{\pi_{h_e}}. \tag{6.1}$$

The results of the simulations are shown in Figure 6-1 – Figure 6-6.

6.1.1 Dimensionless simulation of BST-1

Figure 6-1, Figure 6-2, and Figure 6-3 show the simulated, dimensionless displacement of the center of mass of ABG-01 versus dimensionless time, the simulated angle of rotation of ABG-01 versus dimensionless time, and the simulated, dimensionless displacement of the vehicle versus dimensionless time when using the parameters in Table 6–1.

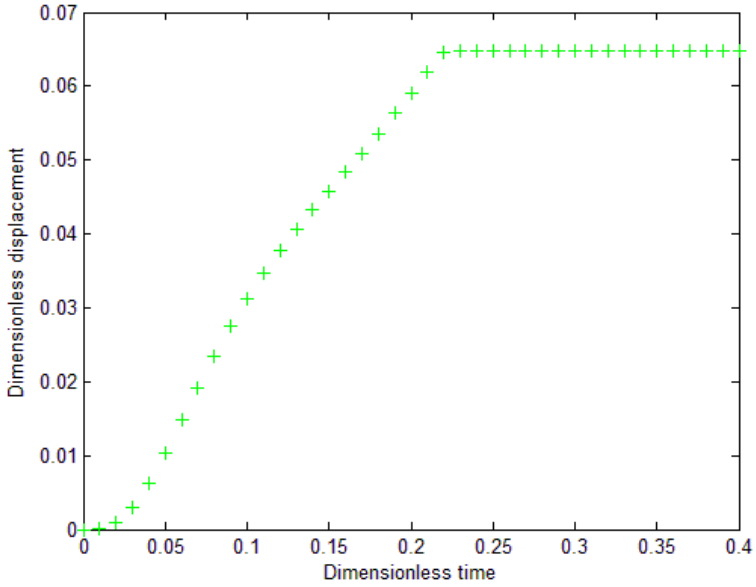

Figure 6-1. Simulated dimensionless displacement of the center of mass of ABG-01 in BST-1 using the DEOM

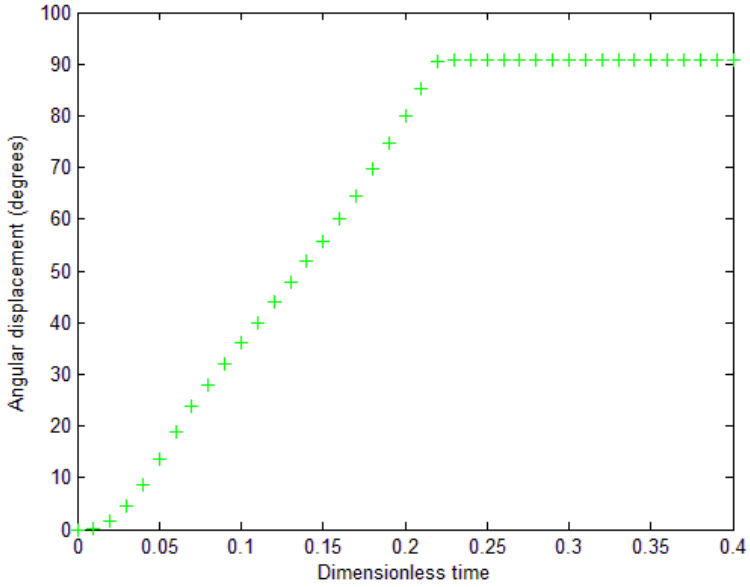

Figure 6-2. Simulated angle of rotation of ABG-01 in BST-1 using the DEOM

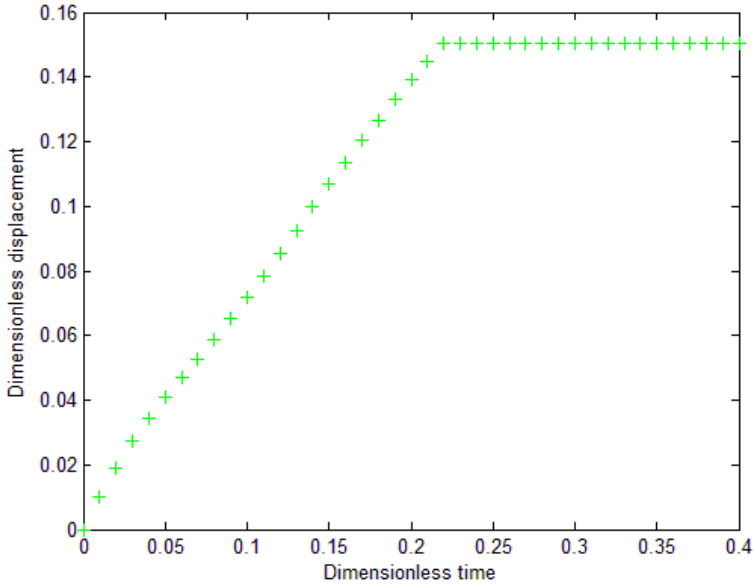

Figure 6-3. Simulated dimensionless displacement of the vehicle from BST-1 using the DEOM

6.1.2 Dimensionless simulation of BST-2

Figure 6-5,Figure 6-6Figure 6-7 show the simulated, dimensionless displacement of the center of mass of RWG-01 versus dimensionless time, the simulated angle or rotation of RWG-01 versus dimensionless time, and the simulated, dimensionless displacement of the vehicle versus dimensionless time when using the π groupings from Table 6–2.

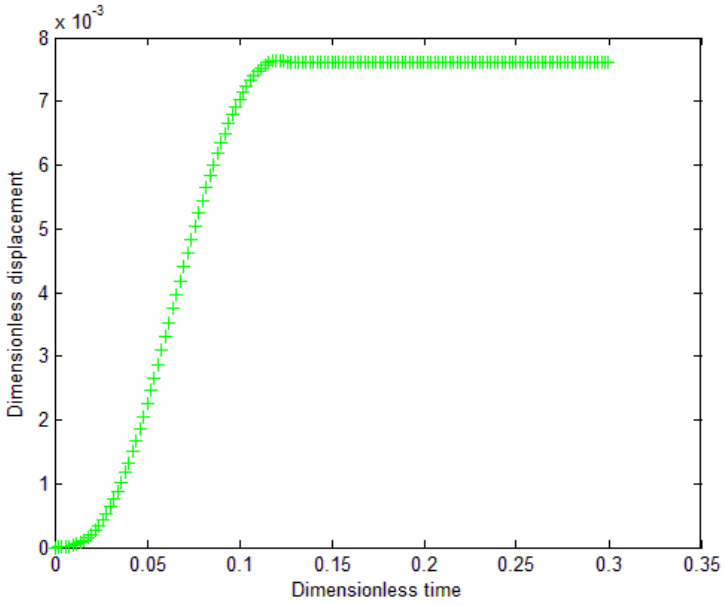

Figure 6-4. Simulated dimensionless displacement of the center of mass of RWG-01 in BST-2 using the DEOM

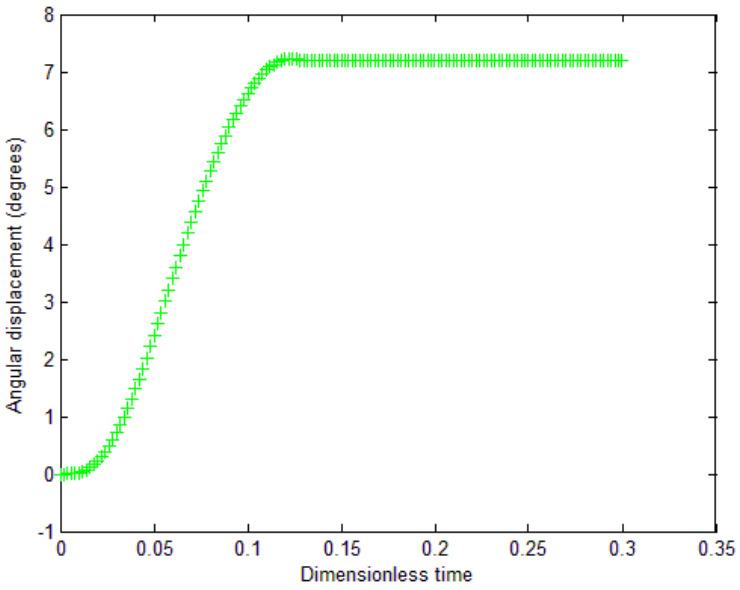

Figure 6-5. Simulated angle of rotation of RWG-01 in BST-2 using the DEOM

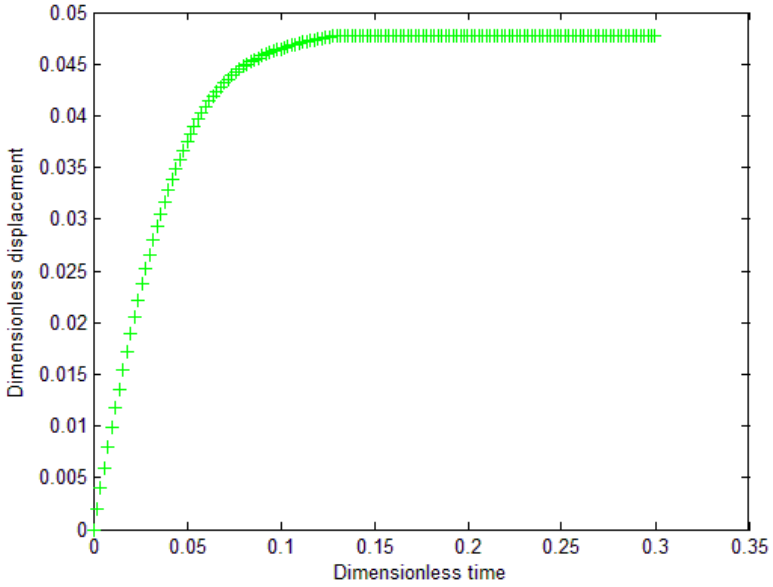

Figure 6-6. Simulated dimensionless displacement of the vehicle from BST-2 using the DEOM

6.1.3 Interpretation of dimensionless simulations

The dimensionless results in Figure 6-1 – Figure 6-6 are easily transformed into any scaled similar size simulation through the use of (5.112) – (5.121). The most straightforward example, perhaps, is transforming the angle of rotation versus dimensionless time into the angle of rotation versus full scale time for BST-2. Since the angle of rotation is inherently dimensionless and does not scale, the time variable is the only scaled parameter. The full scale time is found simply by substituting the dimensionless time vector into (5.121) and solving for the full scale time. Figure 6-7 shows the comparison of the full scale simulation to the scaled results from the dimensionless equations of motion for BST-2.

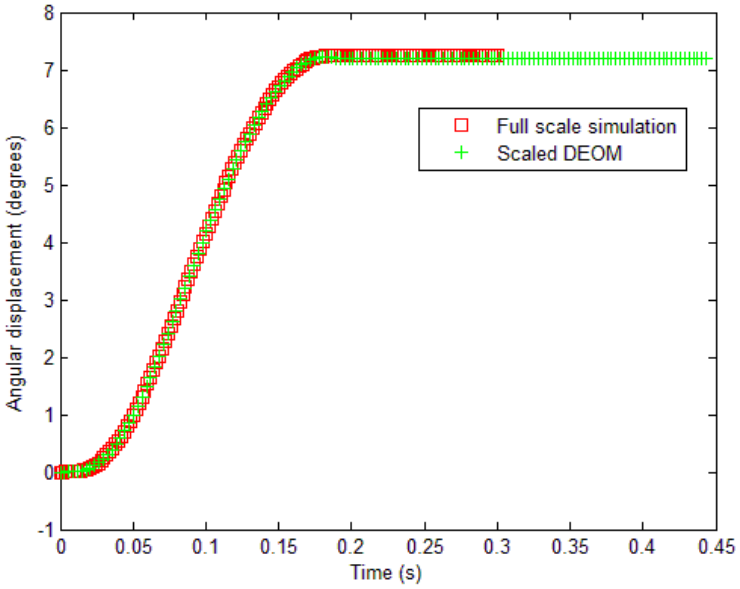

Figure 6-7. Comparison of the boulder angle from the dimensioned EOM to the scaled results from the DEOM

As seen in Figure 6-7, the results are exactly the same, as was expected. The dimensionless π groupings also allow for inverse transformations since the dimensionless π groupings are ratios. The full scale simulation results of the angle of rotation of RWG-01 versus time are transformed back into the dimensionless results by substituting the full scale time vector into (5.121) and solving for π_t.

As a precursor to the comparison of small scale experiments to full scale experiments, the dimensionless π groupings and scaling laws allow for the comparison of small scale simulations to full scale simulations. As presented in Section 6.3, the small scale experiments are performed using an equivalent 8 kg impact vehicle. The resulting desired small scale parameters are found by applying the scaling laws to BST-1 and BST-2 for an 8 kg vehicle and are shown in Table 6–3 and Table 6–4. To avoid confusion with measured small scale parameters, the desired parameters are denoted using an over bar.

Table 6–3. Desired small scale parameters based on the full scale parameters in BST-1

$\overline{m_{v_\delta}} = 8$ kg	$\overline{v_{o_\delta}} = 4.34$ m/s
$\overline{g_\delta} = 9.81$ m/s^2	$\overline{\beta_\delta} = 95$ MN/m^3
$\overline{\rho_{s_\delta}} = 1{,}895.9$ kg/m^3	$\overline{L_\delta} = 0.0805$ m
$\overline{\rho_{b_\delta}} = 3{,}074$ kg/m^3	$\overline{H_\delta} = 0.2323$ m
$\overline{W_\delta} = 0.1073$ m	$\overline{k_{v_\delta}} = 34.6$ kN/m
$\overline{d_\delta} = 0.1267$ m	$\overline{e_\delta} = 0.0796$ m
$\overline{c_{v_\delta}} = 0.503$ kN · s/m	

Table 6–4. Desired small scale parameters based on the full scale parameters in BST-2

$\overline{m_{v_\delta}} = 8$ kg	$\overline{v_{o_\delta}} = 4.72$ m/s
$\overline{g_\delta} = 9.81$ m/s^2	$\overline{\beta_\delta} = 95$ MN/m^3
$\overline{\rho_{s_\delta}} = 1{,}895.9$ kg/m^3	$\overline{L_\delta} = 0.1749$ m
$\overline{\rho_{b_\delta}} = 2{,}596$ kg/m^3	$\overline{H_\delta} = 0.3635$ m
$\overline{W_\delta} = 0.178$ m	$\overline{k_{v_\delta}} = 34.8$ kN/m
$\overline{d_\delta} = 0.2151$ m	$\overline{e_\delta} = 0.0994$ m
$\overline{c_{v_\delta}} = 0.507$ kN · s/m	

Similar to the full scale simulations, the small scale parameters can also be substituted into the dimensioned state-space equations of motion, (3.79) – (3.92), and numerically integrated. Even though the parameters shown in Table 6–3 and Table 6–4 are scaled similar to the full scale simulations of BST-1 and BST-2, the two sets of simulations cannot be directly compared since they are of two different scaled sizes. Either the results from both simulations must be transformed into the dimensionless results and compared as previously presented, or the results

from one of the simulations must be transformed completely into the other scale size. For example, the small scale angular displacement of the boulder can be scaled up into the full scale size by substituting the small scale time into (5.121) and solving for the corresponding full scale time. As shown in Figure 6-8, this procedure once again confirms that the two simulations are dynamically similar.

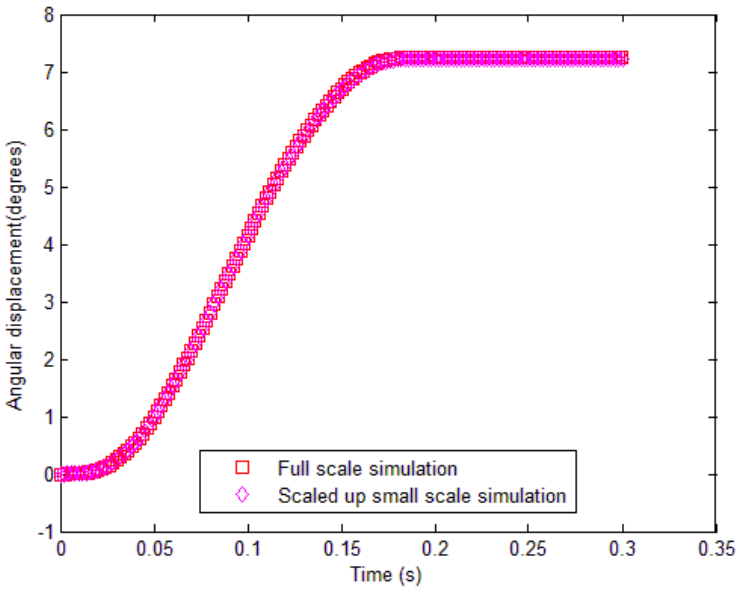

Figure 6-8. Comparison of the scaled-up, simulated, small scale angular displacement of RWG-01 to the simulated full scale angular displacement of RWG-01 in full scale time

6.2 Small scale crash test equipment and procedure

This section will briefly describe the test equipment used in performing a small scale crash test and the procedure for determining the lumped-parameter values found in the low-order model. One of the goals for the equipment which was to be used in small scale testing was not only ensuring repeatability in the lumped-parameter values, but also ease of varying scaled sizes of the crash tests. Rather than using an actual small scale medium-duty sized truck, it was

determined that a rigid-arm pendulum would provide both repeatability in test parameters and ease of varying scaled sizes. Thus, in small scale testing, the vehicle is represented by a rigid-arm pendulum constructed from 3030 sized aluminum 8020® to which various weights and crushable material may be attached. The small scale pendulum will be referred to as the Small Scale Crash Research (SSCR) pendulum and is shown in Figure 6-9.

Figure 6-9. SSCR pendulum used in small scale testing of soil-fixed boulders

The SSCR pendulum is approximately 2.43 m tall and the impact beam is 1.83 m long. This configuration allow for a maximum elevation change of 1.72 m for the impact beam. The maximum horizontal speed of the tip of the impact beam is approximately 6.5 m/s when released from the maximum height. Table 6–5 lists the additional salient measured and calculated parameters of the SSCR pendulum and impact beam.

Table 6–5. Properties of SSCR pendulum

Mass of impact beam	10.9 kg
Mass of mounting hardware	5.4 kg
Radial distance from pivot to mounting hardware	1.65 m
Radial distance form pivot to typical impact point	1.83 m
Calculated mass moment of inertia of impact beam about the pivot point of the pendulum	26.87 kg-m^2

The small scale crash tests are performed by raising the impact beam to a desired initial angular displacement and then using a quick release mechanism to allow the impact beam to swing into the small scale boulder. A crushable material is attached to the impact beam which acts as the observed crush of the full scale vehicles. The material used to model the crush of a vehicle is two empty 12 oz. aluminum drinking cans which are wrapped in Nashua® 300 Series heavy duty duct tape. The aluminum cans were chosen based on the equivalent spring and damper values which are presented in Section 6.3. A more detailed description of the preparation of the crush material is also presented in Section 6.3.

The primary means of data collection for the small scale crash tests the high-speed imaging system used in full scale testing. All small scale tests are recorded using the high-speed camera. Additional data collection devices were used during small scale crash tests when available. Such devices include a US Digital® HD25 incremental industrial rotary encoder which is attached to the rotational shaft at the top of the pendulum, shown in Figure 6-10.

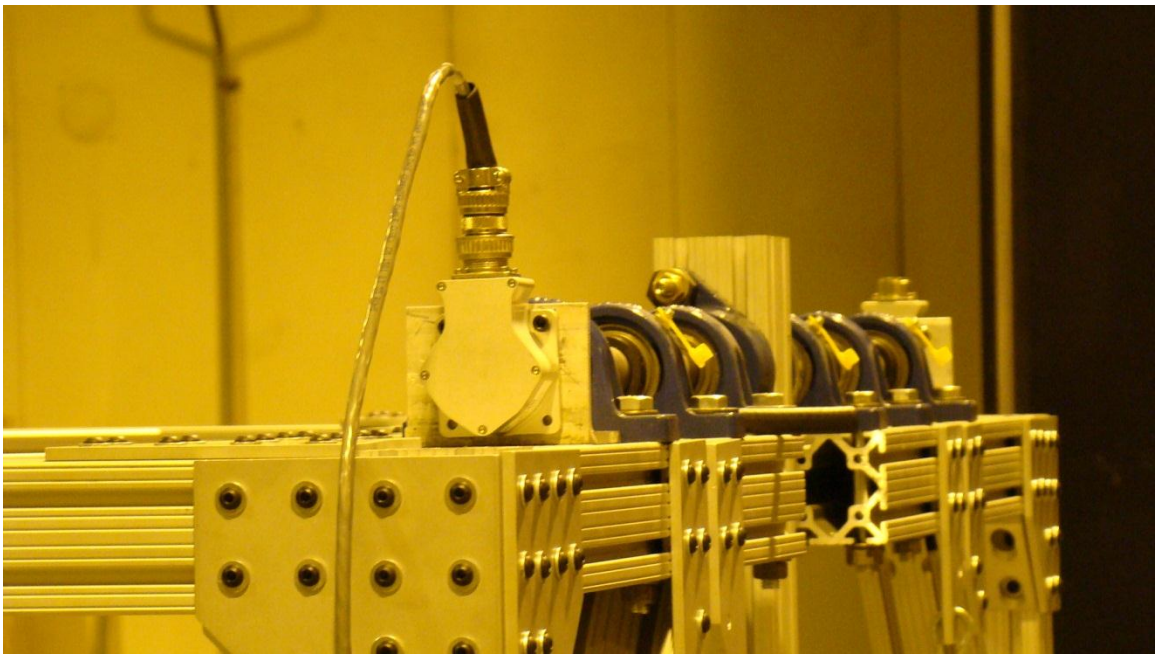

Figure 6-10. US Digital® HD25 incremental industrial rotary encoder as mounted on the SSCR pendulum

The rotary encoder is used to measure the displacement of the impact beam from which the impact velocity of the crash can be estimated. A MATLAB® xPC Target™ data logger and host are used to read and collect the position output from the rotary encoder as well as act as a backup trigger system for the high-speed imaging system. An automatic trigger device was created in conjunction with the use of the high-speed camera and xPC Target™ data logger. Similar to the full scale trigger, the small scale trigger system was designed to send a TTL +5V signal to the data collection devices when the impact beam passes through the proximity sensors mounted to the pendulum frame.

The soil in small scale crash tests was selected such that the base consistency was the same as the soil used in full scale crash tests. The small scale soil is limestone dust obtained from the same quarry which the full scale soil was obtained. The soil is compacted in 2.5 – 7.5 cm layers using an 11 lb. 8” x 8” hand tamper. The soil layer thickness depends on the desired

constant of horizontal subgrade reaction. A higher desired constant of horizontal subgrade reaction requires thinner layers of compacted soil. Figure 6-11 shows the soil in the loose state, and Figure 6-12 shows the compacted soil as prepared for a small scale crash test.

Figure 6-11. Limestone dust used in small scale testing in the loose state

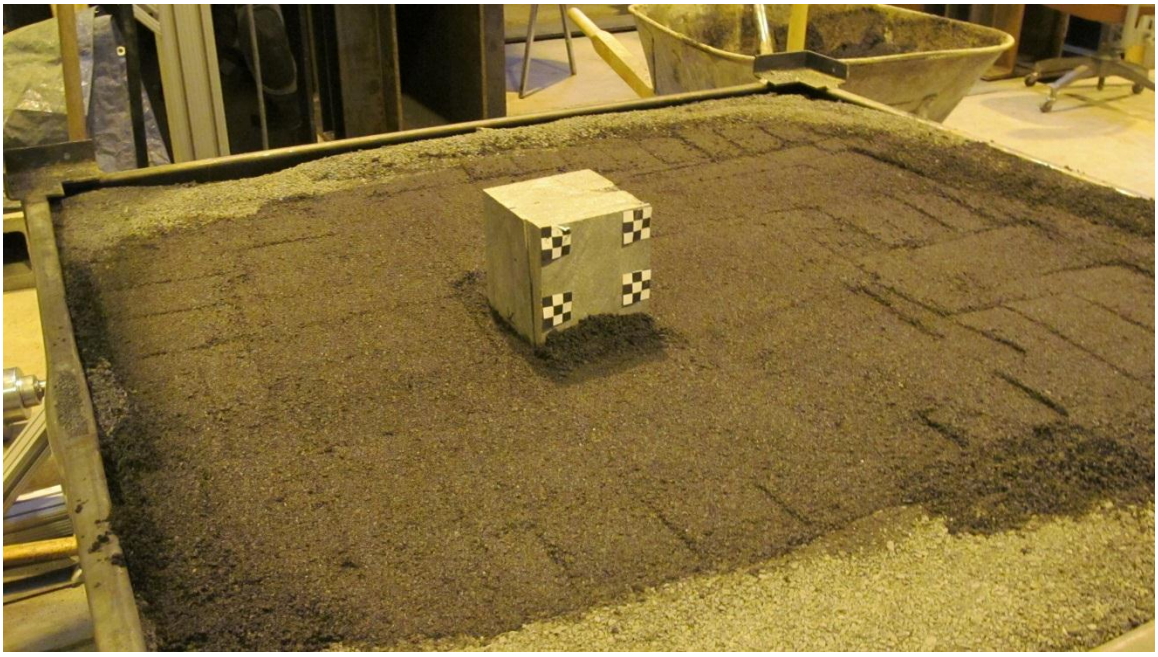

Figure 6-12. Limestone dust as compacted prior to a small scale crash test

As presented in Chapter 4, the maximum density of the limestone dust was found to be 2,010 kg/m^3 by performing a modified proctor test on the limestone dust.

When installing the boulder, a hole is excavated in the center of the soil bin such that enough room is available for the soil wedge to form. The hole is excavated below the desired embedment depth, and soil is then backfilled and tamped until the depth of the hole is equal to the desired boulder embedment depth. The boulder is then inserted into the hole, and the boulder is aligned with the impact beam and crush material such that the boulder is approximately 90° to the centerline of the impact beam. The boulder is also made level using an analog bubble level. The soil is then backfilled and tamped approximately every 5 cm until the soil had reached the top of the hole. A dynamic cone penetrometer is then used to perform the in-situ measurement of the soil properties as presented in Chapter 3.

6.3 Measurement and estimation of commonly used lumped-parameters within small scale crash tests

This section presents the methodology for determining the lumped-parameter values of the variables which do not typically change between small scale tests, such as the equivalent mass, spring constant, and damping constant of the small scale vehicle. First, the equivalent mass of the impacting vehicle is estimated based on the SSCR pendulum properties. The corresponding impact velocity of the vehicle is then found using (5.102) where the gravitational constant and constant of horizontal subgrade reaction are assumed equal between the small and full scale experiments. The remainder of the small scale parameters are calculated as presented in Section 5.6. The crushable material is then parameterized by impacting a rigid structure and fitting (3.58) to the measured the displacement. The small scale boulders are then either cast from concrete or cut from existing granite boulder to the dimensions found through the application of the scaling laws. They are also weighed to determine the mass density of the

boulder. Lastly, the in-situ soil properties are measured after the boulder has been installed and the soil compacted.

The equivalent mass of the impacting small scale vehicle is found by comparing the equations of motion of the vehicle in Chapter 3 to the equation of motion for a rigid-arm pendulum with a spring and damper attached to the end, as shown in Figure 6-13. The variables in Figure 6-13 are the mass moment of inertia of the impact beam and mounting hardware about the pivot point, J_p, the radial distance from the center of mass of the impact beam and mounting hardware to the pivot, c_p, the angle of the impact beam measured from equilibrium, θ_p, the inertial mass, m', and the length of the impact beam, l_p. For illustrative and simplification purposes it is assumed that the spring and damper constants for both the vehicle and pendulum are the same.

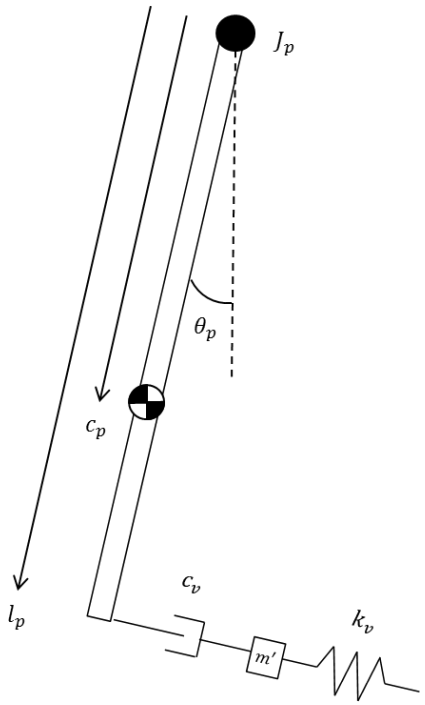

Figure 6-13. Rigid-arm pendulum with equivalent Maxwell model attached to the impact point

The governing equation of motion for the pendulum is

$$J_p\ddot{\theta}_p = -F_v{}'l_p - m_p g c_p \sin\theta_p, \tag{6.2}$$

where $\ddot{\theta}_p$ is the angular acceleration of the pendulum. Since the pendulum only has one degree-of-freedom, the linear acceleration of the impact point, $\ddot{x}_p$, of the pendulum is found using

$$\ddot{x}_p = \ddot{\theta}_p l_p \cos(\theta_p) - \dot{\theta}^2 l_p \sin(\theta_p), \tag{6.3}$$

where $\dot{\theta}$ is the angular velocity of the pendulum. Applying the small angle theorem to (6.3) results in

$$\ddot{x}_p = \ddot{\theta}_p l_p - \dot{\theta}^2 l_p \theta_p. \tag{6.4}$$

As observed in the parameterization of the crush material, the angular acceleration during impact can easily reach values as high as 90 rad/s^2, whereas the maximum angular velocity of the impact beam is 3 rad/s. The angular velocity component of (6.4) may be neglected since the squared maximum angular velocity of the pendulum is an order of magnitude less than the angular acceleration of the pendulum and θ_p goes to zero at equilibrium. Thus, for small angle changes about the equilibrium position, the linear acceleration of the impact point is expressed as

$$\ddot{x}_p = \ddot{\theta}_p l_p. \tag{6.5}$$

Additionally, the moment as a result of gravity acting on the pendulum in (6.2) is also neglected near equilibrium since it is expected to be orders of magnitudes less than the moment due to impact and θ_p approaches zero. Solving (6.5) in terms of the angular acceleration of the pendulum, substituting the results into (6.2), and dividing through by l_p yields

$$J_p \frac{\ddot{x}_p}{{l_p}^2} = -F_v{}' \tag{6.6}$$

Equating (3.17) and (6.6) and solving for the mass of the vehicle results in

$$m_v = \frac{J_p}{{l_p}^2}. \tag{6.7}$$

Equation (6.7), therefore, represents the equivalent mass of the small scale impact vehicle about the equilibrium position when using a rigid-arm pendulum. The equivalent mass of the small scale impact vehicle was calculated to be 8 kg when using the parameters listed in Table 6–5. The remaining small scale parameters are found following the methodology presented in Section 5.6 when using an 8 kg vehicle. Table 6–6 presents the small scale parameters which are typically not varied between small scale crash tests as related to a full scale M30 rated impact. The small scale parameters such as the boulder dimensions and embedment properties are found based on test specific full scale parameters.

Table 6–6. Constant small scale parameters associated with a M30 rated full scale crash test

$m_{v_\delta} = 8$ kg	$v_{o_\delta} = 4.35$ m/s
$g_\delta = 9.81$ m/s^2	$k_{v_\delta} = 34.6$ kN/m
$c_{v_\delta} = 0.503$ kN · s/m	

The two small scale parameters which are not as easily determined or measured are the equivalent spring and damping constants for the vehicle. A series of dynamic crush tests were performed on several materials, and it was determined that two empty aluminum drinking cans wrapped in Nashua® 300 Series heavy duty duct tape most appropriately represent the equivalent spring and damper values in Table 6–6. Figure 6-14 illustrates the typical method for preparing

the cans. The top of can-A is removed and a slit is made from the base of can-A to the open end. Can-B, which remains unaltered, is slid into can-A until it is seated snuggly at the bottom of can-A. The two cans are then wrapped in duct tape starting from the base of the cans such that there is approximately 1.5 cm of exposed tapes between wraps. The cans are only wrapped once, from bottom to top. Figure 6-15 shows the typical 1.5 cm spacing of the tape wrappings.

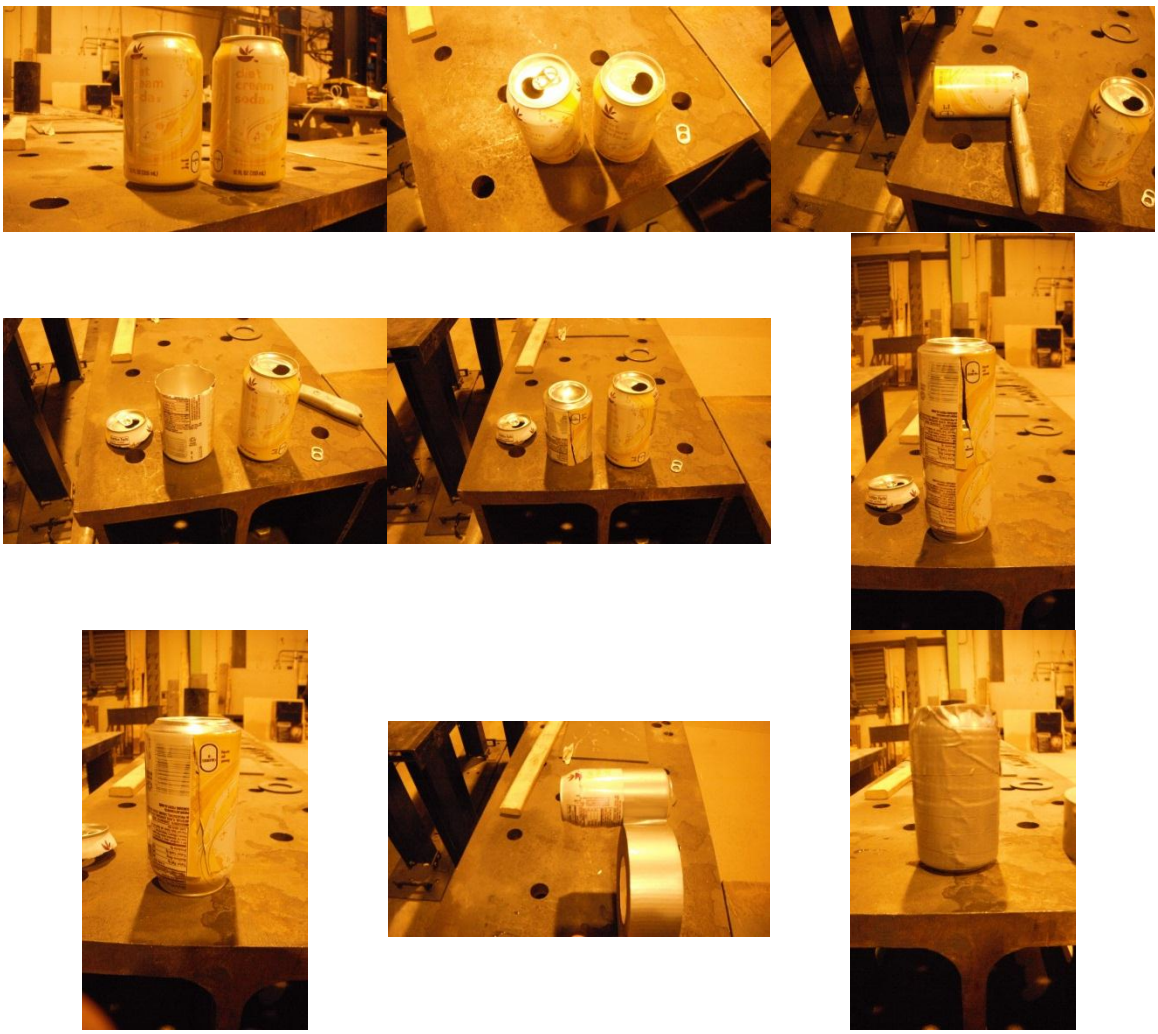

Figure 6-14. Procedure for preparing crush material in 8kg small scale crash tests

Figure 6-15. Typical spacing for duct tape wrappings

The amount of tape was determined by varying the number of wrappings in the rigid-wall, dynamic crush tests. It was determined that a spacing of 1.5 cm, referred to as "lightly taped," most closely resembles the desired spring and damper values. The dynamic crush tests are performed by attaching the crush material the end of the impact beam, raising the impact beam to an initial angular displacement, and allowing the impact beam to swing into a rigid wall or immovable object. When performing a small scale crash test, the cans are attached such that the open end was placed up against the impact beam. The equivalent spring and damper values are then calculated as presented in [2]. A typical high-speed image sequence of the dynamic crush test is shown in Figure 6-16.

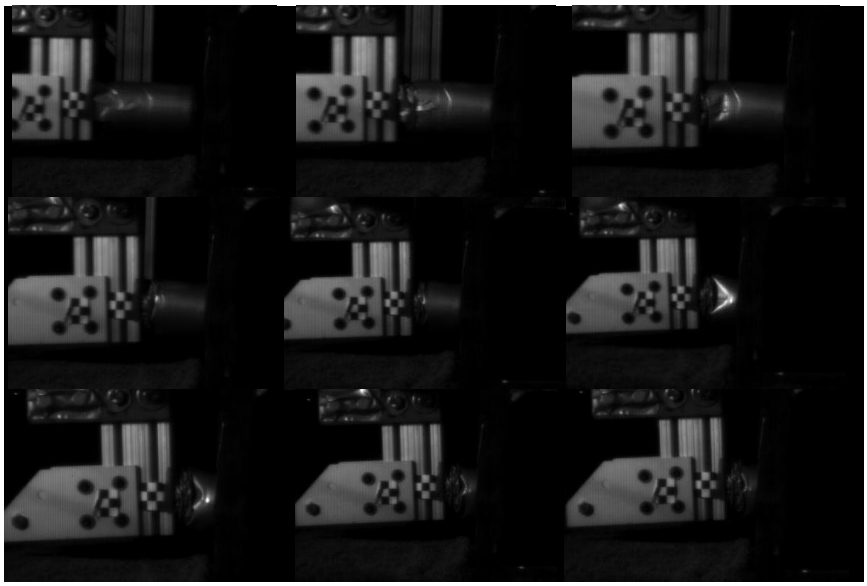

Figure 6-16. High-speed image sequence of dynamic crush test

The equivalent spring and damper values for the average of the dynamic crush tests of the small scale material was calculated to be 35.9 kN/m and 0.538 kN-s/m, respectively. The detailed results and test specific photographs of the crush tests are provided in Appendix C.

6.4 Summary of small scale boulder tests

Two small scale crash tests were performed on dimensionally similar boulders to those found in BST-1 and BST-2. Small-Scale-Boulder-Soil-Test-1 (SSBST-1) was created to be in full similitude with BST-1 in which the boulder was completely flipped out of the soil by the impact vehicle. Small-Scale-Boulder-Soil-Test-2, 3, 4, and 5 (SSBST-2, 3, 4, 5) were created to be in full similitude with BST-2 in there were small boulder displacements. The in-situ soil measurement properties are provided in Appendix B.

6.4.1 Summary of small scale crash test SSBST-1

The small scale parameters in SSBST-1 which provide a dimensionally similar crash test as BST-1 were calculated as presented in Section 5.6 when using the full scale parameters listed in Table 4–1. Table 6–7 shows the desired small scale parameters and the measured small scale parameters for SSBST-1.

Table 6–7. Desired and measured governing parameters for SSBST-1

Parameter	Desired	Measured
$m_{v\delta}$	8 kg	8 kg
$v_{o\delta}$	4.34 m/s	4.31 m/s
g_{δ}	9.81 m/s^2	9.81 m/s^2
β_{δ}	95 MN/m^3	98.6 MN/m^3
$\rho_{soil_{\delta}}$	1,895.9 kg/m^3	1,929.5 kg/m^3
$\rho_{b\delta}$	3,074 kg/m^3	3,074 kg/m^3
L_{δ}	0.0805 m	0.0794 m
W_{δ}	0.1073 m	0.1079 m
H_{δ}	0.2323 m	0.2413m
d_{δ}	0.1267 m	0.127 m
e_{δ}	0.0796 m	0.079 m
$k_{v\delta}$	34.6 kN/m	35.9 kN/m
$c_{v\delta}$	0.503 kN · s/m	0.538 kN s/m

The small scale American Black Granite boulder, SSABG-01, was cut from ABG-01. The pre-test condition of the boulder is shown in Figure 6-17.

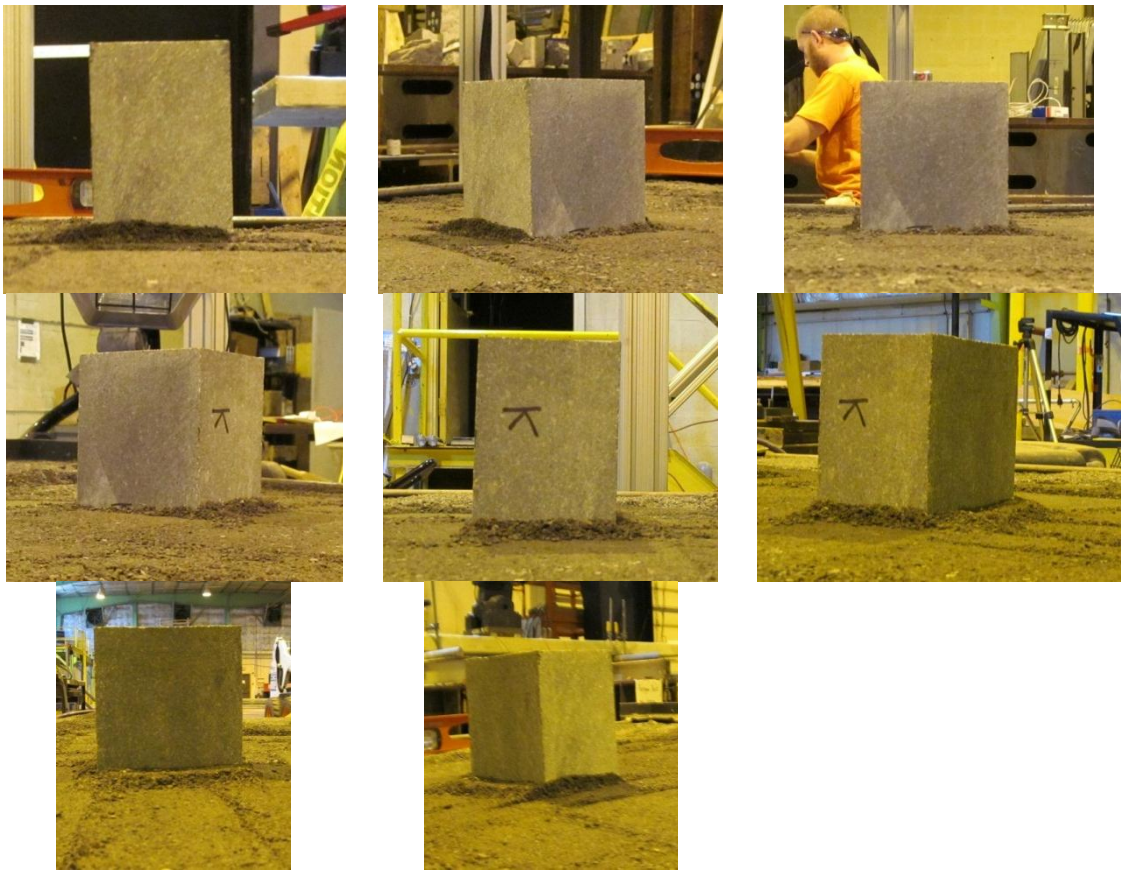

Figure 6-17. Pre-test condition of SSABG-01 in SSBST-1

The orientation of the installed crush material, the centerline of the impact beam relative to the critical impact point, and the eccentricity of the crush material with respect to the boulder are shown in Figure 6-18.

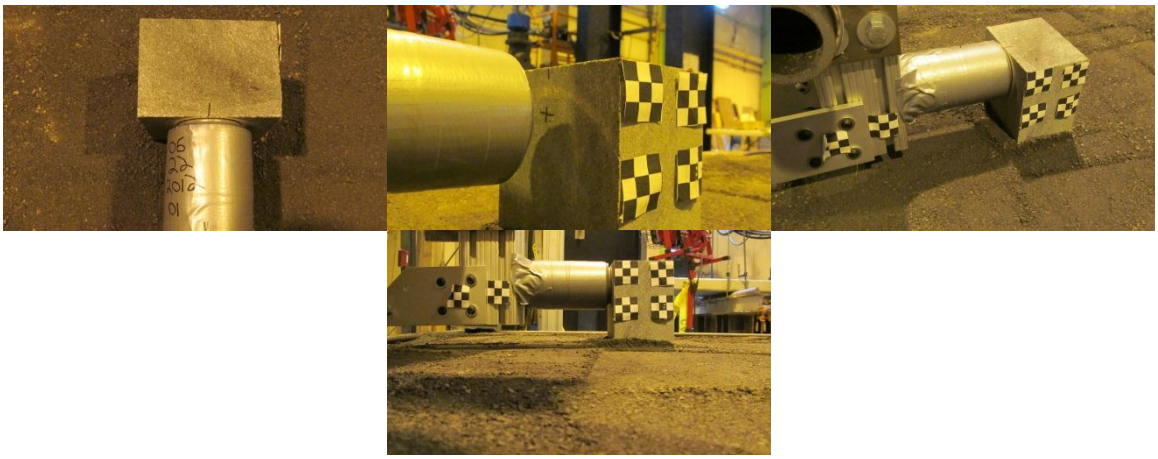

Figure 6-18. Pre-test conditions of the impact beam and crush material in SSBST-1

Figure 6-19 shows the side-view still images extracted from the high-speed video in a chronological sequence of the impact.

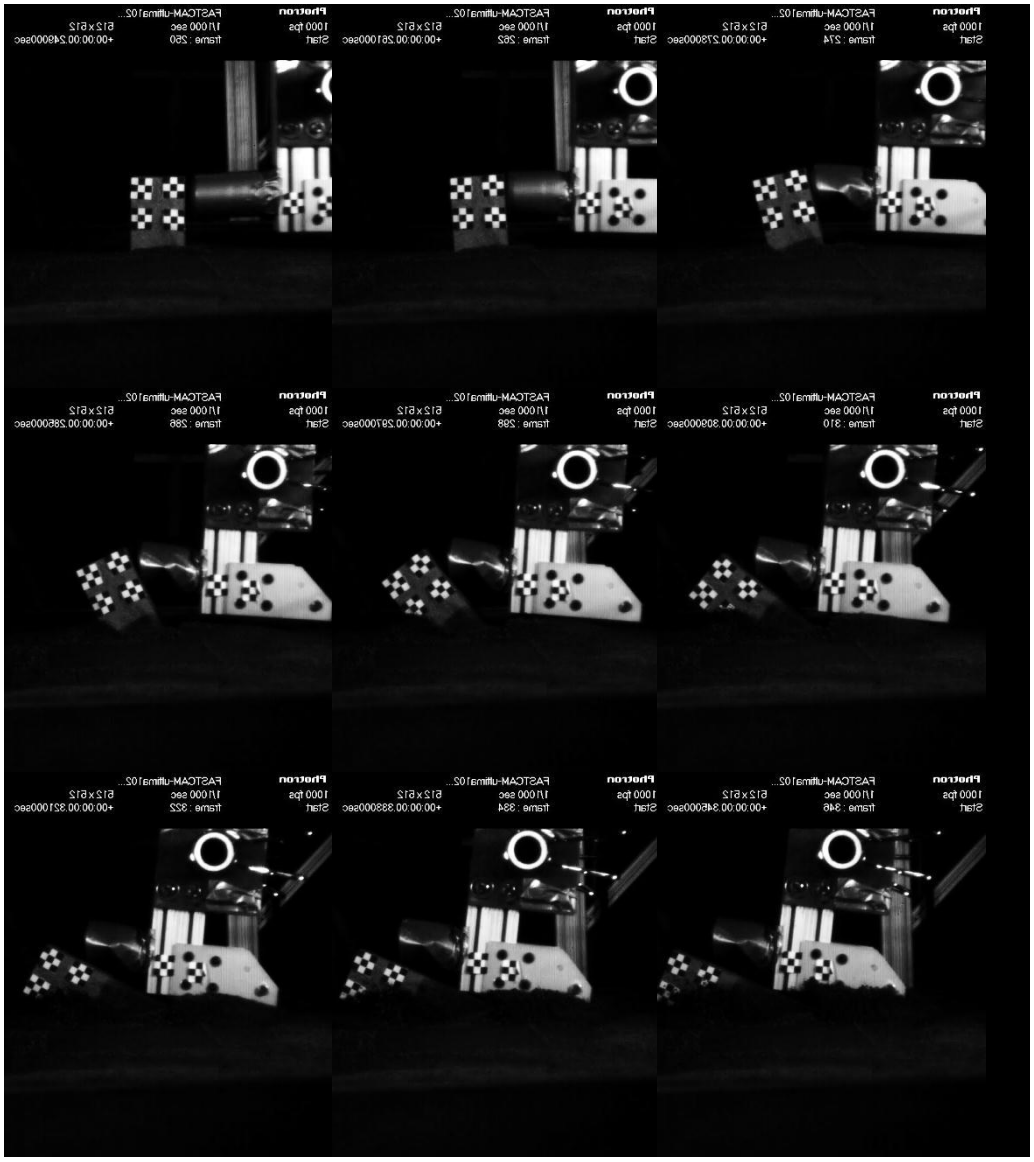

Figure 6-19. High-speed image sequence of SSBST-1

It should be noted that unlike in full scale testing, the pendulum was not able to swing over the boulder due to the base of the rigid arm wedging against the small scale boulder. Figure 6-20 shows the linear displacement of the center of mass of SSABG-01 from the point of impact,

and Figure 6-21 shows the angle of rotation of SSABG-01 from the point of impact. The linear displacement of the impact beam as tracked using the forward fiducial is shown in Figure 6-22.

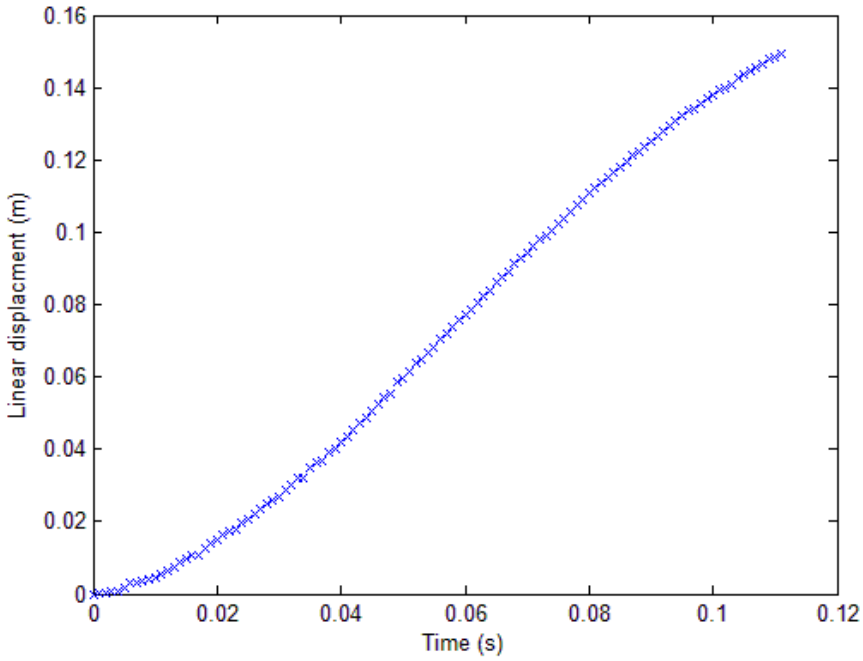

Figure 6-20. Measured linear displacement of the center of mass of SSABG-01 in SSBST-1

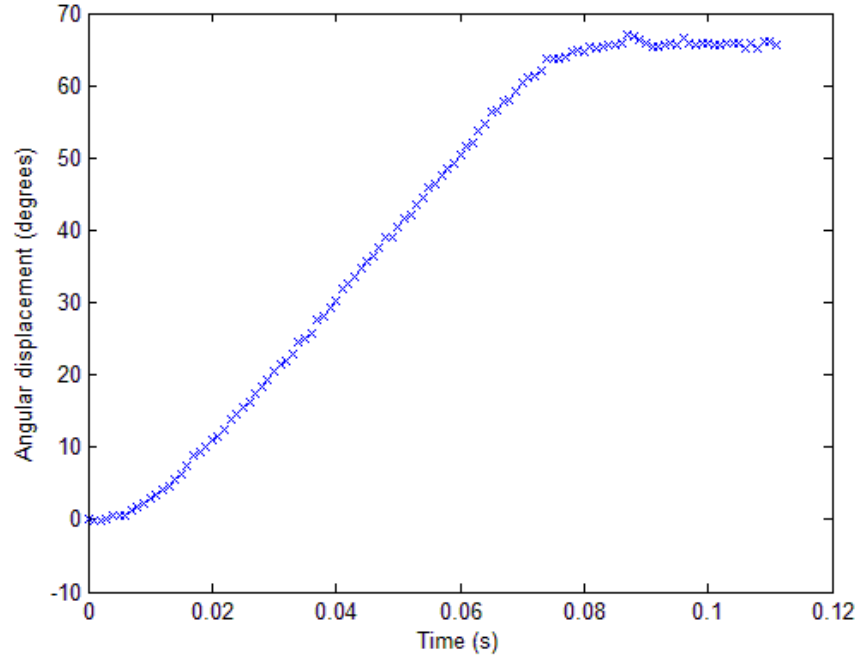

Figure 6-21. Measured angle of rotation of SSABG-01 in SSBST-1

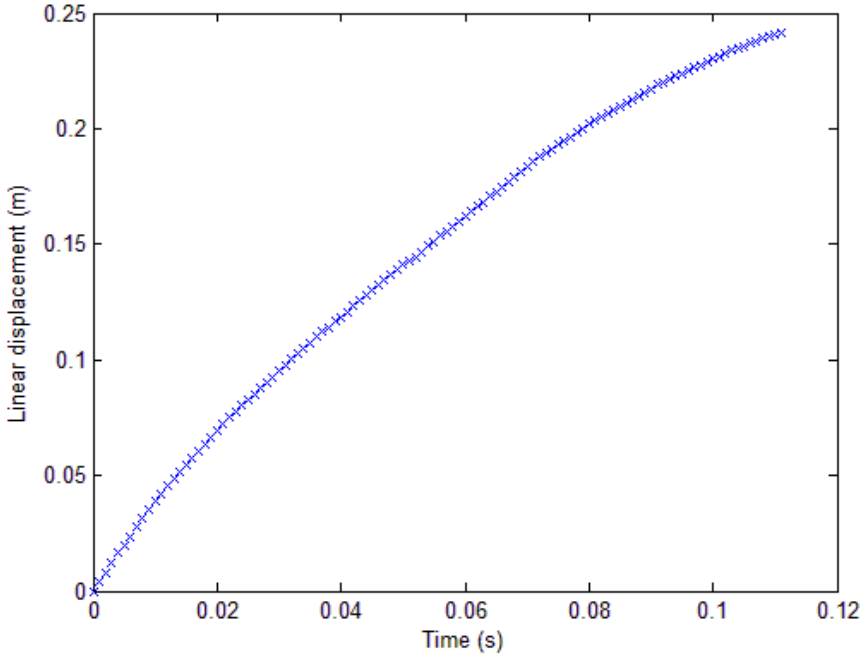

Figure 6-22. Measured linear displacement of the impact beam in SSBST-1

Photographs of the post-test condition of the impact beam are shown in Figure 6-23, and Figure 6-24 shows the post-test condition of SSABG-01 in SSBST-1.

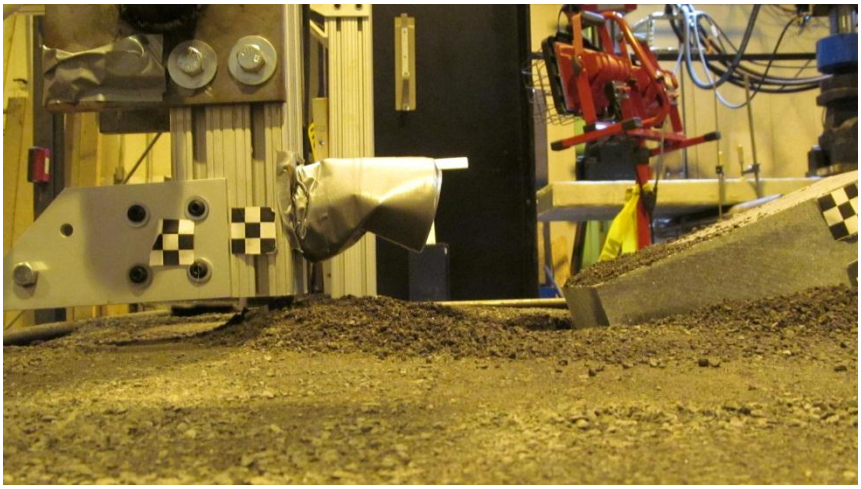

Figure 6-23. Post-test impact beam condition in SSBST-1

Figure 6-24. Post-test condition of SSABG-01 in SSBST-1

6.4.2 Summary of small scale crash test SSBST-2, 3, 4, and 5

The small scale parameters in SSBST-2, 3, 4, and 5 which provide a dimensionally similar crash test as BST-2 were calculated as presented in Section 5.6 when using the full scale parameters listed in Table 4–2. Table 6–8 shows the desired small scale parameters and the measured governing and corresponding dimensionless parameters for SSBST-2, 3, 4, and 5, respectively.

Table 6–8. Desired and measured governing parameters for SSBST-2, 3, 4, and5

	Desired	SSBST-2	SSBST-3	SSBST-4	SSBST-5
$m_{v\delta}$	8 kg	8 kg	8 kg	8 kg	8 kg
$v_{o\delta}$	4.72 m/s	4.81 m/s	4.8 m/s	4.99 m/s	4.94 m/s
g_δ	9.81 m/s^2	9.81 m/s^2	9.81 m/s^2	9.81 m/s^2	9.81 m/s^2
β_δ	95 MN/m^3	90.83 MN/m^3	93.73 MN/m^3	96.87 MN/m^3	91.43 MN/m^3
$\rho_{soil\,\delta}$	1,895.9 kg/m^3	1,856kg/m^3	1,884 kg/m^3	1,907 kg/m^3	1,862 kg/m^3
$\rho_{b\,\delta}$	2,596 kg/m^3	2,379 kg/m^3	2,379 kg/m^3	2,379 kg/m^3	2,379 kg/m^3
L_δ	0.1749 m	0.1746 m	0.1746 m	0.1746 m	0.1746 m
W_δ	0.178 m	0.1778 m	0.1778 m	0.1778 m	0.1778 m
H_δ	0.3635 m	0.3556m	0.3556m	0.3556m	0.3556m
d_δ	0.2151 m	0.215 m	0.22 m	0.21 m	0.225 m
e_δ	0.0994 m	0.099 m	0.098 m	0.094 m	0.096 m
$k_{v\delta}$	34.6 kN/m	35.9 kN/m	35.9 kN/m	35.9 kN/m	35.9 kN/m
$c_{v\delta}$	0.507 kN · s/m	0.538 kN s/m	0.538 kN s/m	0.538 kN s/m	0.538 kN s/m

Concrete was used to create the small scale Rockville White Granite boulder since the measured density of the granite was similar to typical mass densities for concrete. The small scale Rockville White boulder is referenced as SSRWC-01 since it was cast from concrete. SSRWC-01was cast from high strength Quikrete® and #4 rebar such that the overall dimensions were measured to be 0.1746 m-L x 0.1778 m-W x 0.3556 m-H with respect to the impact direction. The concrete was mixed as directed and allowed to cure for one week in an environmental chamber before performing any crash tests. Figure 6-25 shows the creation process of SSRWC-01.

Figure 6-25. Creation of SSRWC-01 (largest center boulder)

After curing, the mass of SSRWC-01 was measured to be 26.25 kg which corresponds to a density of 2,379 kg/m^3. The installation of SSRWC-01 in SSBST-2 is shown in Figure 6-26, and the pre-test condition of the boulder is shown in Figure 6-27. The installation process for SSBST-3, 4, and 5 was carried out in the manner as SSBST-2.

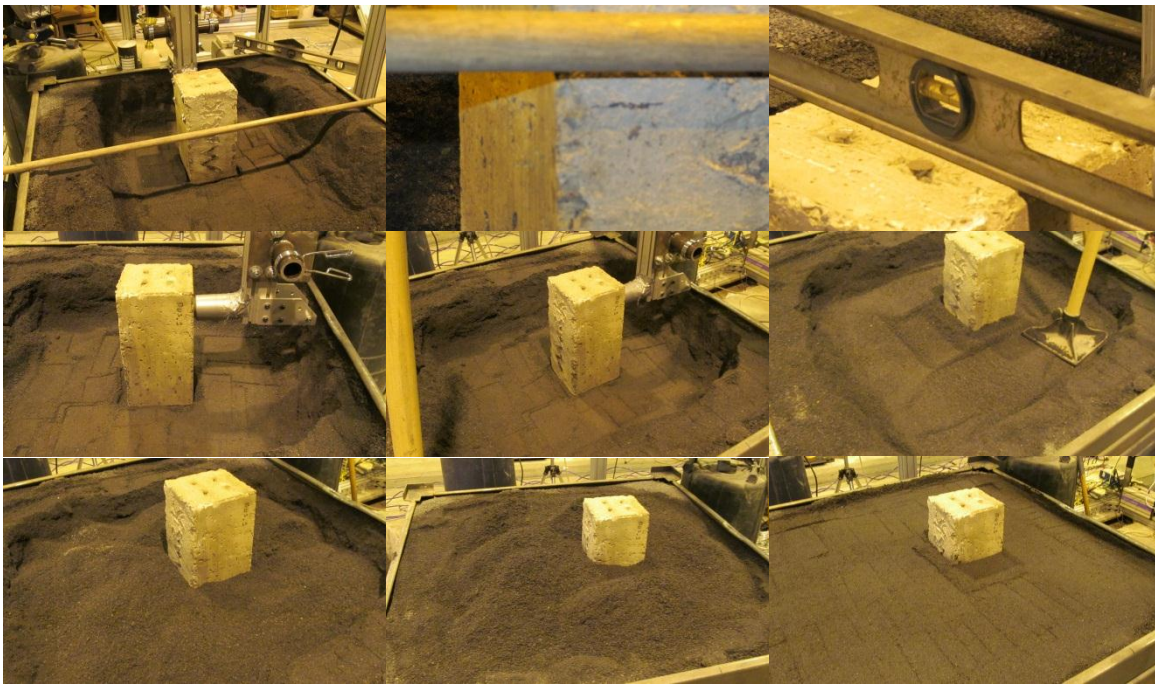

Figure 6-26. Installation of RWG-01 in SSBST-2

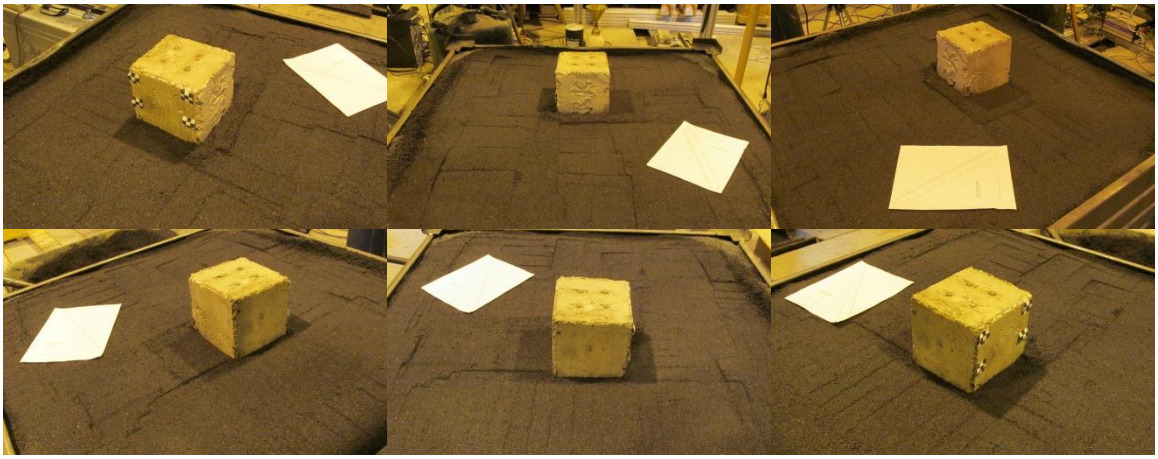

Figure 6-27. Pre-test condition of SSRWC-01 in SSBST-2 (letter sized paper for size reference)

The orientation of the installed crush material, the centerline of the impact beam relative to the critical impact point, and the eccentricity of the crush material with respect to the boulder for SSBST-2 is shown in Figure 6-28. The crush material and orientation for SSBST-3, 4, and 5 were prepared in the manner as SSBST-2.

Figure 6-28. Pre-test conditions of the impact beam and crush material in SSBST-2

Figure 6-29 shows the side-view still images extracted from the high-speed video in a chronological sequence of the impact from SSBST-2.

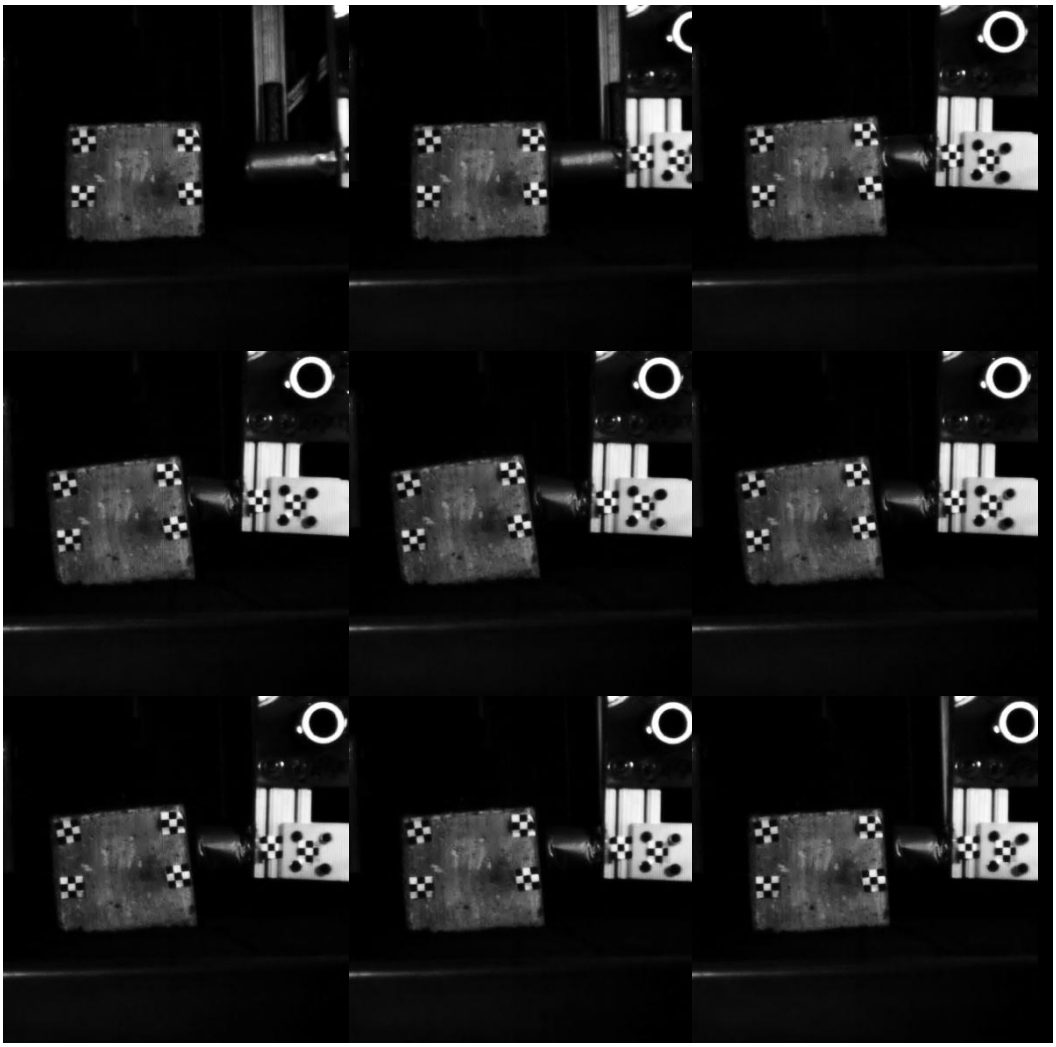

Figure 6-29. High-speed image sequence of SSBST-2

Figure 6-30 shows the linear displacement of the center of mass of SSRWC-01 from the point of impact, and Figure 6-31 shows the angle of rotation of SSRWC-01 from the point of impact. The linear displacement of the impact beam as tracked using the forward fiducial is shown in Figure 6-32.

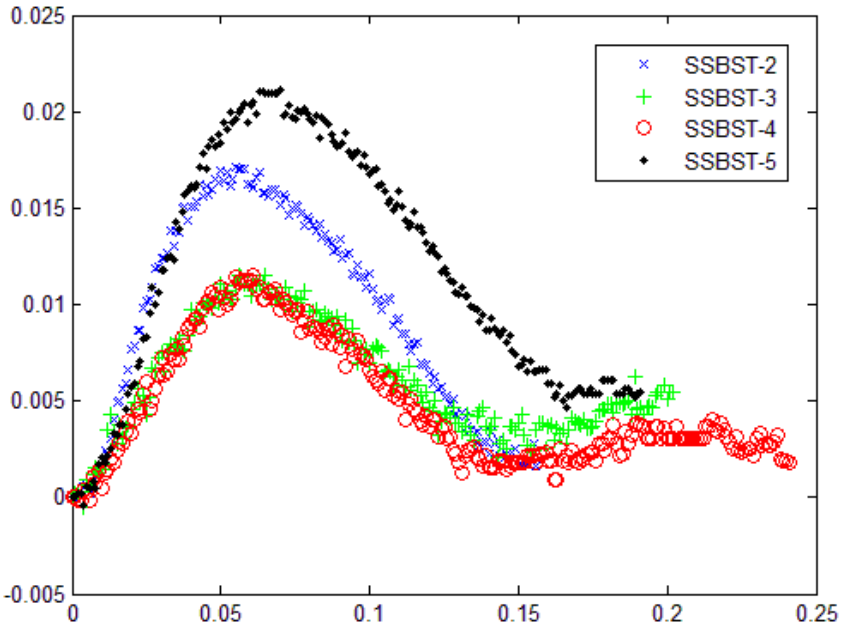

Figure 6-30. Linear displacement of the center of mass of SSRWC-01in SSBST-2, 3, 4, and 5

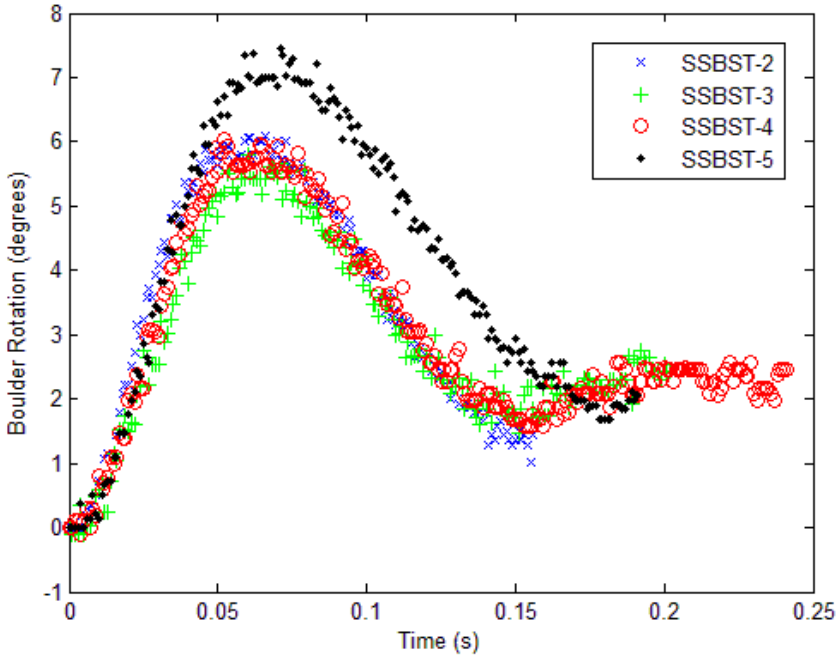

Figure 6-31. Angle of rotation of SSRWC-01 in SSBST-2, 3, 4, and 5

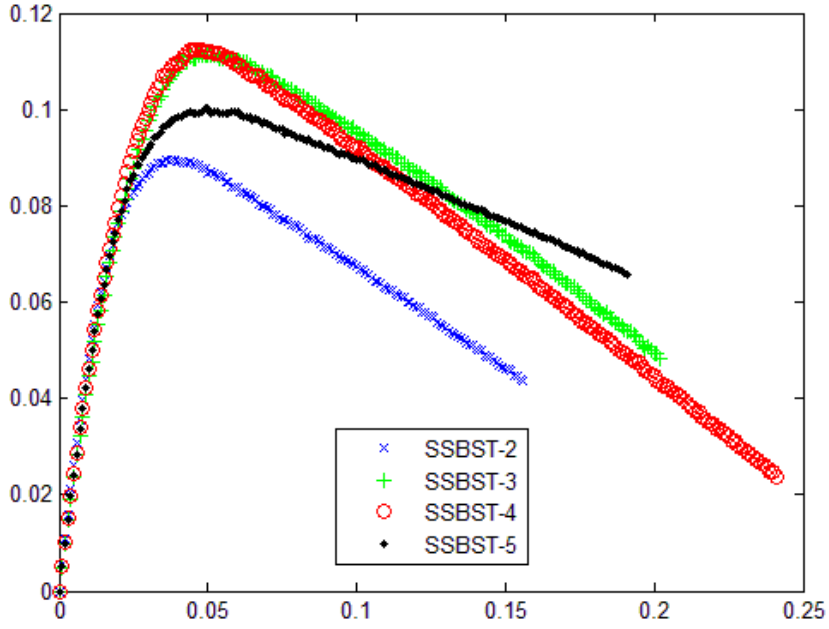

Figure 6-32. Linear displacement of the impact beam in SSBST-2, 3, 4, and 5

Photographs of the post-test condition of the impact beam from SSBST-2 are shown in Figure 6-33, and Figure 6-34 shows the post-test condition of SSRWC-01 from SSBST-2. The post-test conditions for SSBST-3, 4, and 5 were typical of SSBST-2. The post-test conditions for SSBST-3, 4, and 5 were typical as those seen in SSBST-2.

Figure 6-33. Post-test impact beam condition in SSBST-2

Figure 6-34. Post-test condition of SSRWC-01 in SSBST-2

6.5 Comparison of small scale simulations to small scale crash test results

Similar to the full scale simulations, the results from the small scale crash tests can be directly compared to the simulated results by either using the dimensionless state-space equations of motion presented in Chapter 5 or the low-order model presented in Chapter 3.

6.5.1 Comparison of small scale simulation of SSBST-1 to small scale crash test results

Figure 6-35, Figure 6-36, and Figure 6-37 show the comparison of the measured crash test results from SSBST-1 to the simulated low-order results using the measured parameters listed in Table 6–7. Figure 6-35 shows the comparison of the measured and simulated small scale linear displacement of the center of mass of the boulder, Figure 6-36 shows the comparison of the measured and simulated small scale angle of rotation of the boulder, and Figure 6-37 shows the comparison of the measured and simulated small scale linear displacement of the impact vehicle.

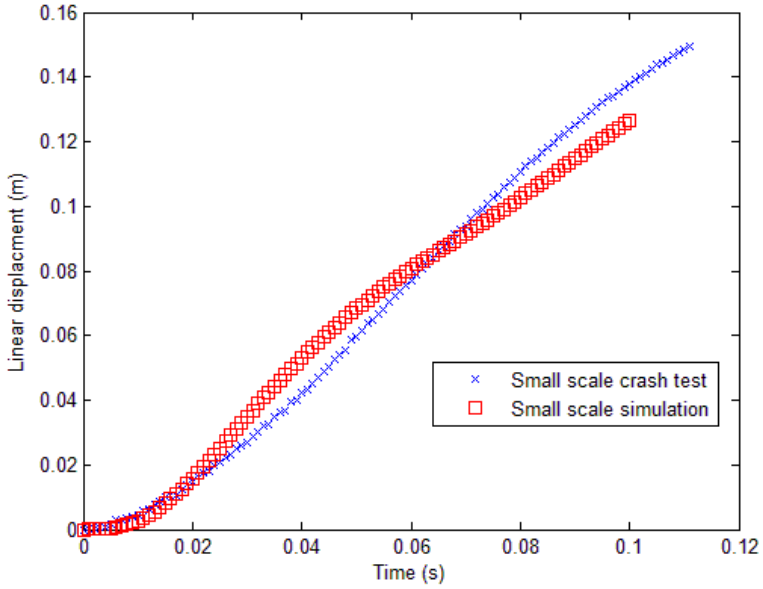

Figure 6-35. Comparison of the measured displacement of the center of mass of SSABG-01 in SSBST-1 to the simulated displacement from the low-order model

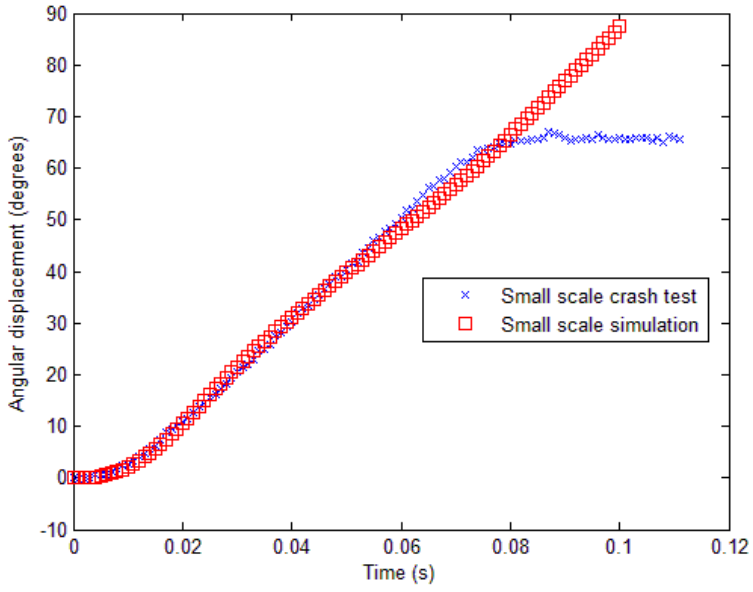

Figure 6-36. Comparison of the measured angle of rotation of SSABG-01 in SSBST-1 to the simulated angle of rotation from the low-order model

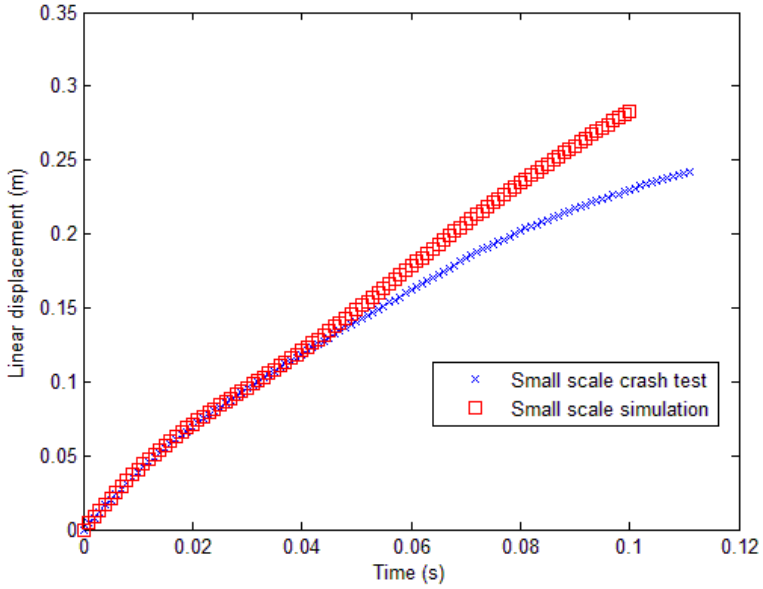

Figure 6-37. Comparison of the measured displacement of the vehicle in SSBST-1 to the simulated displacement from the low-order model

As seen in the comparison of full scale simulations and experiments, the model loses accuracy after approximately 20° of boulder rotation. This is expected because of the small-angle assumptions used to create the model.

6.5.2 Comparison of small scale simulation of SSBST-2, 3, 4, and 5 to small scale crash test results

Figure 6-38, Figure 6-39, and Figure 6-40 show the comparison of the measured crash test results from SSBST-2, 3, 4, and 5 to the simulated, small scale low-order results using the measured parameters listed in Table 6–8. Figure 6-38 shows the comparison of the linear displacement of the center of mass of the boulder, Figure 6-39 shows the comparison of the angle of rotation of the boulder, and Figure 6-40 shows the comparison of the linear displacement of the impact vehicle.

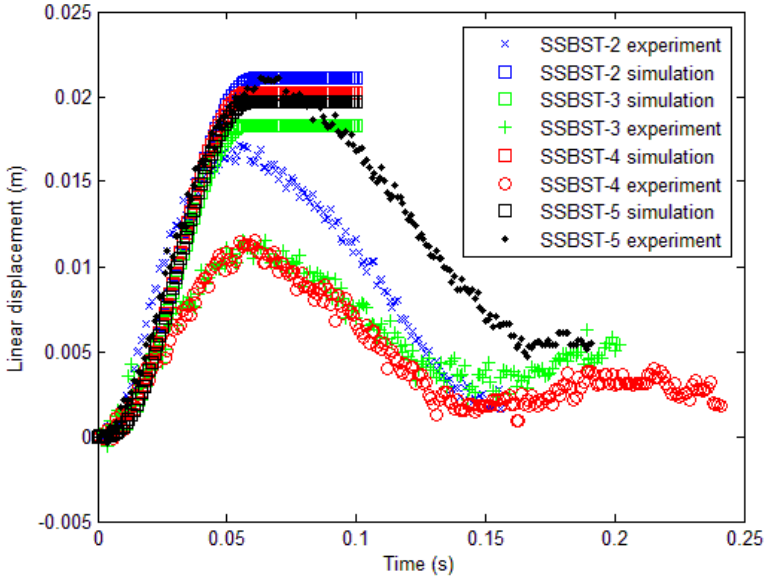

Figure 6-38. Comparison of the small scale measured and simulated displacement of the center of mass of SSRWC-01 in SSBST-2, 3, 4, and 5

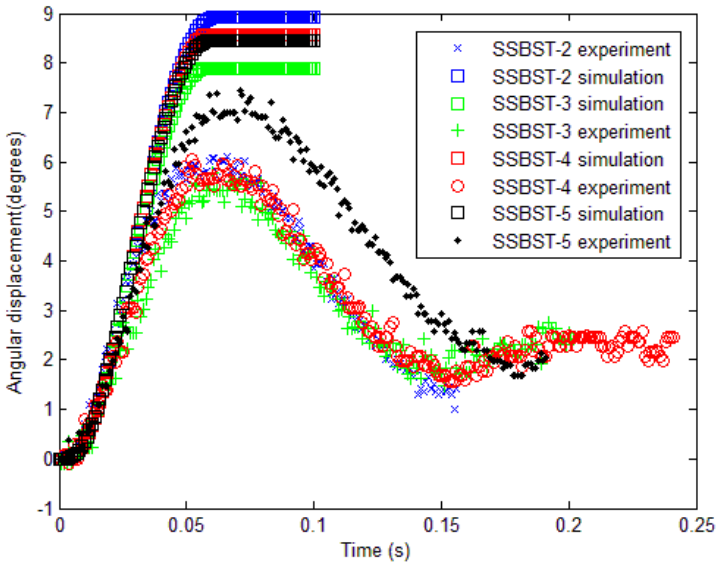

Figure 6-39. Comparison of the small scale measured and simulated angle of rotation of SSRWC-01 in SSBST-2, 3, 4, and 5

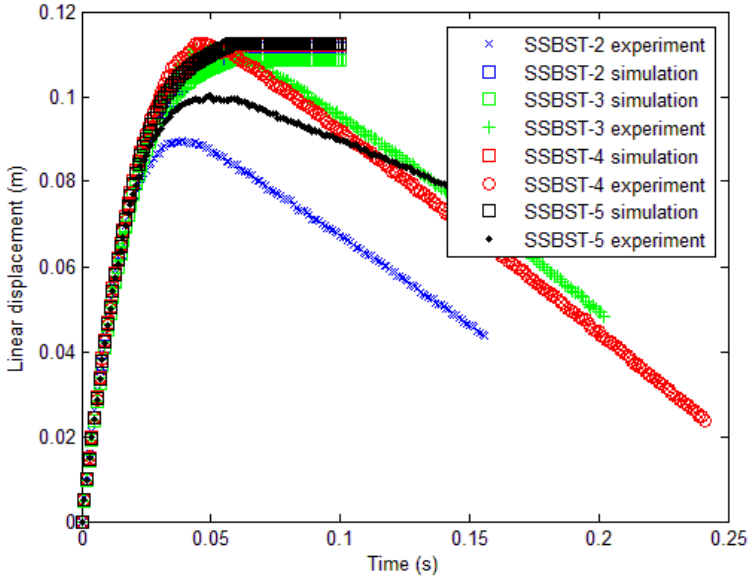

Figure 6-40. Comparison of the small scale measured and simulated displacement of the vehicle in SSBST-2, 3, 4, and 5

6.6 Comparison of dynamically similar small scale crash test results to full scale crash test results

This section shows the comparison of the small scale crash test results to the corresponding dimensionally similar, full scale crash test results presented in Chapter 4. The small scale tests will match the full scale tests better when the two experiments are in full similitude or are scaled similar. Table 6–9 shows the comparison of the governing dimensionless π parameters between BST-1 and SSBST-1, and Table 6–10 shows the comparison of the governing dimensionless π parameters between BST-2 and SSBST-2, 3, 4, and 5.

Table 6–9. Comparison of governing dimensionless parameters of SSBST-1to BST-1

Governing dimensionless π parameter	BST-1	SSBST-1
π_{β}	$8.5841 \cdot 10^{6}$	$8.5305 \cdot 10^{6}$
$\pi_{\rho_{soil}}$	1,680.5	1,637.6
π_{ρ_b}	2,724.9	2,609
π_L	0.0419	0.0419
π_W	0.0558	0.057
π_H	0.1209	0.1274
π_d	0.066	0.0671
π_e	0.0414	0.0417
π_{k_v}	847.05	866.2
π_{c_v}	27.84	29.54

Table 6–10. Comparison of governing dimensionless parameters of SSBST-2, 3, 4, 5 to BST-2

Governing Dimensionless π parameter	BST-2	SSBST-2	SSBST-3	SSBST-4	SSBST-5
π_{β}	$1.4183 \cdot 10^7$	$1.5182 \cdot 10^7$	$1.5472 \cdot 10^7$	$2.0185 \cdot 10^7$	$1.7935 \cdot 10^7$
$\pi_{\rho_{soil}}$	2,776.6	3,043.3	3,051	3,898	3,583
π_{ρ_b}	3,802	3,901	3853	4,863	4,577
π_L	0.077	0.074	0.074	0.068	0.0702
π_W	0.0784	0.0754	0.076	0.07	0.072
π_H	0.16	0.1508	0.1514	0.1401	0.143
π_d	0.0947	0.091	0.0937	0.0827	0.09
π_e	0.0438	0.042	0.0417	0.037	0.039
π_{k_v}	1,008.6	1,078.8	1,074.4	1,161	1,138
π_{c_v}	30.54	32.97	32.91	34.2	33.87

It is expected that the small scale tests results will show good agreement with the full scale results since all of the dimensionless π groupings are similar.

Similar to the comparison between dynamically similar simulations, the small scale crash tests can be compared to various sized crash tests either by scaling the results up to match the full scale parameters, scaling the full scale results down to the match the small scale parameters, or transforming both small and full scale results into the dimensionless form.

6.6.1 Comparisons of scaled up SSBST-1 to BST-1 in full scale time

Figure 6-41 shows the comparison of the impact sequence from the high-speed videos for SSBST-1 and BST-1. It should be noted that the time dimension of the small scale test was scaled up to the full scale size when comparing the high-speed image sequence.

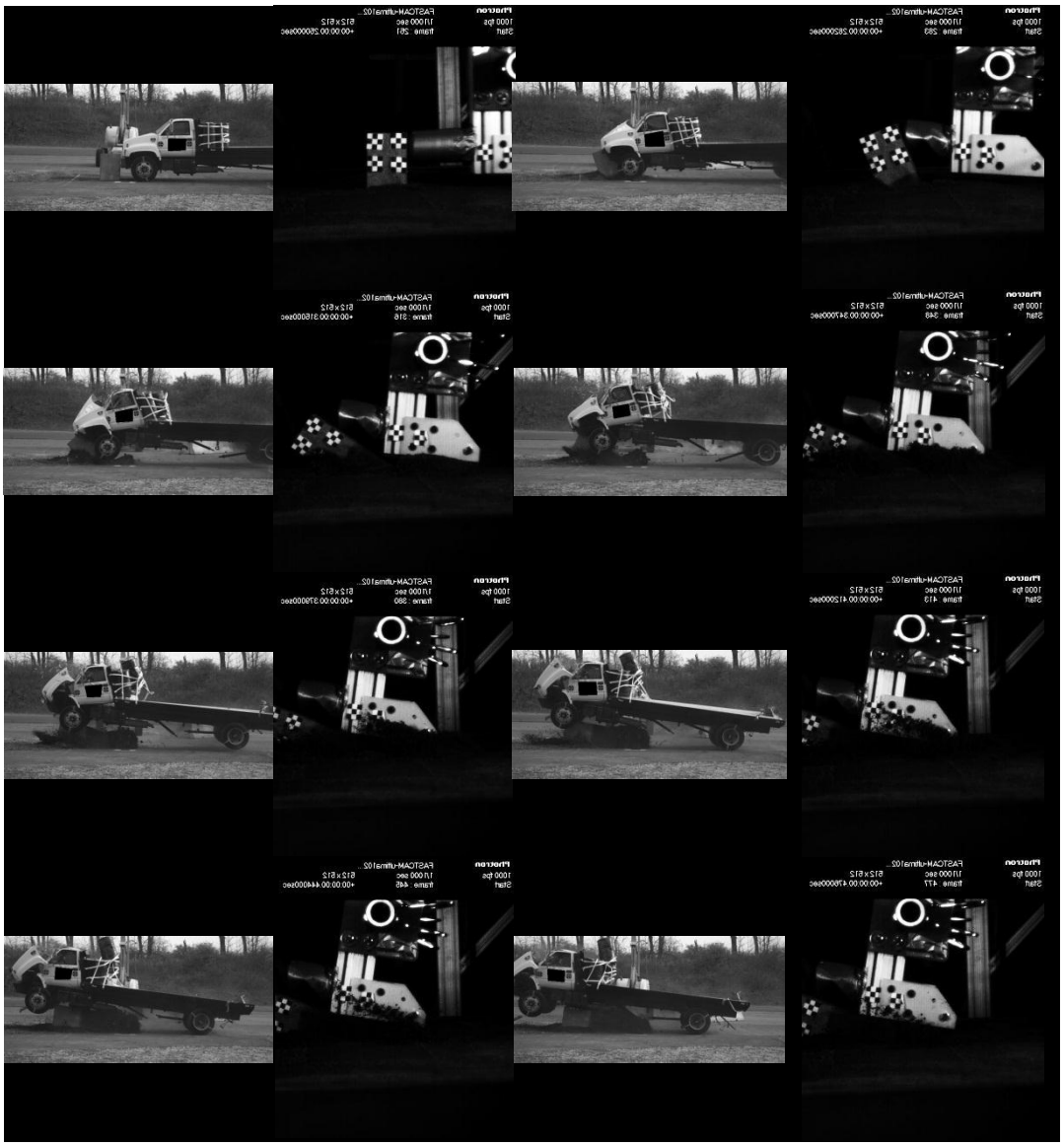

Figure 6-41. Comparison of high-speed image sequences from SSBST-1 and BST-1

Figure 6-42, Figure 6-43, and Figure 6-44 show the comparison of the scaled-up crash test results from SSBST-1 to the measured crash test results from BST-1. Figure 6-42 shows the

comparison of the linear displacement of the center of mass of the boulder, Figure 6-43 shows the comparison of the angle of rotation of the boulder, and Figure 6-44 shows the comparison of the linear displacement of the impact vehicle.

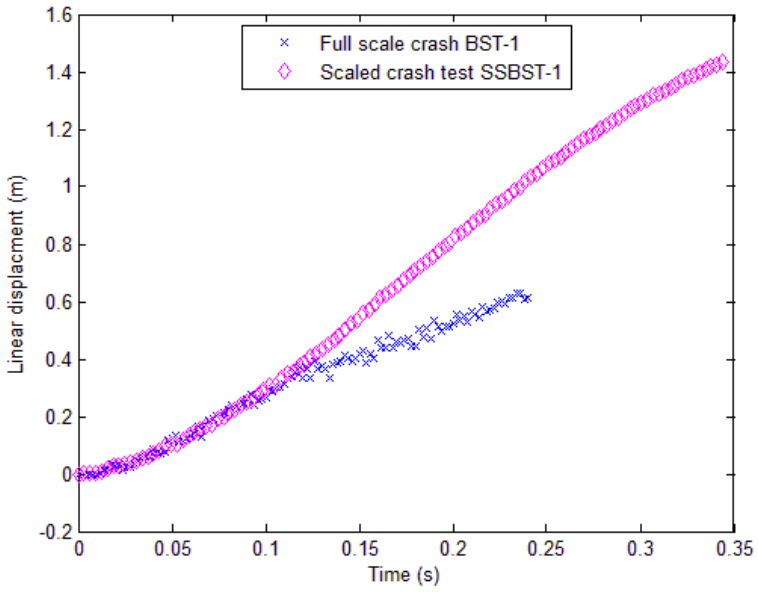

Figure 6-42. Comparison of the small and full scale measured displacement of the center of mass of SSABG-01 in SSBST-1 to ABG-01 in BST-1

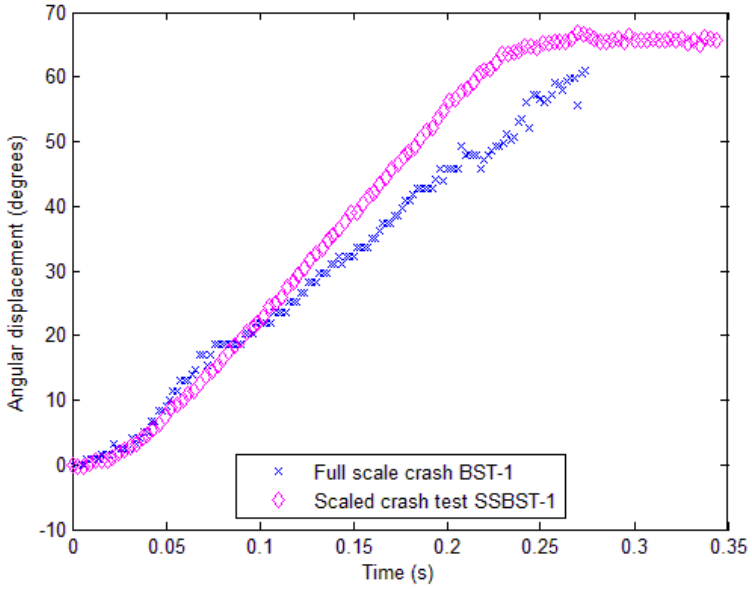

Figure 6-43. Comparison of the small and full scale measured angle of rotation of SSABG-01 in SSBST-1 to ABG-01 in BST-1

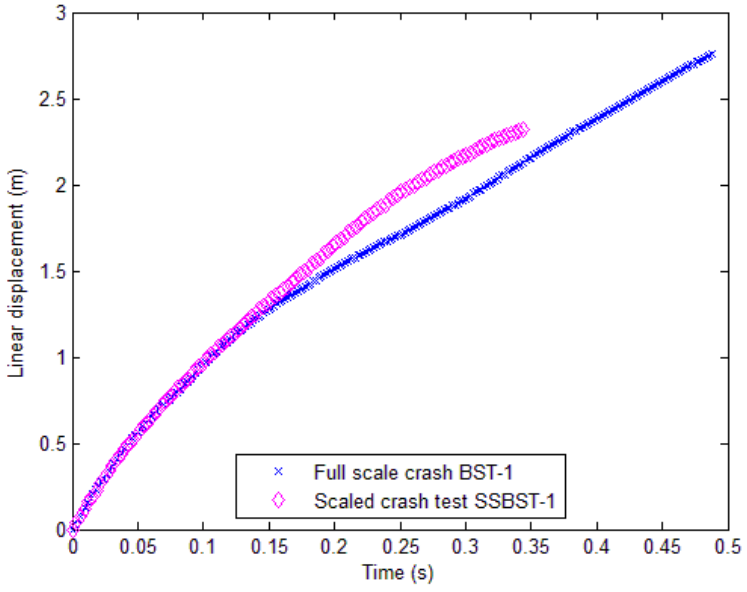

Figure 6-44. Comparison of the small and full scale measured displacement of the vehicle in SSBST-1 and BST-1

It should be noted that the variation in dynamics of the small scale pendulum are more pronounced after 20° of boulder rotation has occurred. The velocity of a full scale vehicle will remain mostly in the horizontal direction even after the boulder has begun to rotate out of the soil, whereas the pendulum will rotate higher as more energy is being converted back into potential form.

6.6.2 Comparisons of scaled up SSBST-2, 3, 4, and 5 to BST-2 in full scale time

Figure 6-45 shows the comparison of the impact sequence from the high-speed videos for SSBST-2 and BST-2. The high-speed comparison for SSBST-3, 4, and 5 were typical of the results seen in Figure 6-45. Again, it should be noted that the time dimension of the small scale test was scaled up to the full scale size when comparing the high-speed image sequence.

Figure 6-45. Comparison of high-speed image sequences from SSBST-2 and BST-2

Figure 6-46, Figure 6-47, and Figure 6-48 show the comparison of the small and full scale measured crash test results from SSBST-2, 3, 4, and 5 and BST-2. Figure 6-46 shows the comparison of the linear displacement of the center of mass of the boulder, Figure 6-47 shows the comparison of the angle of rotation of the boulder, and Figure 6-48 shows the comparison of the linear displacement of the impact vehicle.

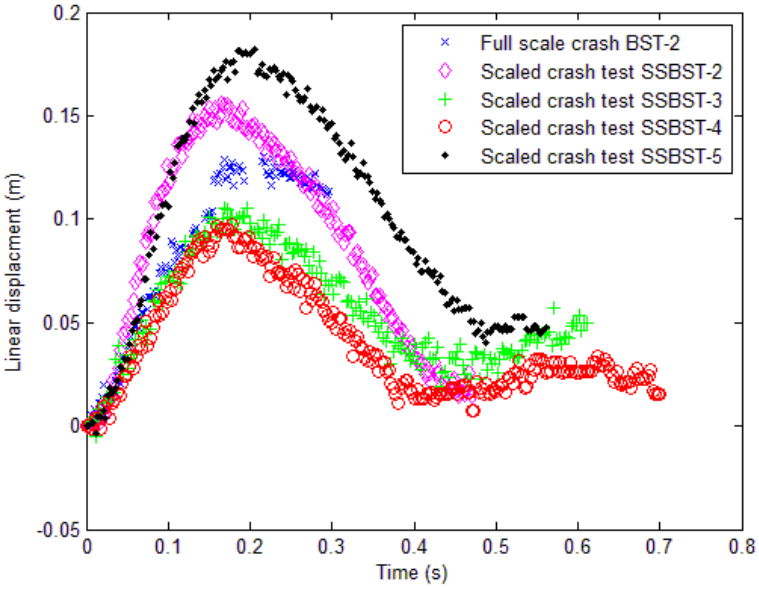

Figure 6-46. Comparison of the small and full scale measured displacement of the center of mass of SSRWC-01 in SSBST-2, 3, 4, and 5 to RWG-01 in BST-2

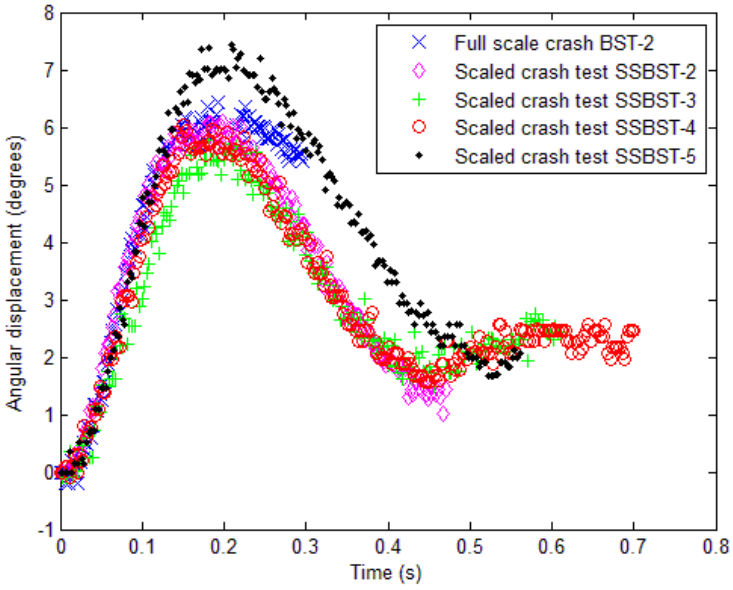

Figure 6-47. Comparison of the small and full scale measured angle of rotation of SSRWC-01 in SSBST-2, 3, 4, and 5 to RWG-01 in BST-2

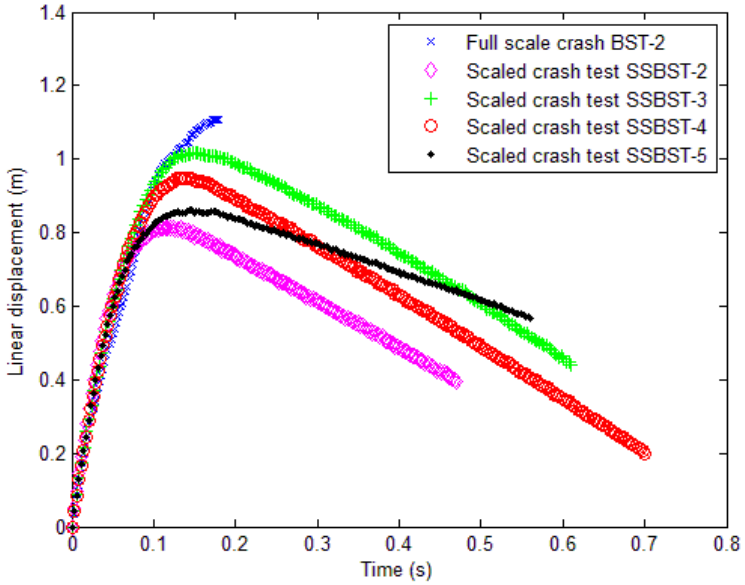

Figure 6-48. Comparison of the small and full scale measured displacement of the vehicle in SSBST-2, 3, 4, and 5 and BST-2

6.7 Contributions of this chapter

The contributions of this chapter are as follows:

(1) Validate dimensionless equations of motion and scaling laws using scaled similar simulations

(2) Present the test equipment and procedure associated with small scale crash tests

(3) Present the methodology for measuring and parameterizing the small scale test setup

(4) Present a summary of the small scale crash tests and crash test results

(5) Compare the small scale crash test results to the low-order model results

(6) Compare the small scale crash test results to the full scale crash test results

CHAPTER 7

INTERPRETATION OF MODEL RESULTS AS PASS/FAIL BOUNDARIES IN THE DESIGN SPACE

Previous chapters showed that both the simulations and scale experiments are able to predict motion of an impacted boulder quite well. The intent of this chapter is to present the results from the low-order model simulations as pass/fail boundaries which can be quickly read and interpreted. The pass/fail boundaries are based solely on variations in boulder geometries and not the soil conditions. The boundaries are represented as 2-D contour plots which span various boulder lengths, widths for a given height. As stated in Chapter 4, the low-order model begins to lose fidelity when the boulder rotates beyond 20° measured from vertical. Therefore, a pass/fail boundary is imposed on the model results at a boulder rotation of 20°. Additionally, a pass/fail boundary is enforced on boulders that are expected to fracture as predicted using the methodology presented in Chapter 3. Lastly, the mass of the boulder is limited to a maximum value.

This chapter is organized as follows:

The methods for creating and interpreting the pass/fail boundaries are presented in Section 7.1. The pass/fail boundaries for a maximum boulder mass and omnidirectional predicted fracture are presented in Section 7.2 and Section 7.3, respectively. The pass/fail boundaries associated with an angular rotation beyond 20° is presented in Section 7.4. The pass/fail contours for a single impact direction are presented in Section 7.5 as a combination of the aforementioned pass/fail boundaries. Lastly, the pass/fail contour plots are presented for omnidirectional impacts in Section 7.6.

7.1 Creation of 2-D contour plots for typical, full scale, governing crash test parameters

The 2-D contour plots are created by iterating the low-order model simulation for various boulder geometries and recording the simulated output. Table 7–1 shows the nominal set of governing parameters which are not varied between simulation iterations. The effect of variations in other model parameters is beyond the scope of this work.

Table 7–1. Nominal parameters used in generating pass/fail contour plots

$\rho_{soil} = 1895.9$ kg/m^3	$k_v = 3{,}103$ kN/m	$\beta = 95$ MN/m^3
$\rho_b = 3{,}074$ kg/m^3	$c_v = 138$ kN s/m	$e = 0.75$ m
$m_v = 6800$ kg	$v_o = 13.4$ m/s	$\varphi' = 43.2°$

The boulder geometries were varied from 0.5 m to 2 m with respect to length and width. The lengths and widths were divided into 100 evenly spaced elements, and the heights of the boulders were varied from 1.5 m to 4 m in increments of 0.5 m. The embedment depth for each boulder was such that 1 m of the boulder protruded above the surface of the soil. For example, a 3 m-H boulder is assumed to have a 2 m embedment depth. The results of the simulations are stored in a matrix format which is then easily represented on 2-D contour plots using MATLAB®. The pass/fail contour plots are presented simply as a black fail zone and a gray pass zone, similar to the fracture contour plot presented in Section 4.6.

7.2 Application of pass/fail boundaries associated with the mass of various sized boulders

The most straightforward pass/fail boundary is imposing a limiting maximum mass of a boulder. It should be obvious that extremely large boulders will not rotate beyond the 20° limit.

It becomes unreasonable, however, to analyze boulders of excessive size from both a computational and experimental standpoint. Experimental limitations are partially due to full scale test setups and apparatus. Particularly, the mass of a boulder should be constrained to adhere to viable installation processes and associated installation equipment.

Assuming the desired test boulder is not at the same location as where it will be installed, the largest allowable mass is assumed to be related to the maximum gross vehicular weight allowed on a road as this will limit the boulder mass according to shipping restrictions. The maximum gross vehicular weight on a United States highway is limited to 80,000 lbs. [29]. Gross vehicular weights may be permitted above 80,000 lbs., but overweight fees must be applied. The 80,000 lbs. (36,287 kg) GVWR is used to determine upper bounds for boulder sizes. It is assumed that towing vehicle and trailer weight approximately 34,000 lbs. (15,422 kg) [30], which imposes a maximum boulder mass of approximately 46,000 lbs. (20,865 kg). Figure 7-1 – Figure 7-6 shows the pass/fail contour plots with respect to a maximum boulder mass.

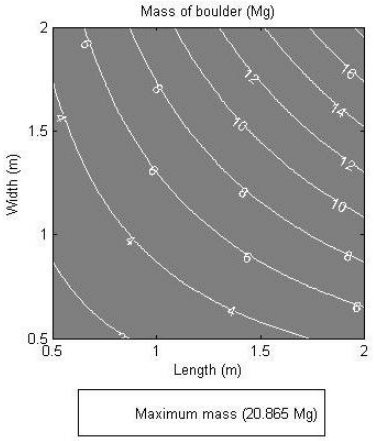

Figure 7-1. Maximum mass pass/fail contour plot for boulders of 1.5 m - H

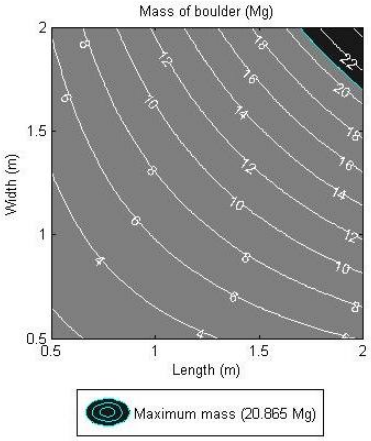

Figure 7-2. Maximum mass pass/fail contour plot for boulders of 2 m - H

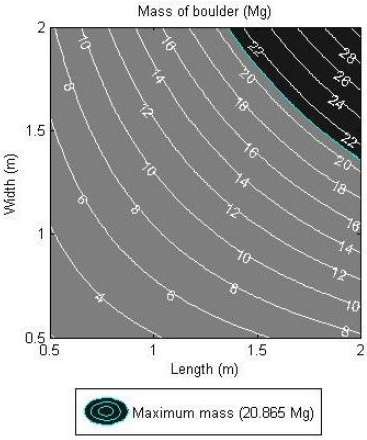

Figure 7-3. Maximum mass pass/fail contour plot for boulders of 2.5 m - H

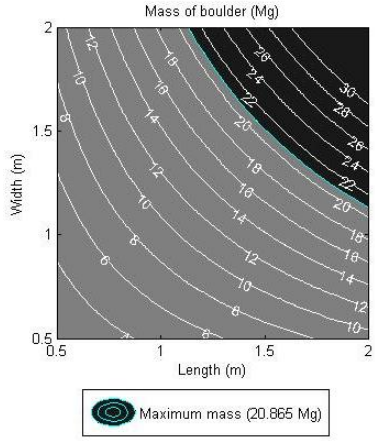

Figure 7-4. Maximum mass pass/fail contour plot for boulders of 3 m - H

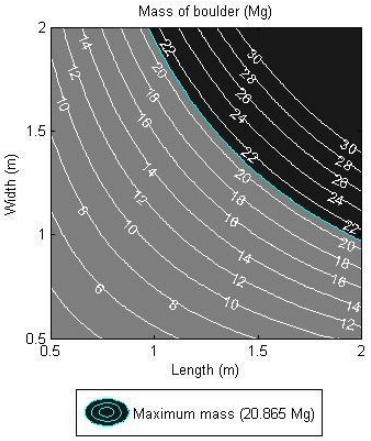

Figure 7-5. Maximum mass pass/fail contour plot for boulders of 3.5 m - H

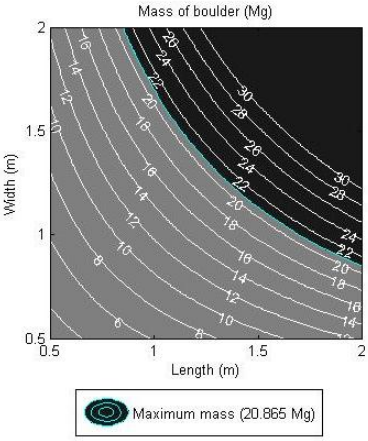

Figure 7-6. Maximum mass pass/fail contour plot for boulders of 4 m - H

7.3 Application of pass/fail boundaries associated with static fracture predictions for boulders

The application of fracture pass/fail conditions simply cuts off all boulder geometries below the pass/fail contours plots presented in Section 4.6. The pass/fail contour is applied for impact conditions with respect to both the length and the width of the boulder. Doing so better ensures that the selected boulder will not fracture regardless of impact direction. Figure 7-7 shows the pass/fail contour plot for an omnidirectional impact. It should be noted that there is only one fracture contour plot since the simulation always assumes that 1 m of the boulder is protruding above the surface of the soil.

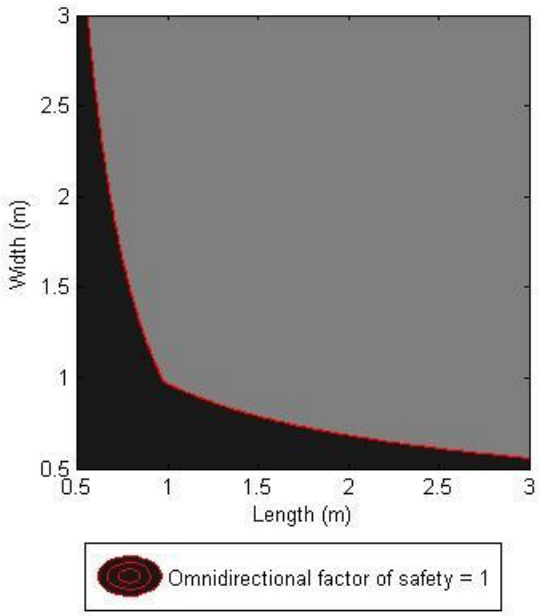

Figure 7-7. Predicted fracture contour plot for omnidirectional impact of rigidly fixed boulders

It should be noted that Figure 7-7 is similar in appearance to Figure 4-68, since it is a transposed overlay of Figure 4-68. It should also be noted that the factors of safety are not shown because of the omnidirectional loading.

7.4 Application of pass/fail boundaries associated with maximum angular rotation of the boulder in a full scale crash test

The maximum angular rotation contour plots formed by imposing a maximum angular rotation of 20° is, which results in Figure 7-8 – Figure 7-13.

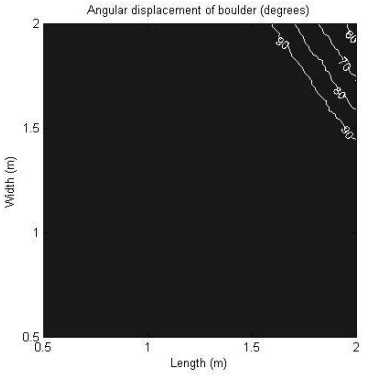

Figure 7-8. Angular pass/fail contour plot for 1.5 m – H

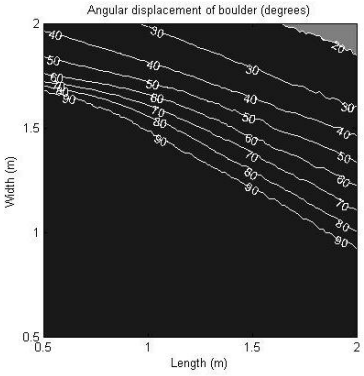

Figure 7-9. Angular pass/fail contour plot for 2 m - H

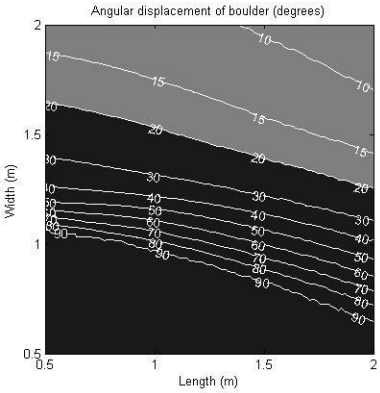

Figure 7-10. Angular pass/fail contour plot for 2.5 m - H

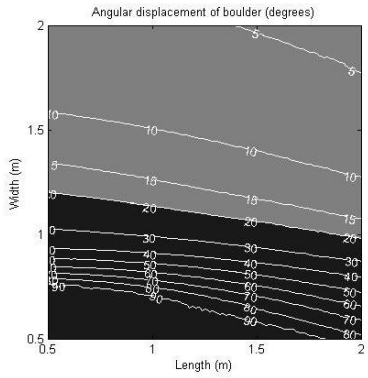

Figure 7-11. Angular pass/fail contour plot for 3 m - H

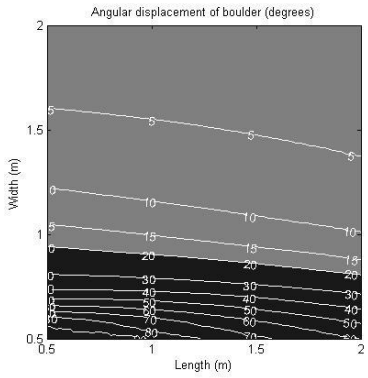

Figure 7-12. Angular pass/fail contour plot for 3.5 m - H

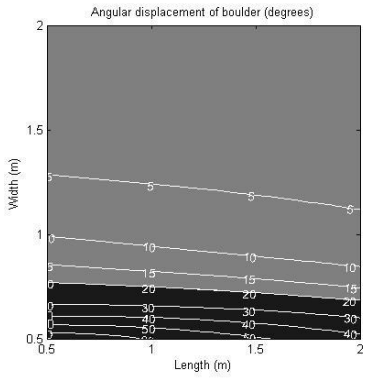

Figure 7-13. Angular pass/fail contour plot for 4 m - H

7.5 Combined Pass/fail contour plots with respect to design criteria in a single direction

The 2-D design contour plots for boulders impacted in a single direction with respect to a typical M30 rated impact are created by overlaying the individual contour plots in Sections 7.2 – 7.4 such that a single fail zone will cause that geometry to be a failure on all of the contour plots. Another way to envision this process is to send all of the pass/fail contour plots through a logical AND gate. The only remaining pass zones are those that demonstrate pass criteria across all contour plots. Figure 7-14 – Figure 7-19 show the final pass/fail design contour plots for various sized boulders.

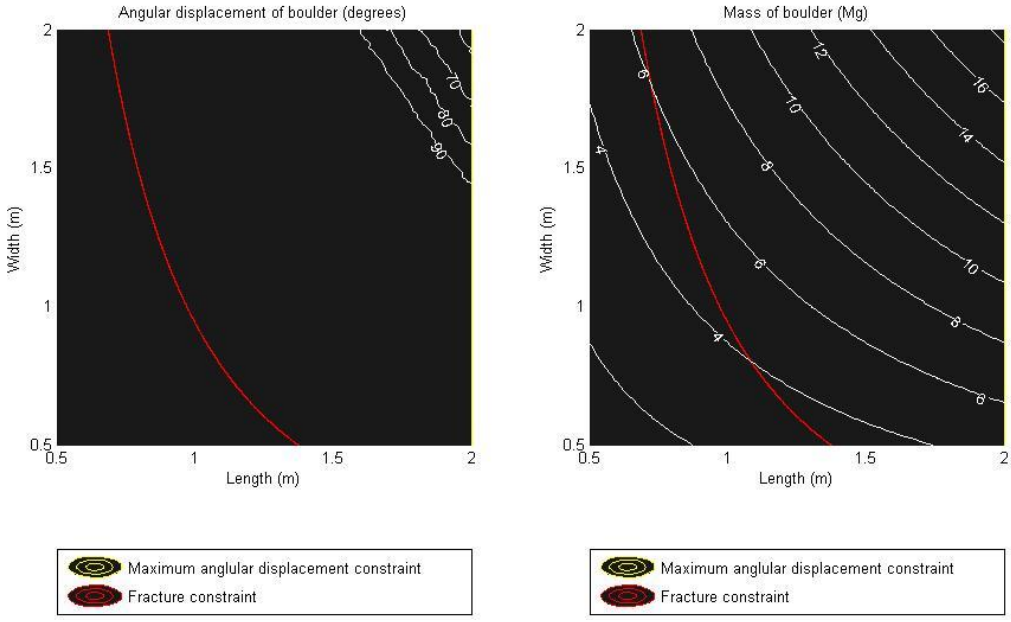

Figure 7-14. Final pass/fail design contour plot for boulders of 1.5 m - H

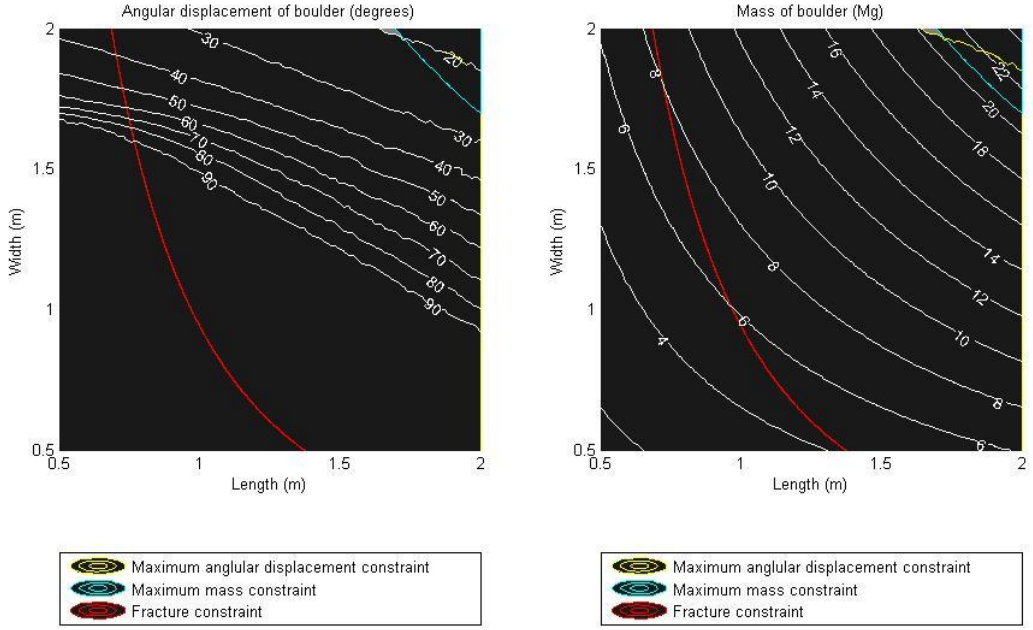

Figure 7-15. Final pass/fail design contour plot for boulders of 2 m - H

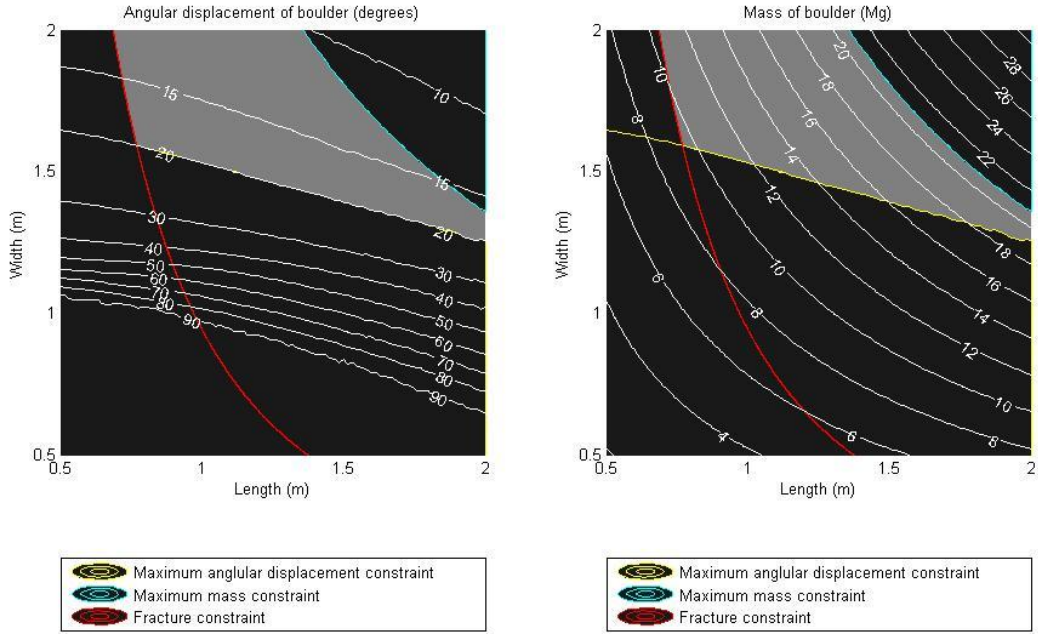

Figure 7-16. Final pass/fail design contour plot for boulders of 2.5 m - H

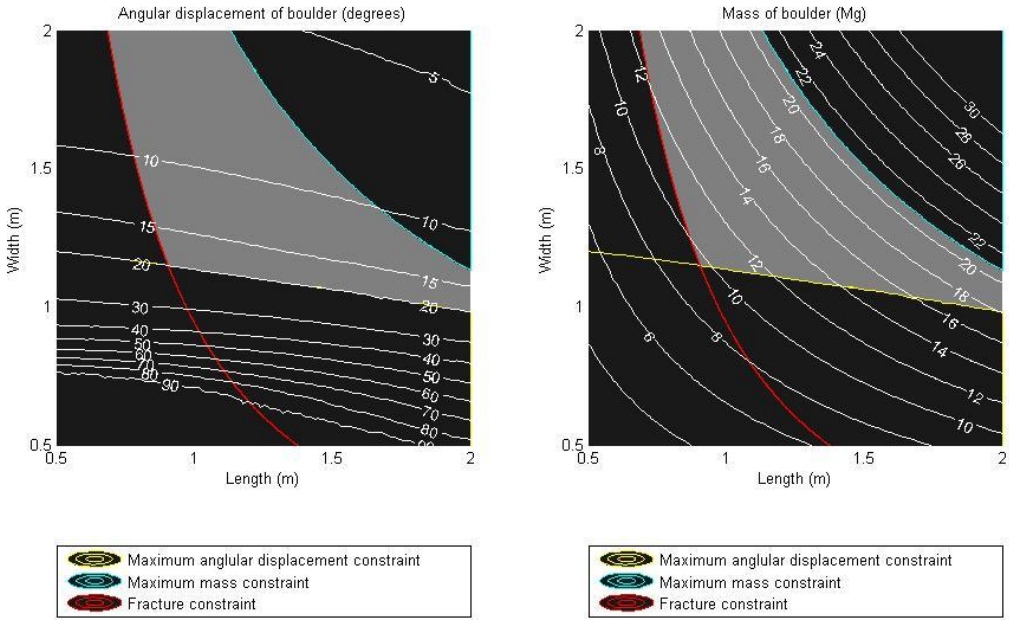

Figure 7-17. Final pass/fail design contour plot for boulders of 3 m - H

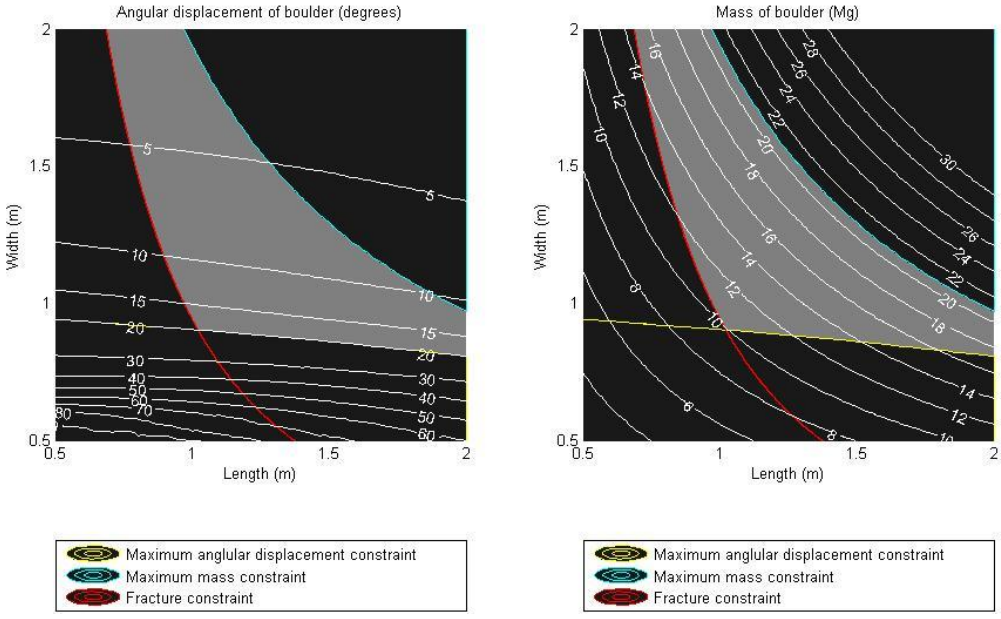

Figure 7-18. Final pass/fail design contour plot for boulders of 3.5 m - H

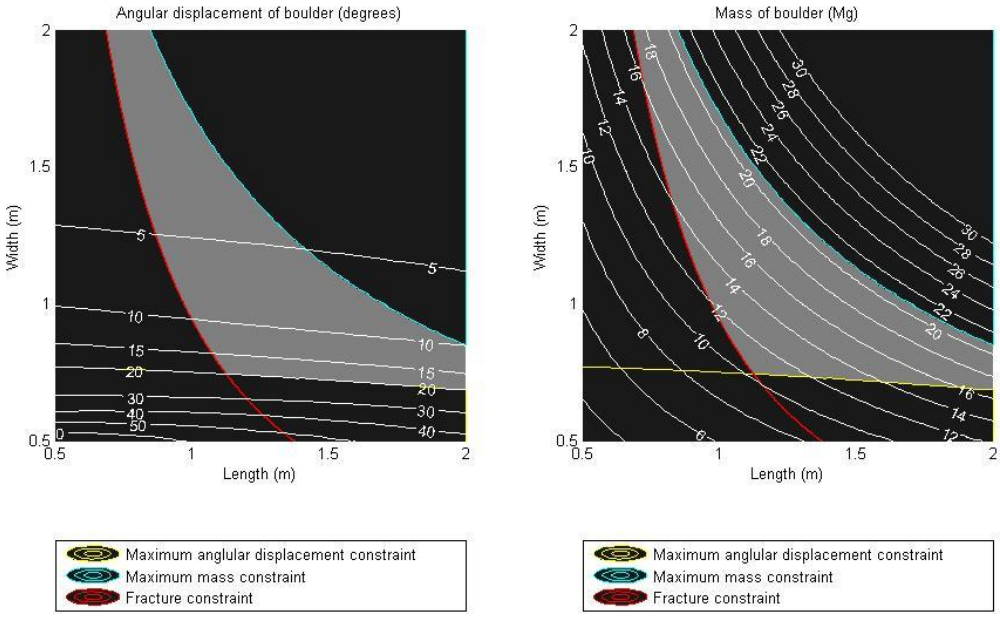

Figure 7-19. Final pass/fail design contour plot for boulders of 4 m - H

7.6 Combined pass/fail contour plots for design criteria for omnidirectional impacts

Figure 7-20 – Figure 7-25 show the pass/fail design contour plots for various sized boulders for omnidirectional impact. Similar to the fracture contour plot, the pass/fail contour for the angular rotation is applied for impact conditions with respect to both the length and the width of the boulder. Doing so better ensures that the selected boulder will not exceed the maximum angular rotation regardless of impact direction. It should be noted that the angular displacements are not shown on the contour plot since the correlation is not one to one.

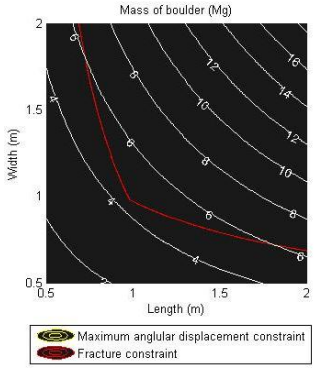

Figure 7-20. Omnidirectional pass/fail design contour plot for boulders of 1.5 m - H

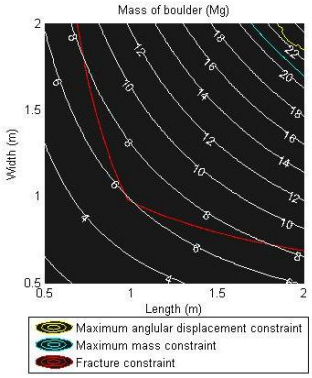

Figure 7-21. Omnidirectional pass/fail design contour plot for boulders of 2 m - H

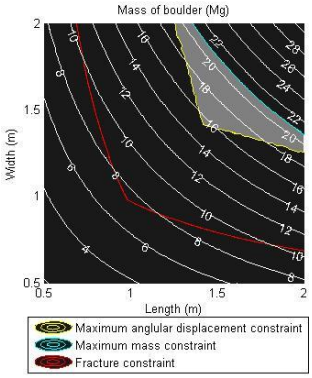

Figure 7-22. Omnidirectional pass/fail design contour plot for boulders of 2.5 m - H

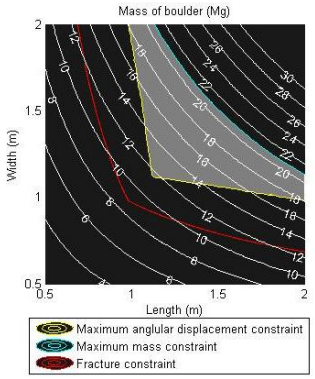

Figure 7-23. Omnidirectional pass/fail design contour plot for boulders of 3 m - H

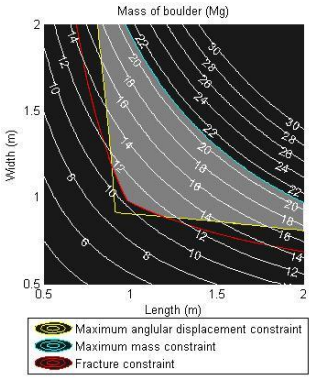

Figure 7-24. Omnidirectional pass/fail design contour plot for boulders of 3.5 m - H

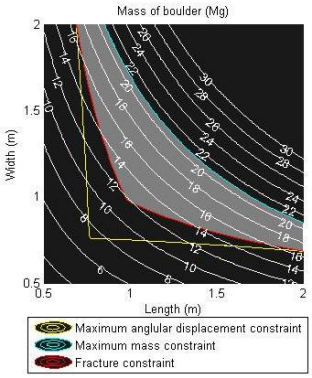

Figure 7-25. Omnidirectional pass/fail design contour plot for boulders of 4 m - H

7.7 Contributions of this chapter

The contributions of this chapter are as follows:

(1) Create 2-D contour plots for representing simulation results of various sized boulders

(2) Create pass/fail contours for maximum boulder mass constraints

(3) Create pass/fail contours fracture constraints

(4) Create pass/fail contours boulder motion constraints

(5) Combine the pass/fail contours into a single design tool for selecting boulder geometries

(6) Present omnidirectional impact pass/fail contours

CHAPTER 8

APPLICATION OF THE LOW-ORDER MODEL AND DIMENSIONAL ANALYSIS

Until this point, the low-order model and small scale crash tests were performed with the goal of model and scaling verification. The intent of this chapter is to present the use of the low-order model and small scale crash tests as a tool used in the design a boulder based on specific dynamic requirements. The design of a potential minimized-mass boulder which exhibits 20° or less of rotation in a M30 rated omnidirectional impact is presented. The design methodology and verification process is presented in chronological stages. First, boulder geometry is selected from the 2-D design contour plots in Chapter 7, and a small scale version of the boulder is created and tested as presented in Chapter 6. Following small scale testing, medium scale testing is performed along with other higher-order simulation models such as LS-DYNA™. Lastly, a full scale experiment is performed to verify the design concept.

At this time, only pass/fail boundaries, small scale testing, and higher-order simulations have been created or performed with respect to the potential minimum-mass boulder. Medium scale testing and the full scale experiment are currently in process.

This chapter is organized as follows:

The selection process of the boulder geometries for a potential minimum-mass boulder is presented in Section 8.1, and the small scale testing of the potential minimum-mass boulder is presented in Section 8.2. The comparison of the low-order model, LS-DYNA™ finite element simulation, and small scale testing is presented in Section 8.3.

8.1 Selection of geometries for a potential minimum-mass boulder

The dimensions of the potential minimum-mass boulder are chosen from the 2-D design contours, Figure 7-20 – Figure 7-25, such that the selected boulder is within the pass zone while potentially achieving a minimum mass. Upon inspection of the 2-D design contours, it can quickly be concluded that no boulder of 1.5, 2, and 2 m– H will meet the design requirements. Similarly the 4 m – H boulders do not meet the minimum mass requirements. For conceptual purposes, the 3 m – H contour plot is chosen for boulder selection. After closer inspection using the low-order model, the corresponding dimensions for the minimum-mass boulder from Figure 7-23 are 1.1 m-L x 1.1 m-W x 3 m-H, and the calculated mass is 11,100 kg when using the density of American Black Granite. The corresponding location of the minimum mass boulder in Figure 7-23 is shown in Figure 8-1.

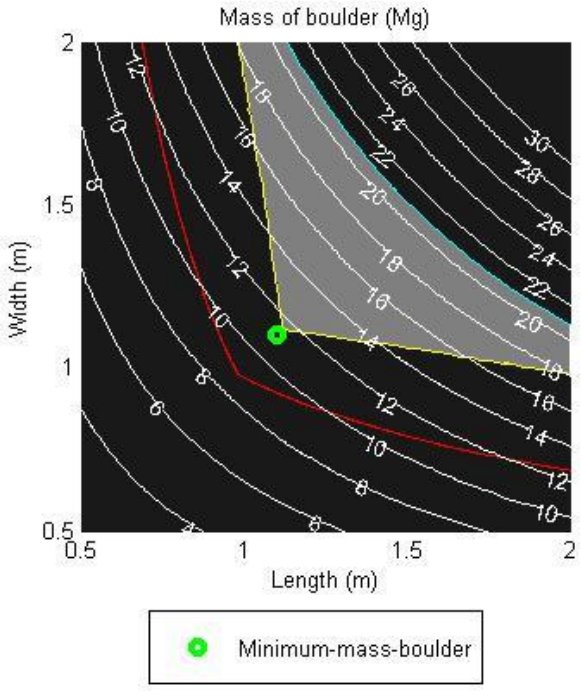

Figure 8-1. Potential minimum-mass boulder for height of 3 m

Table 8–1 shows the corresponding full scale properties for the potential minimum-mass boulder.

Table 8–1. Desired parameters for the full scale minimum-mass boulder

$\rho_{soil} = 1{,}859.9\ \mathrm{kg/m^3}$	$H = 3\ \mathrm{m}$	$\beta = 95\ \mathrm{MN/m^3}$
$\rho_b = 3{,}074\ \mathrm{kg/m^3}$	$d = 2\ \mathrm{m}$	$e = 0.75\ \mathrm{m}$
$L = 1.1\ \mathrm{m}$	$m_v = 6{,}800\ \mathrm{kg}$	$\varphi' = 43.2°$
$W = 1.1\ \mathrm{m}$	$v_o = 13.4\ \mathrm{m/s}$	

8.2 Small scale testing and results

The small scale parameters in SSMMBST-1 were calculated as presented in Section 5.6 when using the full scale parameter listed in Table 8–1. Table 8–2 shows the desired small scale parameters and the measured small scale parameters for SSBST-1. The small scale dimensionally similar boulder was created from American Black granite, and was impacted using the small scale Crash Safety Research pendulum presented in Chapter 5.

Table 8–2. Desired and measured governing parameters for SSMMBST-1

Parameter	Desired	Measured
$m_{v\delta}$	8 kg	8 kg
$v_{o\delta}$	4.34 m/s	4.38 m/s
g_{δ}	9.81 m/s^2	9.81 m/s^2
β_{δ}	95 MN/m^3	95.55 MN/m^3
$\rho_{soil\,\delta}$	1,895.9 kg/m^3	1901 kg/m^3
$\rho_{b\,\delta}$	3,074 kg/m^3	3,074 kg/m^3
L_{δ}	0.1161 m	0.1143 m
W_{δ}	0.1161 m	0.1143 m
H_{δ}	0.3167 m	0.311 m
d_{δ}	0.211 m	0.21m
e_{δ}	0.0792 m	0.079 m
$k_{v\delta}$	34.6 kN/m	35.9 kN/m
$c_{v\delta}$	0.503 kN · s/m	0.538 kN s/m

The small scale minimum-mass boulder test is referred to as SSMMBST-1. The small scale, minimum-mass American Black Granite boulder, SSMMABG-01, was cut from ABG-01 The installation of SSMMABG -01 is shown in Figure 8-2, and the pre-test condition of the boulder is shown in Figure 8-3.

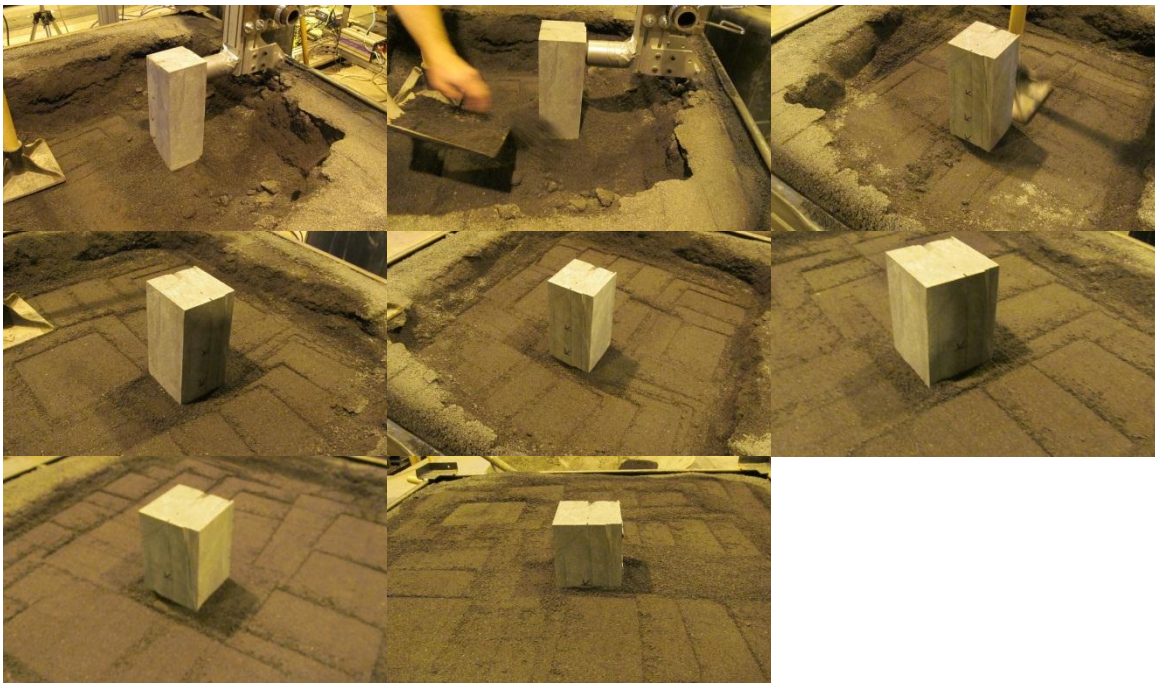

Figure 8-2. Installation of SSMMABG-01 in SSMMBST-1

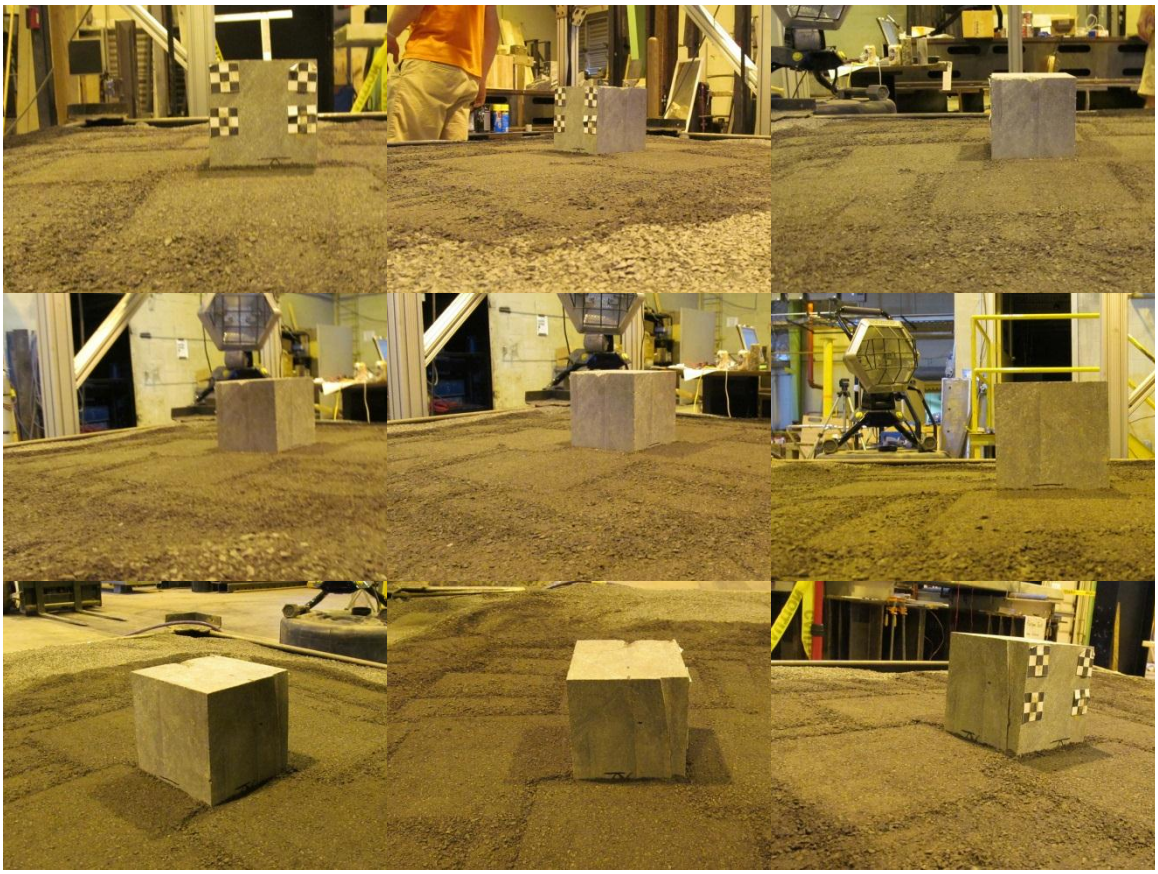

Figure 8-3. Pre-test condition of SSMMABG-01 in SSMMBST-1

The orientation of the installed crush material, the centerline of the impact beam relative to the critical impact point, and the eccentricity of the crush material with respect to the boulder are shown in Figure 8-4.

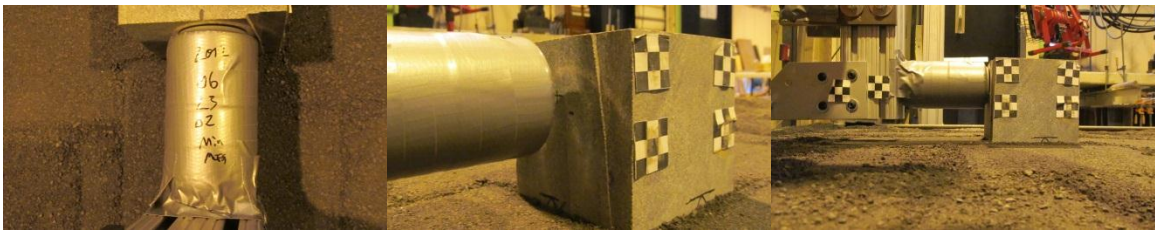

Figure 8-4. Pre-test conditions of the impact beam and crush material in SSMMBST-1

Figure 8-5 shows the side-view still images extracted from the high-speed video in a chronological sequence of the impact.

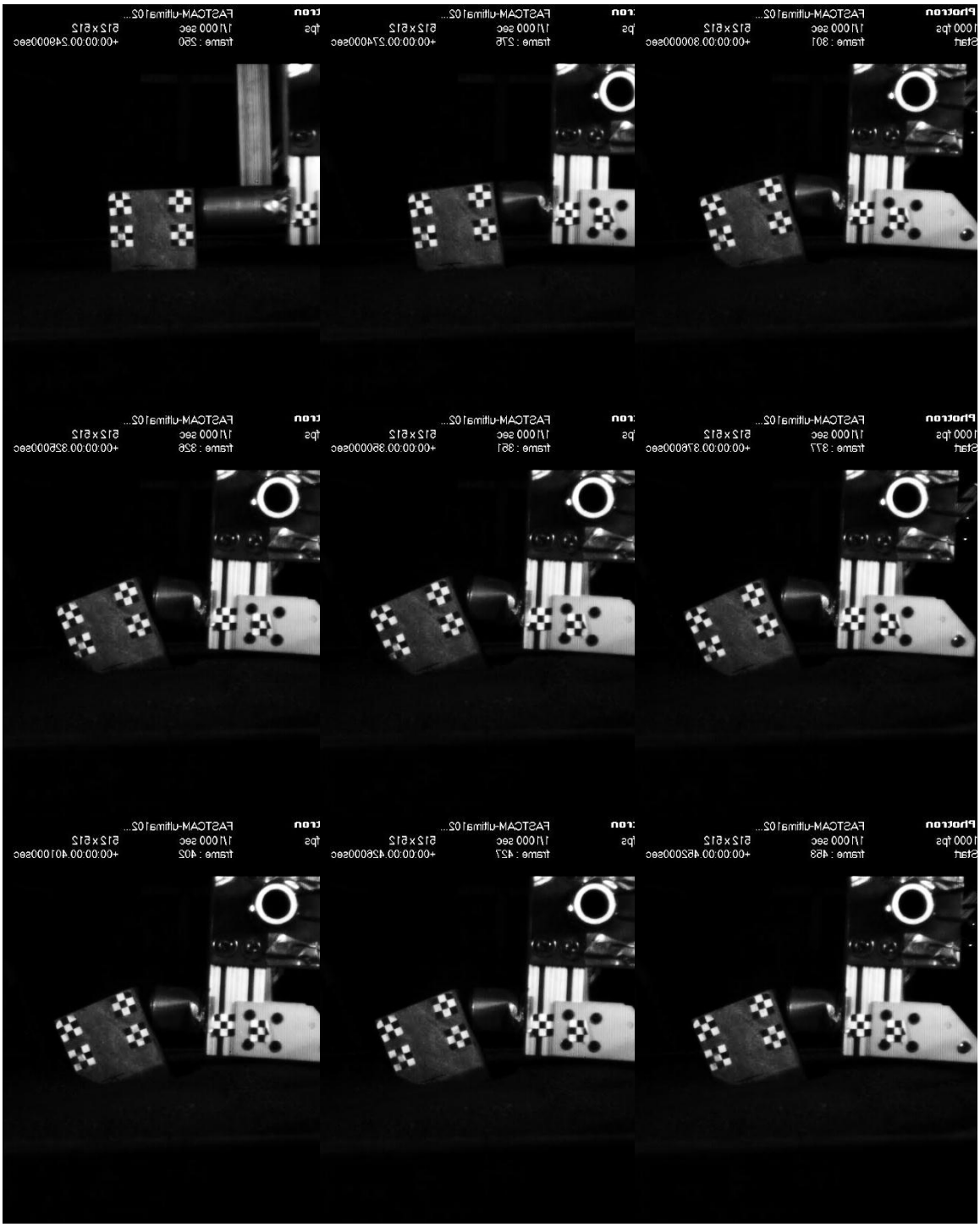

Figure 8-5. High-speed image sequence of SSMMBST-1

Figure 8-6 shows the linear displacement of the center of mass of SSMMABG-01 from the point of impact, and Figure 8-7 shows the angle of rotation of SSMMABG-01 from the point

of impact. The linear displacement of the impact beam as tracked using the forward fiducial is shown in Figure 8-8.

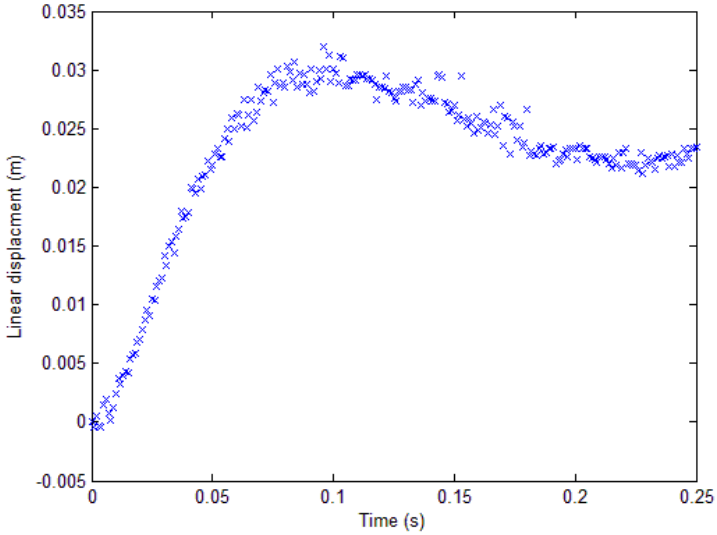

Figure 8-6. Measured displacement of the center of mass of SSMMABG-01 in SSMMBST-1

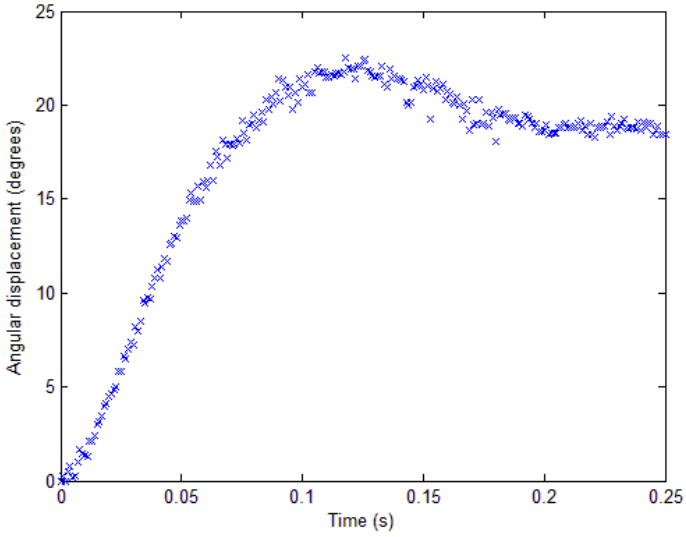

Figure 8-7. Measured angle of rotation of SSMMABG-01 in SSMMBST-1

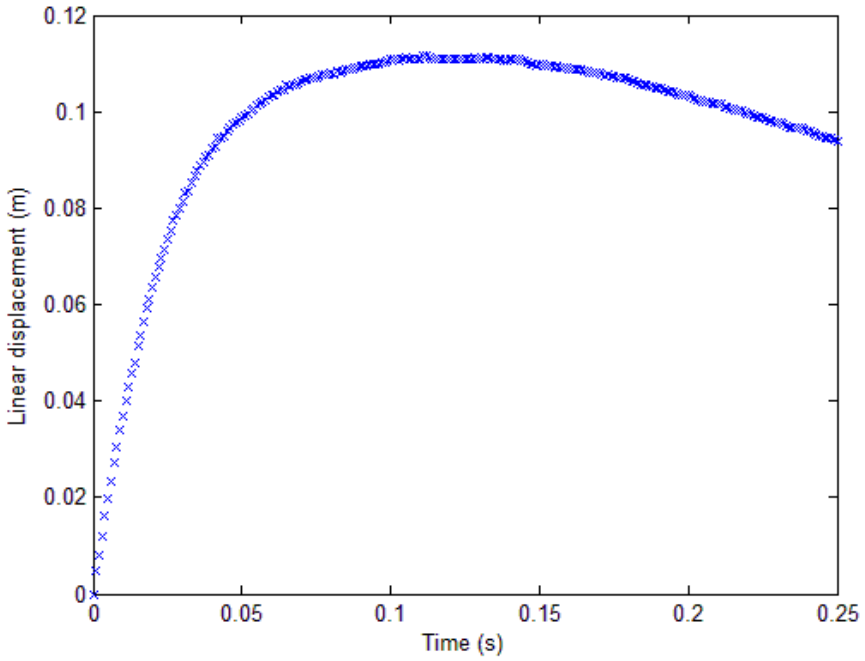

Figure 8-8. Measured linear displacement of the impact beam in SSMMBST-1

Photographs of the post-test condition of the impact beam are shown in Figure 8-9, and Figure 8-10 shows the post-test condition of SSMMABG-01 in SSMMBST-1.

Figure 8-9. Post-test impact beam condition in SSMMBST-1

Figure 8-10. Post-test condition of SSMMABG-01 in SSMMBST-1

8.3 Comparison of scaled up small scale crash test results to full scale low-order and full scale LS-DYNA™ simulations for potential minimum-mass boulder

A LS-DYNA™ finite element simulation was performed by LTI personnel after the low-order model and small scale testing confirmed the dynamics of the potential minimum-mass boulder. Figure 8-11 shows the impact sequence and subsequent boulder and vehicle displacements of the LS-DYNA™ finite element simulation.

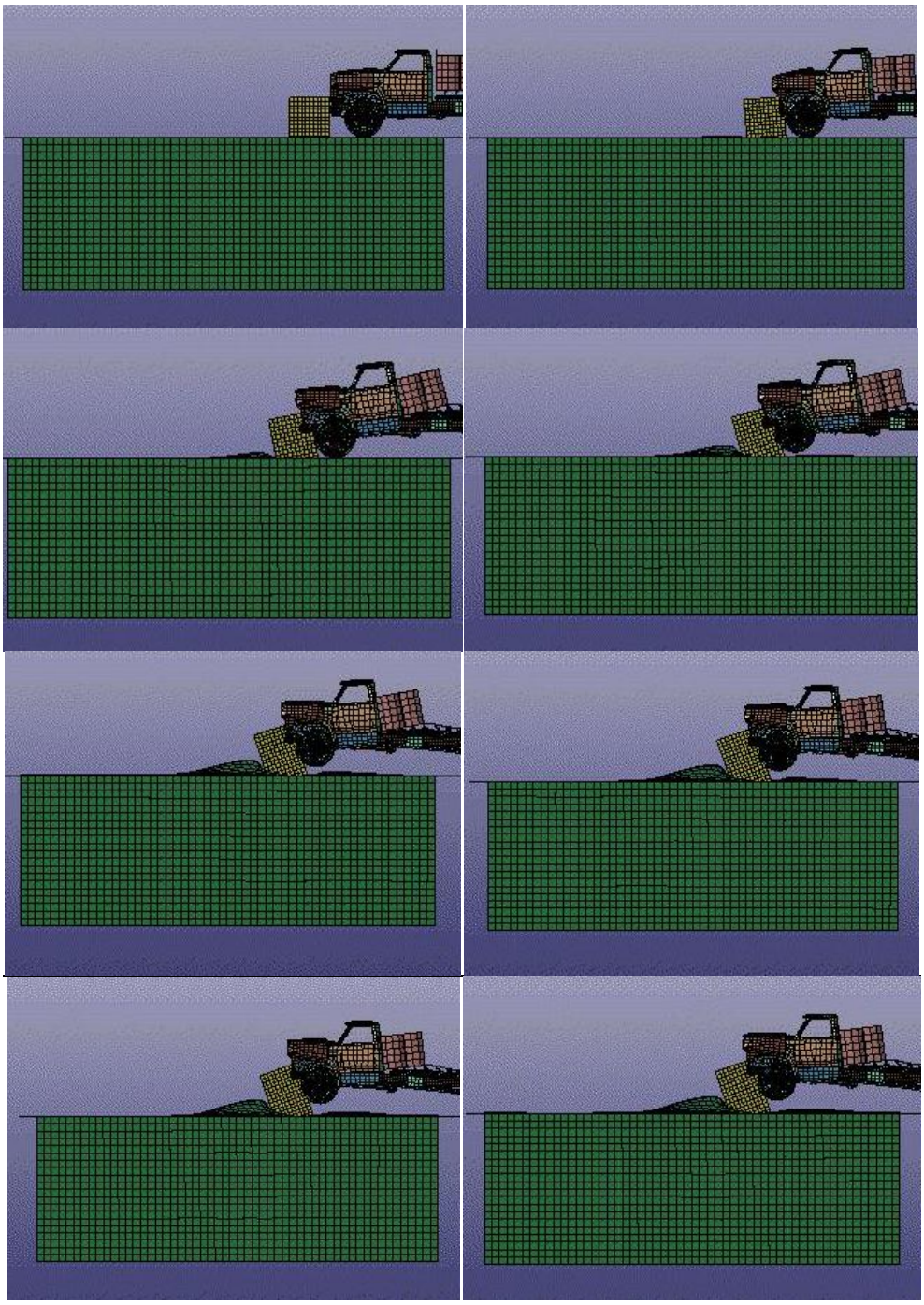

Figure 8-11. Finite Element LS-DYNA™ simulation of an M30 impact upon the full scale minimum-mass boulder

As presented in Chapter 6, the results from the small scale testing can be scaled up to the full scale dimensions though the use of the scaling laws presented in Chapter 5. Figure 8-12 shows the comparison of the impact sequence from the high-speed videos for SSMMBST-1 and the full scale LS-DYNA™ simulation. It should be noted that the time dimension of the small scale test was scaled up to the full scale size when comparing the high-speed image sequence.

Figure 8-12. Comparison of high-speed image sequences from SSMMBST-1 and LS-DYNA™

Figure 8-13, Figure 8-14, and Figure 8-15 show the comparison of the scaled up crash test results from SSMMBST-1 to the equivalent full scale simulated low-order and LS-DYNA™ results using the parameters listed in Table 8–1. Figure 8-13 shows the comparison of the linear displacement of the center of mass of the boulder, Figure 8-14 shows the comparison of the angle of rotation of the boulder, and Figure 8-15 shows the comparison of the linear displacement of the impact vehicle.

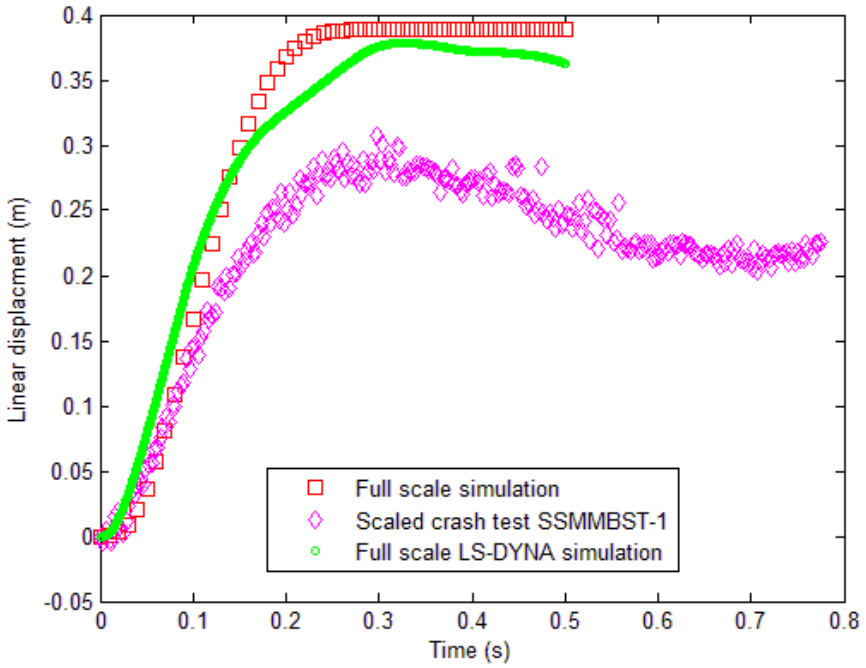

Figure 8-13. Comparison of the scaled up linear displacement of the center of mass of SSMMABG-01 in SSMMBST-1 to the full scale, low-order simulation and LS-DYNA™ simulation

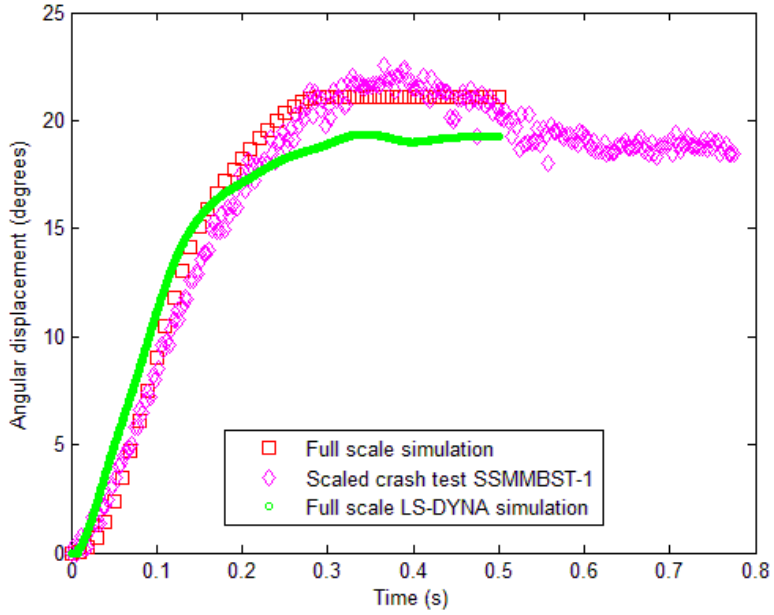

Figure 8-14. Comparison of the scaled up angular displacement of SSMMABG-01 in SSMMBST-1 to the full scale, low-order simulation and LS-DYNA™ simulation

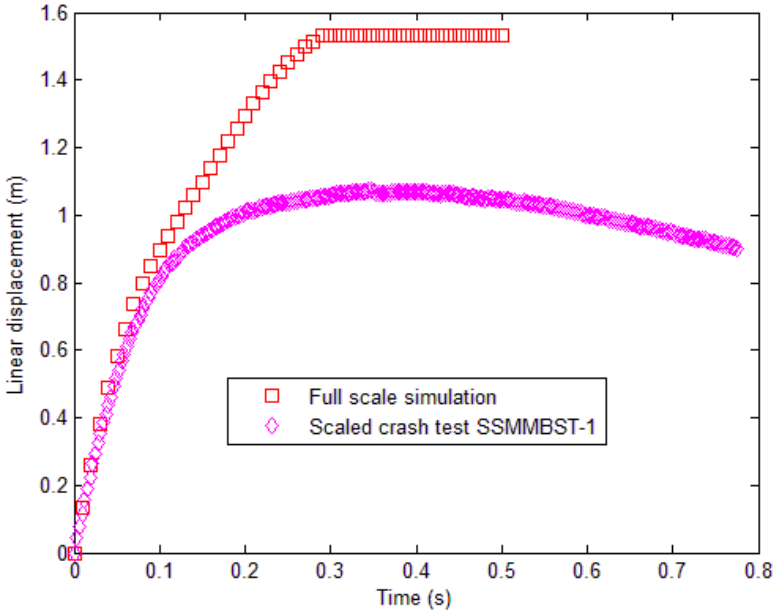

Figure 8-15. Comparison of the scaled up vehicle displacement in SSMMBST-1 to the full scale, low-order simulation and LS-DYNA™ simulation

Figure 8-16, Figure 8-17, and Figure 8-18 show the comparison of the crash test results from SSMMBST-1 to the small scale simulated low-order model results using the measured parameters listed in Table 8–2. Figure 8-16 shows the comparison of the linear displacement of the center of mass of the boulder, Figure 8-17 shows the comparison of the angle of rotation of the boulder, and Figure 8-18 shows the comparison of the linear displacement of the impact vehicle.

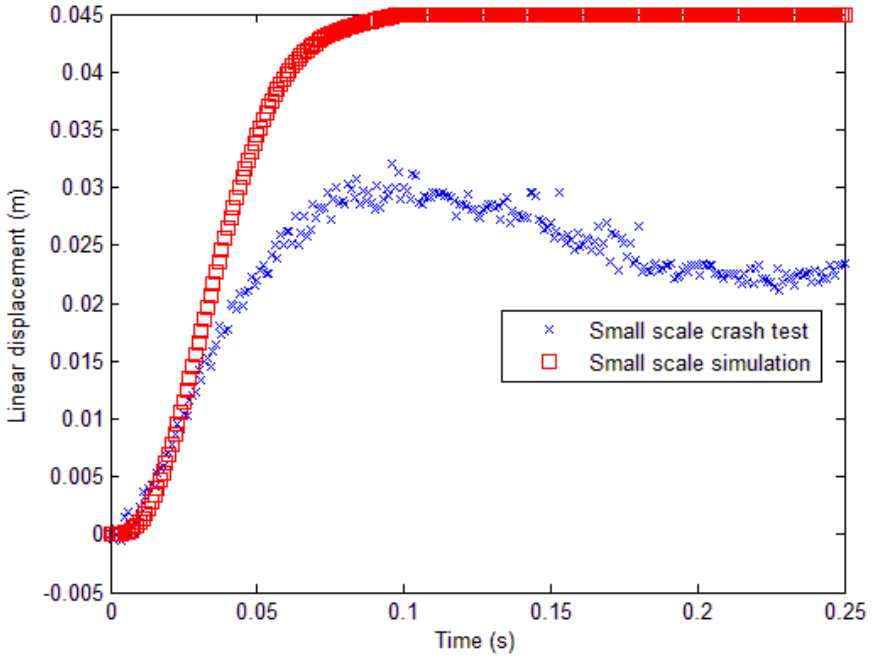

Figure 8-16. Comparison of the linear displacement of the center of mass of SSMMABG-01 in SSMMBST-1 to the small scale, low-order simulation using Table 8–2 measured parameters

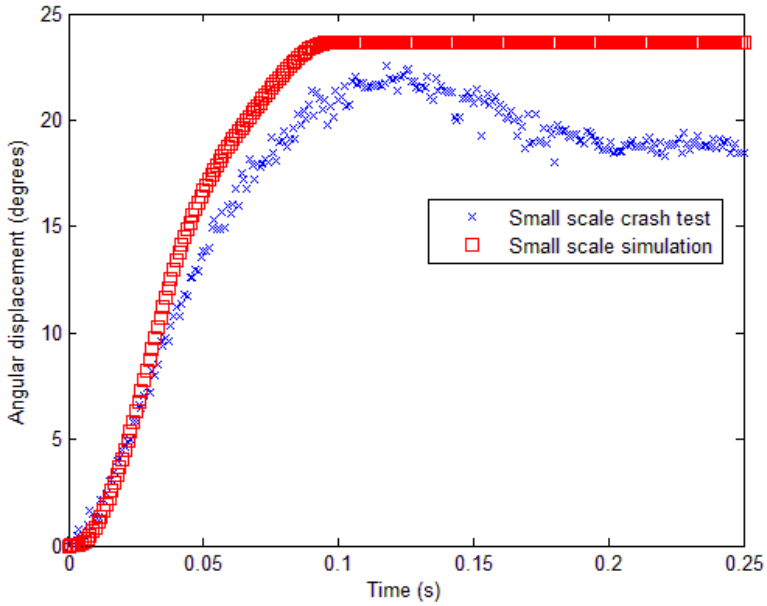

Figure 8-17. Comparison of the angular displacement of SSMMABG-01 in SSMMBST-1 to the small scale, low-order simulation using Table 8–2 measured parameters

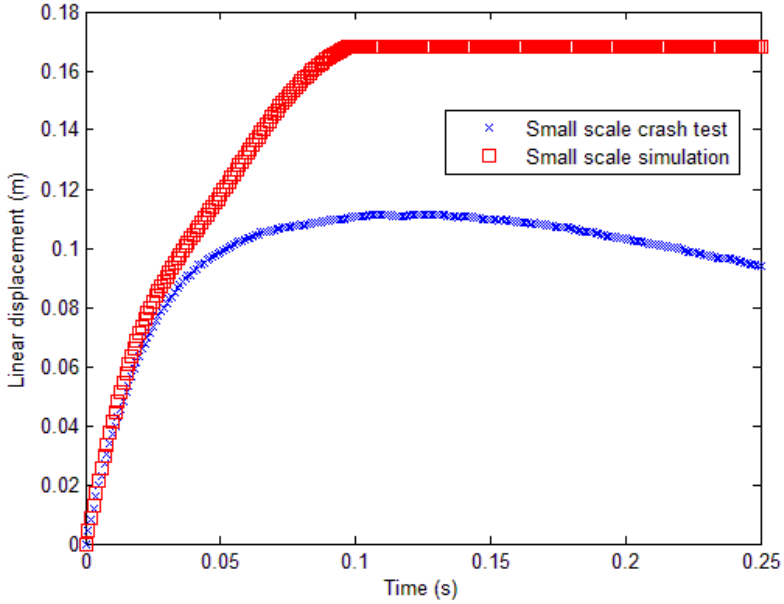

Figure 8-18. Comparison of the vehicle displacement in SSMMBST-1 to the small scale, low-order simulation using Table 8–2 measured parameters

Further tests and simulations have not been performed at this time, but based on the small scale results, it is expected that a medium scale and full scale crash test will confirm the boulder geometries for a 20° rotation. Preparations are currently underway for conducting medium scale crash testing, and full scale crash test preparations are being made to acquire the full scale minimum-mass boulder.

8.4 Contributions of this chapter

The contributions of this chapter are as follows:

(1) Select the geometries for a minimum-mass boulder which is predicted to rotate 20°

(2) Perform small scale crash tests to confirm boulder dynamics

(3) Compare small scale crash test results to low-order simulations and LS-DYNA™ simulations

(4) Propose the methodology for final verification of the minimum-mass boulder

CHAPTER 9

CONCLUSIONS AND FUTURE WORK

The intent of this chapter is to discuss the validation of the low-order model and small scale testing presented in this thesis. Additionally, future work related to the scope of this thesis is proposed which can be used to improve not only the analysis and modeling, but also the methodology for performing small scale crash tests. The conclusions of this thesis are presented in Section 9.1, and the proposed future work is presented in Section 9.2.

9.1 Conclusions

The literature relevant to the topics presented in this thesis was reviewed in Chapter 2. Existing higher and lower-order models for laterally loaded piles were reviewed, and it was determined that use of such existing models did not accurately account for the dynamics observed in a full scale crash test. It was further determined that the existing soil modeling techniques could be combined with the dynamics of a vehicle impacts to create a low-order model for vehicle impacts upon soil-fixed boulders.

A low-order model for vehicle impact upon soil-fixed boulders was presented in Chapter 3. The low-order model is based on three degrees of freedom, the linear translation of the boulder and vehicle and the angular rotation of the boulder. Unlike the models reviewed in literature, the low-order model does not couple the linear translation of the boulder with the angular displacement of the boulder. The soil was modeled using a system of lumped-parameter Kelvin models of which the equivalent soil mass was attached to the boulder. The vehicle was modeled as a lumped-parameter Maxwell model. The governing equations of motion were derived based on the force-moment analysis of the free body diagrams for the vehicle and boulder-soil

subsystem. Fracture prediction methods for the boulders were presented based on the assumed peak force in a M30 rated impact. Additionally, in-situ and experimental methods were presented for determining the lumped-parameter values of the soil and vehicle.

In Chapter 4, the low-order model was simulated using MATLAB® ODE45 and the results were compared to past full scale crash tests. The comparison of the full scale simulations to the full scale crash test results showed good agreement between the low-order model and the crash tests. The low-order model accurately predicts boulder motion until approximately 20° of rotation has occurred. After 20° of rotation, the model loses fidelity and becomes less accurate. The overall results of the simulations however, still predict the overall observed motion of the crash test such as the boulder flipping out of the soil. The presented fracture prediction methodology was compared to two full scale crash tests in which the boulder was rigidly embedded in concrete footings. The fracture prediction methodology accurately predicted that both boulders would indeed break. The fracture model indicated that the boulders were close to the pass/fail line, yet within the failure zone. The deceleration of the vehicle after impact indicates that the boulders absorbed a vast amount of the energy of the vehicle. Thus, it can be inferred and that a slight increase in boulder dimensions would resist fracture. This coincides with the boulders lying near the pass/fail curve in the fracture contour plot.

Dimensional analysis was applied to the low-order model in Chapter 5, from which dimensionless equations of motion and scaling factors were derived. Unlike most scaling laws associated with laterally loaded piles, the salient feature of the scaling factors presented in Chapter 5 is the ability to perform small scale crash tests in a 1G environment with equivalent bulk soil and boulder properties between small and full scale experiments. The dimensionless equations of motion were arranged in a state-space form similar to the governing equations of motion for the low-order model as a precursor to simulating the dimensionless models.

In Chapter 6, the verification of the dimensionless equations of motion and the scaling laws was first made through the simulations of dimensionless models and comparison of small scale and full scale simulations. Small scale experiments were then created to be dimensionally similar to the past full scale crash tests of vehicle impacts on soil-fixed boulders. The small scale low-order model results were directly compared to the small scale crash test results, and the small scale crash test results were scaled up and compared to the full scale crash test results. As anticipated from full scale simulations, the small scale low-order simulations show good agreement with the small scale tests. The scaled results from small scale crash testing also show excellent agreement with the full scale crash results through approximately 20° of boulder rotation.

A set of boulder design parameters for typical M30 impact conditions was presented in Chapter 7. The design parameters were based solely on the variations in boulder geometries and were represented on 2-D design contour plots. Additional constraints were imposed on the contour plots which account for predicted fracture and a limiting maximum boulder mass. The design contour plots allows for extremely quick analysis of boulder dynamics based on the variation in boulder sizes.

Chapter 8 briefly presented the methodology for using the low-order model, small scale crash tests, and 2-D design contour plots as a boulder design tool. The overall boulder dimensions were selected using the 2-D design contour plot presented in Chapter 7, and then small scale tests were created and performed following the methodology presented in Chapter 6. The low-order model results, small scale results, and full scale LS-DYNA™ finite element simulation results were compared and showed good agreement between all three. Medium scale tests are currently being performed, and preparations are being made for full scale testing.

9.2 Future work

The breadth of topics which were presented in this thesis allows for several future works as related to this thesis. The more obvious next immediate step in this research is to complete the verification process of the minimum-mass boulder through the conduction of medium scale crash tests followed by a full scale crash test.

Following the verification of the minimum-mass boulder, the next step logical step would be to perform a parametric study of the variations in dimensionless π groupings and low-order variables. The 2-D design contours presented in Chapter 7 were created by varying only 3 of the 11 governing dimensionless π groupings. It is anticipated that changing the soil and/or soil properties would result in the greatest change in output of the low-order model and small scale testing. A parametric study in the variation of soil properties would allow for extremely quick in-situ evaluations of pre-existing boulders or desired boulder geometries based on on-site conditions.

Additionally, an investigation into cohesive soils would prove to be beneficial to low-order modeling. As seen in literature [31], the modulus of subgrade reaction for cohesive soil does not increase linearly with depth, but rather remains constant. The units for the constant of horizontal subgrade reaction for cohesive soils take the form N/m^2. It is anticipated that even this slight variation in units may result in drastic changes of the dimensionless π groupings.

A similar topic of interest includes a sensitivity study of the effects of partial similitude between crash tests and simulations. The research performed as related to this thesis was done so to be as close as possible to full similitude or perfectly matching π groupings. Obviously perfectly matching π groupings is not feasible, but it would be beneficial to know which π groupings are “hard” variables which cannot be varied without large changes in output and which

π groupings could be considered "soft" variables which can be varied to a certain degree without drastic changes in output.

Additionally, the presently-used low-order model neglects motion in the Y direction. The next step in modeling may be to return to the equations of motion and include the Y component. This is much easier said than done because, unlike the lateral displacement of the boulder, the Y component of the boulder motion is more so coupled with the angular rotation of the boulder. In order to better predict the motion in the Y direction, the time-varying pivot point of rotation for the boulder must be known. As observed in full scale testing, the location of the pivot does not remain constant throughout a crash test; for small angular displacements, the pivot point is near the base of the boulder, whereas for large angular deflection, the pivot point moves towards the surface of the soil. This concept is easily seen in the analysis of ABG01 in BST-1 since the boulder ended up on top of the soil surface. It is this non-trivial aspect of rotation that has driven other models to using a repetitive non-linear approach to solving the equations of motion. It is desirable, however, to be able to calculate the displacement of the boulder in a single calculation, as demonstrated in this thesis.

REFERENCES

[1] C. Gresser, “Soil compaction and stability,” [Online], Available: http://www.gilesengr.com/Literature/soil_compaction_and_stability_long.pdf

[2] W. Pawlus et al., "Development of lumped-parameter mathematical models for a vehicle localized impact," *J. Mech. Sci. and Tech..*, vol. 25, no. 7, pp. 1737-1747, Mar. 2011.

[3] Automotive News, “IIHS Crash Tests Five Budget Coupes: Ford, Volvo Ear Top Safety Picks [Crash Tests],” [Online]. Available: http://v8tvshow.com/component/option,com_smf/Itemid,108/topic,9154.0/

[4] B. Das, "Laterally Loaded Piles," in *Principles of Foundation Engineering*, Pacific Grove, CA, Brooks/Cole, 2004, p. 530.

[5] B. Holmes and G. Sliter, "Scale Modeling of Vehicle Crashes - Techniques, Applicability, and Accuracy; Cost Effectiveness," SAE Technical Paper 740586, 1974, doi:10.4271/740586.

[6] S. Kirkpatrick et al., “Evaluation of Passenger Rail Vehicle Crashworthiness,” International Journal of Crashworthiness, vol. 6, no. 1, pp. 95-106, 2001.

[7] L. Zhang, "Nonlinear analysis of laterally loaded rigid piles in cohesionless soil," *Computers and Geotechnics*, vol. 36, pp. 718-724, 2009.

[8] M. H. E. Naggar and K. Bentley, "Dynamic analysis for laterally loaded piles and dynamic p-y curves," *Canadian Geotechnical Journal*, vol. 37, pp. 1166-1183, 2000.

[9] C. Prasad YVSN, “Lateral capacity of model rigid piles in cohesionless soils,” *J. Geotech. Geoenviron. Eng.*, ASCE, vol. 131, no. 1, pp. 78-83, 2005 .

[10] M. Novak and M. Sheta, “Approximate approach to contact effects of piles,” Proceedings of a Speciality Conference on Dynamic Response of Pile Foundations:

Analytical Aspects, ASCE, Hollywood, FL. Pp. 53-79.

[11] M. H. E. Naggar, “Interpretation of lateral statnamic load test results,” *Geotechnical Testing Journal*, vol. 23, no. 3, pp. 169-179, 1998.

[12] J. Ting et al., “Centrifuge static and dyanmic lateral pile behaviour,” *Canadian Geotechnical Journal*, vol. 24, pp. 198-207, 1987.

[13] C. LeBlanc et al., “Response of stiff piles in sand to long-term cyclic lateral loading,” *Géotechnieque*, vol. 60, no. 2, pp. 79-90, 2010.

[14] B. Broms, “Lateral Resistance of Piles in Cohesive Soils,” *J. Soil Mech. Found. Div*., ASCE, vol. 90, pp. 27-63, 1964.

[15] G. Gautreau, “The Dynamic Cone Penetrometer ‘The DCP’,” [Online], http://www.ltrc.lsu.edu

[16] “Dynamic Cone Penetrometer,” STP 240-20, Seskatchewan Highways and Transportation, 1994.

[17] R. Salgado and S. Yoon, "Dynamic Cone Penetration Test (DCPT) for Subgrade Assessment," Joint Transportation Research Program, Indiana Department of Transportation and Purdue University, West Lafayette, Indiana, 2003. doi: 10.5703/1288284313196

[18] G. Sowers and C. Hedges, “Dynamic Cone for Shallow In-Situ Penetration Testing,” *Vane Shear and Cone Penetration Resistance Testing of In-Situ Soils, ASTM STP 399*, Am. Soc. Testing Mats., 1966, p. 29.

[19] S. Webster et al., “Force Projection Site Evaluation Using the Electric Cone Penetrometer (ECP) and the Dyanmic Cone Penetrometer (DCP),” Technical Report GL-94-17, US Army Corps of Engineering, Waterways Experiment Station, AD-A282

411, Apr. 1994.

[20] J. Zhao, “Applicability of Mohr-Coulomb and Hoek-Brown strength criteria to the dynamic strength of brittle rock,” *Int. J. of Rock Mech. & Min. Sci*., vol. 37, pp. 1115-1121, 2000.

[21] S. Cho et al., "Strain-rate dependency of the dynamic tensile strength of rock," *Int. J. of Rock Mech. & Min. Sci*, vol. 40, pp. 763-777, 2003.

[22] Y. Kim et al., "Wedge Failure Analysis of Soil Resistance on Laterally Loaded Piles in Clay," *J. Geotech. and Geoenviorn. Eng.*, ASCE, pp. 678-694, Jul. 2011

[23] J. Meyer, “Analysis and design of pile foundations: proceedings of a symposium sponsored by the ASCE Geotechnical Engineering Division and a session sponsored by the ASCE Technical Council on Codes and Standards in conjunction with the ASCE National Convention, San Francisco, California, October 1-5, 1984,” ASCE, pp. 176-177, 1984.

[24] J. Diaz-Rodriguez et al., "Strain-Rate Effects in Mexico City Soil," *J. Geotech.and Geoenviron. Eng.g*, ASCE, pp. 300-305, Feb. 2009.

[25] D. Croney, “Determination of Equivalent Californian Bearing Ratio by Plate Bearing Test,” SalierGeotechnical Limited, Lab Test Refernce 610

[26] Suggested methods for determining the uniaxial compressive strength and deformability of rock materials, *Int. J. Rock Mech. Min. Sci. & Geomech. Abstr*., Vol. 16, No.2, pp. 135-140, 1979.

[27] Suggested Methods for Determining Tensile Strength of Rock Materials, *Int. J. Rock Mech. Min Sci. & Geomech. Abstr.*, vol. 15, pp. 99-103, 1978.

[28] S. Brennan, “On size and control: the use of dimensional analysis in controller design,”

Ph.D. disseration, Dept. Mech. Sc. and Eng., University of Illinois at Urbana-Champaign, Urbana, IL, 2002.

[29] "Freight," U.S. Deparment of Transporation Federal Highway Administration, [Online], Available: http://ops.fhwa.dot.gov/freight/sw/overview/index.htm.

[30] International® Trucks, [Online], Available: http://www.internationaltrucks.com/

[31] L. Zhang and S. Ahmari, "Nonlinear analysis of laterally loaded rigid piles in cohesive soil," *Int. J. Numer. Anal. Meth. Geomech*., 2011. DOI: 10.1002/nag.1094

APPENDIX A

DATA SHEETS FOR VEHICLES USED IN FULL SCALE CRASH TESTS

BST-1 VEHICLE DATA SHEET

	Device being tested: Granite Boulder
Test Date: 11/15/2010	Test Procedure: ☐NCHRP 350 ☐US DOS 02.01A ☒Other ASTM F265

Date: 11/12/2010	VIN No.: 1GBJ7H1C12J512763		
	Make: GM/Chevrolet	Model: C6500	Year: 2002
	GVWR:	Engine: Diesel	Odometer: 135,789
Device:	Tire Size (front): 9R22.5	LF Tire Pressure (psi):	RF Tire Pressure (psi):
	Tire Size (rear): 9 R22.5	LR Tire Pressure (psi):	RR Tire Pressure (psi):

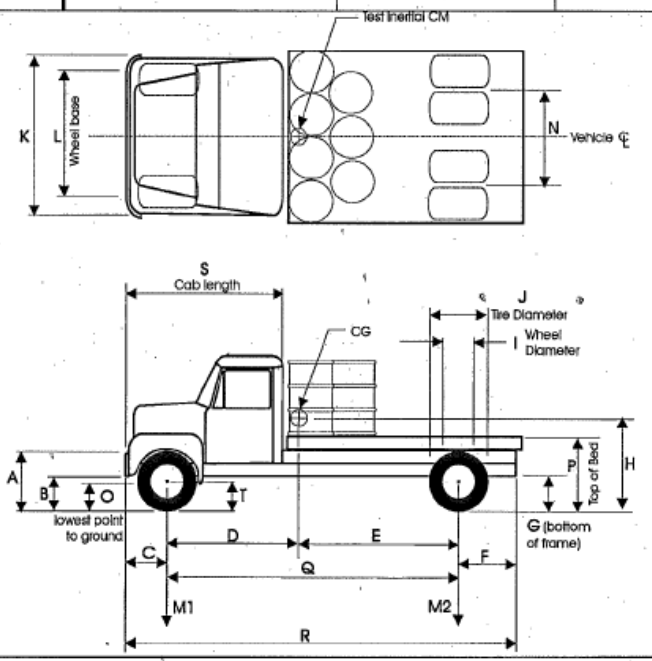

Geometry – in. (cm)

A	35"	B	20"	C	34"	D	calculated	E	calculated
F	56"	G	28 3/4"	H	calculated	I	23 1/2"	J	F 36 1/2" R 37 1/2"
K	91"	L	80"	N	70"	O	8 3/4"	P	54"
Q	229 1/2"	R	29' 4 1/2"	S	106"	T	F 17 7/8 R 18 3/4"		

Mass Distribution – lb (kg)

Curb	LF	2240	RF	2800	LR	2560	RR	2500
Test	LF	4250	RF	3810	LR	3580	RR	3340

	Curb	*Test*
$M_{1\ (front)}$	5040	8060
$M_{2\ (rear)}$	5060	6920
M_{Total}	10,100	14,980

Target Locations (from outside edges of black dots on targets):
side targets 32 13/16" between large black circles
top targets 71 13/16" " " " "

BST-2 VEHICLE DATA SHEET

VEHICLE DATA SHEET

Date: 10/26/11	VIN No.: 1HTSCAAL9YH215844				
	Make: International	Model: 4700		Year: 1999	
	GVWR: 25500	Engine: Diesel		Odometer: 12522	
Device:	Tire Size (front): 11R 22.5	Inflation Pressure (LF): 100		Inflation Pressure (RF): 100	
	Tire Size (rear): 11R 22.5	Inflation Pressure (LR): 100		Inflation Pressure (RR): 100	

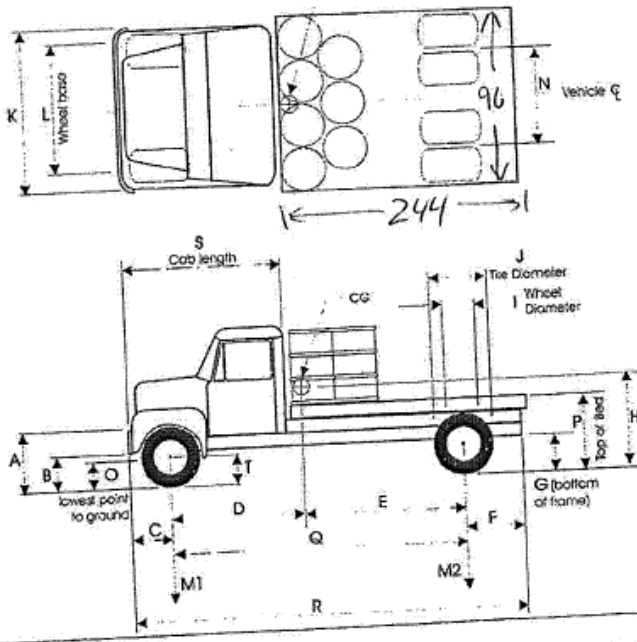

Geometry – in. (cm)												
A	29 1/2	B	19 3/4	C	31 1/2	D	calculated	E	calculated
F	122	G	29	H	calculated	I	24	J	40 1/2
K	93 1/2	L	90	N	73	O	9 1/4	P	54 3/4
Q	195	R	350	S	100	T	19 1/2		

Mass Distribution – lb (kg)								
Curb (as arrived)	LF		RF		LR		RR	
Empty (as modified)	LF	3130	RF	2960	LR	2820	RR	3060
Loading	LF	3830	RF	3660	LR	3630	RR	4020
Loading	LF	3840	RF	~~3630~~	LR	3630	RR	4270
Final Test	LF	3840	RF	~~3650~~ 3660	LR	3690	RR	~~3680~~

	Curb	Test ~~3680~~
$M_{1\ (front)}$		
$M_{2\ (rear)}$		
M_{Total}		

Visual Target Locations:

side targets 37 1/2

top targets 26 11/16 Between

In-Vehicle DAS Location:

1516

AHH ~~1480~~ 1480

BFT-1 VEHICLE DATA SHEET

PENN STATE — The Larson Institute — Crash Safety Research Manual

Filename	Revision/Version	Page Number	Issuer	Approved	Implementation Date
VEHICLE _Preparation.docx	A/0	5 of 6	RAT		11/22/2010

Test # 2011-06-03-01

VEHICLE DATA SHEET

Date: 4-8-11	VIN No.: 1GBJ7H1C61J507931			
	Make: Chevrolet	Model: C6500	Year: 02	
	GVWR: 25300	Engine: Diesel 4cyl	Odometer: 200621	
Device: Boulder in Foundation	Tire Size (front): 9R22.5	Inflation Pressure (LF): 90	Inflation Pressure (RF): 90	95
	Tire Size (rear): 9R22.5	Inflation Pressure (LR): 90	Inflation Pressure (RR): 90	

Test Inertial CM

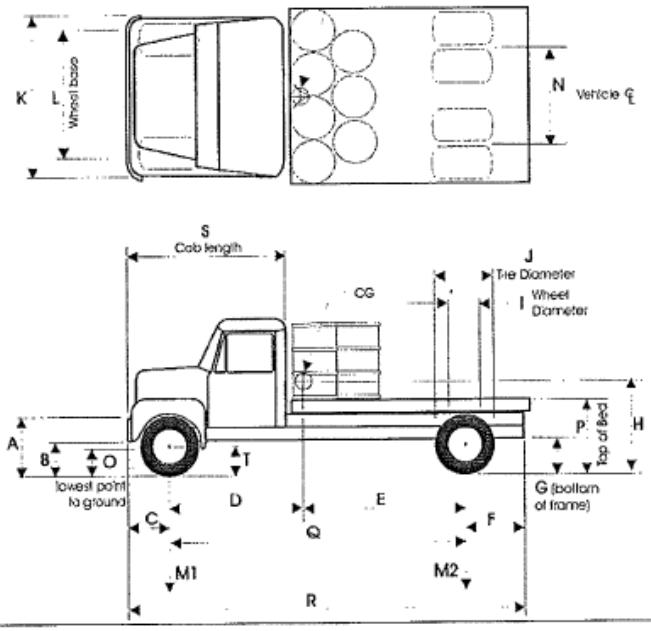

Geometry – in. (cm)

A	33"	B	18 5/8"	C	32"	D	calculated	E	calculated
F	58" to Frame	G	28 1/2"	H	calculated	I	24"	J	39"
K	92" 95"	L	79 3/4"	N	72"	P	9 1/2" front	P	54 1/2"
Q	228"	R	29' 4 1/2"	S	105"	T	173/4" 9" pumpkin back		

Mass Distribution – lb (kg)

Curb (as arrived)	LF		RF		LR		RR	
Empty (as modified)	LF	3100	RF	2850	LR	1850	RR	2000
Loading	LF	4300	RF	4100	LR	3050	RR	3375
Loading	LF		RF		LR		RR	
Final Test	LF		RF		LR		RR	

= 9800
= 14825
+ 150
14975

	Curb	Test
$M_{1\,(front)}$		
$M_{2\,(rear)}$		4055/8 RAT
M_{Total}		

Visual Target Locations:
side targets 40 5/16"
top targets 18 3/4"
black leading edge to leading edge

In-Vehicle DAS Location:
℄ truck @ 47 1/4"
244" bed length
175" from back of bed

BFT-2 VEHICLE DATA SHEET

PENNSTATE The Larson Institute			Vehicle Systems & Safety Program Crash Safety Research Manual	
VEHICLE _Preparation.docx	6 of 6	RAT	ZR	8/1/2011
Filename	*Page Number*	*Issuer*	*Approved*	*Implementation Date*

VEHICLE DATA SHEET

Test ID Number:

Date: 11-15-11	VIN No.: 1HTSCAAM9SH634602		
	Make: International	Model: 4700	Year: 1994
	GVWR:	Engine: Diesel	Odometer: 322,939
Device:	Tire Size (front):	Inflation Pressure (LF):	Inflation Pressure (RF):
	Tire Size (rear):	Inflation Pressure (LR):	Inflation Pressure (RR):

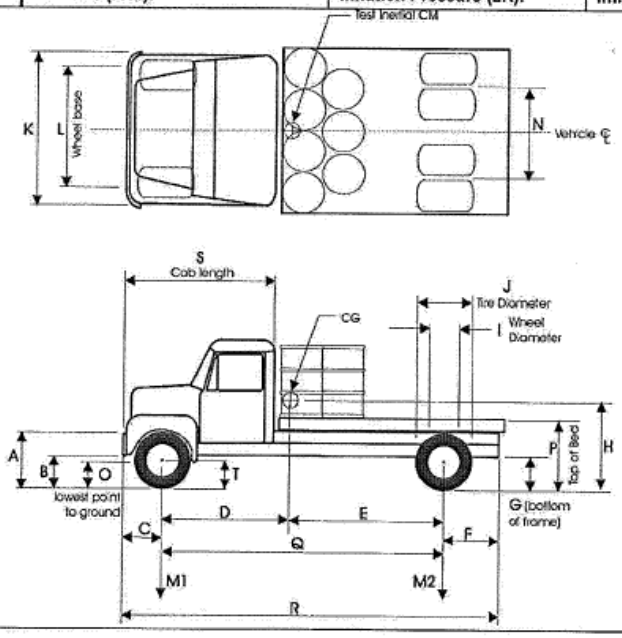

Geometry – in. (cm)

A		B		C		D	calculated	E	calculated
F		G		H	calculated	I		J	
K		L		N		O		P	
Q		R		S		T			

Mass Distribution – lb (kg)

Curb (as arrived)	LF	3030	RF	2880	LR	3040	RR	3400
Empty (as modified)	LF		RF		LR		RR	
Loading	LF		RF		LR		RR	
Loading	LF		RF		LR		RR	
Final Test	LF	3780	RF	3610	LR	3600	RR	3970

	Curb	*Test*
$M_{1\ (front)}$		
$M_{2\ (rear)}$		
M_{Total}		

Visual Target Locations:

side targets

top targets

In-Vehicle DAS Location:

APPENDIX B

IN-SITU SOIL MEASUREMENTS AND MODIFIED PROCTOR TEST RESULTS

MODIFIED PROCTOR TEST RESULTS

Test number	**1**	**2**	**3**	**4**
Mass of mold + base plate, M1	4132.8	4132.8	4132.8	4132.8
Mass of mold + base plate + moist soil, M2	6047	6222	6311	6333
Mass of moist soil, M2-M1	1914.2	2089.2	2178.2	2200.2
Moist density	1.94514	2.122968	2.213407	2.235762
Moisture can	1	2	3	4
mass of moisture can, M3	33.8	35.47	34.77	21.45
mass of can + moist soil, M4	112.1	199.4	110.3	99.2
Mass of can + dry soil, M5	106.5	184.5	103.4	91.5
Moisture content	7.702889	9.997987	10.05391	10.99215
dry density of compaction	1.806024	1.930006	2.011202	2.014343

mold volume in^3		m^3
	60.05309481	984.0939

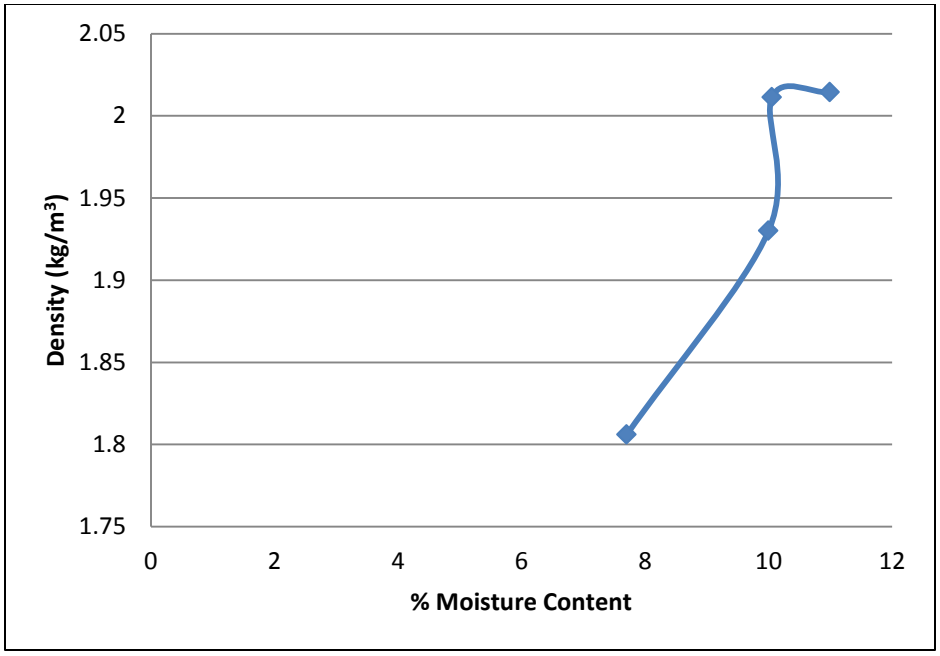

Figure B-1. Compaction level of the limestone dust vs. moisture content

DCPT RESULTS

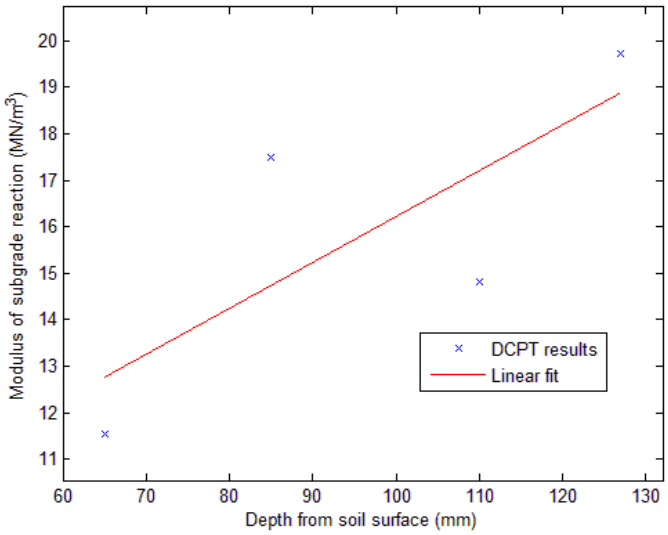

Figure B-2. DCPT results for SSBST-1

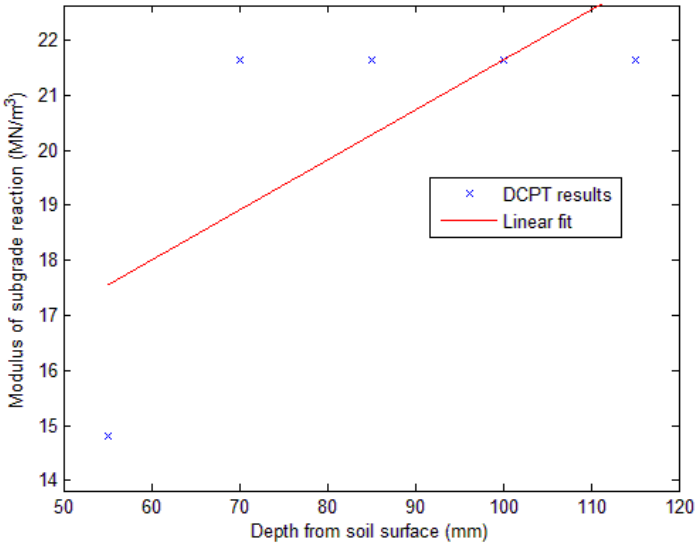

Figure B-3. DCPT results for SSBST-2

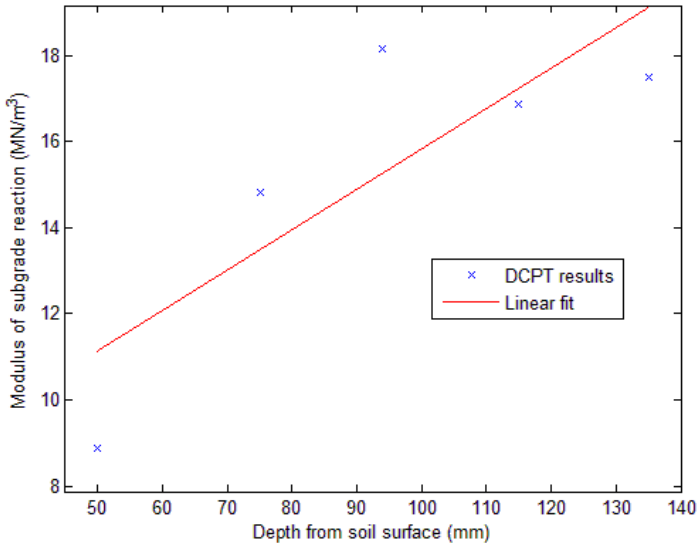

Figure B-4. DCPT results for SSBST-3

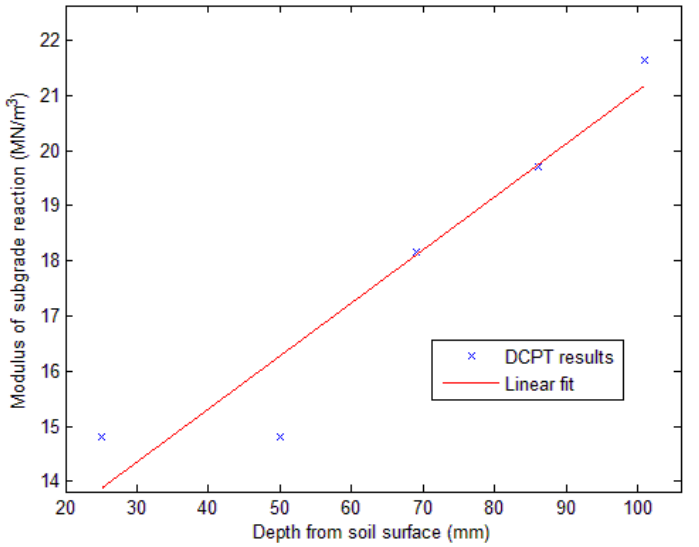

Figure B-5. DCPT results for SSBST-4

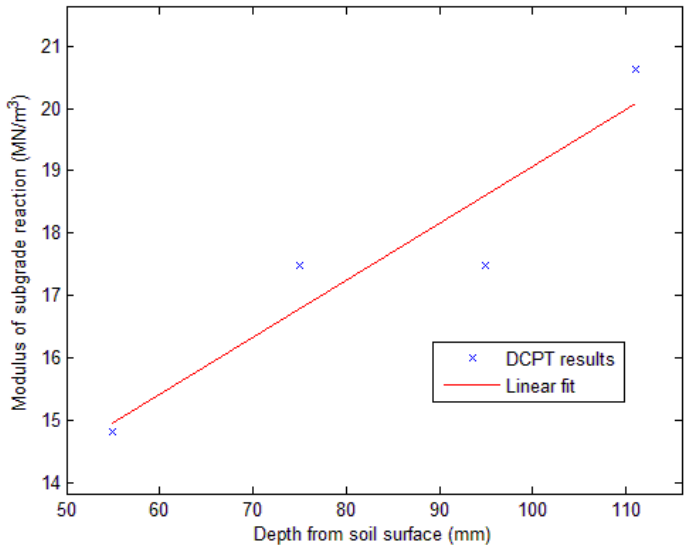

Figure B-6. DCPT results for SSBST-5

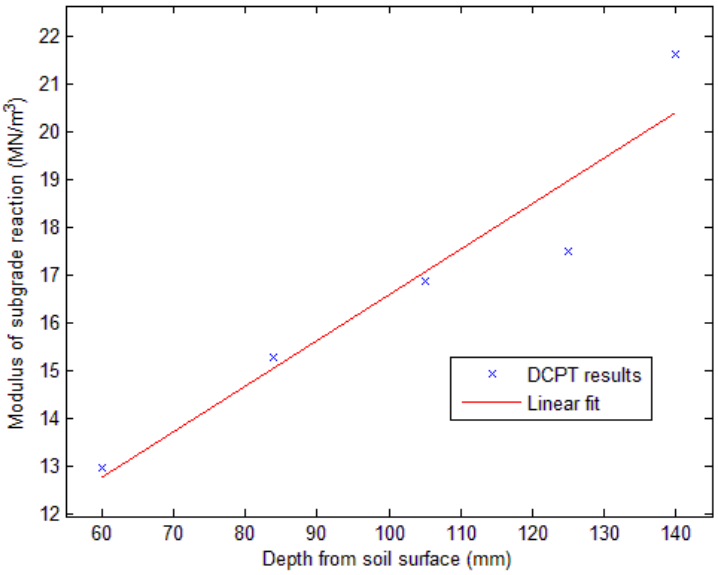

Figure B-7. DCPT results for SSMMSBT-1

APPENDIX C

SMALL SCALE RIGID WALL CRUSH TEST RESULTS

The results from the parameterization of the small scale crush material are presented in increasing tape spacing. The tape spacing was varied roughly between three amounts, heavily taped (1 cm spacing), medium taped (1.25 cm spacing), and lightly taped (1.5 cm spacing). As expected, the amount of tape is directly correlated to the equivalent spring and damping values such that heavily taped cans generally exhibited the highest equivalent spring and damper values. An additional method for loosely determining the spring and damper values, or more so the applicability of the specific crush material, one can simply scale the measured crush test results and compare them to the full scale LS-DYNA™ and low-order model simulation results. This method provides for an instant knowledge basis on the parameters of the material since scaled similar parameters will more or less match. The traversed distance was measured using the rotary encoder described in 6.2.

This appendix is organized as follows:

The heavily taped crush test results are first presented, followed by the medium taped results, and then the lightly taped results. The comparison of all three is then shown at the end of this appendix.

RESULTS OF HEAVILY TAPED (1 CM SPACING) CRUSH TESTS

Six heavily taped crush tests were performed using the small scale crash safety research pendulum. Figure C-1 – Figure C-6 show the pre-test and post-test condition of the heavily taped cans (HTC). Figure C-7 and Figure C-8 show the linear displacement of the individual tests with the resulting average displacement and the scaled up comparison to the LS-DYNA and low-order simulations.

Figure C-1. HTC-1

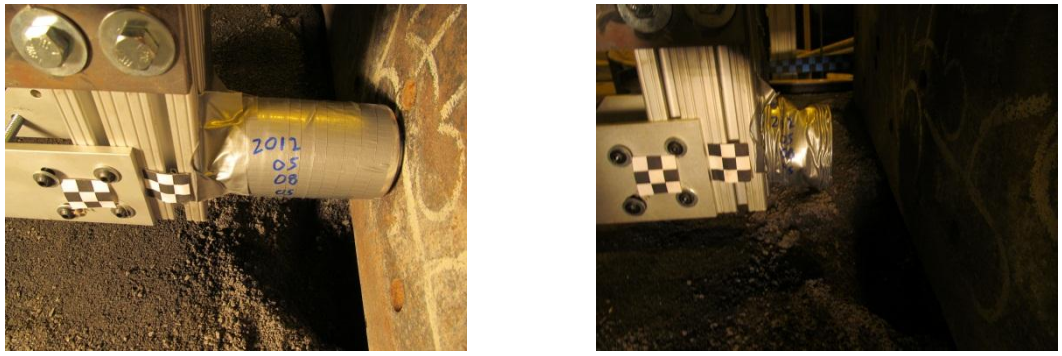

Figure C-2. HTC-2

Figure C-3. HTC-3

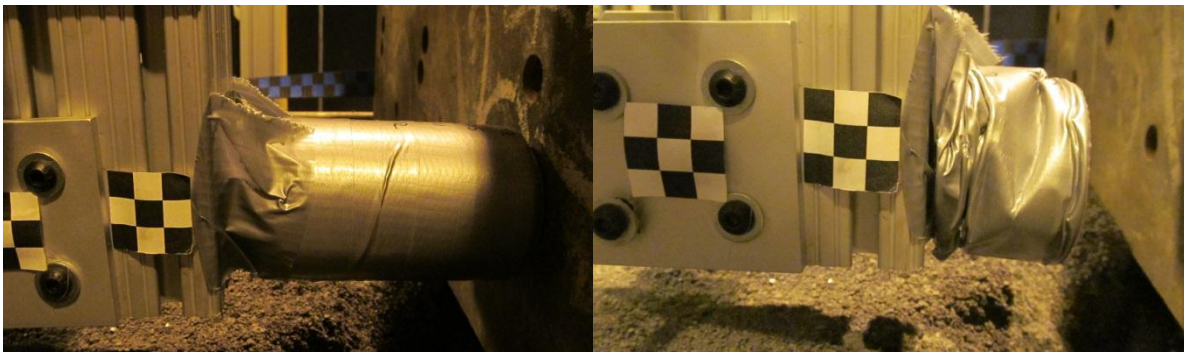

Figure C-4. HTC-4

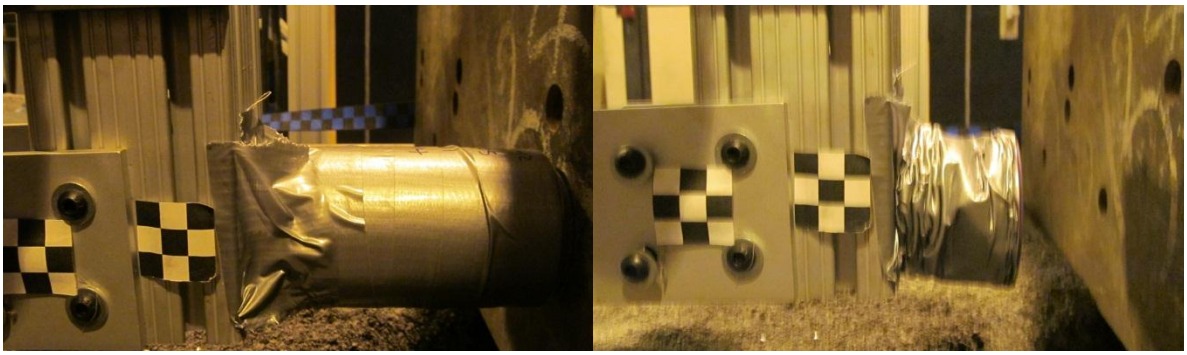

Figure C-5. HTC-5

Figure C-6. HTC-6

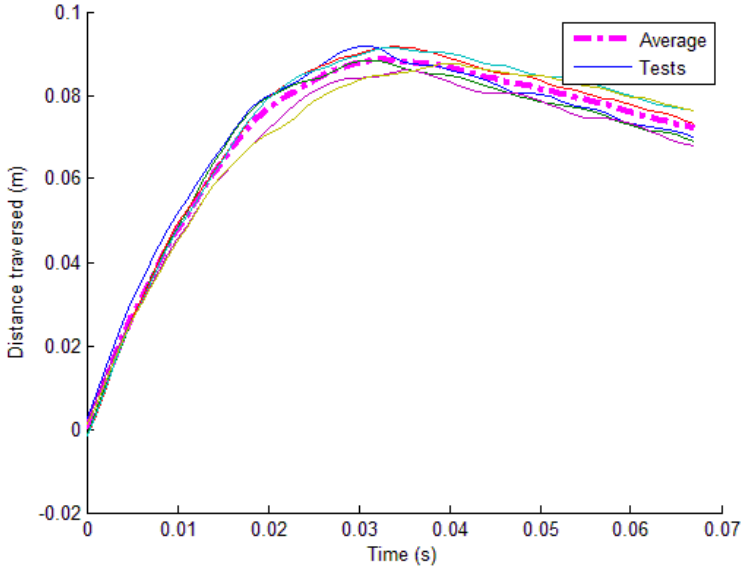

Figure C-7. Crush of heavily taped cans

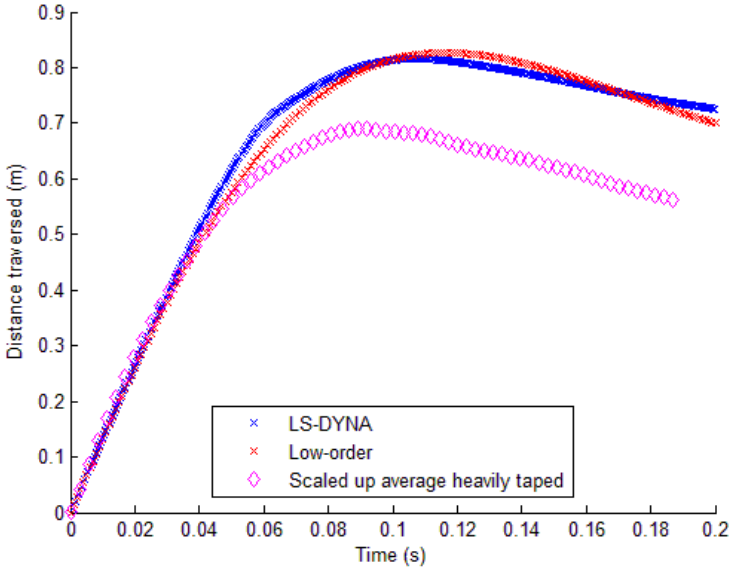

Figure C-8. Comparison of heavily taped cans to full scale crush simulations

RESULTS OF MEDIUM TAPED (1.25CM SPACING) CRUSH TESTS

13 medium taped crush tests were performed using the small scale crash safety research pendulum. Figure C-9 – Figure C-21 show the pre-test and post-test condition of the heavily taped cans (MTC). Figure C-22 and Figure C-23 show the linear displacement of the individual tests with the resulting average displacement and the scaled up comparison to the LS-DYNA and low-order simulations.

Figure C-9. MTC-1

Figure C-10. MTC-2

Figure C-11. MTC-3

Figure C-12. MTC-4

Figure C-13. MTC-5

Figure C-14. MTC-6

Figure C-15. MTC-7

Figure C-16. MTC-8

Figure C-17. MTC-9

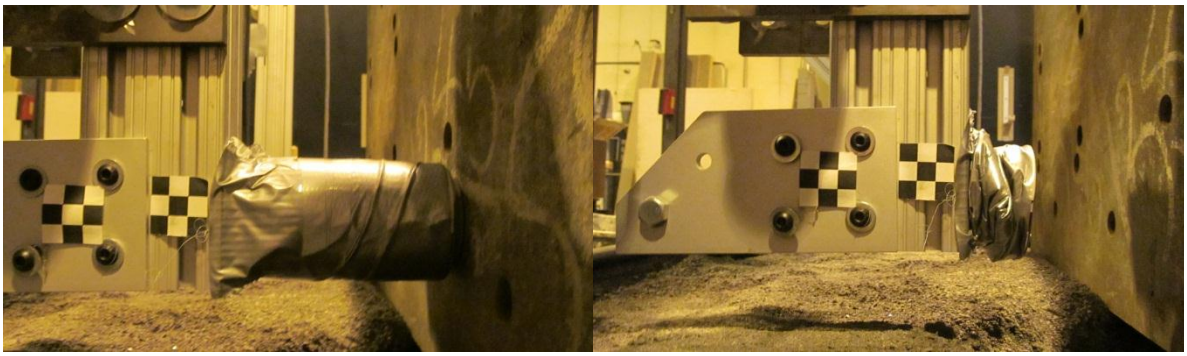

Figure C-18. MTC-10

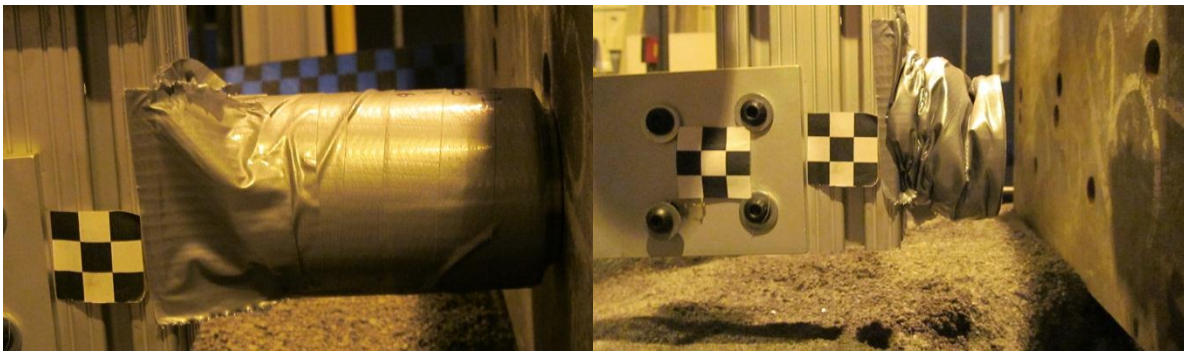

Figure C-19. MTC-11

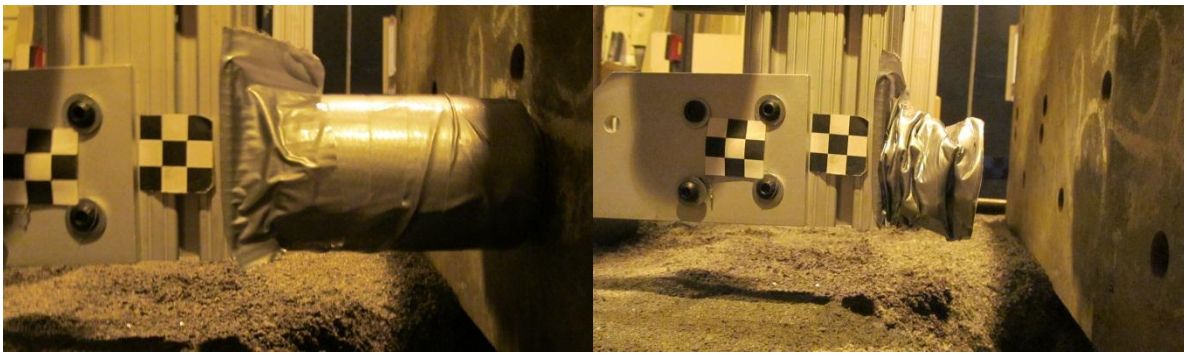

Figure C-20. MTC-12

Figure C-21. MTC-13

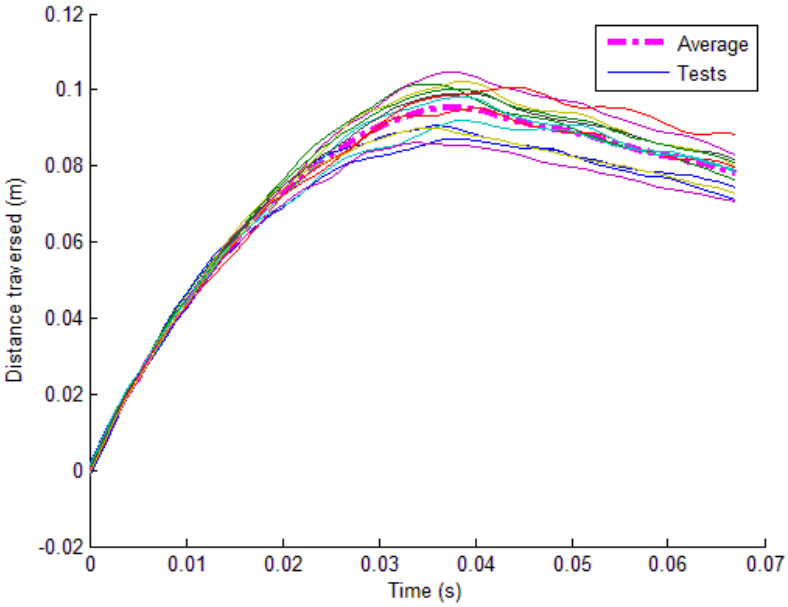

Figure C-22. Crush of medium taped cans

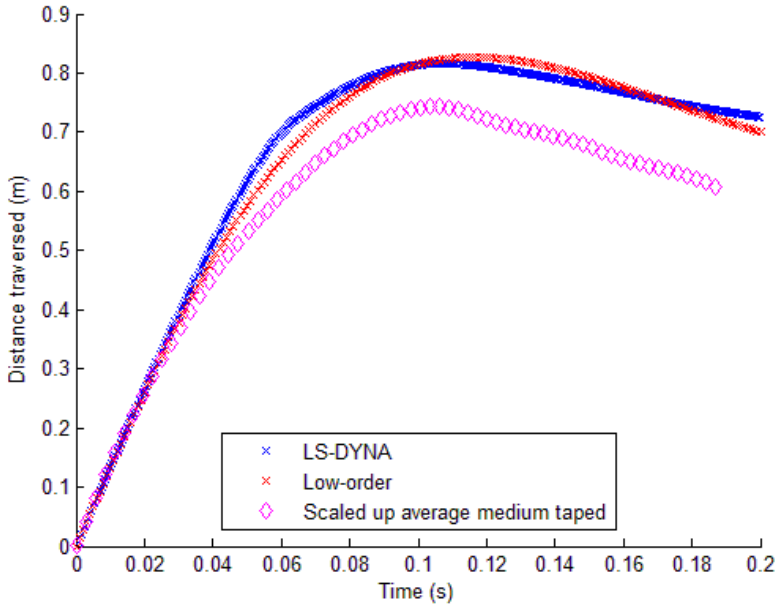

Figure C-23. Comparison of medium taped cans to full scale crush simulations

RESULTS OF LIGHTLY TAPED (1.5 CM SPACING) CRUSH TESTS

8 lightly taped crush tests were performed using the small scale crash safety research pendulum. Figure C-24 – Figure C-31 show the pre-test and post-test condition of the lightly taped cans (LTC). Figure C-32 and Figure C-33 show the linear displacement of the individual tests with the resulting average displacement and the scaled up comparison to the LS-DYNA and low-order simulations.

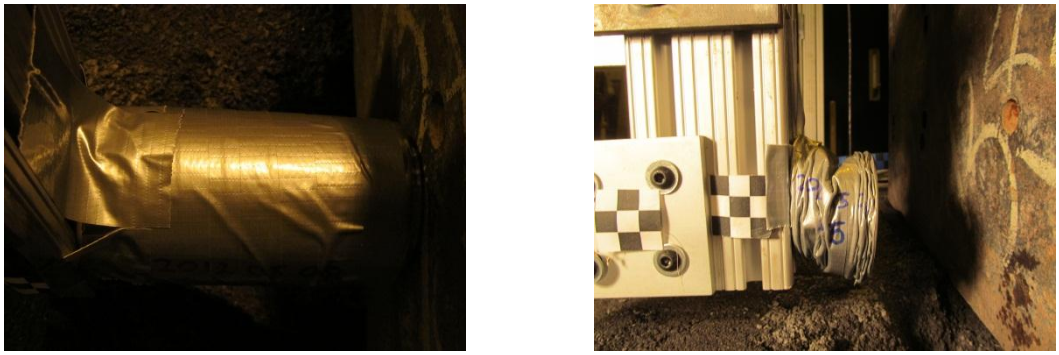

Figure C-24. LTC-1

Figure C-25. LTC-2

Figure C-26. LTC-3

Figure C-27. LTC-4

Figure C-28. LTC-5

Figure C-29. LTC-6

Figure C-30. LTC-7

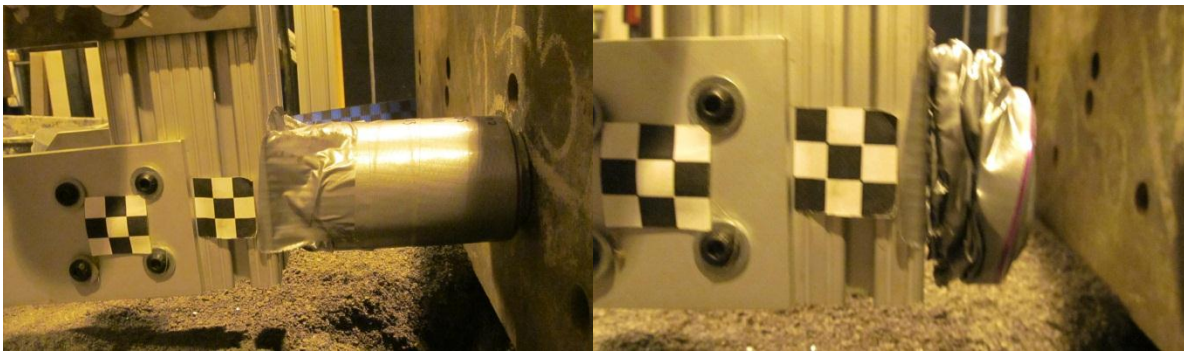

Figure C-31. LTC-8

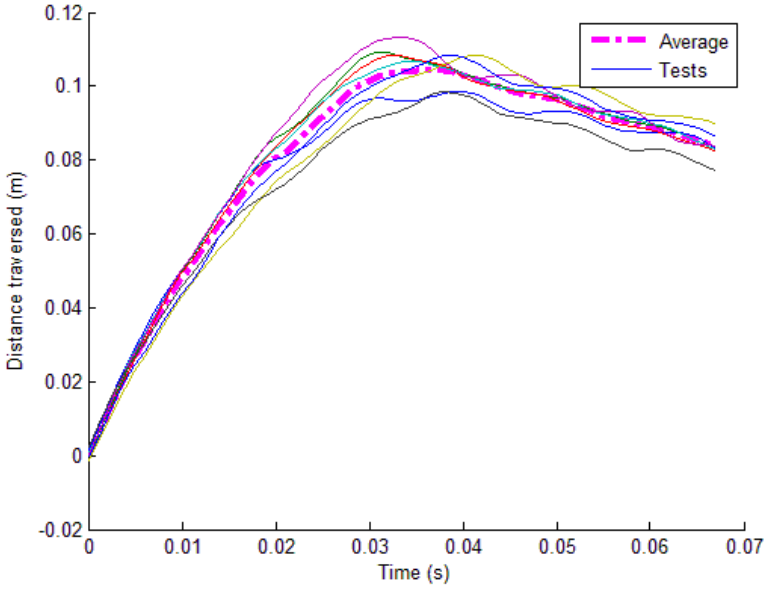

Figure C-32. Crush of lightly taped cans

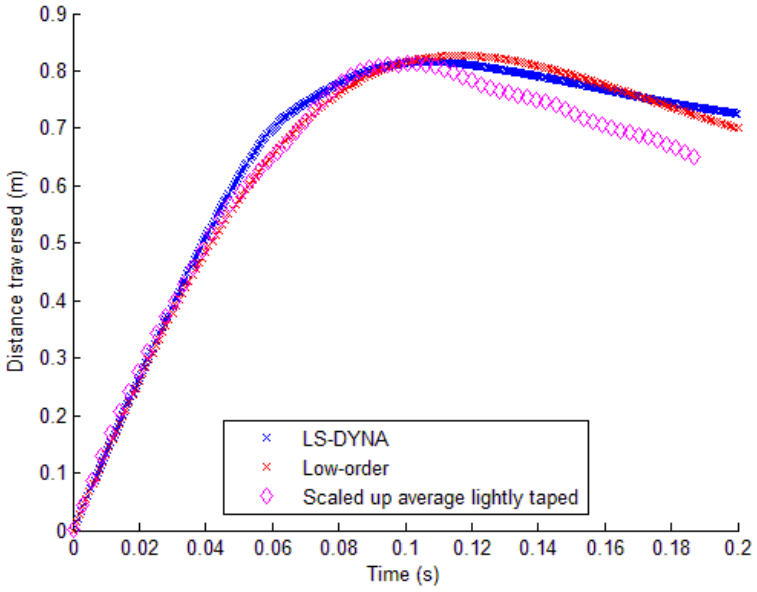

Figure C-33. Comparison of lightly taped cans to full scale crush simulations

COMPARISON OF CRUSH TEST RESULTS

Figure C-34 shows the comparison and resulting fits for the crush tests.

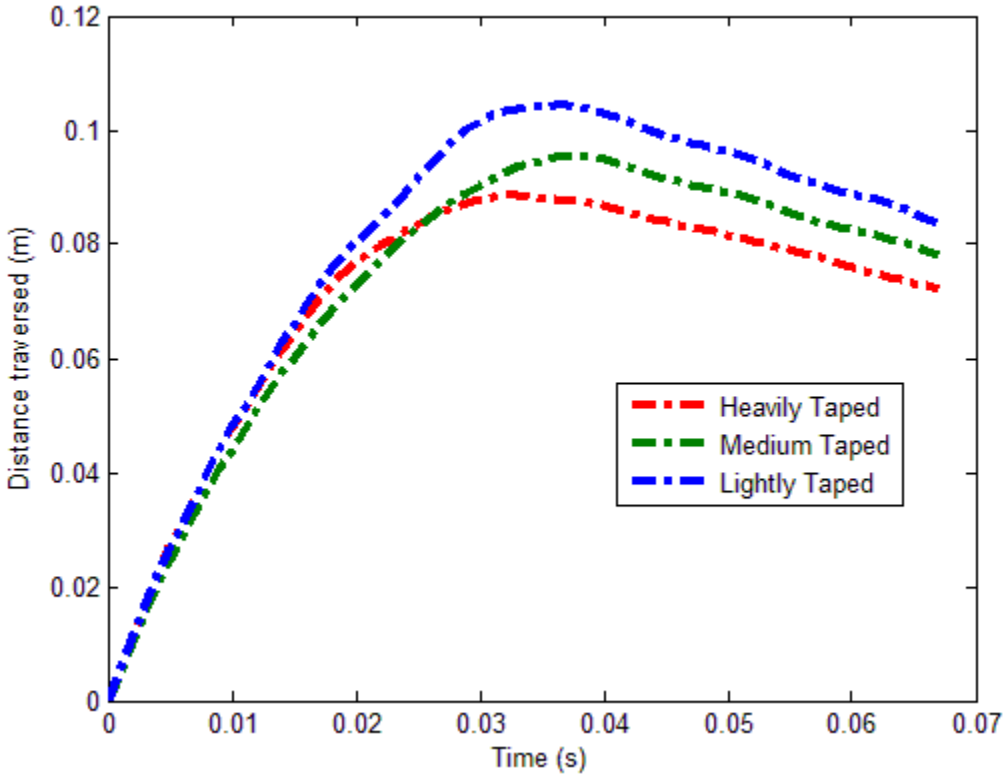

Figure C-34. Comparison of the three levels of taping for the small scale crush material

The average initial velocity of the heavily taped can tests was approximately 5.1, and the resulting spring and damping coefficients were then calculated to be 48.8 kN/m and 0.556 kN-s/m. The average initial velocity of the medium taped can tests was approximately 4.9 m/s, and the resulting spring and damping coefficients were then calculated to be 58.9 kN/m and 0.503 kN-s/m. The average initial velocity of the lightly taped can tests was approximately 5.25 m/s, and the resulting spring and damping coefficients were then calculated to be 35.9 kN/m and 0.538 kN-s/m.

APPENDIX D

EXAMPLE LOW-ORDER MODEL MATLAB® CODE

The example MATLAB® code is presented using the parameters associated with BST-2. Various other geometries and conditions can be simulated by simply changing the desired parameters Pi_Parameters.m. The script defaults to simulating the theoretical small scale parameters and not the measured small scale parameters. If the as-measured small scale parameters are to be simulated, they must be entered manually. The order for running the codes is as follows:

(1) Prepare the variables for simulation

   a. The full scale crash test parameters are entered in Pi_Parameters.m

   b. The corresponding small scale test size is entered as m_truck_model

   c. The as measured small scale test parameters are entered, if desired

   d. Pi_Parameters.m is saved after modifications have been made.

(2) Either script_Simulation.m, script_Simulation_small.m, or script_Simulation_dimensionless.m is opened and ran

PI_PARAMETERS.M

```
%this script will calculate the groupings of the scaling factors

%Mark P. Keske; mark.keske@gmail.com
close all
clear all
clc

%% perform D.A.

% A = [mt vt g], the set of repeating parameters in
% [Length
%           Mass
%                   Time]
A = [0  1  1;...
     1  0  0;...
     0 -1 -2];

 %lets figure out some sizes so we can make matrix inversion and allocation
 %real nice and quick
[rows_A cols_A] = size(A);

% B = rho_soil
%         rho_rock
%            c_truck
%                k_truck
%                   es
%                       W
%                         L
%                           H
%                             d
%                               d_truck
%                                    time
%                                       velocity
%                                           acceleration
%                                               angular vel
%                                                  angular vel
%                                                      Moment

B = [-3 -3  0  0 -2 -1  1  1  1  1  1  0  1  1  0  0  2;...
      1  1  1  1  1  1  0  0  0  0  0  0  0  0  0  0  1;...
      0  0 -1 -2 -2 -2  0  0  0  0  0  1 -1 -2 -1 -2  0];

% determine the size of B for future allocations
[rows_B cols_B] = size(B);

%create I vector for computation and allocations
E = eye(cols_B);

%Perform the matrix inversion and transpose for finding the pi parameters
S = -inv(A)*B*E;
S = S';

%Fill out Complete Matrix, Totes will have the entire dimensional set
%filled, so all you have to do is copy Totes into a spreadsheet that has
%variables orangized
```

```
Totes = zeros(cols_A+cols_B);
Totes(1:rows_B,1:cols_B) = B;
Totes(1:rows_A,end-cols_A+1:end) = A;
Totes(rows_B+1:end,1:cols_B) = E;
Totes(rows_B+1:end,end-cols_A+1:end) = S;

%% Apply D.A. to obtain small scale parameters

%give the prototype parameters to be scaled

%estimated modulus value for a full scale test using modified 2A limestone
%gravel, ASTM F2656-07 states that the soil should be no less than 90%
%compacted, where 95 MN/m^3 modulus correlates to a 94% compaction state
Modulus=95; %MN/m^3

% calcuate the relative density of the soil based on the modulus
D_r = 1/(2*.01221)*(0.1748+sqrt(0.1748^2-4*0.01221*(2.86-Modulus))); %...%,
%its in percent

%constants from curve fit of the relation between relative density and
%angle of internal friction
p1 = 0.0015;
p2 = 0.02;
p3 = 28;

%calcuate the effective angle of internal friction for the density
phi = p1*D_r^2+p2*D_r+p3; %degrees
phi = phi*pi/180; %radians

%give the reamining measured prototype parameters to be scaled, prototype
%means full scale

%rock mass density
rho_rock_proto = 2596;  %kg/m^3

%soil mass density
rho_soil_proto = 2010*D_r/100; %kg/m^3

%soil modulus of subgrade reaction
E_soil_proto = Modulus*10^6; %N/m^3

%graviational constant
g_proto =9.81;%m/s/s

%mass of the truck from BST-1
m_truck_proto = 6722;%kg

%initial velocity of the truck from BST-1
v_truck_proto = 14.5;%m/s

%Length, Width, and Height
L_proto = 1.65;         %m
W_proto = 1.68;         %m
H_proto = 3.44;         %m

%embedment depth
d_proto = 2.03;    %m
```

```
%distance from the soil surface to the equivalent point load of the truck,
%dimensions are taken from the vehicle data sheets
d_truck_proto = (1.4-18.75*.0254)/2+18.75*.0254;%.0254 means meters

%equivalent damping and spring of a M30 truck
c_truck_proto = 1.3891e5; %N-s/m
k_truck_proto = 3.1033e6; %N/m

%time at which to end the simulation and time step size
t_end_proto = .3;%s
t_step_proto = .002;%s

%just for curiosity's sake how big is this boulder?
m_rock_proto = L_proto*W_proto*H_proto*rho_rock_proto;%kg

%number of elements in the soil model
nelements_proto = 5000; %#

%height of soil elements based on equal spacing
delta_proto = d_proto/nelements_proto; %m

%% Group the parameters and calculate the pieye parameters
%determine the pi parameter values
%all of the variables use the same nomenclature as above, and the parameter
%is always on the left
pi_rho_rock = rho_rock_proto*v_truck_proto^6/(m_truck_proto*g_proto^3);

pi_rho_soil = rho_soil_proto*v_truck_proto^6/(m_truck_proto*g_proto^3);

pi_c_truck = c_truck_proto*v_truck_proto/(m_truck_proto*g_proto);

pi_k_truck = k_truck_proto*v_truck_proto^2/(m_truck_proto*g_proto^2);

pi_Es = E_soil_proto*v_truck_proto^6/(m_truck_proto*g_proto^4);

pi_L = L_proto*g_proto/v_truck_proto^2;

pi_d_truck = d_truck_proto*g_proto/v_truck_proto^2;

pi_W = W_proto*g_proto/v_truck_proto^2;

pi_H = H_proto*g_proto/v_truck_proto^2;

pi_d = d_proto*g_proto/v_truck_proto^2;

pi_t = t_end_proto*g_proto/v_truck_proto;

pi_t_step = t_step_proto*g_proto/v_truck_proto;

pi_delta = delta_proto*g_proto/v_truck_proto^2;

pi_nelements = pi_d/pi_delta;

pi_m_truck = 1;
pi_v_truck = 1;
```

```
pi_g = 1;

%% Find model parameters based on scaling laws
%model means small scale
%give the model constants, you can alter E_soil, which will then give you a
%different set of pi parameters
E_soil_model = E_soil_proto;
g_model = g_proto;

%reverse the direction of the pigh parameters to solve for the small scale
%parameters.

%it all starts with one
m_truck_model = 8; %kg

%and the rest just fall out like an uneasy jinga tower balancing on a
%single block...that's not in the middle.
v_truck_model = (pi_Es*m_truck_model*g_model^4/E_soil_model)^(1/6);

rho_rock_model = pi_rho_rock*m_truck_model*g_model^3/v_truck_model^6;

rho_soil_model = pi_rho_soil*m_truck_model*g_model^3/v_truck_model^6;

k_truck_model = pi_k_truck*m_truck_model*g_model^2/v_truck_model^2;

c_truck_model = pi_c_truck*m_truck_model*g_model/v_truck_model;

W_model = pi_W*v_truck_model^2/g_model;

L_model = pi_L*v_truck_model^2/g_model;

H_model = pi_H*v_truck_model^2/g_model;

d_model = pi_d*v_truck_model^2/g_model;

d_truck_model = pi_d_truck*v_truck_model^2/g_model;

t_end_model = pi_t*v_truck_model/g_model;

t_step_model = pi_t_step*v_truck_model/g_model;

delta_model = (pi_delta)*(v_truck_model^2/(g_model));

nelements_model = d_model/delta_model;

% now, lets save all these numbas so we can use them in the script

save('Model Parameters','L_model','W_model','H_model','d_model',...
    'd_truck_model','m_truck_model',...
    'v_truck_model','k_truck_model','c_truck_model','E_soil_model',...
    'g_model','rho_soil_model','rho_rock_model','rho_soil_proto',...
    't_end_model','t_step_model',...
    'delta_model','nelements_model','phi');

save('Proto Parameters','L_proto','W_proto','H_proto','d_proto',...
    'd_truck_proto','m_truck_proto',...
```

```
    'v_truck_proto','k_truck_proto','c_truck_proto','E_soil_proto',...
    'g_proto','rho_soil_proto','rho_rock_proto',...
    't_end_proto','t_step_proto',...
    'delta_proto','nelements_proto','phi');

save('Dimensionless Parameters','pi_m_truck','pi_v_truck','pi_g',...
    'pi_rho_rock','pi_rho_soil',...
    'pi_c_truck','pi_k_truck','pi_Es','pi_L','pi_d_truck','pi_W',...
    'pi_H','pi_d','pi_t','pi_t_step','pi_delta','phi','pi_nelements')
```

SCRIPT_SIMULATION.M

```
%% Rotation Model based on FEA of soil parameters
% Mark P. Keske, mark.keske@gmail.com
% Alex Brown, aab5009@psu.edu
% Sean Brennan, sbrennan@psu.edu,

clc
clear
close all

%Just in case there were other parameters that had been loaded, we're going
%to run the code here at the beginning
Pi_Parameters

%this code is created such that Pi_Parameters_Appendix is all that needs to
%be changed, it will load all of the parameters defined in the above .m

%define the number of soil elements
nelements = nelements_proto;

%% Define constants
%soil and rock density
rho_soil = rho_soil_proto; % kg/m^3
rho_rock = rho_rock_proto; % kg/m^3

%vehicle mass and initial velocity
m_truck = m_truck_proto; %kg
v_truck = v_truck_proto; %m/s

%graviational constant
g = g_proto; %m/s^2

% equivalent distance for the point load above the soil surface
d_truck = -d_truck_proto; %m

%equivalent damper and spring values for the truck
c_truck = c_truck_proto; %N-s/m
k_truck = k_truck_proto; %N/m

%angle of the soil wedge as measured from vertical down
theta = pi/4+phi/2;

%Modulus of subgrade reaction
E_soil = E_soil_proto;  %N/m^3

%Strain rate scaling factor for laterally loaded soil
Kg = tan(theta)/cos(phi);

%length of the assumed cantilever for fracture calcuations
lengthCantilever = 0.75;%m

%peak force from a rigid wall impact
peakForce = m_truck*g*100; %N

%Conversion from ksi to MPa
```

```
ksi2Mpa = 6.89475728;

%material properties for American Black Granite, tensile and compressive
%strengths
sigmaTensileUltimate = 4.63*ksi2Mpa;%MPa
sigmaCompressionUltimate = 26.4*ksi2Mpa;%MPa


%% Define boulder geometry
% Inputs are arranged as Height, Embedment depth, Length, all measured in
Lengths = L_proto;
Widths = W_proto;
Heights = H_proto;

% Initialize arrays for multiple Lengths, Widths and Heights for contour
% plots, not demonstrated in this code

%matrix for the maximum distance traversed by the boulder
distanceMoved = zeros(length(Widths),length(Lengths),length(Heights));

%matrix for the maximum angle traversed by the boulder
angleTraversed = zeros(length(Widths),length(Lengths),length(Heights));

%matrix for the mass of the various sized boulders
massBoulder   = zeros(length(Widths),length(Lengths),length(Heights));

%matrix for the peak stress for a given boulder geometry wrt fracture
peakStress = zeros(length(Widths),length(Lengths),length(Heights));

%matrix for the factor of safety wrt fracture
factorSafety = zeros(length(Widths),length(Lengths),length(Heights));

%matrix for the maximum mass for the boulders
max_massBoulder = zeros(length(Widths),length(Lengths),length(Heights));

%matrix for saving the maximum distance traversed by the vehicle
distanceTruckMoved = zeros(length(Widths),length(Lengths),length(Heights));

%% Permutate through the different rock geometries
for H=Heights
    for W=Widths
        for L=Lengths

            %set the indices for the above variables which will be saved
            i_width = find(Widths == W); %row
            j_length = find(Lengths == L);%column
            k_height = find(Heights == H);%depth

            %boulder embedment depth,
            d = d_proto;%m

            % Calculate initial fixed mass of the boulder and the mass
            % moment of inertia about the boulder C.G., note this will
            % later be translated over to the boulder-soil subsystem C.G.
            m_boulder =rho_rock*H*L*W;  %kg
            I_b = m_boulder*(H^2+L^2)/12;  %kg-m^2
```

```
%check to see if the boulder is embedded, if not then skip
%straight to the function
if d>0
    %total spring stiffness of the soil elemetns, as idealized
    %from a long slender rod, cross section area divided by the
    %intial undeformed length of the soil element
    k_soil_total = E_soil*d*W/(d/tan(phi)*nelements); %N/m^2

    %total soil damping constant, density times swept area,
    %will be mulitplied by the velocity squared of each element
    c_soil_total = rho_soil*d*W; %N-s^2/m^2

    %total mass of the soil wedge, treated as a triangle
    m_soil_total = rho_soil*d*W*(d*tan(theta))/2;%kg

    %distribute the spring and damping constants, the spring
    %constant increases linearly with depth, the soil damping
    %value is assumed to remain constant with depth and is even
    %distributed
    ki = k_soil_total*linspace(0,abs(d),nelements); %N/m
    ci = c_soil_total/nelements; %N -s^2/m^2

    %set the height of the soil elements
    delta = delta_proto;%m

    %calculate the mass of each trapezoidal soil element
    %treated as a rectangle with a triangle attached to the end

    %length of the base of the soil wedge
    L_wedge = d*tan(theta); %m

    %length of each soil element along the top
    L_delta = (1:nelements)*delta*tan(theta); %m

    %length of each soil element along the bottom, short side
    L_flat = L_wedge-L_delta;%m

    %mass of the end triangle of each soil element
    m_tip = 1/2*delta*W*L_delta(1)*rho_soil;%kg

    %cross sectional area of each soil element
    Af = W*delta;%m^2

    %mass vector of the soil elements from soil surface to
    %bottom of boulder
    mi = Af*L_flat*rho_soil+m_tip;%kg


    %calcuate the center of mass of the boulder-soil subsystem

    %divide the embedment depth of the boulder into nelements
    %along the boulder
    spaces = d*linspace(1,0,nelements); %m

    %calculate the center of mass wrt x from the impact side of
    %the boulder
    mass_center_x = 1/(sum(mi)+m_boulder)*...
        (sum(mi)*L+m_boulder*L/2);%m
```

```
    %calcuate the center of mass wrt y from the bottom of the
    %boulder
    mass_center_y = 1/(sum(mi)+m_boulder)*...
        (sum(mi.*spaces)+m_boulder*H/2);%m

    %distribute the soil elements wrt the center of mass of the
    %boulder-soil subsystem such that elements above the C.M.
    %have negative distances and elements below are positive
    %x positive right, y positive down from the C.M.

    %pretty self explanitory
    cg_from_bottom = mass_center_y;%m

    %determine where the surface of the soil is wrt the C.M.
    % if this is a negative number, soil line is ABOVE CG.
    soil_line_y = (cg_from_bottom-d);%m

    %redistribute the soil elements wrt the C.M.
    di = linspace(soil_line_y,cg_from_bottom,nelements);%m

else %if the boulder aint burried, then don't burry it
    k_soil_total = 0;
    c_soil_total = 0;
    m_soil_total = 0;
    ki = 0;
    ci = 0;
    mi = 0;

    %the distance to the bottome
    di = H/2;
end

%calculate the radial distance from the C.M. to the soil
%elements
li = sqrt(di.^2+(L-mass_center_x)^2); %m

%calcuate the angle from vertical for the soil elements
gamma = atan(di/(L-mass_center_x))+pi/2;   %radians

%calcuate the distance from the boulder C.G. to the
%boulder-soil subsystem C.M. to be used in the // axis theorem
r_center = (H/2-mass_center_y)^2+(L/2-mass_center_x)^2;%m

%apply the parallel axis theorem
I_b = I_b + m_boulder*r_center; %kg-m^2

%time to create a time vector for ODE45
tspan = 0:t_step_proto:t_end_proto;

%initial velocity of the truck drives the simulation
% states = [xb, xbdot, thetab, thetabdot, xt, xtdot, xtddot],
% the maxwell model uses jerk, so acceleratoin is a state
x0 = [0 0 0 0 0 v_truck 0];%states

%truck-boulder model
%run numerical integration
options = [];
```

```
            %Send the function all of the goodies so we get the time and
            %states back from ODE45
            [t_r,x_r] = ode45(@fcn_Low_Order_EOM,tspan,x0,options,mi,...
                ki,ci,m_boulder,I_b,di,c_truck,k_truck,m_truck,d_truck,...
                L,H,li,gamma,mew,d,phi,rho_soil,W,g,mass_center_x,...
                mass_center_y,v_truck,Kg);

            %send the fracture function its goodies so it will tell us the
            %resulting factor of safety, n, and the principle stress
            [n,sigma1] = fcn_fracture(lengthCantilever,peakForce,W,L,...
                sigmaTensileUltimate,sigmaCompressionUltimate);


            %Pass/Fail Criteria used with contour plots

            %based on experiments and the simulation, a failure criterion
            %for angle.
            AngleCriteria = 20; %degrees,

            %save the distance the boulder translates
            distanceMoved(i_width,j_length,k_height) = max(x_r(:,1));

            %save the angle traversed wrt the pass/fail criteria.  A
            %positive value indicates a failure since it would go + degrees
            %past 20
            angleTraversed(i_width,j_length,k_height) = max(x_r(:,3)*...
                180/pi)-AngleCriteria; %degrees

            %save the principle stress
            peakStress(i_width,j_length,k_height) = sigma1; % Units are MPa

            %save the factor of safety, the factors of safety are
            %represented as negative number for contour plotting, abs(n)>1
            %indicated expected pass
            factorSafety(i_width,j_length,k_height) = n;

            %save the masses of the boulders
            massBoulder(i_width,j_length,k_height) = m_boulder/1000;%Mg
            max_massBoulder(i_width,j_length,k_height) = ...
                massBoulder(i_width,j_length,k_height)-27.215;  % Mg

            %save the distance the truck moved
            distanceTruckMoved(i_width,j_length,k_height) = max(x_r(:,5));
            %m

            %since things are pretty well commented, lets take a peek at
            %how far the boulder rotated
            disp(angleTraversed);
        end
    end
end

%save the data as a .mat file for later usage
save('BST-2 Results', 'Lengths','Widths','Heights','distanceMoved',...
    'angleTraversed','massBoulder','max_massBoulder','distanceTruckMoved');

%% Plotting time
```

```
figure;
plot(t_r,x_r(:,3)*180/pi,'sr')
xlabel('Time (s)')
ylabel('Angular displacement (degrees)')
legend('Full scale crash test','Full scale simulation','location','best')
saveas(gcf,'fig Full Scale BAB30 Angle and Simulation.fig')

%calculate the linear displacement of the center of the boulder since the
%video tracking is done wrt the boulder C.G. and not the boulder-soil
%subsystem

%calculate radial distance form the center of mass of the boulder to the
%boulder-soil subsystem
Rbp = sqrt((mass_center_x-L/2)^2+(mass_center_y-H/2)^2);%m

%calculate the angle from center of mass of the boulder-soil subsystem to
%the boulder C.G.
gamma_bp = atan((mass_center_x-L/2)/(mass_center_y-H/2));%radians

%fix the corridinate locations such that the angle is measure from the
%positive x direction
if gamma_bp<0
    gamma_bp = abs(gamma_bp)+pi/2;
    xb = x_r(:,1)+Rbp*cos(gamma_bp-x_r(:,3))-Rbp*cos(gamma_bp);
elseif gamma_bp>0
    gamma_bp = (gamma_bp)+pi/2;
    xb = x_r(:,1)+Rbp*cos(gamma_bp+x_r(:,3))-Rbp*cos(gamma_bp);
end

figure;
plot(t_r,xb,'sr')
legend('Full scale crash test','Full scale simulation','location','best')
xlabel('Time (s)')
ylabel(Linear displacement (m)')
saveas(gcf,'fig Full Scale BAB30 CG Disp and Simulation.fig')


figure;
plot(t_r,x_r(:,5),'sr')
legend('Full scale crash test','Full scale simulation','location','best')
xlabel('Time (s)')
ylabel('Linear displacement (m)')
saveas(gcf,'fig Full Scale BAB30 Truck and Simulation.fig')
```

SCRIPT_SIMULATION_SMALL.M

```
%% Rotation Model based on FEA of soil parameters
% Mark P. Keske, mark.keske@gmail.com
% Alex Brown, aab5009@psu.edu
% Sean Brennan, sbrennan@psu.edu,

clc
clear
close all

%Just in case there were other parameters that had been loaded, we're going
%to run the code here at the beginning
Pi_Parameters

%this code is created such that Pi_Parameters_Appendix is all that needs to
%be changed, it will load all of the parameters defined in the above .m

%define the number of soil elements
nelements = nelements_model;

%% Define constants
%soil and rock density
rho_soil = rho_soil_model; % kg/m^3
rho_rock = rho_rock_model; % kg/m^3

%vehicle mass and initial velocity
m_truck = m_truck_model; %kg
v_truck = v_truck_model; %m/s

%graviational constant
g = g_model; %m/s^2

% equivalent distance for the point load above the soil surface
d_truck = -d_truck_model; %m

%equivalent damper and spring values for the truck
c_truck = c_truck_model; %N-s/m
k_truck = k_truck_model; %N/m

%angle of the soil wedge as measured from vertical down
theta = pi/4+phi/2;

%Modulus of subgrade reaction
E_soil = E_soil_model;  %N/m^3

%Strain rate scaling factor for laterally loaded soil
Kg = tan(theta)/cos(phi);

%length of the assumed cantilever for fracture calcuations
lengthCantilever = 0.75;%m

%peak force from a rigid wall impact
peakForce = m_truck*g*100; %N

%Conversion from ksi to MPa
```

```
ksi2Mpa = 6.89475728;

%material properties for American Black Granite, tensile and compressive
%strengths
sigmaTensileUltimate = 4.63*ksi2Mpa;%MPa
sigmaCompressionUltimate = 26.4*ksi2Mpa;%MPa


%% Define boulder geometry
% Inputs are arranged as Height, Embedment depth, Length, all measured in
Lengths = L_model;
Widths = W_model;
Heights = H_model;

% Initialize arrays for multiple Lengths, Widths and Heights for contour
% plots, not demonstrated in this code

%matrix for the maximum distance traversed by the boulder
distanceMoved = zeros(length(Widths),length(Lengths),length(Heights));

%matrix for the maximum angle traversed by the boulder
angleTraversed = zeros(length(Widths),length(Lengths),length(Heights));

%matrix for the mass of the various sized boulders
massBoulder   = zeros(length(Widths),length(Lengths),length(Heights));

%matrix for the peak stress for a given boulder geometry wrt fracture
peakStress = zeros(length(Widths),length(Lengths),length(Heights));

%matrix for the factor of safety wrt fracture
factorSafety = zeros(length(Widths),length(Lengths),length(Heights));

%matrix for the maximum mass for the boulders
max_massBoulder = zeros(length(Widths),length(Lengths),length(Heights));

%matrix for saving the maximum distance traversed by the vehicle
distanceTruckMoved = zeros(length(Widths),length(Lengths),length(Heights));

%% Permutate through the different rock geometries
for H=Heights
    for W=Widths
        for L=Lengths

            %set the indecies for the above variables which will be saved
            i_width = find(Widths == W); %row
            j_length = find(Lengths == L);%column
            k_height = find(Heights == H);%depth

            %boulder embedment depth,
            d = d_model;%m

            % Calculate initial fixed mass of the boulder and the mass
            % moment of inertia about the boulder C.G., note this will
            % later be translated over to the boulder-soil subsystem C.G.
            m_boulder =rho_rock*H*L*W;  %kg
            I_b = m_boulder*(H^2+L^2)/12;  %kg-m^2
```

```
%check to see if the boulder is embedded, if not then skip
%straight to the function
if d>0
    %total spring stiffness of the soil elemetns, as idealized
    %from a long slender rod, cross section area divided by the
    %intial undeformed length of the soil element
    k_soil_total = E_soil*d*W/(d/tan(phi)*nelements); %N/m^2

    %total soil damping constant, density times swept area,
    %will be mulitplied by the velocity squared of each element
    c_soil_total = rho_soil*d*W; %N-s^2/m^2

    %total mass of the soil wedge, treated as a triangle
    m_soil_total = rho_soil*d*W*(d*tan(theta))/2;%kg

    %distribute the spring and damping constants, the spring
    %constant increases linearly with depth, the soil damping
    %value is assumed to remain constant with depth and is even
    %distributed
    ki = k_soil_total*linspace(0,abs(d),nelements); %N/m
    ci = c_soil_total/nelements; %N -s^2/m^2

    %set the height of the soil elements
    delta = delta_model;%m

    %calculate the mass of each trapezoidal soil element
    %treated as a rectangle with a triangle attached to the end

    %length of the base of the soil wedge
    L_wedge = d*tan(theta); %m

    %length of each soil element along the top
    L_delta = (1:nelements)*delta*tan(theta); %m

    %length of each soil element along the bottom, short side
    L_flat = L_wedge-L_delta;%m

    %mass of the end triangle of each soil element
    m_tip = 1/2*delta*W*L_delta(1)*rho_soil;%kg

    %cross sectional area of each soil element
    Af = W*delta;%m^2

    %mass vector of the soil elements from soil surface to
    %bottom of boulder
    mi = Af*L_flat*rho_soil+m_tip;%kg


    %calcuate the center of mass of the boulder-soil subsystem

    %divide the embedment depth of the boulder into nelements
    %along the boulder
    spaces = d*linspace(1,0,nelements); %m

    %calculate the center of mass wrt x from the impact side of
    %the boulder
    mass_center_x = 1/(sum(mi)+m_boulder)*...
        (sum(mi)*L+m_boulder*L/2);%m
```

```
    %calcuate the center of mass wrt y from the bottom of the
    %boulder
    mass_center_y = 1/(sum(mi)+m_boulder)*...
        (sum(mi.*spaces)+m_boulder*H/2);%m

    %distribute the soil elements wrt the center of mass of the
    %boulder-soil subsystem such that elements above the C.M.
    %have negative distances and elements below are positive
    %x positive right, y positive down from the C.M.

    %pretty self explanitory
    cg_from_bottom = mass_center_y;%m

    %determine where the surface of the soil is wrt the C.M.
    % if this is a negative number, soil line is ABOVE CG.
    soil_line_y = (cg_from_bottom-d);%m

    %redistribute the soil elements wrt the C.M.
    di = linspace(soil_line_y,cg_from_bottom,nelements);%m

else %if the boulder aint burried, then don't burry it
    k_soil_total = 0;
    c_soil_total = 0;
    m_soil_total = 0;
    ki = 0;
    ci = 0;
    mi = 0;

    %the distance to the bottome
    di = H/2;
end

%calculate the radial distance from the C.M. to the soil
%elements
li = sqrt(di.^2+(L-mass_center_x)^2); %m

%calcuate the angle from vertical for the soil elements
gamma = atan(di/(L-mass_center_x))+pi/2;   %radians

%calcuate the distance from the boulder C.G. to the
%boulder-soil subsystem C.M. to be used in the // axis theorem
r_center = (H/2-mass_center_y)^2+(L/2-mass_center_x)^2;%m

%apply the parallel axis theorem
I_b = I_b + m_boulder*r_center; %kg-m^2

%time to create a time vector for ODE45
tspan = 0:t_step_model:t_end_model;

%initial velocity of the truck drives the simulation
% states = [xb, xbdot, thetab, thetabdot, xt, xtdot, xtddot],
% the maxwell model uses jerk, so acceleratoin is a state
x0 = [0 0 0 0 0 v_truck 0];%states

%truck-boulder model
%run numerical integration
options = [];
```

```
            %Send the function all of the goodies so we get the time and
            %states back from ODE45
            [t_r,x_r] = ode45(@fcn_Low_Order_EOM,tspan,x0,options,mi,...
                ki,ci,m_boulder,I_b,di,c_truck,k_truck,m_truck,d_truck,...
                L,H,li,gamma,mew,d,phi,rho_soil,W,g,mass_center_x,...
                mass_center_y,v_truck,Kg);

            %send the fracture function its goodies so it will tell us the
            %resulting factor of safety, n, and the principle stress
            [n,sigma1] = fcn_fracture(lengthCantilever,peakForce,W,L,...
                sigmaTensileUltimate,sigmaCompressionUltimate);


            %Pass/Fail Criteria used with contour plots

            %based on experiments and the simulation, a failure criterion
            %for angle.
            AngleCriteria = 20; %degrees,

            %save the distance the boulder translates
            distanceMoved(i_width,j_length,k_height) = max(x_r(:,1));

            %save the angle traversed wrt the pass/fail criteria.  A
            %positive value indicates a failure since it would go + degrees
            %past 20
            angleTraversed(i_width,j_length,k_height) = max(x_r(:,3)*...
                180/pi)-AngleCriteria; %degrees

            %save the principle stress
            peakStress(i_width,j_length,k_height) = sigma1; % Units are MPa

            %save the factor of safety, the factors of safety are
            %represented as negative number for contour plotting, abs(n)>1
            %indicated expected pass
            factorSafety(i_width,j_length,k_height) = n;

            %save the masses of the boulders
            massBoulder(i_width,j_length,k_height) = m_boulder/1000;%Mg
            max_massBoulder(i_width,j_length,k_height) = ...
                massBoulder(i_width,j_length,k_height)-27.215;  % Mg

            %save the distance the truck moved
            distanceTruckMoved(i_width,j_length,k_height) = max(x_r(:,5));
            %m

            %since things are pretty well commented, lets take a peek at
            %how far the boulder rotated
            disp(angleTraversed);
        end
    end
end

%save the data as a .mat file for later usage
save('BST-2 Results', 'Lengths','Widths','Heights','distanceMoved',...
    'angleTraversed','massBoulder','max_massBoulder','distanceTruckMoved');

%% Plotting time
```

```
figure;
plot(t_r,x_r(:,3)*180/pi,'sr')
xlabel('Time (s)')
ylabel('Angular displacement (degrees)')
saveas(gcf,'fig Small Scale BAB30 Angle and Simulation.fig')

%calculate the linear displacement of the center of the boulder since the
%video tracking is done wrt the boulder C.G. and not the boulder-soil
%subsystem

%calculate radial distance form the center of mass of the boulder to the
%boulder-soil subsystem
Rbp = sqrt((mass_center_x-L/2)^2+(mass_center_y-H/2)^2);%m

%calcuate the angle from center of mass of the boulder-soil subsystem to
%the boulder C.G.
gamma_bp = atan((mass_center_x-L/2)/(mass_center_y-H/2));%radians

%fix the corridinate locations such that the angle is measure from the
%positive x direction
if gamma_bp<0
    gamma_bp = abs(gamma_bp)+pi/2;
    xb = x_r(:,1)+Rbp*cos(gamma_bp-x_r(:,3))-Rbp*cos(gamma_bp);
elseif gamma_bp>0
    gamma_bp = (gamma_bp)+pi/2;
    xb = x_r(:,1)+Rbp*cos(gamma_bp+x_r(:,3))-Rbp*cos(gamma_bp);
end

figure;
plot(t_r,xb,'sr')
xlabel('Time (s)')
ylabel('Linear displacement (m)')
saveas(gcf,'fig Small Scale BAB30 CG Disp and Simulation.fig')


figure;
plot(t_r,x_r(:,5),'sr')
xlabel('Time (s)')
ylabel('Linear displacement (m)')
saveas(gcf,'fig Small Scale BAB30 Truck and Simulation.fig')
```

SCRIPT_SIMULATION_DIMENSIONLESS.M

```
%% Rotation model based on FEA of soil parameters
% Mark P. Keske, mark.keske@gmail.com
% Alex Brown, aab5009@psu.edu
% Sean Brennan, sbrennan@psu.edu,

clc
clear
close all

%Just in case there were other parameters that had been loaded, we're going
%to run the code here at the beginning
Pi_Parameters

%this code is created such that Pi_Parameters_Appendix is all that needs to
%be changed, it will load all of the parameters defined in the above .m

%define the number of soil elements
nelements = nelements_model;

%% Define constants
%soil and rock density
rho_soil = rho_soil_model; % kg/m^3
rho_rock = rho_rock_model; % kg/m^3

%vehicle mass and initial velocity
m_truck = m_truck_model; %kg
v_truck = v_truck_model; %m/s

%graviational constant
g = g_model; %m/s^2

% equivalent distance for the point load above the soil surface
d_truck = -d_truck_model; %m

%equivalent damper and spring values for the truck
c_truck = c_truck_model; %N-s/m
k_truck = k_truck_model; %N/m

%angle of the soil wedge as measured from vertical down
theta = pi/4+phi/2;

%Modulus of subgrade reaction
E_soil = E_soil_model;  %N/m^3

%Strain rate scaling factor for laterally loaded soil
Kg = tan(theta)/cos(phi);

%length of the assumed cantilever for fracture calcuations
lengthCantilever = 0.75;%m

%peak force from a rigid wall impact
peakForce = m_truck*g*100; %N

%Conversion from ksi to MPa
```

```
ksi2Mpa = 6.89475728;

%material properties for American Black Granite, tensile and compressive
%strengths
sigmaTensileUltimate = 4.63*ksi2Mpa;%MPa
sigmaCompressionUltimate = 26.4*ksi2Mpa;%MPa


%% Define boulder geometry
% Inputs are arranged as Height, Embedment depth, Length, all measured in
Lengths = L_model;
Widths = W_model;
Heights = H_model;

% Initialize arrays for multiple Lengths, Widths and Heights for contour
% plots, not demonstrated in this code

%matrix for the maximum distance traversed by the boulder
distanceMoved = zeros(length(Widths),length(Lengths),length(Heights));

%matrix for the maximum angle traversed by the boulder
angleTraversed = zeros(length(Widths),length(Lengths),length(Heights));

%matrix for the mass of the various sized boulders
massBoulder   = zeros(length(Widths),length(Lengths),length(Heights));

%matrix for the peak stress for a given boulder geometry wrt fracture
peakStress = zeros(length(Widths),length(Lengths),length(Heights));

%matrix for the factor of safety wrt fracture
factorSafety = zeros(length(Widths),length(Lengths),length(Heights));

%matrix for the maximum mass for the boulders
max_massBoulder = zeros(length(Widths),length(Lengths),length(Heights));

%matrix for saving the maximum distance traversed by the vehicle
distanceTruckMoved = zeros(length(Widths),length(Lengths),length(Heights));

%% Permutate through the different rock geometries
for H=Heights
    for W=Widths
        for L=Lengths

            %set the indecies for the above variables which will be saved
            i_width = find(Widths == W); %row
            j_length = find(Lengths == L);%column
            k_height = find(Heights == H);%depth

            %boulder embedment depth,
            d = d_model;%m

            % Calculate initial fixed mass of the boulder and the mass
            % moment of inertia about the boulder C.G., note this will
            % later be translated over to the boulder-soil subsystem C.G.
            m_boulder =rho_rock*H*L*W;  %kg
            I_b = m_boulder*(H^2+L^2)/12;  %kg-m^2
```

```
%check to see if the boulder is embedded, if not then skip
%straight to the function
if d>0
    %total spring stiffness of the soil elemetns, as idealized
    %from a long slender rod, cross section area divided by the
    %intial undeformed length of the soil element
    k_soil_total = E_soil*d*W/(d/tan(phi)*nelements); %N/m^2

    %total soil damping constant, density times swept area,
    %will be mulitplied by the velocity squared of each element
    c_soil_total = rho_soil*d*W; %N-s^2/m^2

    %total mass of the soil wedge, treated as a triangle
    m_soil_total = rho_soil*d*W*(d*tan(theta))/2;%kg

    %distribute the spring and damping constants, the spring
    %constant increases linearly with depth, the soil damping
    %value is assumed to remain constant with depth and is even
    %distributed
    ki = k_soil_total*linspace(0,abs(d),nelements); %N/m
    ci = c_soil_total/nelements; %N -s^2/m^2

    %set the height of the soil elements
    delta = delta_model;%m

    %calculate the mass of each trapezoidal soil element
    %treated as a rectangle with a triangle attached to the end

    %length of the base of the soil wedge
    L_wedge = d*tan(theta); %m

    %length of each soil element along the top
    L_delta = (1:nelements)*delta*tan(theta); %m

    %length of each soil element along the bottom, short side
    L_flat = L_wedge-L_delta;%m

    %mass of the end triangle of each soil element
    m_tip = 1/2*delta*W*L_delta(1)*rho_soil;%kg

    %cross sectional area of each soil element
    Af = W*delta;%m^2

    %mass vector of the soil elements from soil surface to
    %bottom of boulder
    mi = Af*L_flat*rho_soil+m_tip;%kg


    %calcuate the center of mass of the boulder-soil subsystem

    %divide the embedment depth of the boulder into nelements
    %along the boulder
    spaces = d*linspace(1,0,nelements); %m

    %calculate the center of mass wrt x from the impact side of
    %the boulder
    mass_center_x = 1/(sum(mi)+m_boulder)*...
        (sum(mi)*L+m_boulder*L/2);%m
```

```
    %calcuate the center of mass wrt y from the bottom of the
    %boulder
    mass_center_y = 1/(sum(mi)+m_boulder)*...
        (sum(mi.*spaces)+m_boulder*H/2);%m

    %distribute the soil elements wrt the center of mass of the
    %boulder-soil subsystem such that elements above the C.M.
    %have negative distances and elements below are positive
    %x positive right, y positive down from the C.M.

    %pretty self explanitory
    cg_from_bottom = mass_center_y;%m

    %determine where the surface of the soil is wrt the C.M.
    % if this is a negative number, soil line is ABOVE CG.
    soil_line_y = (cg_from_bottom-d);%m

    %redistribute the soil elements wrt the C.M.
    di = linspace(soil_line_y,cg_from_bottom,nelements);%m

else %if the boulder aint burried, then don't burry it
    k_soil_total = 0;
    c_soil_total = 0;
    m_soil_total = 0;
    ki = 0;
    ci = 0;
    mi = 0;

    %the distance to the bottome
    di = H/2;
end

%calculate the radial distance from the C.M. to the soil
%elements
li = sqrt(di.^2+(L-mass_center_x)^2); %m

%calcuate the angle from vertical for the soil elements
gamma = atan(di/(L-mass_center_x))+pi/2;   %radians

%calcuate the distance from the boulder C.G. to the
%boulder-soil subsystem C.M. to be used in the // axis theorem
r_center = (H/2-mass_center_y)^2+(L/2-mass_center_x)^2;%m

%apply the parallel axis theorem
I_b = I_b + m_boulder*r_center; %kg-m^2

%time to create a time vector for ODE45
tspan = 0:pi_t_step:pi_t;

%initial velocity of the truck drives the simulation
% states = [xb, xbdot, thetab, thetabdot, xt, xtdot, xtddot],
% the maxwell model uses jerk, so acceleratoin is a state
x0 = [0 0 0 0 0 1 0];%states

%truck-boulder model
%run numerical integration
options = [];
```

```
            %Send the function all of the goodies so we get the time and
            %states back from ODE45
            [pi_t_r,x_r] = ode45(@fcn_DEOM,tspan,x0,options,mi,...
                ki,ci,m_boulder,I_b,di,c_truck,k_truck,m_truck,d_truck,...
                L,H,li,gamma,mew,d,phi,rho_soil,W,g,mass_center_x,...
                mass_center_y,v_truck,Kg);

            %send the fracture function its goodies so it will tell us the
            %resulting factor of safety, n, and the principle stress
            [n,sigma1] = fcn_fracture(lengthCantilever,peakForce,W,L,...
                sigmaTensileUltimate,sigmaCompressionUltimate);


            %Pass/Fail Criteria used with contour plots

            %based on experiments and the simulation, a failure criterion
            %for angle.
            AngleCriteria = 20; %degrees,

            %save the distance the boulder translates
            distanceMoved(i_width,j_length,k_height) = max(x_r(:,1));

            %save the angle traversed wrt the pass/fail criteria.  A
            %positive value indicates a failure since it would go + degrees
            %past 20
            angleTraversed(i_width,j_length,k_height) = max(x_r(:,3)*...
                180/pi)-AngleCriteria; %degrees

            %save the principle stress
            peakStress(i_width,j_length,k_height) = sigma1; % Units are MPa

            %save the factor of safety, the factors of safety are
            %represented as negative number for contour plotting, abs(n)>1
            %indicated expected pass
            factorSafety(i_width,j_length,k_height) = n;

            %save the masses of the boulders
            massBoulder(i_width,j_length,k_height) = m_boulder/1000;%Mg
            max_massBoulder(i_width,j_length,k_height) = ...
                massBoulder(i_width,j_length,k_height)-27.215;  % Mg

            %save the distance the truck moved
            distanceTruckMoved(i_width,j_length,k_height) = max(x_r(:,5));
            %m

            %since things are pretty well commented, lets take a peek at
            %how far the boulder rotated
            disp(angleTraversed);
        end
    end
end

%save the data as a .mat file for later usage
save('BST-2 Results', 'Lengths','Widths','Heights','distanceMoved',...
    'angleTraversed','massBoulder','max_massBoulder','distanceTruckMoved');

%% Plotting time or shood I say, plotting pi time
```

```
figure;
plot(pi_t_r,x_r(:,3)*180/pi,'+g')
xlabel('Dimensionless time')
ylabel('Angular displacement (degrees)')
saveas(gcf,'fig Full Scale BAB30 Angle and Simulation.fig')

%calculate the linear displacement of the center of the boulder since the
%video tracking is done wrt the boulder C.G. and not the boulder-soil
%subsystem

%calculate radial distance form the center of mass of the boulder to the
%boulder-soil subsystem and then turn it into the dimensionless radial
%distnace, since the output of the numerical integration were the
%dimensionless states
Rbp = sqrt((mass_center_x-L/2)^2+(mass_center_y-H/2)^2)*g/v_truck^2;

%calcuate the angle from center of mass of the boulder-soil subsystem to
%the boulder C.G.
gamma_bp = atan((mass_center_x-L/2)/(mass_center_y-H/2));

%fix the corridinate locations such that the angle is measure from the
%positive x direction
if gamma_bp<0
    gamma_bp = abs(gamma_bp)+pi/2;
    xb = x_r(:,1)+Rbp*cos(gamma_bp-x_r(:,3))-Rbp*cos(gamma_bp);
elseif gamma_bp>0
    gamma_bp = (gamma_bp)+pi/2;
    xb = x_r(:,1)+Rbp*cos(gamma_bp+x_r(:,3))-Rbp*cos(gamma_bp);

end


figure;
plot(pi_t_r,xb,'+g')
xlabel('Dimensionless time')
ylabel('Dimensionless displacement')


figure;
plot(pi_t_r,x_r(:,5),'+g')
xlabel('Dimensionless time')
ylabel('Dimensionless displacement')
```

FCN_LOW_ORDER_EOM.M

```
function xprime = fcn_Low_Order_EOM(~,x,mi,ki,ci,m_boulder,...
    I_b,di,ct,kt,m_truck, dt,L,H,li,gamma,mew,d,phi,...
    rho_soil,W,g,mass_center_x,mass_center_y,v_initial,Kg)

%Mark P. Keske, mark.keske@gmail.com, Alex Brown, aab5009@psu.edu

%this file is commented such that the comments in line with the variables
%describes the units

%state vector is [x boulder; v boulder; theta boulder; w boulder; x truck;
%v truck; a truck]

%calcuate the position of the restoring reaction
gamma_reac = atan(mass_center_y/(L-mass_center_x));%radians
lr = sqrt((H-mass_center_y)^2+(L-mass_center_x)^2);%m

%divide the embedment depth into N equally spaced elements
depth = linspace(0,d,length(mi));%m

%Passive earth pressure coefficent
Kp = tan(pi/4+phi/2)^2;

%Preallocate vectors used within the soil force loop
Fix= zeros(length(di),1);%total force from soil
Fki= zeros(length(di),1);%soil spring force
Fci= zeros(length(di),1);%soil damping force
Mi = zeros(length(di),1);%moments of the soil forces about C.M.
xi = zeros(length(di),1);%linear position of each soil element
xi_dot = zeros(length(di),1);%linear velocity of soil elements
delta_xi = zeros(length(di),1);%change in linear positio of soil elements
Pu_max = zeros(length(di),1);%maximum lateral pressure for soil
%based on depth
Area = zeros(length(di),1);%Cross sectional area of soil elements
max_force = zeros(length(di),1);%maximum lateral force for soil

%% Calculate the Soil Forces and Moments

%from the top of soil surface to bottom of boulder
for z = 1:length(di)

    %calcuate the linear position of the soil element
    xi(z) = x(1)+li(z)*sin(gamma(z)+x(3));%m

    %calcuate the change in linear position of the soil element
    delta_xi(z) = xi(z)-li(z)*sin(gamma(z));%m

    %calcuate the linear velocity of the soil element
    xi_dot(z) = x(2)+x(4)*li(z)*cos(gamma(z)+x(3));%m/s

    %check to ensure that the boulder is embedded, if not then don't try to
    %calculate soil forces that aren't there
    if d>0

        %calculate the soil element spring force
```

```
        Fki(z) = ki(z)*(delta_xi(z));%N

        %calcuate the ultimate lateral load for soil at the given depth
        Pu_max(z) = Kp^2*rho_soil*W*depth(z)*g*Kg/depth(end);%Pa

        %calcuate the height of a single soil element
        delta = depth(2)-depth(1);%m

        %calculate the cross sectional area of one soil element
        Area(z) = W*delta;%m^2

        %calculate the ultimate lateral force for the given depth
        max_force(z) = Pu_max(z)*Area(z);%N

        %apply limiting conditions on spring force such that the spring
        %force cannot exceed the ultimate lateral load
        if abs(Fki(z))>max_force(z)
            Fki(z)=sign(Fki(z))*max_force(z);%N
        end

        %calculate the soil element damping force
        Fci(z) = ci*(xi_dot(z))^2 *sign(xi_dot(z));%N

        %calculate the total force from the soil element
        Fix(z) = -(Fki(z)+Fci(z));%N

        %calculat the resulting moment of the soil force for the element
        Mi(z) = -Fix(z)*li(z)*cos(gamma(z)+x(3)-pi);%N-m

    end
    %end of soil depth if statement
end
%end of for loop for soil elements

%display the states to the workspace; it's fun to watch the numbers scroll!
clc
disp(x)

%% Calculate the Truck Force and Moment

%calcuate the radial distance of the truck wrt C.M. of boulder-soil
%subsystem
lt = sqrt((di(1)+dt)^2+mass_center_x^2);%m

%calcuate the angle of the truck wrt C.M. of boulder-soil subsystem
gamma_t = atan(mass_center_x/(di(1)+dt));%radians

%calculate the linear velocity of the impact point on the boulder
x_dot_truck_boulder = x(2) + x(4)*lt*cos(gamma_t+x(3));%m/s

%calcuate the foce acting on the truck
F_truck = -m_truck*x(7);%N

%truck rebound criteria
if F_truck<0
    F_truck = 0;
end
```

```
%calculate the resultin moment of the truck acting on the boulder
M_truck = F_truck*lt*cos((gamma_t+x(3)));%N-m


%% Calculte the estimated restoring moment due to gravity

%calculate the total moment acting on the boulder without the restoring
%moment and set the restoring moment initially as the sum with opposite
%sign

if(sum(Mi)+sum(M_truck))~=0
    M_reac = -sign(sin(gamma_reac+x(3)))*...
        (sum(Mi)+sum(M_truck));%N-m
else
    M_reac = 0;
end

%calculate the maximum restoring momement
M_reac_max = -sign(sin(gamma_reac+x(3)))*...
    m_boulder*g*lr*cos((gamma_reac+x(3)));

%limit the restoring moment to the maximum theoretical moment
if abs(M_reac)>abs(M_reac_max)%N-m
    M_reac = M_reac_max;%N-m
end


%% EOMS
%Collect all of the forces and plug into the state space EOM


% set up boundaries so the boulder will not oscilate in the soil or
% continue to rotate beyond 90 degrees as there is no truck or mother earth
% to push back up on the boulder and 90 degrees is well beyond the
% approximation methods used thus far

if x(3)<pi/2&&x(4)>-.1
    xprime = [x(2);...%x dot is v
        1/(m_boulder+sum(mi))*(sum(Fix)+sum(F_truck));...EOMr xb
        x(4);... %theta dot is omega
        1/(I_b+sum(mi.*(di.^2+(L-mass_center_x)^2)))*...
        (sum(Mi)+sum(M_truck)+M_reac);... EOM for theta
        x(6);... %xt dot is v_truck
        x(7);... %vt dot is a_truck
        -kt/m_truck*x(6)-kt/ct*x(7)+kt/m_truck*x_dot_truck_boulder];
        %EOM for the truck
else % if the boulder goes beyond 90 degrees or starts to rock backwards,
    %kill the sum beech
    xprime = [0;0;0;0;0;0;0];
end
```

FCN_DEOM.M

```
function xprime = fcn_DEOM(~,x,mi,ki,ci,m_boulder,...
    I_b,di,ct,kt,m_truck, dt,L,H,li,gamma,mew,d,phi,...
    rho_soil,W,g,mass_center_x,mass_center_y,v_initial,Kg)

%Mark P. Keske, mark.keske@gmail.com, Alex Brown, aab5009@psu.edu


%this file is commented such that the comments in line with the variables
%describe the units

%state vector is [pi_xb; pi_xb_dot; theta boulder; pi_omega_b; pi_x_v;
%pi_x_v_dot; pi_x_v_double_dot]

%Transform the dimensionless parameters into dimensioned form to calcuate
%the forces.  The forces will then be transformed back into the
%dimensionless state prior to evaluating the DEOM

%Based on scaling laws, xb = pi_xb*vo^2/g, ...
x_boulder = x(1)*v_initial^2/g;%m
x_boulder_dot = x(2)*v_initial;%m/s
theta = x(3);%radians
theta_dot = x(4)*g/v_initial;%rad/s
x_truck = x(5)*v_initial^2/g;%m
x_truck_dot = x(6)*v_initial;%m/s
x_truck_double_dot = x(7)*g;%m/s/s

%calcuate the position of the restoring reaction
gamma_reac = atan(mass_center_y/(L-mass_center_x));%radians
lr = sqrt((H-mass_center_y)^2+(L-mass_center_x)^2);%m

%divide the embedment depth into N equally spaced elements
depth = linspace(0,d,length(mi));%m

%Passive earth pressure coefficent
Kp = tan(pi/4+phi/2)^2;

%Preallocate vectors used within the soil force loop
Fix= zeros(length(di),1);%total force from soil
Fki= zeros(length(di),1);%soil spring force
Fci= zeros(length(di),1);%soil damping force
Mi = zeros(length(di),1);%moments of the soil forces about C.M.
xi = zeros(length(di),1);%linear position of each soil element
xi_dot = zeros(length(di),1);%linear velocity of soil elements
delta_xi = zeros(length(di),1);%change in linear positio of soil elements
Pu_max = zeros(length(di),1);%maximum lateral pressure for soil
%based on depth
Area = zeros(length(di),1);%Cross sectional area of soil elements
max_force = zeros(length(di),1);%maximum lateral force for soil

%% Soil Forces and Moments

%from the top of soil surface to bottom of boulder
for z = 1:length(di)
```

```
    %calcuate the linear position of the soil element
    xi(z) = x_boulder+li(z)*sin(gamma(z)+theta);   %m

    %calcuate the change in linear position of the soil element
    delta_xi(z) = xi(z)-li(z)*sin(gamma(z));   %m

    %calcuate the linear velocity of the soil element
    xi_dot(z) = x_boulder_dot+theta_dot*li(z)*cos(gamma(z)+theta);   %m

    %check to ensure that the boulder is embedded, if not then don't try to
    %calculate soil forces that aren't there
    if d>0

        %calcuate the height of a single soil element
        delta = depth(2)-depth(1);   %m

        %calculate the soil element spring force
        Fki(z) = ki(z)*(delta_xi(z));   %m

        %calcuate the ultimate lateral load for soil at the given depth
        Pu_max(z) = Kp^2*rho_soil*W*depth(z)*g*Kg/depth(end);%Pa

        %calculate the cross sectional area of one soil element
        Area(z) = W*delta;   %m^2

        %calculate the ultimate lateral force for the given depth
        max_force(z) = Pu_max(z)*Area(z);   %N

        %apply limiting conditions on spring force such that the spring
        %force cannot exceed the ultimate lateral load
        if abs(Fki(z))>max_force(z)
            Fki(z)=sign(Fki(z))*max_force(z);%N
        end

        %calculate the soil element damping force
        Fci(z) = ci*(xi_dot(z))^2 *sign(xi_dot(z));%N

        %calculate the total force from the soil element
        Fix(z) = -(Fki(z)+Fci(z));%N

        %calculat the resulting moment of the soil force for the element
        Mi(z) = -Fix(z)*li(z)*cos(gamma(z)+theta-pi);%N-m


    end
    %end of soil depth if statement
end
%end of for loop for soil elements

%display the states to the workspace; it's fun to watch the numbers scroll!
clc
disp(x)

%% Calculate the Truck Force and Moment

%calcuate the radial distance of the truck wrt C.M. of boulder-soil
%subsystem
```

```
lt = sqrt((di(1)+dt)^2+mass_center_x^2);%m

%calcuate the angle of the truck wrt C.M. of boulder-soil subsystem
gamma_t = atan(mass_center_x/(di(1)+dt));    % in thesis

%calcuate the foce acting on the truck
F_truck = -m_truck*x_truck_double_dot;%N

%truck rebound criteria
if F_truck<0
    F_truck = 0;%we don't want the truck to influence the boulder if it
    %'rebounds'.
end

%truck rebound criteria
if x_truck<0
    F_truck = 0;
end

%calculate the resultin moment of the truck acting on the boulder
M_truck = F_truck*lt*cos((gamma_t+theta));%N-m


%% Calculte the estimated restoring moment due to gravity

%calculate the total moment acting on the boulder without the restoring
%moment and set the restoring moment initially as the sum with opposite
%sign

if(sum(Mi)+sum(M_truck))~=0
    M_reac = -sign(sin(gamma_reac+x(3)))*...
        (sum(Mi)+sum(M_truck));%N-m
else
    M_reac = 0;
end

%calculate the maximum restoring momement
M_reac_max = m_boulder*g*lr*cos((gamma_reac+x(3)));

%limit the restoring moment to the maximum theoretical moment
if abs(M_reac)>abs(M_reac_max)%N-m
    M_reac = sign(M_reac)*M_reac_max;%N-m
end


%% DEOM
%Collect all of the forces and plug into the state space EOM

% set up boundaries so the boulder will not oscilate in the soil or
% continue to rotate beyond 90 degrees as there is no truck or mother earth
% to push back up on the boulder and 90 degrees is well beyond the
% approximation methods used thus far
if theta<pi/2&&theta_dot>-.1


    %convert the dimensioned form of all the forces into the equivalent pi
    %parameters as seen in CH.5
```

```
    %it should be noted that the states x[] are used within the DEOM and
    %not xb, xt, etc.

    %This is done quite simpley by multiplying the entire right hand side
    %of the equations by the scaling factor for force or moment

    %the force scaling factor is which is 1/(mg) and moment is 1/(mv^2)

%the states are driven by the dimensionless initial velocity of the truck
%which is 1.  v_o_truck/v_o_truck = 1;  It can also be conceptualized using
%the velocity vector of the truck after a simulation.  The dimensioned form
%will start at 13.4 m/s say, and the it is transformed into the
%dimesnionless zone by dividing the entire vector by the repeating
%parameter v_o_truck, which low and behold gives you 1 at the time of
%impact.
    xprime = [x(2);...%pi_dot_xb is pi_xbdot, the dimensionless rate
        %of change of the parameter is the next parameter

    %the left hand side of the xb_dotdot code is the dimensionless form of
    %the effective mass of the system.  meff is turned into pi_meff simply
    %by dividing by the repeating parameter m_truck. the ratio is inverted
    %in the xdd line because of state space form, governing DEOM for the
    %boulder in the X direciton is mxdd = ... so xdd = 1/m*forces.
        m_truck/(m_boulder+sum(mi))*...
        ((sum(Fix)+sum(F_truck))/(m_truck*g));... EOM for xb

        x(4);... %pi_dot_theta (if you will), is pi_thetadot

        %similar to the boulder translation, the boulder rotation is made
        %dimensionless by multiplying both sides by the representative
        %repeating parameter grouping.  pi_J = g^2*J/(mv^4) therefore, it
        %is inverted and multiplied with the dimesnionless moments as
        %created using pi_Mommy = M/(mv^2) , Nm / (kgm^2/s^2) is indeed
        %dimensionless
        m_truck*v_initial^4/(g^2*(I_b+sum(mi.*...
        (di.^2+(L-mass_center_x)^2))))*((sum(Mi)+sum(M_truck)+M_reac)...
        /(m_truck*v_initial^2));... EOM for pi_dot_thetadot
        %or pi_thetadotdot

        x(6);... %pi_dot_xt is pi_xtdot

        x(7);... %pi_dot_vt is pi_xtdotdot

        %samesies as the boulder x dirction
        %this one is a bit more intricate since the equation was not
        %written explicitly in terms of forces, but rather it had k_truck,
        %c_truck, etc. etc.  Therefore each parameter was turned into the
        %dimensionless form.
        -kt*(v_initial^2/(m_truck*g^2))*x(6)-kt*(v_initial^2/...
        (m_truck*g^2))/(ct*(v_initial/(m_truck*g)))*x(7)+...
        kt*(v_initial^2/(m_truck*g^2))*(x(2)+...
        x(4)*lt*g/v_initial^2*cos(gamma_t+x(3)))];  %DEOM for a
    %dimensionless truck, ba ba baaaaa ghost truck.

else% if the boulder goes beyond 90 degrees or starts to rock backwards,
    %kill the sum beech
    xprime = [0;0;0;0;0;0;0];
end
```

FCN_FRACTURE.M

```
function [n,sigma1] = fcn_fracture(lengthCantilever,peakForce,W,L,...
    sigmaTensileUltimate,sigmaCompressionUltimate)

%Mark P. Keske, mark.keske@gmail.com

%% Calculate the factor of safety for the given boulder geometries

%Calculate the maximum bending moment from the impact
peakMoment = peakForce*lengthCantilever; %N-m

%Calculate area moment of inertia, assuming impact is along the length axis
I_area = 1/12*W*L^3; %m^4
A_area = L*W;%m^2

%Normal stress as a result of bending
sigmaX = peakMoment*L/2 / I_area; %N/m^2;

%Shear force from impact
tauXY = peakForce/A_area;  %N/m^2;

%Calculate the principle stresses
sigma1 = (sigmaX/2 + sqrt((sigmaX/2)^2+tauXY))/1e6;  %MN/m^2
sigma2 = (sigmaX/2 - sqrt((sigmaX/2)^2+tauXY))/1e6;  %MN/m^2

%Apply Brittle Coulomb Mohr failure criteria since it is more
%conservative than Modified Mohr

%negative value used for contour plotting

if (sigma1>=sigma2 && sigma2>=0)  %First Quadrant of o2 vs. o1
    n = -(sigmaTensileUltimate/sigma1-1);
elseif (sigma1>=0 && 0>=sigma2)  %4th Quadrant of o2 vs. o1
    n = -((sigma1/sigmaTensileUltimate-sigma2/sigmaCompressionUltimate)^-1-1);
else
    n = -(-sigmaCompressionUltimate/sigma2-1);
end
```